Journal of Nanomaterials

# Nanomaterials for Sustainable Development using Green Chemistry, Engineering and Technologies (GCET)

Lead Guest Editor: Sesha Srinivasan
Guest Editors: Ganga Ram Chaudhary, Scott L. Wallen, Mousami Munot, and Rajeev Kumar

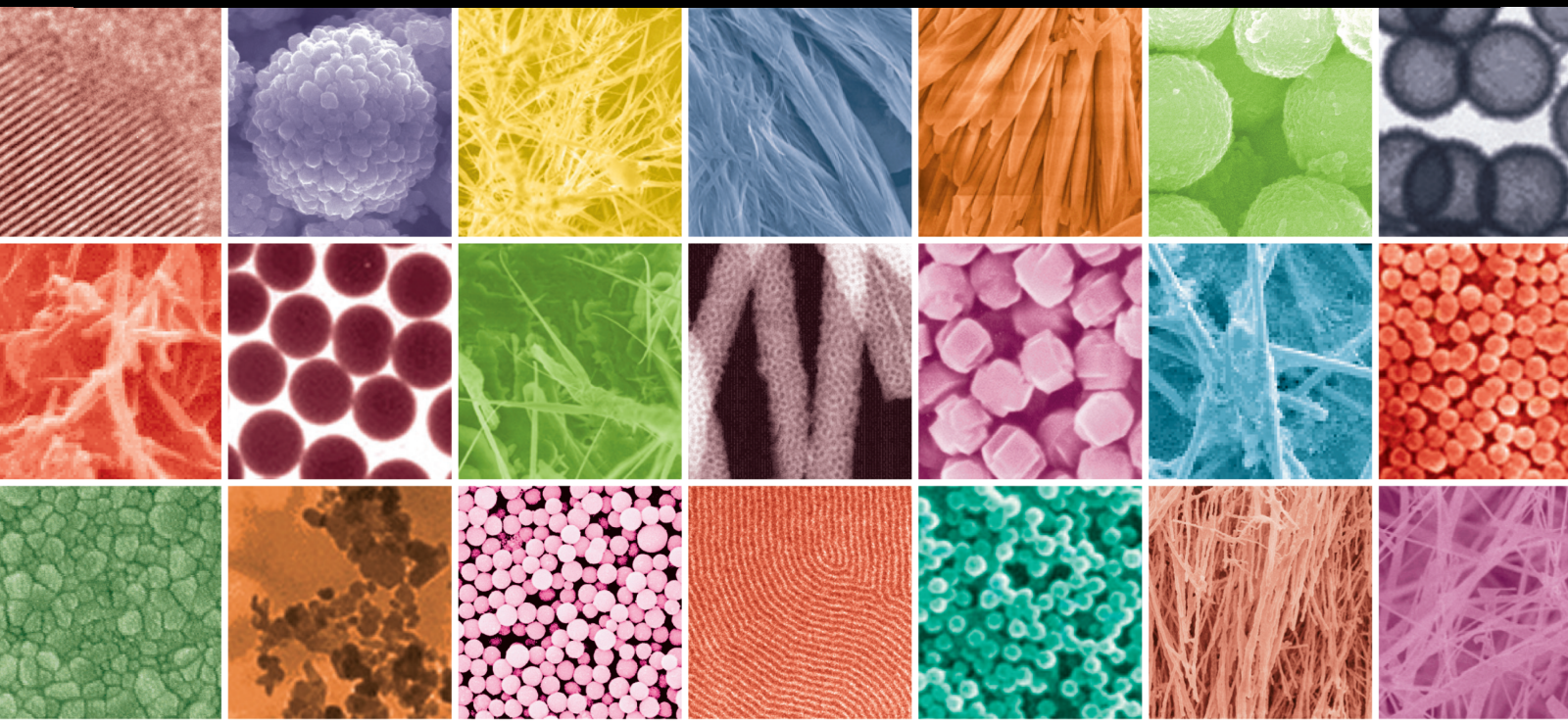

# Nanomaterials for Sustainable Development using Green Chemistry, Engineering and Technologies (GCET)

Journal of Nanomaterials

# Nanomaterials for Sustainable Development using Green Chemistry, Engineering and Technologies (GCET)

Lead Guest Editor: Sesha Srinivasan
Guest Editors: Ganga Ram Chaudhary, Scott L. Wallen, Mousami Munot, and Rajeev Kumar

# Contents

Hindawi
Journal of Nanomaterials
Volume 2020, Article ID 6123178, 15 pages
https://doi.org/10.1155/2020/6123178

*Research Article*

# Proficient Photocatalytic and Sonocatalytic Degradation of Organic Pollutants Using CuO Nanoparticles

**Moondeep Chauhan,[1] Navneet Kaur,[1] Pratibha Bansal,[1] Rajeev Kumar,[1] Sesha Srinivasan,[2] and Ganga Ram Chaudhary[1]**

[1]*Department of Chemistry & Center of Advanced Studies in Chemistry and Department of Environmental Studies, Panjab University, 160014, Chandigarh, India*
[2]*Department of Natural Sciences, Division of Science, Arts and Mathematics (SAM), Florida Polytechnic University, Florida-33805, USA*

Correspondence should be addressed to Sesha Srinivasan; ssrinivasan@floridapoly.edu

Received 26 September 2019; Revised 19 March 2020; Accepted 4 April 2020; Published 10 June 2020

Academic Editor: Silvia Licoccia



In recent years, due to the advancement in nanotechnology, advanced oxidation processes (AOPs), especially sonocatalysis and photocatalysis, have become a topic of interest for the elimination of pollutants from contaminated water. In the research work reported here, an attempt has been made to study and establish a physicochemical mechanism for the catalytic activity of copper oxide nanoparticles (CuO NPs) in AOPs using the degradation of dyes as model contaminants. CuO NPs exhibited brilliant sonocatalytic and photocatalytic activities for the degradation of a cationic dye (Victoria Blue) as well as an anionic dye (Direct Red 81). The degradation efficiency of CuO NPs was calculated by analysing the variation in the absorbance of dye under a UV-Vis spectrophotometer. The influence of different operating parameters on the catalytic activity of CuO NPs, such as the amount of catalysts dose, pH of the solution, and the initial dye concentration, was thoroughly investigated. In addition, the kinetic process for the degradation was also examined. It was observed that both dyes exhibited and followed the pseudo-first-order kinetics relation. The rate constant for sonocatalysis was high as compared to photocatalysis. The rate constant for both sonocatalysis and photocatalysis was successfully established, and reusability tests were done to ensure the stability of the used catalysts. To get an insight into the degradation mechanism, experiments were performed by using $^{\cdot}OH$ radical scavengers. The efficacy of CuO NPs for dye decolorization was found to be superior for the sonocatalyst than the photocatalyst.

## 1. Introduction

Although awareness of the need to avoid contamination of the environment has increased, large amounts of synthetic or natural pollutants, such as dyes, heavy metals, pharmaceutical waste, and agrotoxic waste, like pesticides, continue to be discharged in the environment by different industries [1]. Among these, synthetic organic dyes are one of the leading contributors to environmental pollution since dyes are used by various industries, such as plastic, paper, textile, leather, cosmetic, and food industries [2, 3]. As dyes have a complex aromatic structure and are difficult to degrade, their presence in the aquatic environment can cause problems, such as color change, odor alteration, eutrophication, under-oxygenation, and bioaccumulation [4]. Therefore, their removal from industrial wastewater is highly desirable to achieve concentrations below environmentally accepted levels for safe disposal.

At present, several techniques have been developed for the removal of pollutants from wastewater, such as adsorption, chemical coagulation, filtration, sedimentation, and advance oxidation process (AOPs) [5–8]. Recently, AOPs are gaining significant importance due to their ability to generate a sufficient number of highly reactive radicals for effective water decontamination. Among numerous AOPs, photocatalysis and sonocatalysis with metal oxide nanoparticles (NPs) have

attracted more attention as efficient techniques for the degradation of toxic organic contaminants [9–18].

In the case of photocatalytic degradation, irradiation with photon energy greater than the band gap of NPs leads to the formation of electron and hole pairs, which further helps in the generation of highly reactive oxygen species (ROS) that eventually participate in the degradation of toxic compounds [19–23]. It is evident that the limiting factor for catalytic degradation depends upon the ability to form greater numbers of ROS [24]. On the other hand, sonocatalytic degradation of toxic compounds is caused by a chemical effect of ultrasonic (US) waves which arises from acoustic cavitation, i.e., formation, growth, and collapse of bubbles in a liquid [25]. The transient bubble collapse generates a localized hot spot with a very high temperature (near about 5000 K) and pressure (~500 bars). Under such extreme conditions, thermal decomposition of water takes place, resulting in the formation of highly reactive radical species such as ·OH, ·H, and ·O, which can oxidize and degrade organic contaminants in water [26].

In keeping with environmental concerns, there is a significant shift towards the use of nanoparticles in developing green and environmentally friendly approaches in synthetic chemistry [27]. In our previous work, we have reported the synthesis of CuO NPs and further investigated their catalytic activity in the synthesis of xanthenes [28]. The synthesis of CuO NPs was carried out with microwaves, using a greener approach, which has achieved many advantages in the synthesis of xanthenes, such as low energy, cost effectiveness, shorter processing time, less pollution, utilization of a green solvent, and a lower reaction temperature with high yield as compared to other methods [28]. As determined through X-ray diffraction studies, the as-synthesized NPs were composed of a pure CuO phase with a monoclinic structure without any peaks of impurity (Figure S1, supplementary data). Particle size, as calculated from FWHM of reflection (111/200) of monoclinic CuO structure using the Debye Scherrer formula, was found to be 18 nm. For determining the morphology, the TEM micrograph of CuO NPs was taken and NPs were observed to be almost spherical in shape, well dispersed, and within the narrow range of size distribution (17–22 nm) (Figure S2, S3, supplementary data) [28].

In the present work, we have explored CuO NPs as a catalyst for degradation of Victoria Blue (VB) and Direct Red 81 (DR) dyes as model organic contaminants. To find out which energy source is better in terms of the synergistic effect with CuO NPs for the degradation of dyes, we have used UV-visible light and US waves as sources of energy. The effect of pH, catalyst dosage, and initial dye concentration with respect to contact time has been particularly evaluated. An attempt has also been made to recover the CuO NPs from the reaction mixture in both cases and to reuse them in subsequent processes. The kinetics rate constant of dyes under both energy sources has been evaluated and found to have significant efficiency.

## 2. Experimental Details

*2.1. Materials and Techniques.* Victoria Blue (VB) and Direct Red 81 (DR) dyes were obtained from Sigma-Aldrich. Dimethyl sulfoxide and sodium bicarbonate were purchased from Qualigens, and absolute ethanol (purity 99.9%) was purchased from Changshu Yangyuan Chemicals, China. All of the chemicals were used as received, and double distilled water was used for the preparation of different solutions. Characterization of recycled nanoparticles was done by transmission electron microscope (TEM) (TEM; Hitachi-H-7500) operating at 80 kV. The crystallinity and X- ray diffraction pattern of the samples were performed at room temperature utilizing X-ray diffraction (XRD; PANanalytical X'Pert Pro) equipped with Cu-k$\alpha$ radiation ($\lambda = 1.54178$ Å) with A scanning speed of 8 $min^{-1}$, in the 2ϴ range of 0–90°. The zeta potential of the CuO NPs was examined at different pH ranges with a Malvern Zetasizer (ZS 90) at room temperature.

*2.2. Synthesis and Characterization of CuO NPs.* CuO NPs have been synthesized via a cost-effective and greener approach by using microwave and DI water as the medium. Within 4 minutes of reaction time, very high yields of CuO NPs were achieved. Detailed procedure and characterization have been reported earlier [5]. To study the photocatalytic and sonocatalytic efficiency of the NPs, surface area of the nanoparticles should be known. BET (Branauer-Emmett-Teller) surface area of CuO NPs was studied using Quantachrome Instrument (version 3.01).

*2.3. Sonocatalytic and Photocatalytic Degradation Reaction Procedures.* To evaluate the catalytic (photocatalytic and sonocatalytic) activity of CuO NPs and to further understand the degradation mechanism of both the dyes, batch experiments were performed at room temperature. Before exposing to ultrasonic waves or UV-visible light, the suspensions (dye+NPs) were kept in dark conditions and stirred for 10 minutes to get the adsorption-desorption equilibrium of the dye on the CuO NPs. Therefore, the effect of adsorption during sonocatalysis or photocatalysis could be calculated accurately.

In case of sonocatalysis, these suspensions were placed in an ultrasonic bath apparatus (PCI Analytics) for a definite interval of time. After ultrasonic irradiation, CuO NPs were separated from the suspension by centrifugation and percent degradation was calculated by measuring the change in the absorbance of dye using UV-Vis spectrophotometer. In the case of photocatalysis, the experiment was carried out by placing the suspended solution in a UV-visible photoreactor (125 W, 198.4 $mWS^{-2}$) for a definite time interval. After exposure to UV-visible radiations for a desired time interval, samples were withdrawn from the chamber and CuO NPs were separated from the suspension by centrifugation. The degradation rates of the dyes at given time intervals were calculated by measuring the changes in the absorption profile at their maximum absorbance wavelength ($\lambda_{max}$) using a UV-vis spectrophotometer (UV 2100, Shimadzu). The degradation observations were performed under ambient conditions and the temperature was kept at 25-30°C. Typically, 20 ml of $10 \times 10^{-5}$ M solutions of both dyes with initial solution pH 10 for VR dye and 4.0 for DR dye were taken, and 25 mg of catalyst dose was taken in general throughout the whole investigation. For sonocatalysis, ultrasonic irradiation of 50 kHz frequency and 50 W power were used, and for photocatalysis,

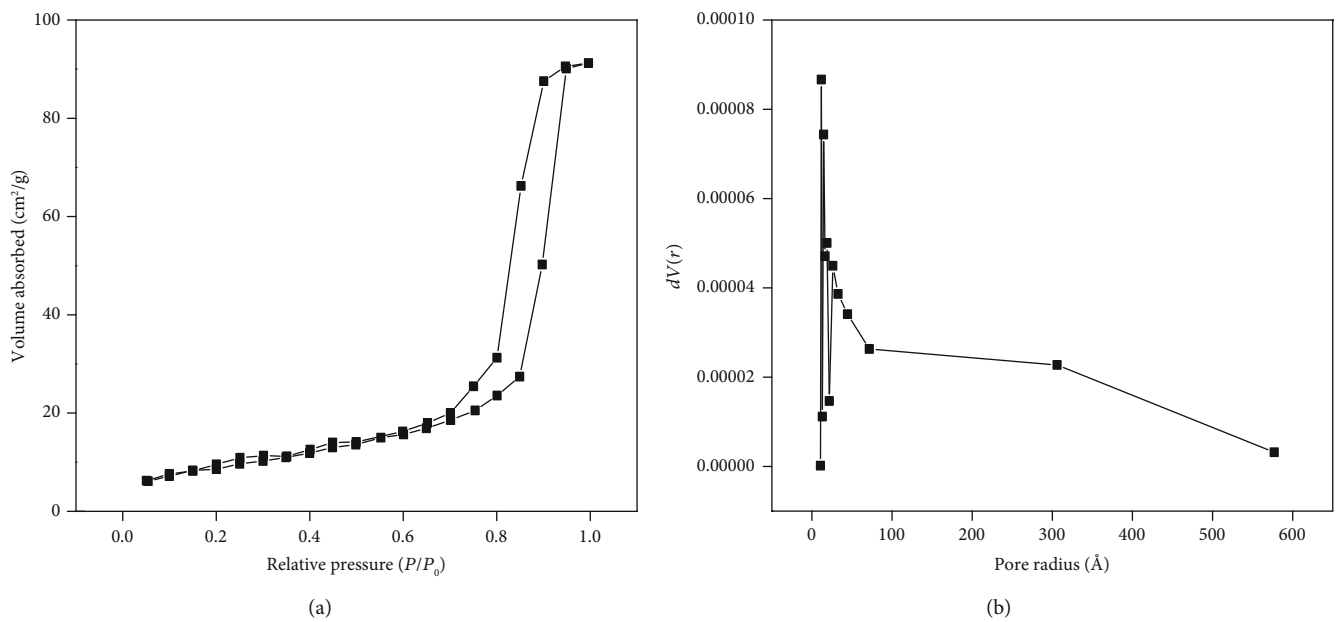


Figure 1: (a) $N_2$ adsorption-desorption BET isotherms and (b) BJH pore size distributions (from the adsorption branch of the isotherms) of synthesized CuO NPs.

at UV-visible irradiation frequency 198.4 mWS$^{-2}$ and 125 W power. In addition, the pH of the dye solutions was adjusted to required pH by adding 0.1 M HCl or NaOH solution. The pH value of solutions was measured by a CyberScan 510 digital pH meter.

The following equation (equation (1)) was used for calculating the degradation efficiency (percent degradation) of dyes:

$$\text{Degradation efficiency } (\%) = \frac{C_0 - C_t}{C_0} \times 100, \quad (1)$$

where $C_0$ is the initial concentration of the dye before irradiation and $C_t$ is the concentration of the dye at a certain reaction time $t$ (min) after irradiation. The sonocatalytic activity of CuO NPs, in terms of the degradation of VB and DR, was compared with that of the photocatalytic activity of CuO NPs under UV-visible irradiation. Multiple factors are responsible for the sonocatalytic efficiency of CuO NPs which are difficult to quantify individually. Moreover, sonocatalysis and photocatalysis are two completely different phenomenon; therefore it is hard to find a correlation factor between the US and UV-Vis energy sources.

## 3. Results and Discussion

*3.1. Characterization of CuO NPs.* The BET isotherms and their relative Barret–Joyner–Halender (BJH) pore size distributions obtained from the adsorption branch of the isotherms of the CuO NPs are displayed in Figure 1(a). It was observed that the prepared CuO NPs possess a mesoporous surface as the isotherms are of type IV. The multipoint BET-specific surface area for CuO NPs was found to be 49.33 m$^2$g$^{-1}$. The CuO NPs were found to have an average pore radius of 1.1764 nm (Figure 1(b)).

*3.2. Percentage Degradation of VB and DR under Different Processes.* The degradation efficiency of VB (pH 10) and DR (pH 4) was investigated by exposing the dye solution to UV-visible irradiation or ultrasonication in the absence and in the presence of CuO NPs (25 mg). Both dyes undergo negligible decomposition under direct UV-visible irradiation or US radiation in the absence of CuO NPs. On the other hand, the presence of CuO NPs showed excellent results as a photocatalyst and sonocatalyst in the degradation of both dyes (Figure 2).

*3.3. Effect of pH.* The pH of the solution is an important parameter that plays a significant role in the sonocatalytic and photocatalytic degradation of various target pollutants [13, 29]. The zeta potential of the CuO NP dispersions was measured over pH values ranging from 2 to 10, and the corresponding pHzpc was found to be ~8.5 (Figure S4 supplementary data). The effect of pH on the photocatalytic activity of CuO was tested using acidic, neutral, and basic media, and the results are shown in Figures 3 and 4, respectively. It was observed that CuO NPs in both degradation processes follow a pseudo-first-order kinetics at different pH [30]. The equation used is as follows:

$$\ln \frac{C_0}{C_t} = kt, \quad (2)$$

where $k$ is the pseudo-first-order rate constant (min$^{-1}$), $C_0$ is the initial concentration (at time $t = 0$) of the dye, and $C_t$ is the concentration of the dye at reaction time $t$. As can be seen in Table 1, rate constant $k$ value increases for the VB dye from pH 4 to pH 10, and for the DR dye, the $k$ value decreases from pH 10 to pH 4. Thus, the increase in pH leads to an enhanced degradation rate of VB dye and it reached maximum at pH 10. However, in the case of the DR dye,

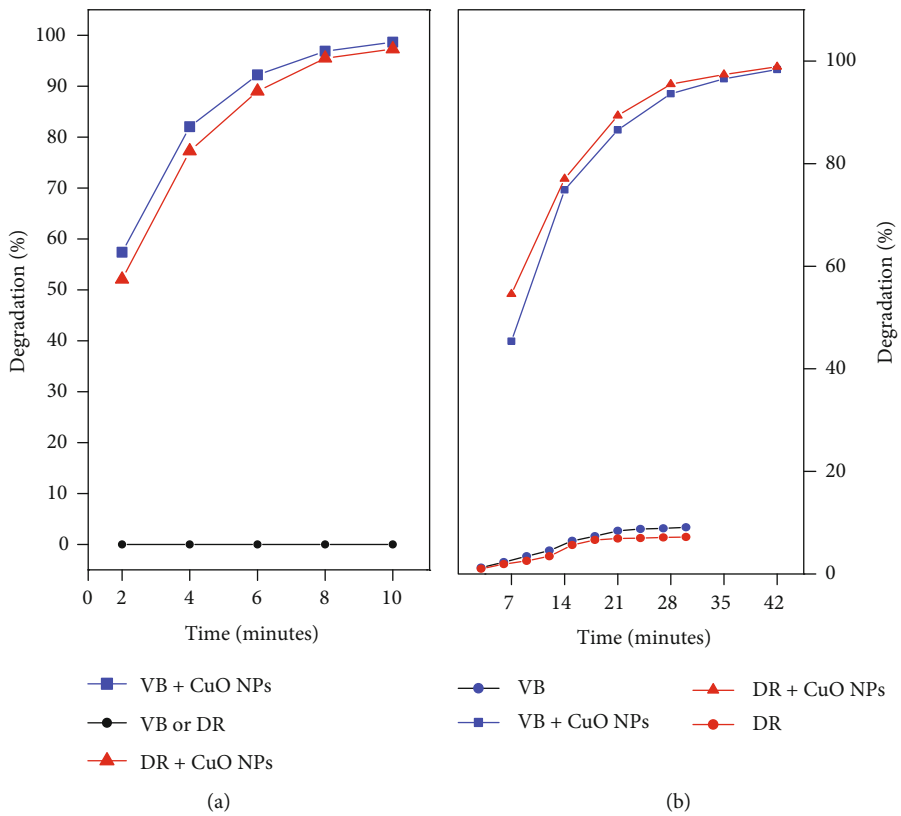


Figure 2: Degradation of VB and DR dye treated with different process $10 \times 10^{-5}$ M dye solution, CuO NP is 25 mg. (a) US irradiation. (b) UV-visible irradiation.

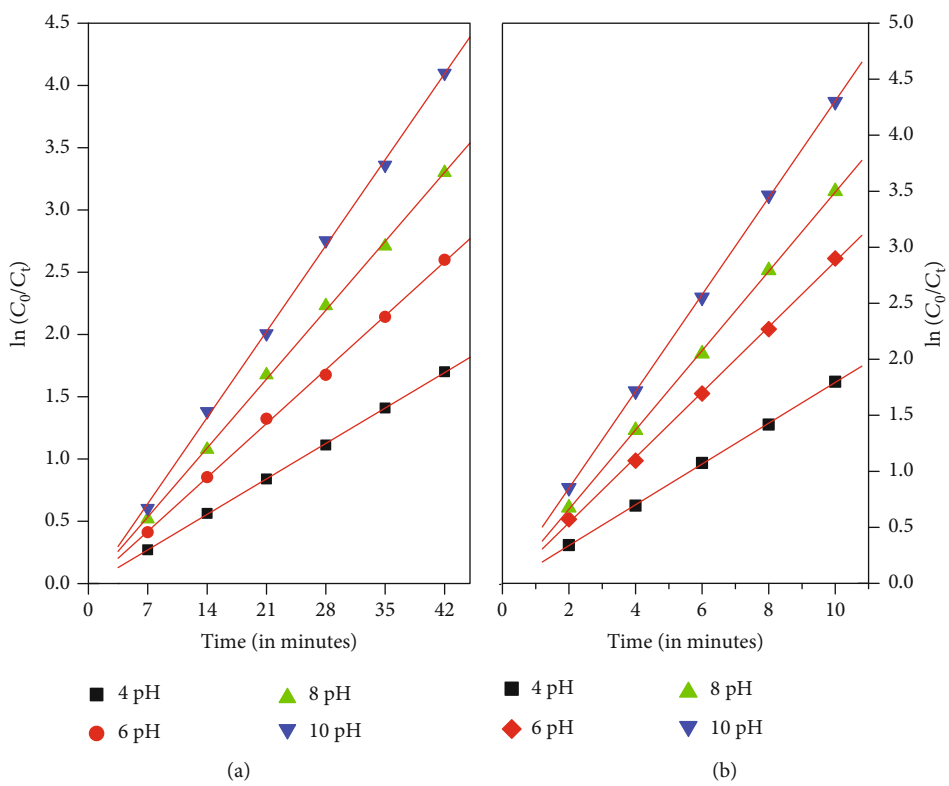


Figure 3: Effect of pH on degradation of VB under (a) UV-visible irradiation and (b) US irradiation.

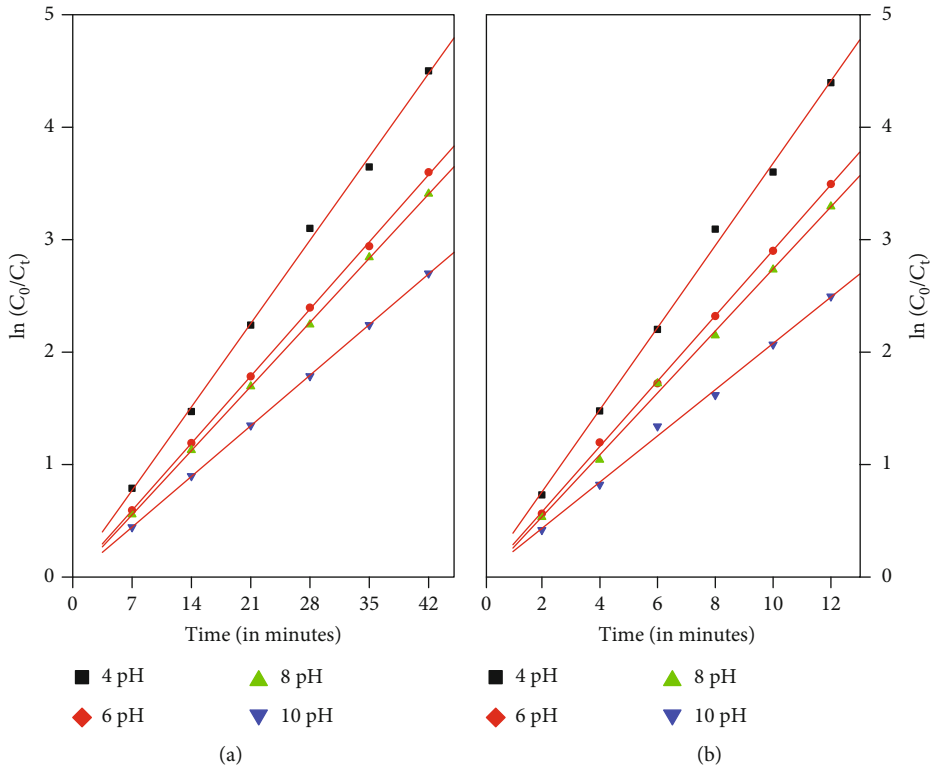


Figure 4: Effect of pH on degradation of DR under (a) UV-visible irradiation and (b) under US irradiation.

Table 1: Pseudo-first-order kinetics rate constants for the degradation of VB and DR under both sources of energy and for different pH.

| Dyes | pH | Sonocatalysis $k$ ($min^{-1}$) | Photocatalysis $k$ ($min^{-1}$) | $R$ sonocatalysis | $R$ photocatalysis |
|---|---|---|---|---|---|
| Victoria Blue (VB) | 4 | 0.182 | 0.04067 | 0.99986 | 0.99991 |
| | 6 | 0.29153 | 0.06185 | 0.99955 | 0.99944 |
| | 8 | 0.35388 | 0.07903 | 0.9999 | 0.99959 |
| | 10 | 0.43209 | 0.09861 | 0.99992 | 0.99954 |
| Direct Red (DR) | 4 | 0.3656 | 0.10587 | 0.9985 | 0.99888 |
| | 6 | 0.29098 | 0.08525 | 0.99983 | 0.99982 |
| | 8 | 0.27584 | 0.08144 | 0.99901 | 0.99996 |
| | 10 | 0.20578 | 0.06428 | 0.99825 | 0.99998 |

the results indicated that the sonodegradation and photodegradation of the dye were maximally efficient in acidic conditions and the optimal pH was observed at about 4.0.

For VB, higher degradation efficiency in the basic medium must be ascribed to the surface charge properties of CuO NPs (zero-point charge (zpc) ~8.5). The surface charge is positive at pH values lower than $pH_{zpc}$, neutral at $pH_{zpc}$ and negative at higher $pH_{zpc}$ value. At higher pH, the CuO NP surface is negatively charged, so it enhances its interaction with the cationic dye (VB) through electrostatic force of attraction [31] (Scheme 1). Whereas in the case of DR, at lower pH, the surface of CuO NPs is positively charged so there is an enhancement of electrostatic force of attraction with the anionic dye (DR). Therefore, there is more degradation of DR dye at pH 4 [32] (Scheme 1).

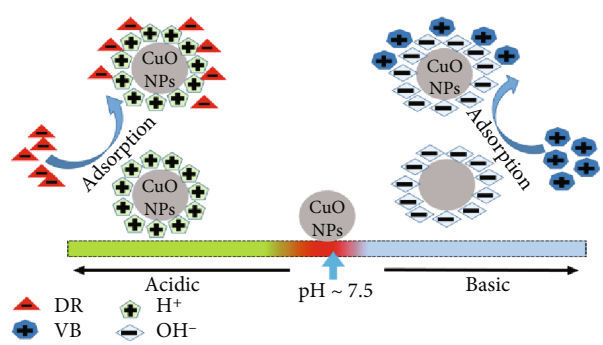


Scheme 1: Role of zero-point charge of NPs on the adsorption of cationic and anionic dyes.

*3.4. Effect of Catalyst Dose.* The effect of the catalyst dose on the degradation of VB and DR was studied by varying the amount of the catalyst from 3 mg to 30 mg in 20 ml of $10 \times 10^{-5}$ M dye solution at initial pH of 10 (VB) and 4 (DR) for reaction time, i.e., 7 minutes for sonocatalysis and

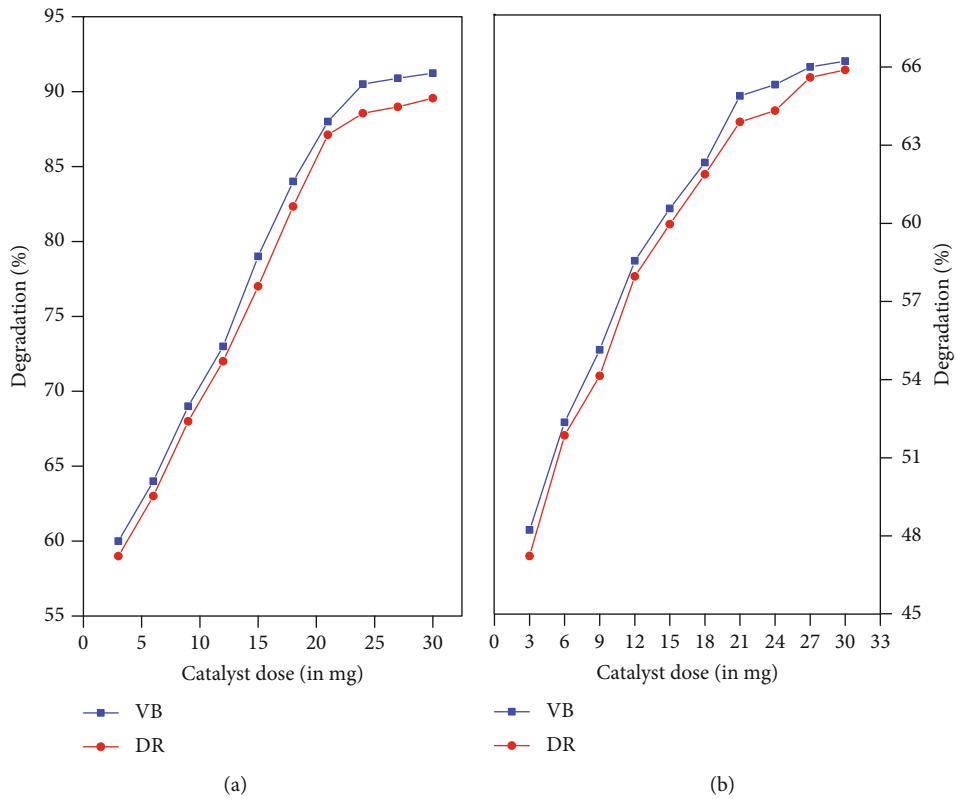


Figure 5: Effect of catalyst dose on degradation of VB and DR for (a) UV-visible irradiation and (b) under US irradiation.

12 minutes for photocatalysis. Figure 5 revealed that increasing the catalyst dose from 3 to 25 mg resulted in an increase in the degradation efficiency, while further increase in the amount of the catalyst dose to 30 mg caused an insignificant increase in the (%) degradation efficiency (Table S1–S4 supplementary data). Enhanced catalytic activity with increasing CuO NP content could be interpreted by two speculations: (1) there will be more availability of active sites and (2) deactivation of activated dye molecules by collision with molecules in the ground state [13]. $^{\cdot}$OH radicals were the actual oxidants for the decomposition of the VB and DR dyes, whose concentration increases with an increase in catalyst dosage [13].

*3.5. Effect of Initial Dye Concentration.* From an application point of view, it is important to study the effect of initial VB and DR concentration on its sonocatalytic or photocatalytic degradation efficiency (%). It was studied by varying initial dye concentration in the range among $10 \times 10^{-5}$, $12 \times 10^{-5}$, and $15 \times 10^{-5}$ M using an NP dosage of 25 mg in 20 ml of dye solution and at a suitable pH. The results showed that the degradation efficiency (%) of dyes is inversely proportional to its initial concentration. As a result, increasing the initial dye concentration led to a decrease in the degradation (%) of dyes (Figures 6 and 7). This negative effect may be caused by the following: (i) The number of dye molecules that was adsorbed on the surface of the catalyst increases with the increasing dye concentration. In addition, at a high dye concentration, a significant amount of UV light or ultrasonic irradiation may be absorbed by the dye molecules rather than by the catalyst, thereby reducing the efficiency of the catalytic reaction. (ii) The generation of $^{\cdot}$OH radicals on the surface of the catalyst is likely to be reduced since active sites on the surface of the catalyst are occupied by the dye ions. (iii) With the increasing dye concentration, the number of hydroxyl radicals required for the degradation of dye molecules increases, although the formation of hydroxyl radicals remains constant for a given catalyst dosage, irradiation time, and intensity [13].

*3.6. Mechanism.* In the case of photocatalysis, as UV-visible irradiation falls on semiconducting CuO NPs, it induces the formation of electron-hole pairs through the photoexcitation of electrons from the valence band to the conduction band (equation (3)) [33].

$$\mathrm{CuO} \xrightarrow{\text{UV-visible}} \mathrm{h}^{+} + \mathrm{e}^{-}. \tag{3}$$

Photogenerated electrons react with dissolved molecular oxygen, forming a superoxide ion $O_2^{\cdot -}$ (equation (4)), which further react with a proton to form a hydroperoxide radical ($HO^{\cdot}_2$) (equation (5)).

$$\mathrm{e}^{-} + \mathrm{O}_2 \longrightarrow \mathrm{O}_2^{\cdot -} \tag{4}$$

$$\mathrm{O}_2^{\cdot -} + \mathrm{H}^{+} \longrightarrow \mathrm{HO}_2^{\cdot} \tag{5}$$

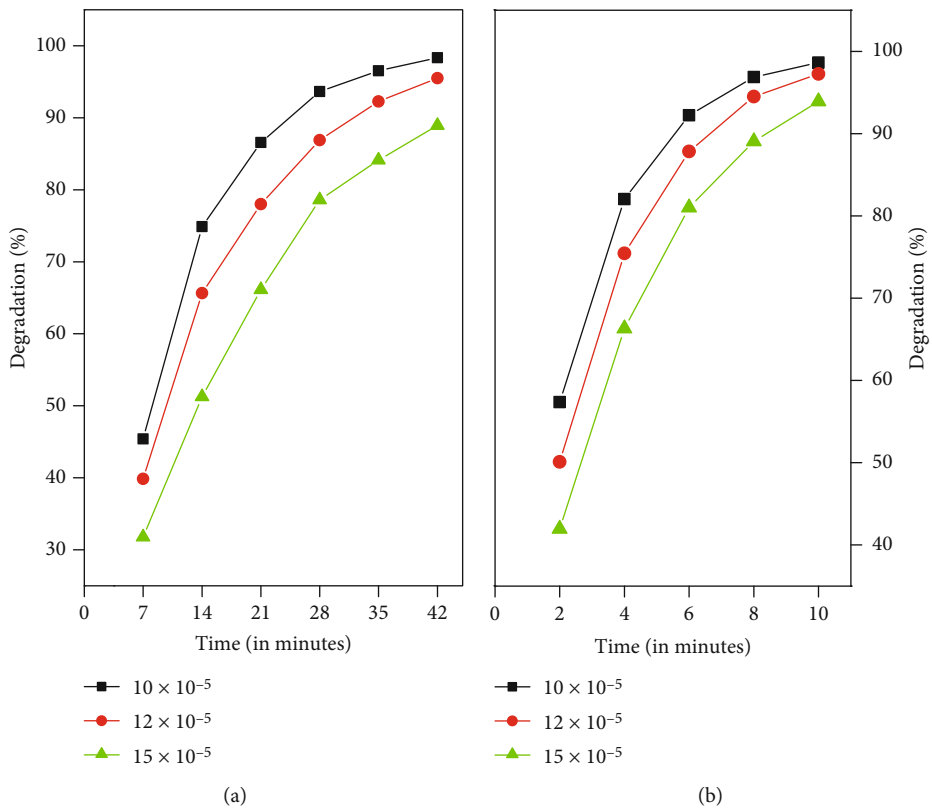


Figure 6: Effect of initial concentration VB dye on degradation under (a) UV-visible irradiation and (b) US irradiation.

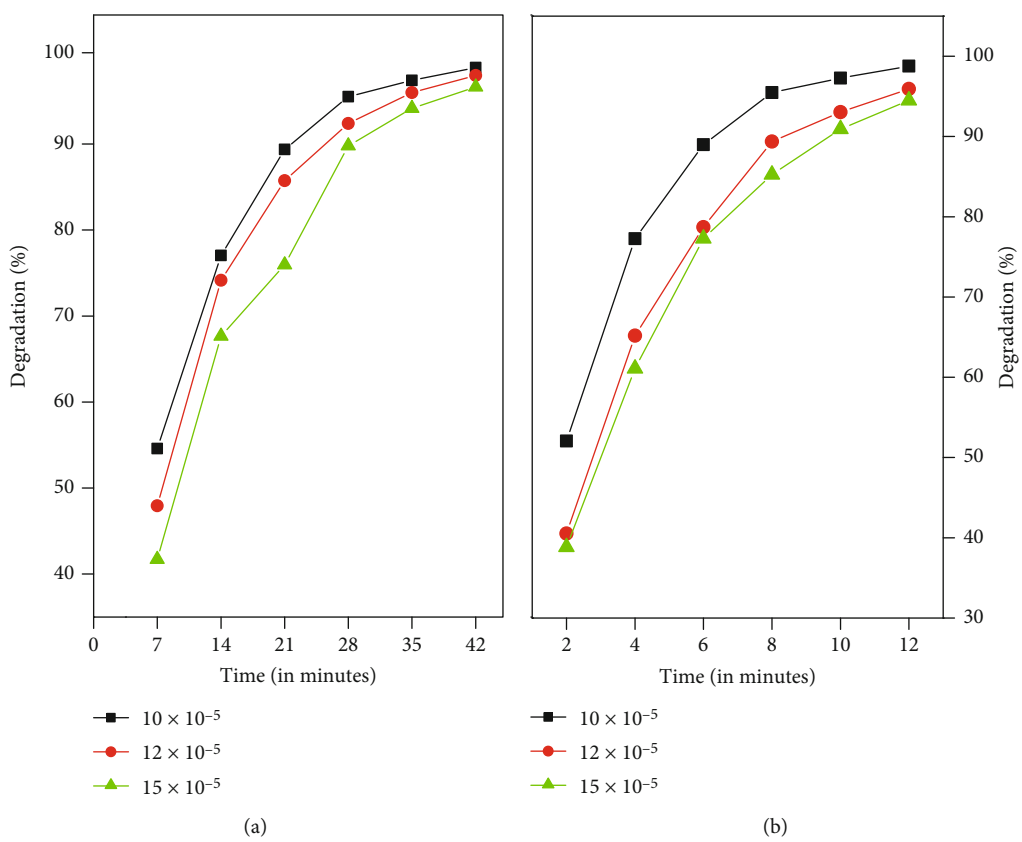


Figure 7: Effect of initial concentration DR dye on degradation under (a) UV-visible irradiation and (b) US irradiation.

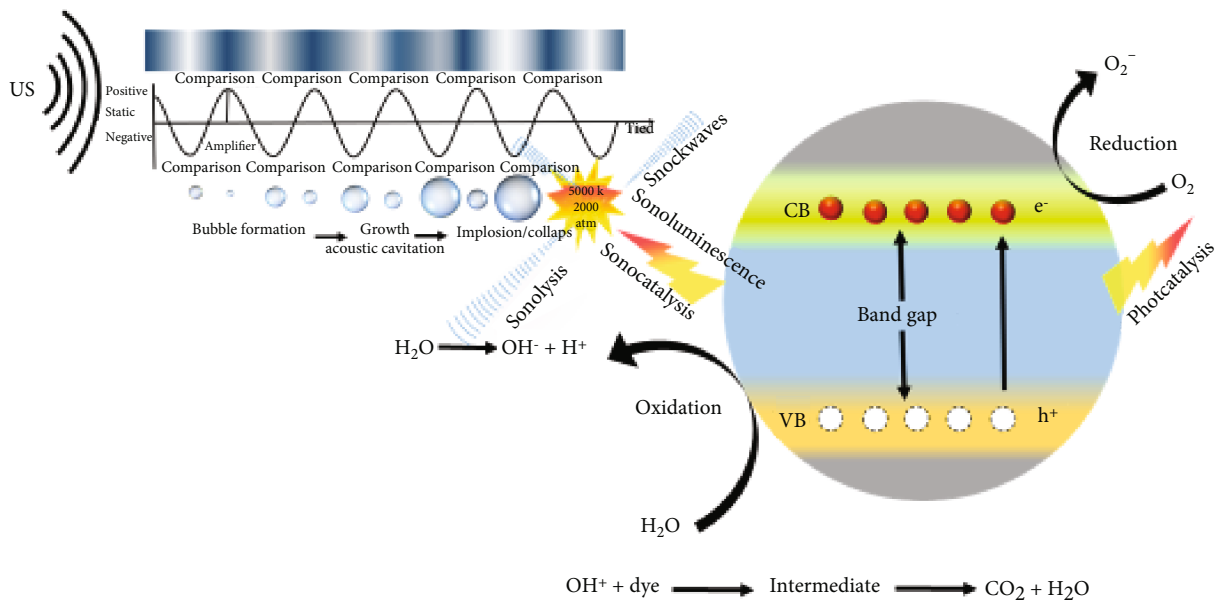


Scheme 2: Schematic diagram representing the photocatalytic and sonocatalytic degradation mechanisms.

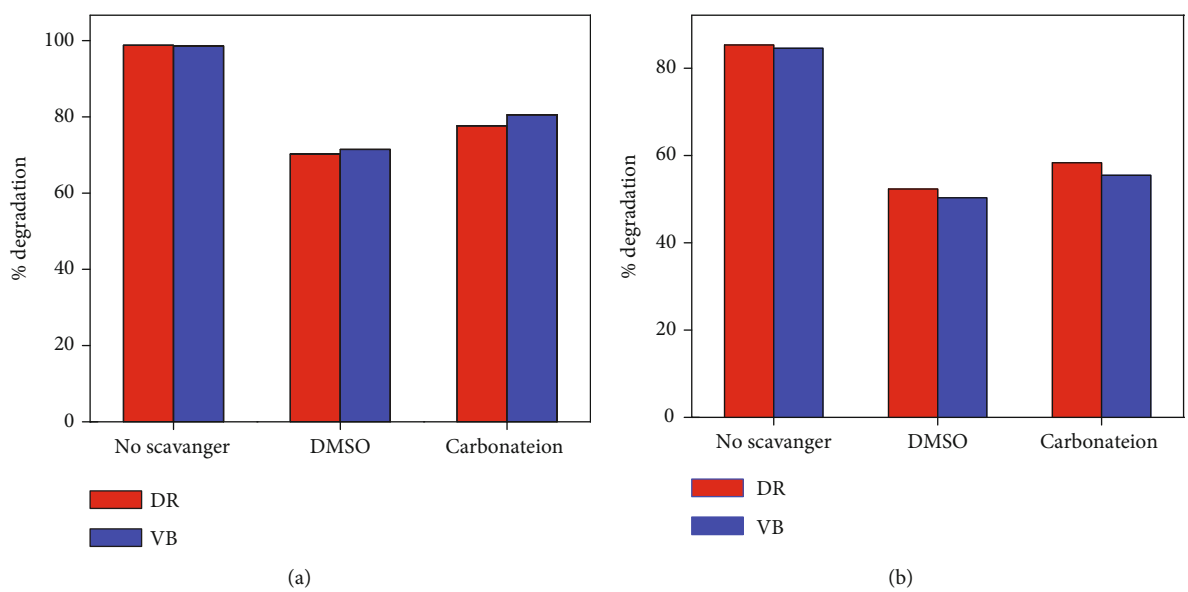


Figure 8: Influence of adding different scavengers (DMSO and carbonate ion). Experimental conditions: scavenger concentration 1 M, catalyst weights 30 mg, pH 8 (VB), and 4 (DR) (a) under US irradiation and (b) under UV-visible irradiation.

Simultaneously, photogenerated holes can react with water molecules (equation (6)) and the hydroxide anions ($OH^-$) to form highly active hydroxyl radicals (•OH) (equation (7)).

$$h^+ + H_2O \longrightarrow h^+ + HO^{\cdot} \tag{6}$$

$$h^+ + OH^- \longrightarrow HO^{\cdot} \tag{7}$$

The superoxide and hydroxyl radicals have strong oxidation performance, which can completely oxidize the VB/DR dye molecules into the final products $CO_2$ and $H_2O$ (equations (8) and (9)).

$$\text{VB/DR} + \text{catalyst} - OH^{\cdot} \xrightarrow{\text{US/UV-visible}} CO_2 + H_2O + \text{inorganic} \tag{8}$$

$$\text{VB/DR} + \text{catalyst} - O_2^{\cdot -} \xrightarrow{\text{US/UV-Visible}} CO_2 + H_2O + \text{inorganic} \tag{9}$$

On the other hand, the chemical effects of ultrasound are due to the phenomenon of cavitation which is the nucleation, growth, and collapse of bubbles in a liquid

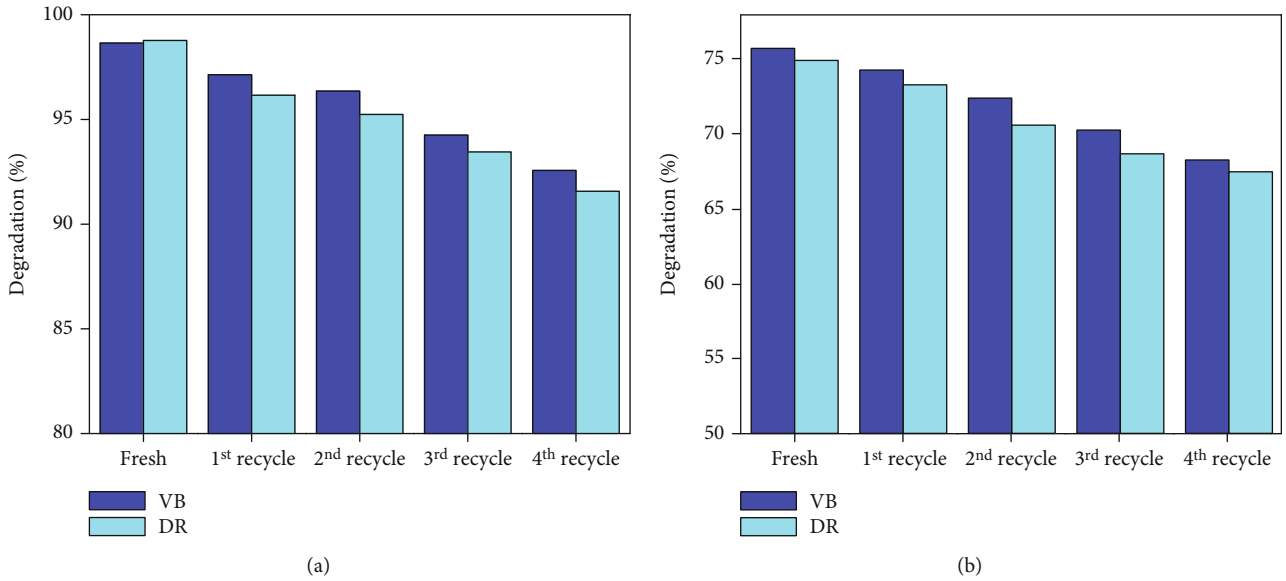


Figure 9: Recyclability of CuO NPs (25 mg) for the degradation of VB (pH 10) and DR (pH 4) dyes, time 12 minutes under (a) US irradiation and (b) UV-visible irradiations.

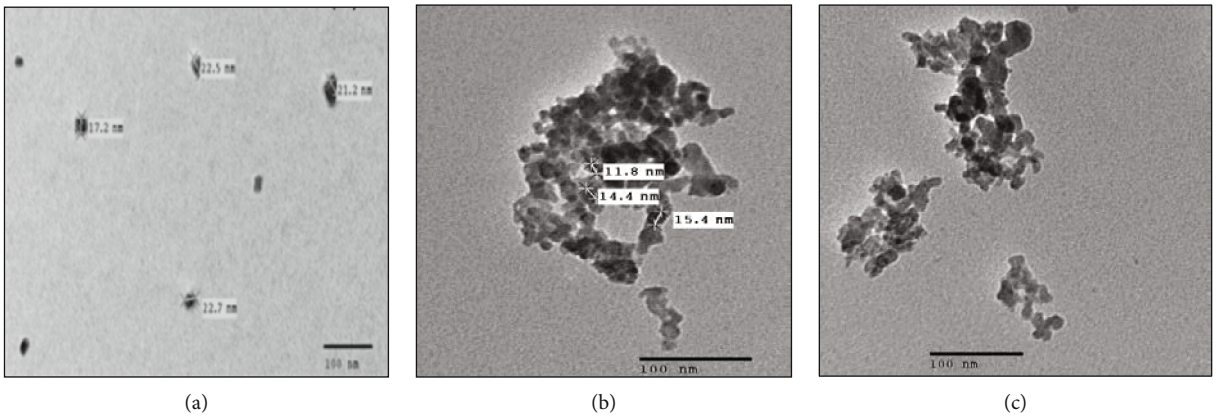


Figure 10: TEM of CuO NPs (a) first time synthesized, (b) recycled after sonocatalytic degradation, and (c) recycled after photocatalytic degradation.

[34]. The collapse of the bubbles induces high-energy phenomena, i.e., high temperature and pressure (~5000 K and 500 bars), electrical discharges, and plasma effects. The consequences of these extreme conditions are the direct thermal dissociation (sonolysis) of dissolved dioxygen and water molecules into highly reactive radical species such as $^{\cdot}OH$, hydrogen ($^{\cdot}H$), and oxygen ($^{\cdot}O$).

$$H_2O \xrightarrow{\text{US|Sonolysis}} OH^{\cdot} + H^{\cdot} \quad (10)$$

$$O_2 \xrightarrow{\text{US|Sonolysis}} 2O^{\cdot} \quad (11)$$

These oxygen radicals react with water to form hydroxyl radicals ($^{\cdot}OH$)

$$H_2O + O^{\cdot} \longrightarrow 2OH^{\cdot} \quad (12)$$

Moreover, it has been reported that during the transient collapse of cavitation bubbles, emission of light called "sonoluminescence" also takes place. The spectrum of this emission ranges from the ultraviolet region to well beyond the red end of the visible wavelength range, with a peak at 310 nm. This sonoluminescent spectrum of water is associated with the formation of high-energy species (e.g., excited hydroxyl radicals) from molecular fragmentation of compressed gases, rather than with black body radiation [35, 36].

Hence, sonochemistry also involves the emission of light energy for a short period of time, although molecular excitation is thermal, unlike the electronic excitation felt by molecules in photochemical processes. The radiation may lead to the photoexcitation of electrons from the valence band to the conduction band, thus leading to the formation of electron-hole pairs in a similar manner as described above for the photocatalysis (Scheme 2).

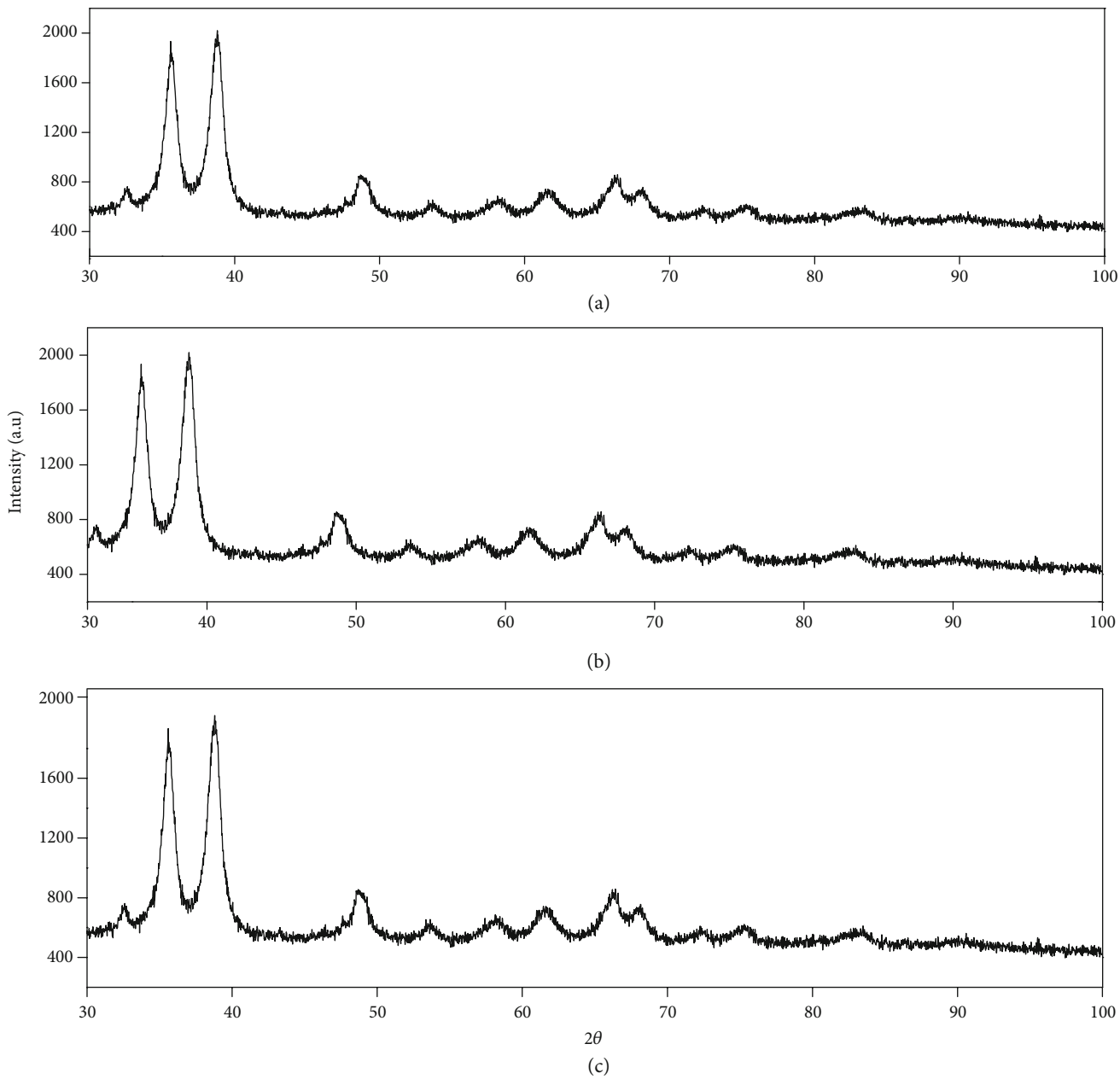


Figure 11: XRD of CuO NPs (a) first time synthesized, (b) recycled after sonocatalytic degradation, and (c) recycled after photocatalytic degradation.

*3.7. Effect of Hydroxyl Radical Scavengers on Degradation of Dyes.* To gain insight into the degradation mechanism, experiments were conducted using $^{\cdot}OH$ radical scavengers. As depicted in earlier research, $^{\cdot}OH$ free radical oxidation is a key mechanism in all AOPs [32, 37]. To measure the quantitative effect of $^{\cdot}OH$ radicals on VB and DR degradation, studies were carried out in the presence of DMSO and carbonate ions, which have a hydroxyl radical-scavenging property [13, 38]. To analyse the effect of scavengers on sonocatalytic degradation and UV-visible photocatalytic degradation of both dyes, experiments were done using 20 ml of $10 \times 10^{-5}$ M dye concentration and CuO NP dosage of 25 mg in the presence of radical scavengers. The solution was irradiated with US (50 W) for 10 minutes and UV-visible irradiation for 20 minutes. It was observed that the degradation efficiency of both the dyes decreased in the presence of radical scavengers (Figure 8). The plausible mechanism in the presence of DMSO and carbonate ion is shown below

$$(CH_3)_2SO + OH^{\cdot} \longrightarrow CH_3SO_2H + CH_3^{\cdot} \quad (13)$$

$$CO_3^{2-} + OH^{\cdot} \longrightarrow CO_3^{-} + OH^{-} \quad (14)$$

The major decline of degradation efficiency demonstrated that $^{\cdot}OH$ radical plays a vital role in both the

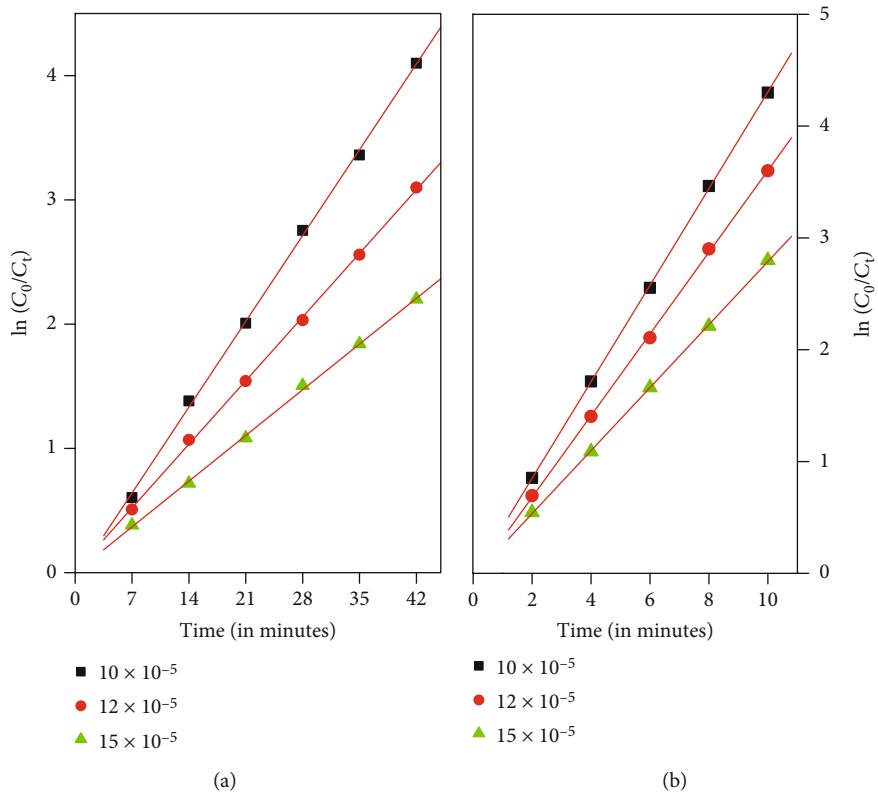


Figure 12: Pseudo-first-order kinetics plot of VB at different concentrations under (a) UV-visible irradiation and (b) US irradiation.

degradation processes and confirms that free radical attack is the dominant controlling mechanism in the degradation of both the DR and VB dyes.

*3.8. Reusability of Catalyst.* An examination of the sonocatalytic and photocatalytic activities of the recycled CuO NPs was investigated by collecting the NPs from a sample solution after centrifugation. The separated NPs were thoroughly washed with water and ethanol. The reusability test of CuO NPs under UV-visible and ultrasonic irradiation on the same organic dyes show the stability of the catalyst. As shown in Figure 9, the reused catalyst showed very little change in the degradation efficiency in both cases, i.e., sonocatalysis and photocatalysis. This emphasizes the excellent chemical stability of the catalyst, making it beneficial for practical wastewater remediation applications. A slight decrease in the photocatalytic activity in each successive cycle can be attributed to several reasons like a degradation of the photocatalyst (CuO NPs) itself, unavoidable loss of photocatalyst during the recycling processes, and slight aggregation of NPs after the photocatalytic process. To find out why there is a decrease in the activity of used CuO NPs after 4 cycles, the recycled CuO NPs have been characterized by TEM and XRD [Figures 10 and 11]. The characteristic XRD diffraction peaks of CuO NPs are clearly visible and show no notable differences before and after recycling the NPs, indicating that CuO NPs are chemically stable. In contrast, TEM images of CuO NPs before and after photocatalytic reaction (4 cycles) (Figure 11) shows the slight aggregation of CuO NPs, possibly by the interactions between CuO NPs and intermediates formed during the degradation process, thus decreasing the electrostatic energy barrier between NPs and increasing the aggregation behaviour. As these recycled CuO NPs form clusters, hence, the surface to volume ratio of NPs decreases and their catalytic activity also decreases.

*3.9. Comparison of Efficiency of Photocatalysis and Sonocatalysis of CuO NPs.* Competitive analysis of CuO NPs as sonocatalysts and photocatalysts as shown in Figure 2 reveals that % decomposition is far better in the case of sonocatalysis. In the presence of CuO NPs and under different sources of energy, both dyes demonstrated enhanced degradation than without NPs. This is due to an increase in the generation of hydroxyl radicals by enhancing the electron-hole pair formation rate due to the excitation of the catalyst surface by energy source [5, 13]. To further quantify, kinetics of sonocatalytic and photocatalytic degradation of the VB and DR dyes was studied by conducting reactions at an initial concentration ($10 \times 10^{-5}$, $12 \times 10^{-5}$, and $15 \times 10^{-5}$) with a catalyst dose of 25 mg. The graph is plotted for $\ln(C_0/C_t)$ vs. the time for photocatalytic and sonocatalytic degradation which resulted in approximately straight lines, as shown in Figures 12 and 13. The kinetic studies were performed on the basis of disappearance of the dye.

The photocatalyst and sonocatalyst with as-prepared samples could be expressed by Langmuir-Hinshelwood mode, Figures 12 and 13. These figures imply that the degradation of VB and DR in both cases follows a pseudo-first-order kinetics.

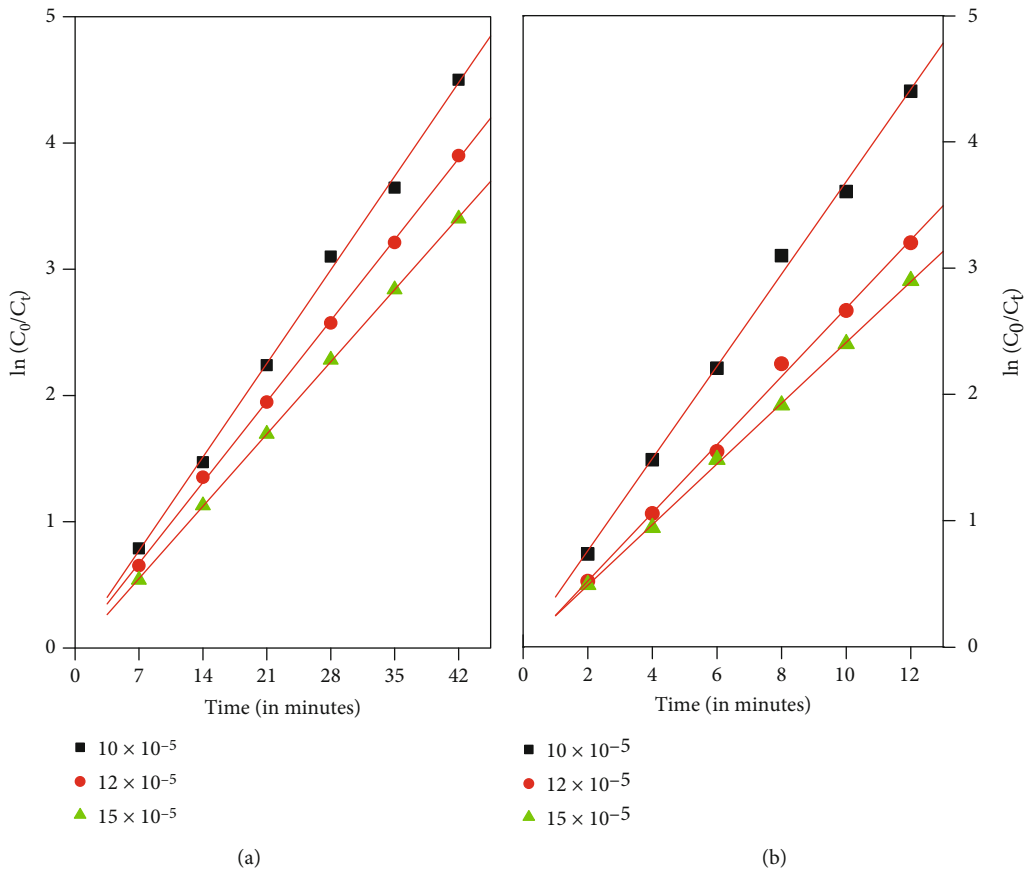


Figure 13: Pseudo-first-order kinetics plot of DR at different concentrations under (a) UV-visible irradiation and (b) US irradiation.

Table 2: Pseudo-first-order kinetics rate constants for the degradation of VB and DR under both sources of energy and for different concentration.

| Dyes | Dye concentration | Sonocatalysis $k$ ($min^{-1}$) | Photocatalysis $k$ ($min^{-1}$) | $R$ sonocatalysis | $R$ photocatalysis |
|---|---|---|---|---|---|
| Victoria Blue (VB) | $10 \times 10^{-5}$ M | 0.43209 | 0.09861 | 0.99992 | 0.99952 |
| | $12 \times 10^{-5}$ M | 0.36536 | 0.07314 | 0.99975 | 0.99965 |
| | $15 \times 10^{-5}$ M | 0.28177 | .05255 | 0.99988 | 0.99933 |
| Direct Red (DR) | $10 \times 10^{-5}$ M | 0.3656 | 0.10587 | 0.9985 | 0.99888 |
| | $12 \times 10^{-5}$ M | 0.27036 | 0.09159 | 0.99925 | 0.99962 |
| | $15 \times 10^{-5}$ M | 0.24064 | 0.08172 | 0.99915 | 0.99811 |

Table 3: Comparison of efficiency of photocatalysis and sonocatalysis of CuO NPs.

| Dyes | NPs | Photocatalysis $k$ ($min^{-1}$) | Sonocatalysis $k$ ($min^{-1}$) |
|---|---|---|---|
| Victoria Blue (VB) $10 \times 10^{-5}$ M | CuO | 0.09861 | 0.43209 |
| Direct Red (DR) $10 \times 10^{-5}$ M | CuO | 0.10587 | 0.3656 |

The rate constants are determined by fitting the experimental data in equation (2). The pseudo-first-order reaction rate constant $k$ and regression $R$ calculated from Figures 12 and 13 are given in Table 2. On comparing the kinetic constant ($k$) of sonocatalysis with $k$ of photocatalysis for both dyes, it was found that the obtained value of $k$ for the sonocatalyst is much higher than for the photocatalyst. Hence, proving that US irradiations are a better source than UV-visible irradiation for the degradation of dyes in the presence of CuO NPs. CuO NPs have a lower band gap (2.3 eV (Figure S5 supplementary data)) so electron-hole recombination is faster and easier. Therefore, the formation of hydroxyl radicals is difficult, which results in lower degradation of dyes in the case of photocatalysis. In the presence of CuO NPs, the sonocatalytic efficiency to decompose organic pollutants was enhanced. This is due to synergistic effects of ultrasound and solid catalyst, namely [39], (i) added powders could provide additional nuclei for cavitation bubble formation, (ii) US irradiation enhances the

mass transfer of organic pollutants between the liquid phase and the catalyst surface, (iii) US irradiation increases the active surface area due to ultrasound deaggregating, and (iv) the catalyst can be excited by ultrasound-induced luminescence which has a wide wavelength and increased production of $^{\cdot}OH$ in the reaction mixture (Ghosh et al., 2013). Thus, sonocatalysis seems to enhance the degradation ratio of organic pollutants due to the increase in the generation of $^{\cdot}OH$.

*3.10. Comparison of Efficiency of Photocatalysis and Sonocatalysis of CuO NPs.* On comparing the photocatalytic and sonocatalytic activities CuO NPs, it was found that the CuO NPs are superior as sonocatalysts than the photocatalysts (Table 3). This may be attributed to the presence of a smaller band gap of CuO NPs (2.3 eV in the present case) which enables the electron-hole recombination to be less or slower, so there is more formation of ROS for the degradation of dyes. Additionally, the CuO NPs being better as sonocatalysts is because of the higher surface area calculated by BET of CuO NPs (49.33 $m^2g^{-1}$). Higher surface area leads to the formation of more cavitation bubbles, which, in turn, produces more local temperature and pressure effects and eventually creates more ROS for the degradation of dyes.

## 4. Conclusion

In summary, we have demonstrated the comparison of the catalytic effect of CuO NPs on the degradation of the cationic (VB) and anionic (DR) dyes under different energy sources, i.e., UV-visible irradiation and US radiations. The synergistic effect of CuO NPs and sonocatalysis has been demonstrated to be more effective in degrading both dyes as compared to CuO NPs and photocatalysis. High catalyst dosage and low initial dye concentration were favoured for the sonocatalytic or photocatalytic degradation of both dyes. Degradation follows the formation of a free radical mechanism, which is further verified by the addition of radical scavengers which reduced the sonocatalytic or photocatalytic degradation. Comparison of the efficiency of photocatalysis and sonocatalysis of CuO NPs was examined and reported. Overall, the application of CuO NPs can be a promising and efficient approach for the sonocatalysis of both the cationic and anionic dyes with high reusability potential.

## Data Availability

Data of all by measurements can be available with the authors and shared upon request. Data are stored in secured devices at the author's institutions. Data can be used to reproduce the results and also generate new sets of results. The authors have full access to these data and full permissions to make it available public for greater use to the scientific community.

## Conflicts of Interest

The authors declare that they have no conflicts of interest.

## Acknowledgments

Authors would like to acknowledge the support of UGC, India under INDO-US 21st Century Knowledge Initiative Project (F. No. 194-2/2016 (IC)). SS would like to acknowledge the USA funding sources, Florida Industrial and Phosphate Research Institute Grant (GR-1800010) and Hinkley Center for Solid and Hazardous Waste Management. The authors also acknowledge the support of SAIF/CIL, Chandigarh, for providing instrumentation facilities.

## Supplementary Materials

Figure S1 represents the X-ray diffraction pattern of the as-synthesized nanoparticles, where it is composed of a pure CuO phase with a monoclinic structure without any peaks of impurity. The particle size, as calculated from FWHM of reflection (111/200) of a monoclinic CuO structure using the Debye Scherrer formula was found to be 18 nm. For determining the morphology, TEM micrograph of CuO NPs was taken and the NPs were observed to be almost spherical in shape, well dispersed, and within a narrow range of size distribution (17–22 nm) as demonstrated in Figures S2 and S3 below [28]. The zeta potential of the CuO NP dispersions was measured over pH values ranging from 2 to 10, and the corresponding pHzpc was found to be ~8.5 as shown in Figure S4. The lower band gap of CuO NPs (~2.3 eV) as obtained from the Tauc plot is depicted in Figure S5, and it leads for faster and easier electron-hole recombination processes during the sonocatalytic and photocatalytic processes. Supplementary Table S1–S4. Tables S1–S4 are the statistical analysis data (*P* value) obtained via the ANOVA for the effect of catalyst dose on the degradation of DR and VB dyes under UV-Vis and US irradiations. *(Supplementary Materials)*

## References

[1] P. Srivastava, S. Goyal, and P. K. Patnala, "Degradation of reactive, acid and basic textile dyes in the presence of ultrasound and rare earths [lanthanum and praseodymium]," *Ultrasonics Sonochemistry*, vol. 21, no. 6, pp. 1994–2009, 2014.

[2] S. Chaudhary, Y. Kaur, B. Jayee, G. R. Chaudhary, and A. Umar, "NiO nanodisks: highly efficient visible-light driven photocatalyst, potential scaffold for seed germination of Vigna radiata and antibacterial properties," *Journal of Cleaner Production*, vol. 190, pp. 563–576, 2018.

[3] S. A. Larik, A. Khatri, S. Ali, and S. H. Kim, "Batchwise dyeing of bamboo cellulose fabric with reactive dye using ultrasonic energy," *Ultrasonics Sonochemistry*, vol. 24, no. 2015, pp. 178–183, 2015.

[4] J. R. Steter, W. R. P. Barros, M. R. V. Lanza, and A. J. Motheo, "Electrochemical and sonoelectrochemical processes applied to amaranth dye degradation," *Chemosphere*, vol. 117, pp. 200–207, 2014.

[5] S. S. Srinivasan, J. Wade, and E. K. Stefanakos, "Visible light photocatalysis via CdS/TiO2 nanocomposite materials," *Journal of Nanomaterials*, vol. 2006, article 87326, 7 pages, 2006.

[6] A. Karci, "Degradation of chlorophenols and alkylphenol ethoxylates, two representative textile chemicals, in water by advanced oxidation processes: the state of the art on

transformation products and toxicity," *Chemosphere*, vol. 99, pp. 1–18, 2014.

[7] S. Chaudhary, Y. Kaur, A. Umar, and G. R. Chaudhary, "1-butyl-3-methylimidazolium tetrafluoroborate functionalized ZnO nanoparticles for removal of toxic organic dyes," *Journal of Molecular Liquids*, vol. 220, pp. 1013–1021, 2016.

[8] K. Govindan, M. Raja, S. U. Maheshwari, and M. Noel, "Analysis and understanding of amido black 10B dye degradation in aqueous solution by electrocoagulation with the conventional oxidants peroxomonosulfate, peroxodisulfate and hydrogen peroxide," *Environmental Science: Water Research & Technology*, vol. 1, no. 1, pp. 108–119, 2015.

[9] P. Sathishkumar, R. V. Mangalaraja, O. Rozas et al., "Sonophotocatalytic degradation of Acid Blue 113 in the presence of rare earth nanoclusters loaded $TiO_2$ nanophotocatalysts," *Separation and Purification Technology*, vol. 133, pp. 407–414, 2014.

[10] S. S. Srinivasan, J. Wade, and E. K. Stefanakos, "Synthesis and characterization of photocatalytic TiO2-ZnFe2O4 nanoparticles," *Journal of Nanomaterials*, vol. 2006, article 45712, 4 pages, 2006.

[11] P. Saharan, G. R. Chaudhary, S. Lata, S. K. Mehta, and S. Mor, "Ultra fast and effective treatment of dyes from water with the synergistic effect of Ni doped ZnO nanoparticles and ultrasonication," *Ultrasonics Sonochemistry*, vol. 22, pp. 317–325, 2015.

[12] D. Rajamanickam, P. Dhatshanamurthi, and M. Shanthi, "Preparation and characterization of $SeO_2/TiO_2$ composite photocatalyst with excellent performance for sunset yellow azo dye degradation under natural sunlight illumination," *Spectrochimica Acta Part A: Molecular and Biomolecular Spectroscopy*, vol. 138, pp. 489–498, 2015.

[13] A. Khataee, A. Karimi, S. Arefi-Oskoui et al., "Sonochemical synthesis of Pr-doped ZnO nanoparticles for sonocatalytic degradation of Acid Red 17," *Ultrasonics Sonochemistry*, vol. 22, pp. 371–381, 2015.

[14] H. Y. He and J. Lu, "Highly photocatalytic activities of magnetically separable reduced graphene oxide-$CoFe_2O_4$ hybrid nanostructures in dye photodegradation," *Separation and Purification Technology*, vol. 172, pp. 374–381, 2017.

[15] M. L. A. Kumari and L. G. Devi, "New insights into the origin of the visible light photocatalytic activity of Fe (III) porphyrin surface anchored $TiO_2$," *Environmental Science: Water Research and Technology*, vol. 1, pp. 177–187, 2015.

[16] S. S. Srinivasan, S. L. Wallen, and J. Douyon, "Synergistic chemical oxidative and photocatalytic enhancer system (scopes) for wastewater remediation," 2018, US Patent 16/425,590.

[17] C. Li, S. Srinivasan, N. Kislov, M. Schmidt, E. K. Stefanakos, and D. Y. Goswami, "Enhancement of $TiO_2$ photocatalytic activity by N- doping using the gas phase impregnation method," *MRS Proceedings*, vol. 1217, pp. Y03–Y35, 2009.

[18] R. I. MacCuspie, H. Hyman, C. Yakymyshyn, S. S. Srinivasan, J. Dhau, and C. Drake, "A framework for identifying performance targets for sustainable nanomaterials," *Sustainable Materials and Technologies*, vol. 1-2, pp. 17–25, 2014.

[19] S. Wang, X. Zhang, L. Pan et al., "Controllable sonochemical synthesis of $Cu_2O/Cu_2(OH)_3NO_3$ composites toward synergy of adsorption and photocatalysis," *Applied Catalysis B: Environmental*, vol. 164, pp. 234–240, 2015.

[20] A. Bhattacharjee, M. Ahmaruzzaman, and T. Sinha, "Surfactant effects on the synthesis of durable tin-oxide nanoparticles and its exploitation as a recyclable catalyst for the elimination of toxic dye: a green and efficient approach for wastewater treatment," *RSC Advances*, vol. 4, no. 93, pp. 51418–51429, 2014.

[21] D. Yang, J. Zhao, H. Liu et al., "Enhancing photoactivity of TiO2(B)/anatase core-shell nanofibers by selectively doping cerium ions into the TiO2(B) core," *Chemistry - A European Journal*, vol. 19, no. 16, pp. 5113–5119, 2013.

[22] R. Abazari, A. R. Mahjoub, and S. Sanati, "A facile and efficient preparation of anatase titania nanoparticles in micelle nanoreactors: morphology, structure, and their high photocatalytic activity under UV light illumination," *RSC Advances*, vol. 4, no. 99, pp. 56406–56414, 2014.

[23] F. Mirhoseini and A. Salabat, "Ionic liquid based microemulsion method for the fabrication of poly(methyl methacrylate)–TiO2nanocomposite as a highly efficient visible light photocatalyst," *RSC Advances*, vol. 5, no. 17, pp. 12536–12545, 2015.

[24] A. R. Khataee, M. Zarei, and R. Ordikhani-Seyedlar, "Heterogeneous photocatalysis of a dye solution using supported $TiO_2$ nanoparticles combined with homogeneous photoelectrochemical process: molecular degradation products," *Journal of Molecular Catalysis A: Chemical*, vol. 338, pp. 84–91, 2011.

[25] A. Khataee, R. Darvishi, R. D. C. Soltani, A. Karimi, and S. W. Joo, "Sonocatalytic degradation of a textile dye over Gd-doped ZnO nanoparticles synthesized through sonochemical process," *Ultrasonics Sonochemistry*, vol. 23, pp. 219–230, 2011.

[26] N. A. Fernandez, L. Rodriguez-Freire, M. Keswani, and R. Sierra-Alvarez, "Effect of chemical structure on the sonochemical degradation of perfluoroalkyl and polyfluoroalkyl substances (PFASs)," *Environmental Science: Water Research & Technology*, vol. 2, no. 6, pp. 975–983, 2016.

[27] N. Kaur, G. Kaur, A. Bhalla, J. S. Dhau, and G. R. Chaudhary, "Metallosurfactant based Pd-Ni alloy nanoparticles as a proficient catalyst in the Mizoroki Heck coupling reaction," *Green Chemistry*, vol. 20, no. 7, pp. 1506–1514, 2018.

[28] G. R. Chaudhary, P. Bansal, N. Kaur, and S. K. Mehta, "Recyclable CuO nanoparticles as heterogeneous catalysts for the synthesis of xanthenes under solvent free conditions," *RSC Advances*, vol. 4, no. 90, pp. 49462–49470, 2014.

[29] B. P. Nenavathu, A. V. R. Krishna Rao, A. Goyal, A. Kapoor, and R. K. Dutta, "Synthesis, characterization and enhanced photocatalytic degradation efficiency of Se doped ZnO nanoparticles using trypan blue as a model dye," *Applied Catalysis A: General*, vol. 459, pp. 106–113, 2013.

[30] H. T. Chandran, S. Thangavel, C. V. Jipsa, and G. Venugopal, "Study on inorganic oxidants assisted sonocatalytic degradation of Resazurin dye in presence of $\beta$-$SnWO_4$ nanoparticles," *Materials Science in Semiconductor Processing*, vol. 27, pp. 212–219, 2014.

[31] A. Raizada, D. Ganguly, and M. M. Mankad, "A highly efficient copper oxide nanopowder for adsorption of methylene blue dye from aqueous medium," *Journal of Chemical Engineering Research*, vol. 2, pp. 249–258, 2014.

[32] A. Nezamzadeh-Ejhieh and Z. Salimi, "Solar photocatalytic degradation of o-phenylenediamine by heterogeneous CuO/X zeolite catalyst," *Desalination*, vol. 280, no. 1-3, pp. 281–287, 2011.

[33] N. Talebian, M. R. Nilforoushan, and F. J. Mogaddas, "Comparative study on the sonophotocatalytic degradation of hazardous waste," *Ceramics International*, vol. 39, no. 5, pp. 4913–4921, 2013.

[34] T. Ghosh, K. Ullah, V. Nikam, C. Y. Park, Z. D. Meng, and W. C. Oh, "The characteristic study and sonocatalytic performance of CdSe–graphene as catalyst in the degradation of azo dyes in aqueous solution under dark conditions," *Ultrasonics Sonochemistry*, vol. 20, no. 2, pp. 768–776, 2013.

[35] T. Philippe, P. Pichat, C. Guillard, P. Christian, and T. Chopin, "Degradation of phenyltrifluoromethylketone in water by separate or simultaneous use of $TiO_2$ photocatalysis and 30 or 515 kHz ultrasound," *Physical Chemistry Chemical Physics*, vol. 1, no. 19, pp. 4663–4668, 1999.

[36] C. Balaji, V. S. Moholkar, A. B. Pandit, and M. Ashokkumar, "Mechanistic investigations on sonophotocatalytic degradation of textile dyes with surface active solutes," *Industrial and Engineering Chemistry Research*, vol. 50, no. 20, pp. 11485–11494, 2011.

[37] A. R. Khataee and M. Zarei, "Photocatalysis of a dye solution using immobilized ZnO nanoparticles combined with photoelectrochemical process," *Desalination*, vol. 273, no. 2-3, pp. 453–460, 2011.

[38] M. J. Burkitt and R. P. Mason, "Direct evidence for in vivo hydroxyl-radical generation in experimental iron overload: an ESR spin-trapping investigation," *Proceedings of the National Academy of Sciences*, vol. 88, no. 19, pp. 8440–8444, 1991.

[39] S. E. Karekar, B. A. Bhanvase, S. H. Sonawane, M. P. Deosarkar, D. V. Pinjari, and A. B. Pandit, "Synthesis of zinc molybdate and zinc phosphomolybdate nanopigments by an ultrasound assisted route: advantage over conventional method," *Chemical Engineering and Processing*, vol. 87, pp. 51–59, 2015.

Hindawi
Journal of Nanomaterials
Volume 2020, Article ID 9341983, 25 pages
https://doi.org/10.1155/2020/9341983

*Review Article*

# Polyol Silver Nanowire Synthesis and the Outlook for a Green Process

**Shohreh Hemmati**,[1,2,3] **Michael T. Harris**,[1] **and Dale P. Barkey**[2]

[1]*Davidson School of Chemical Engineering, Purdue University, Forney Hall of Chemical Engineering, 480 Stadium Mall Drive, West Lafayette, Indiana 47907, USA*
[2]*Department of Chemical Engineering, University of New Hampshire, Kingsbury Hall, 33 Academic Way, Durham, NH 03824, USA*
[3]*School of Chemical Engineering, Oklahoma State University, 420 Engineering North, Stillwater, OK 74078, USA*

Correspondence should be addressed to Shohreh Hemmati; shohreh.hemmati@okstate.edu

Received 13 June 2019; Revised 22 September 2019; Accepted 5 October 2019; Published 29 February 2020

Guest Editor: Ganga Ram



Silver nanowires (AgNWs) have a broad range of applications including nanoelectronics, energy conversion, health care, solar cells, touch screens, sensors and biosensors, wearable electronics, and drug delivery systems. As their characteristics depend strongly on their size and morphology, it is essential to find the optimal and most cost-effective synthesis method with precise control over the size and morphology of the wires. Various methods for AgNW synthesis have been reported along with process optimization and novel techniques to increase the yield and aspect ratios of synthesized AgNWs. The most promising processes for synthesis of AgNWs are wet chemical techniques, in which the polyol process is low cost and simple and provides high yield compared to other chemical methods. Reaction mechanism is one of the most important factors in strategies to control the process. Our purpose here is to provide an overview on the main findings regarding synthesis, preparation, and characterization of AgNWs. Recent efforts in the polyol synthesis of AgNWs are summarized with respect to product morphology and size, reaction conditions, and characterization techniques. The effect of essential factors such as reagent concentration and preparation, temperature, and reaction atmosphere that control the size, morphology, and yield of synthesized AgNWs is reviewed. Moreover, a review on the novel modified polyol process and reactor design such as continuous millifluidic and flow reactors to increase the yield of synthesized AgNWs on large scales is provided. The most recent proposed growth mechanisms and kinetics behind the polyol process are addressed. Finally, comparatively few available studies in green and sustainable development of 1D silver nanostructures through the application of natural products with inherent growth termination, stabilization, and capping characteristics are reviewed to provide an avenue to natural synthesis pathways to AgNWs. Future directions in both chemical and green synthesis approaches of AgNWs are addressed.

## 1. Introduction

The transition from the micro to the nanoscale leads to essential changes in the physical and chemical properties of particles because of both quantum effects and the resulting high ratio of the surface area to the volume. Nanowires show specific electrical conduction characteristics due to their quantum directional configuration. This configuration includes two quantum confined directions, as well as one unconfined direction that provides electrical conductivity. Nanowires are exceptional compared to bulk materials because of their electronic state density and high aspect ratio [1–5]. Metal one-dimensional (1D) nanostructures can play a valuable role in several applications and have recently gained much research attention because of their unique electrical, optical, mechanical, thermal, and catalytic properties.

Having the highest bulk electrical and thermal conductivity among metals ($6.3 \times 10^7$ S/m), silver is one of the most promising metal nanowire materials [3, 6–10]. Silver metal has a range of characteristics that can be improved, adjusted, or developed by control of particle morphology on the nanometer scale. Silver has a face-centered-cubic (fcc) structure

with lattice parameters similar to gold [5, 11]. The variety of metal nanoparticles that have been produced illustrate the various biochemical and physiochemical properties that enable novel technologies and devices [12]. Among these, silver nanoparticles (AgNPs) have unique and outstanding shape- and size-dependent electrical, thermal, optical, catalytical, optoelectronic, anticancer, biosensing, medicinal, antiviral, and biological characteristics which make them exceptional for several applications in a variety of fields and disciplines such as dentistry, drug delivery, biomedical, anticancer, antimicrobial, antioxidant, food science, agriculture, cosmetic, clothing, water treatment, larvicides, forensic science, pollution control, waste management, and photovoltaics [12–21]. Silver has an inhibitory activity toward several microorganisms and bacterial strains and can be used in arthroplasty, medicine, and to prevent bacterial colonization [22]. The ionic form of silver ($Ag^+$) is an eco-friendly antimicrobial that can be used against several fungal and bacterial pathogens. Moreover, among metal nanoparticles, AgNPs are a promising candidate for Surface Enhanced Raman Scattering (SERS) applications because of their high optical cross section in the visible region [23]. 1D metal nanostructures have several applications that are unattainable with nanospheres [2, 24]. Moreover, by the application of various capping, growing, and shape control agents in metal nanoparticle synthesis, 1D structures such as nanorods, nanotubes, and nanowires can be produced.

Structural and dimensional properties of nanowires, which play an important role in determination of their characteristics, can be probed by several imaging techniques [25, 26]. Due to the nanoscale size, which is comparable to or less than the wavelength of visible light, electron microscopic techniques are required to create images of the particles. These include but are not limited to Transmission Electron Microscopy (TEM), Scanning Electron Microscopy (SEM), and High-Resolution Transmission Electron Microscopy (HRTEM). Scanning Tunneling Probes (STP) and X-ray analysis may also be used to characterize nanowire [3]. Based on the specific application, other characterization methods may be used to evaluate the electrical, mechanical, rheological, and catalytic characteristics of AgNWs.

There are a broad range of applications of AgNWs in several areas including but not limited to nanoelectronics, sensors, biosensors, catalytic, medical, energy devices, agriculture, and food science. AgNWs can be utilized as conductive filler to formulate conductive inks and create conductive patterns [2, 9, 27–29]. They also may be used to enable sensors and biosensors to detect different chemical and biochemical components [30–32] or as wearable electronic devices as strain, pressure, and human activity sensors [33–36]. Moreover, they may be used to create transparent conductive electrodes for applications such as solar cells, LCDs, LEDs, and touch screens [37–47]. Finally, there are challenges and drawbacks in using the alternative material Indium Tin Oxide (ITO) which is chemically unstable, increasing in cost with a limited supply of indium, and in some applications, forms brittle films. All of these reasons make it necessary to replace ITO, and AgNW has gained attention as a promising material to replace ITO for Transparent Conductor (TC) device fabrication in touch screens, solar cells, and displays [48].

This review article is helpful for new researchers to select the appropriate direction in polyol synthesis of AgNWs with desired size and morphology. Moreover, this article would lead them toward the green and sustainable synthesis of 1D silver nanostructures that have not been reviewed in previous studies.

## 2. Effect of AgNW Size and Morphology on Material Characteristics

The physical and chemical characteristics of AgNWs such as thermal, electrical, catalytical, optical, mechanical, rheological, and antimicrobial behaviors in different applications are strongly size and morphology dependent. It has been shown that the conductance of metal nanowire such as AgNW is quantized due to their dimension that is comparable to the electron Fermi wavelength that makes them a unique candidate for nanoelectronics [4]. The correlation between electronic characteristics and structural properties of AgNWs has been confirmed by theoretical calculations [5]. The application of AgNWs in transparent conductive electrodes (TCE) due to their size- and morphology-dependent electrical resistance and transmittance for electronic and optoelectronic applications has been proved [10, 27, 29, 33, 49]. Size- and morphology-dependent characteristics of AgNWs make them more potent antibacterial with lower cytotoxicity compared to other silver nanoparticles [21]. AgNW has also been used in sensor and biosensor applications in which its photon-plasmon interaction and electromagnetic scattering characteristics are strongly depend on its size and morphology [30]. In the application of metal nanostructures as catalysts, their selectivity and activity strongly depend on the atomic arrangement and surface crystal plane [50].

Hemmati et al. showed that conductive inks formulated with high aspect ratio AgNW (length of 30 $\mu$m and diameter of 40 and 90 nm) content as low as 3 wt.% provide high-quality screen printing with sharp-line definition, which is difficult to achieve with low aspect ratio AgNW, micrometer-sized silver particles, or silver flake at the same content. Based on the viscosity measurements under conditions designed to mimic screen printing, it was shown that the dynamic viscosity of the ink depends strongly on AgNW content. This effect was stronger at higher concentration of AgNWs [2].

These size- and morphology-dependent characteristics of AgNWs point to the necessity to utilize a synthesis process in which size and morphology of the synthesized AgNWs can be precisely controlled with narrow size distribution.

## 3. Polyol Synthesis and Characterization of AgNWs

There are several methods for AgNW synthesis, which can be broadly categorized as template-free and template-directed methods. The chemistry of AgNW synthesis can

be categorized into vapor phase and liquid phase methods. The latter has been used widely because of the variety of suitable solvents, easy monitoring, low cost, and a homogenous reaction regime [3]. The most promising processes for synthesis of AgNWs are wet chemical techniques. Among these, the polyol technique is a superlative method compared to other chemical methods as it is low cost and simple and provides high yield [6, 7, 9]. Fievet et al. investigated and illustrated the advantages of polyol process compared to other methods for metal nanoparticle synthesis [51]. Size distribution, shape selectivity, and morphology control are the essential challenges in nanomaterial synthesis [52, 53]. It is crucial to control the mean and variance of length and diameter.

Most recently, Fahad et al. provided an overview on AgNW synthesis and their application as conducting material. Their overview on different synthesis methods including photoreduction method, template method, wet chemical method, and solution-based synthesis concluded that the polyol-assisted solution-based method is the dominant one in synthesis of homogeneous high aspect ratio AgNWs. The factors that affect the morphology and size of synthesized AgNWs include mole ratio, capping agent molecular weight and its rate of addition, reaction atmosphere, reaction temperature, reaction time, and stirring rate were reviewed [54]. Zhang et al. reviewed advances in synthetic methods and applications of silver nanostructures. They summarized the preparation of various sizes and morphologies of silver nanostructures including nanospheres, nanocubes, nanowires, and nanorods and provided a summary of reaction conditions for their synthesis [55]. Zhang et al. also provided a review on synthesis, growth mechanism, and multifunctional applications of AgNWs specifically as conductive materials and component of electronic devices. Examples of silver nanostructures include perfect/truncated cube, beam, right bipyramid, rectangular bar, tetrahedron, octahedron, triangular/hexagonal plate, decahedron, rod, and wire. Based on the conventional definition of AgNWs, diameters are in the range of 10-200 nm and lengths in the range of 5-100 $\mu$m. Based on this definition, AgNWs have aspect ratios of more than 10 and similar structures with smaller aspect ratio are called nanorods [56].

In this review, we focus on the polyol synthesis which was introduced by Fievet et al. to synthesize submicron-sized metallic nanostructures [57, 58]. A polyol solvent in the presence of a salt precursor and a polymeric capping agent is heated to produce a metal colloid. In the case of AgNWs, ethylene glycol (EG), silver nitrate ($AgNO_3$), and poly(vinyl pyrrolidone) (PVP) usually function as the polyol, salt precursor, and capping agent, respectively. The synthesis process is chemical reduction of Ag ions in the presence of a polymeric capping agent, in which a small amount of suitable salt can facilitate the growth of the silver seeds to the wire shape [9]. Several factors affect the morphology and yield of AgNWs, including reagent concentration, rate of reagent addition, preparation of the silver ion solution, capping agent molecular weight, type of salt, type and power of stirring, reactor volume in batch synthesis, and residence time in flow synthesis [59–69].

Because of their influence on material properties, the size and morphology of nanowires, including their shape and crystal structure, must be accurately guided during synthesis. As the nanoparticle size can be studied and monitored by UV-visible absorption spectroscopy, this technique plays an essential role in investigations of the nanoparticle synthesis reaction mechanism. *In situ* UV-vis characterization can be also used to investigate the kinetics of the reaction [70] or to monitor the extent of reaction [71]. In the case of silver nanowires (AgNWs), a broad peak around 400 nm is due to transverse plasmon absorbance, while a shoulder peak around 350 nm is due to the plasmon resonance of bulk silver [8, 72, 73]. The full width at half maximum (FWHM) can be used to determine quantitatively the size and size distribution of the synthesized metal nanostructures [74]. Fourier Transfer Infrared (FTIR) is used to identify functional groups from the position of the peaks in the spectrum [19, 75]. With FTIR analysis, it is also possible to identify metabolites such as amine, ketone, alcohol, aldehyde, carboxylate, or other functional groups attached to the nanowires [76, 77]. Structure changes on the surface of nanoparticles can be investigated by X-ray Photoelectron Spectroscopy (XPS) [78]. Small Angle X-ray Scattering (SAXS) can provide a precise and statistically feasible way to investigate the uniformity of metal nanoparticles and their size distribution [79]. Electron microscopy methods such as TEM, HRTEM, and SEM are used to investigate the morphology of the synthesized nanostructures and their size or the morphology of the different structures ex situ. *In situ* X-ray adsorption spectroscopy (XAS) is a versatile technique that permits investigation of the reaction dynamics and mechanism of AgNW growth by observation of oxidation state changes, time-resolved bond formation, coordination, and local order.

Xia's group has published several studies of AgNW synthesis relevant to our subject [80, 81]. In one of these, Sun et al. described a polyol process in which platinum nanoparticles act as seeds for heterogeneous nucleation and growth of silver particles in the presence of PVP to produce AgNWs. In another study, they used seed-assisted solution-based polyol AgNW synthesis and investigated the effect of reagent addition procedures on the yield and morphology [82, 83]. In another study by this group, Wiley et al. investigated the polyol synthesis of Ag nanostructures including cuboctahedra, pentagonal, nanowires, bipyramids, nanocubes, nanobars, and nanobeams with controlled properties and shape [11]. Skrabalak et al. investigated glycolaldehyde (GA) as a reducing agent in polyol synthesis of Ag nanostructures. By a spectrophotometric method, they showed that heating EG in air results in its oxidation to GA, which acts as a reductant for noble metal ions such as silver [84]. In a recent study, Luo et al. introduced the facile synthesis of Ag nanorods in the presence of palladium nanostructures (decahedra of 16 nm) as seeds to direct the nucleation, deposition, and growth of the Ag atoms into a 5-fold twinning axis to facilitate the growth to the wire shape. In this mechanism, the diameter of the Ag nanorods depends on the lateral dimensions of the seed. In their process, poly(diallyldimethylammonium chloride) (PDDA) functions as both an anion provider and

a cation provider and as a capping agent to facilitate growth of nanorods [85].

Korte et al. investigated the rapid synthesis of AgNWs in the presence of PVP as a stabilizer and CuCl or $CuCl_2$ as a salt mediator. They showed that both $Cl^-$ and $Cu^+$, which is a product of the reduction of $Cu^{2+}$ by EG, are necessary for AgNW growth. $Cl^-$ is responsible for stabilization of silver seeds by binding silver ions as AgCl and releasing $Ag^+$ slowly to prevent supersaturation in the beginning of the reaction. $Cu^+$ serves to adsorb atomic oxygen from the surface of silver seeds and facilitates further growth to the wire shape [6].

Based on these studies and other studies regarding the effect of synthesis conditions on the morphology and formation of silver nanowires in the polyol process [86], it is clear that essential factors include reagent concentrations, salt mediator type and concentration, capping agent concentration and molecular weight, reagent solution preparation condition, and reaction temperature that predominantly affect and control the polyol synthesis of AgNWs.

*3.1. Effect of Temperature in the Polyol Synthesis of AgNWs.* Temperature is one of the essential factors in the polyol synthesis of AgNWs. A high temperature (110-200°C) is required at the beginning of the reaction to generate a reducing agent and to reduce the silver ions to silver atoms.

There are some studies that have investigated the effect of the reaction temperature on the morphology and yield of AgNWs or introduced new heating methods or processes. Coskun et al. investigated the effect of temperature on the length and diameter of AgNWs. They found that the conversion of EG to GA occurs at high temperature and a critical temperature (130-150°C) is required for the formation of a high aspect ratio of AgNWs. Subsequently, the growth of AgNWs is based on the formation of the multitwinned particles at that temperature [87]. Jiu et al. showed that a high temperature is necessary to promote AgCl solubility, while too high temperature produces an undesirably high ratio of the etching rate to the nucleation rate [88]. Lai et al. showed that a reaction temperature in the range of 130-175°C affects the morphology of Ag nanostructures (particles, rods, cubes, and wires) corresponding to different surface plasmon resonance (SPR) properties [89]. Kaili et al. emphasized the importance of temperature in the range of 110-160°C as it determines the diffusion and reaction (nucleation and growth) rates. They showed that nanowire size decreases as the temperature increases due to increasing nucleation and growth [90]. Nghia et al. used a microwave technique (800 W microwave oven equipped with a condenser) to synthesize AgNWs quickly with an irradiation time of 3.5 minutes and found that morphology depends strongly on the rate of heat [59]. Liu et al. also utilized a microwave-assisted (400 W microwave oven with an irradiation time of 3 minutes) to control morphology [91]. Lim et al. reported high yield synthesis of AgNWs by a heated-up (heating from room temperature to desired one at a specific heating rate) polyol process. They observed that the heat-up method can facilitate the formation of seeds and their growth to the wire structure rather than the hot injection polyol method [92].

*3.2. Effect of $AgNO_3$ Concentration, Its Preparation, and Injection Rate in the Polyol Synthesis of AgNWs.* Silver nitrate ($AgNO_3$) usually functions as a metal precursor in AgNW polyol synthesis. Its concentration, preparation method, and the rate of injection are among the most important parameters in the process. At low $AgNO_3$, the resulting nanostructures consist mainly of particles, spheres, triangle bipyramids, and cubes. With increasing $AgNO_3$ concentration, the yield of AgNWs compared to other structures increases up to a limit. When $AgNO_3$ concentration is too high (0.188 M), again there are other nanostructures rather than 1D nanostructures because of the resulting high concentration of seeds early in the process. The injection rate is also crucial as it is important to not have supersaturation of Ag at the beginning of the reaction. This can be achieved either by adding the $AgNO_3$ solution dropwise or by using a salt mediator that can form the corresponding Ag-based salt (AgM in which M can be different anions such as $Cl^-$) and consequently release the Ag ions slowly. Finally, sonication time of the $AgNO_3$ solutions is also essential as it affects the size of the particles that formed as sonication continues.

Nghia et al. investigated the effect of $AgNO_3$ concentration (15-90 mM) on the morphology and yield of synthesized AgNWs in a microwave-assisted polyol process. They reported the formation of cubes and bipyramids at low concentration and 89% yield of AgNWs at high concentration [59]. Lim et al. investigated the effect of $AgNO_3$ concentration, and their results showed that the concentration and injection rate of $AgNO_3$ and the reaction temperature have a strong effect on the growth characteristics of AgNWs. They found that AgNW diameter decreases with increasing $AgNO_3$ concentration and consequently the wire aspect ratio increases [92]. Wu et al. synthesized AgNWs in a one-pot method without chloride ion. They varied the reagent concentration and injection rate of $AgNO_3$ and PVP to produce AgNWs with different lengths and widths [93]. Gebeyehu et al. varied and adjusted the concentration of the $AgNO_3$ (20.6, 30.5, 60.4, and 90.3 mM) and molar ration of [PVP]/[$AgNO_3$] concentration to control wire morphology. They synthesized AgNWs with aspect ratios of more than 1000 and average diameter of 20 nm by adding 30.5 mM of $AgNO_3$ and [PVP]/[$AgNO_3$] of 6 : 1, followed by 2–3 cycles selective precipitation to purify AgNWs and separate all of other nanoparticles that had produced as a byproduct [94]. Srivastava et al. investigated the effect of $AgNO_3$ concentration on the nanostructure morphology and size for highly sensitive SERS sensors. They showed that nanowires can be synthesized at lower concertation of $AgNO_3$ whereas higher concentration caused formation of nanocubes [95].

Lee et al. found that the sonication time of the $AgNO_3$ solution is important to produce high yield and high aspect ratio AgNWs. They reported that the optimum sonication time is 7 minutes [7].

The injection rate of reagent solutions specifically $AgNO_3$ solution is essential and can control wire yield and morphology. Coskun et al. showed that the injection rate (1, 3, 5, 6, 8,

and 300 mL/h) affects the morphology and yield of synthesized AgNWs as there were micrometer-sized Ag particles as well as AgNWs at very low or very high injection rates [87]. Amirjani et al. investigated the effect of the rate of $AgNO_3$ addition on the aspect ratio through a response surface method (RSM). Their statistical results showed that the first order of this parameter and $Cl^-$ concentration has a similar effect on the AgNW aspect ratio and their integration is statistically significant. They found the optimum value of <0.047 mmol/min $AgNO_3$ addition to synthesize uniform AgNWs [96].

*3.3. Effect of PVP Concentration and Molecular Weight as a Capping Agent in the Polyol Synthesis of AgNWs.* PVP usually functions as a capping agent in the polyol synthesis of AgNWs to stabilize and control the growth of the silver multitwinned seeds to 1D nanostructures. PVP molecular weight is an essential factor in the strength of interaction between PVP and silver seeds, and it strongly affects the morphology of the nanostructures. There are several studies aimed at investigating the effect of PVP concentration and molecular weight or the PVP/$AgNO_3$ ratio.

Sonntag et al. showed the necessity to use a minimum PVP chain length to synthesize AgNWs. They concluded that at their reaction condition the minimum MW of 55 kDa is required to synthesize AgNWs with a small diameter distribution [97]. Coskun et al. showed that the PVP : $AgNO_3$ molar ratios (3 : 1, 4.5 : 1, 6 : 1, 7.5 : 1, 9 : 1, and 11 : 1) affect strongly the final morphology of the silver nanostructures. They showed that, at very low molar ratio, passivation the {100} faces are incomplete and, by increasing the ratio, the AgNW diameter can be decreased gradually. At a very high molar ratio, there are some micron-sized Ag particles attributed to excess PVP coverage on all faces of the silver seeds rather than selective coverage of {100} faces. They reported an optimum value of 7.5 : 1 [87]. Song et al. investigated the effect of PVP molecular weight (MW = 8,000, 29,000, 40,000, and 1,300,000) on the morphology and shape of Ag nanostructures. They proposed that adsorption and steric effects are responsible for the effect of PVP on morphology. They suggested that when the PVP MW is low, selective adsorption of PVP on {100} facets is dominant, whereas at higher MW chemical adsorption is distributed on all facets. They also concluded that the MW of PVP is more critical than its concentration [60]. Lim et al. demonstrated that AgNWs with a high aspect ratio can be produced with a PVP/$AgNO_3$ concentration mole ratio of 16 [92]. Zhu et al. utilized PVP as a capping agent with various MWs (15,000-80,000) and subsequently introduced long-chain PVP to improve the process [98]. Lee et al. showed that AgNW diameter can be controlled by varying PVP concentration [99]. Yang et al. synthesized AgNWs by a modified polyol process in the PVP concentration range of 4.53-13.75 wt.% to produce AgNWs embedded in PVP fibers [100]. Chen et al. synthesized nano-Ag/PVP composites, and the effect of main parameters such as degree of the polymerization of PVP was investigated. They showed that PVP as a capping agent improves the performance of nanosilver dispersion in several solvents due to its great solvent adaptability [74]. Kaili et al. showed that PVP as a capping agent not only plays an essential role in preventing seed agglomeration but also helps heterogeneous growth of MTPs to wire shape. They investigated the effect of PVP molecular weight (55,000, 360,000, and 13,000,000) on the diameter and length of synthesized AgNWs and showed that while PVPs with large MW provide better product quality, very large MW (13,000,000) PVP is not suitable for synthesis of AgNWs with a high aspect ratio without nanoparticles as byproducts due to the viscous effect of the polymers [90].

*3.4. Effect of the Salt Mediator in the Polyol Synthesis of AgNWs.* In the polyol process, a small amount of a suitable salt is necessary to assist growth of silver nuclei to wire shape. The required anion and cation can be provided by several types of salts such as $CuCl_2$, CuCl, NaCl, $FeCl_3$, NaBr, KBr, and $CoCl_2$. Several studies have investigated the effect of the salt type and its concentration on morphology and yield.

Zhang et al. conducted polyol AgNW synthesis in the presence of several metal ions including NaCl, $CoCl_2$, $FeCl_3$, and $CrCl_3$ with concentration of 86 $\mu$M to investigate their influence on morphology and yield of synthesized AgNWs. They concluded that the $Cr^{+3}$ as a novel and promising metal ion in polyol AgNW synthesis not only can scavenge the atomic oxygen and prevent oxidative etching but also provides a more stable reaction environment when coupled with hydrothermal synthesis. AgNWs with lengths of up to 160 $\mu$m and yield of more than 90% were reported [101]. Yuan et al. used tetrabutylammonium dibromochloride (TBADBC) as organic auxiliary in an AgNW polyol process to synthesize AgNWs with diameters as small as 16 nm with aspect ratios over 2000. They attributed this result to passivation by $AgClBr_2$ particles on the {100} crystal facet of the initially formed Ag pentahedral seeds [102]. Chen et al. investigated how the diameter of AgNWs could be adjusted by introducing specific control agents, including metal cations, inorganic anions, and molecules such as KBr, KOH, KCl, $Fe(NO_3)_3$, $PdCl_2$, $Na_2S$, and ascorbic acid [103]. Nghia et al. introduced NaCl as a salt mediator to control the silver reduction rate and initial seed formation in a microwave-assisted polyol process. They showed that in the absence of NaCl, AgNP formation is dominant (around 96%) [59]. Jiu et al. explained how a trace amount of suitable salt including $FeCl_3$, NaCl, or $Na_2CO_3$ is necessary for AgNW growth because of the formation and dissolution of $Ag_xA_y$ between Ag ions and anion in salt [88]. Coskun et al. investigated the effect of NaCl concentration (0, 8.5, 12, 17.1, 25.6, and 85.5 $\mu$M) and showed that in the absence of $Cl^-$ ions there are only silver nanoparticles (AgNPs) due the rapid reduction of $Ag^+$ to $Ag^0$. Addition of NaCl facilitates the formation of the AgNWs due to the formation of AgCl and slows the release of the Ag ions [87]. Zhang et al. synthesized single-crystal AgNWs with smooth surfaces through a sulfide-mediated polyol process by utilizing $Na_2S$ as a salt mediator [30]. Liu et al. utilized a $(NH_4)_2CO_3$-mediated polyol process instead of a conventional salt-mediated polyol process to improve metal purity and showed that the resulting AgNWs had rounded ends instead of {111} crystal planes [104]. Johan et al. proposed a growth mechanism based on various

mediating agents such as $CuCl_2$ and NaCl. They concluded that the presence of both cation and anion is necessary for the formation of AgNWs and showed that in the absence of mediating agents the final products include particles as well as wires [62]. Amirjani et al. investigated the effect of the $Cl^-$ concentration in a $CuCl_2$-mediated polyol process on aspect ratio of AgNWs, and they found an optimum value of <2 mM $Cl^-$ to produce uniform AgNWs [96]. Schuette et al. utilized NaCl as a salt mediator and showed that it is responsible for AgCl nanocube formation with different sizes as heterogeneous nucleants for subsequent wire growth. As the AgNW diameter was almost independent of AgCl size, they showed that the nucleation event had little influence on the AgNW diameter. Their kinetic investigation showed that the AgNW length, diameter, and aspect ratio grow in parallel and consequently proved that growth is limited by the rate of reduction through a surface-catalyzed reduction in which Ostwald ripening or aggregation of NPs is essential component of the growth mechanism [105]. Li et al. utilized a polyol process not only to synthesize AgNWs but also to control their diameter and consequently their optoelectronic properties through addition of bromide (NaBr) [106]. Lee et al. utilized a polyol process in the presence of propylene glycol (PG) as a solvent and a reducing agent, PVP as a capping agent, and 1-butyl-3-methylimidazolium chloride (BMIM-Cl) as a growth controller. They showed that AgNW length can be adjusted by changing the PVP/BMIM-Cl concentration ratio [99]. Zhang et al. introduced a new one-pot polyol synthesis by using KBr as a conucleant to NaCl, which is advantageous for AgNW reduction size [107]. Silva et al. introduced a method for the facile synthesis of AgNWs by using both PVP and $Br^-$ ion as a capping agent. They showed that the ratio of PVP to $Br^-$ ions controls the reduction kinetics and can be used to form Ag seeds with decahedral shape and consequently facilitate growth in the desired direction [108]. Zhu et al. investigated the importance of several cations and anions such as $Fe^{3+}$, $Cu^{2+}$, $K^+$, $Na^+$, $H^+$, $SO_4^{2-}$, $NO_3^-$, and $Cl^-$ as control agents in the polyol synthesis of AgNWs. They explained these effects by slow release of $Ag^+$, decrease of the surface oxidation etching phenomenon due to the presence of cations, and low solubility of products due to the presence of anions [65]. Wang et al. investigated the effect of $Cu^{2+}$ ion concentration to rapidly produce long AgNWs. They showed that AgNWs are longer at higher $Cu^{2+}$ concentration [66]. Wang et al. also investigated the effect of chloride ions to produce very long AgNWs in a rapid process. They attributed this rapid (~40 min) polyol synthesis to the presence of a high concentration of $Cl^-$ that facilitates the production of multitwinned Ag seeds during nucleation [67]. Abbasi et al. tried cobalt chloride ($CoCl_2$) as a salt mediator or growth-promoting additive in the presence of an optimum ratio of glycerol/water (G/W) as a solvent to synthesize AgNWs not only rapidly but with morphology control as well [109]. Satoungar et al. investigated the effect of several mediation agents ($FeCl_2$, $FeCl_3$, and $AlCl_3$) on the morphology of AgNWs through the use of 1,2-propandiol and EG as a solvent and a reducing agent. They showed that $Cl^-$ ions are responsible for electrostatic stabilization and AgCl colloid formation in the initial stage of silver seed formation [68]. Liu et al. utilized a microwave-assisted (400 W for 3 min) polyol method to control nanostructure morphology by varying the $Na_2S$ concentration with all other reaction parameters held constant. They found a spherical-cube-linear morphology progression as the concentration of $Na_2S$ was increased [91]. Zhao et al. regulated the morphology and size of AgNWs with ferric chloride ($FeCl_3$) as a mediation and nucleation agent and PVP as a capping agent to synthesize AgNWs with aspect ratio up to 570 (from 250 to 570) [110]. Rui et al. investigated the effect of $Cl^-$ and $Br^-$ in the polyol synthesis of high yield (>85%) and high aspect ratio (up to 2500) of AgNWs. They used the electron trap distribution (ETD) of the silver halide crystals to investigate the simultaneous effect of $Cl^-$ and $Br^-$ ions in the synthesis of high aspect ratio AgNWs of small diameter by providing uniform EDT through formation of silver halide $AgBr_{1-x}Cl_x$ [111]. Bobinger et al. tailored the various polyol parameters such as the temperature, PVP to the $AgNO_3$ ratio, rate of stirring, and type of PVP to synthesize AgNWs with an aspect ratio of 800. They found that a small amount of KCl can reduce the AgNW diameter as well as increase dispersion and stability. They demonstrated the role of KCl as a cocapping agent in the presence of PVP [112]. Trung et al. also illustrated the necessity of a suitable mixture of metal salts. They showed that the diameter of the AgNWs can be decreased and their length increased by an increase in the NaCl concentration. They also showed that the addition of NaBr at an appropriate ratio can further decrease the diameter of the synthesized AgNWs [113]. Lei et al. controlled the diameter and length of AgNWs by varying the concentration of KBr and $MnCl_2$. A kinetic investigation (reaction rate and reaction activation energy) of the Ag ion conversion to Ag atoms proved that their introduction to the process plays an essential role in producing very long AgNWs with a high aspect ratio [114].

*3.5. Effect of the Mixing Type and Rate in the Polyol Synthesis of AgNWs.* Provision of a high, uniform, and consistent rate of mass and heat transfer is required in the polyol synthesis particularly when the synthesis is carried out on a large scale. This can be achieved by efficient mixing to generate seeds, nanoparticles, and consequently nanowires in sufficient quantity. There are some studies that investigated the effect of the rate and power of stirring on nanowire morphology.

Coskun et al. investigated the effect of the stirring rate (10-1000 rpm) along with the effects of other reaction parameters on product morphology to optimize reaction conditions. They observed formation of AgNWs at all stirring rates and even in stagnant solution. In stagnant solution, they observed formation of micron-sized particles as well as large-diameter nanowires [87]. Andres et al. reported a rapid (less than 1 hr) one-pot polyol synthesis process to produce very long AgNWs by adjusting the temperature and stirring rate [115]. Amirjani et al. in another study also investigated the effect of the agitation rate on the polyol synthesis of AgNWs. They showed that by increasing the agitation rate, oxidation etching would be enhanced leading to formation of various nanostructures such as nanoparticles, nanorods, and nanowires. They illustrated that agitation is not necessary for AgNW synthesis, but the AgNW diameter can be decreased

by setting the stirring rate at 200 rpm [116]. Junaidi et al. investigated the effect of the rate of stirring on AgNW polyol synthesis using polyvinyl alcohol (PVA) as a capping agent and a stabilizer without adding any salt mediator. They showed that optimal formation of AgNWs would be achieved at 350 rpm [69].

*3.6. Modified Polyol Processes.* There are also some studies that investigated modified polyol processes such as the successive multistep growth method (SGM), novel solvents or cosolvents, novel capping agents, or novel reaction conditions such as high pressure.

Lu et al. proposed a modified multistep polyol process including two $AgNO_3$ additions corresponding to two extents of conversion of the silver precursor into MTPs as well as the NW growth step. They also utilized a novel separating reagent (formamide) to remove the organic solvent and extra surfactant on the surface of synthesized AgNWs [117]. Fahad et al. carried out the polyol AgNW synthesis process in a salt-free environment and Argon atmosphere. Their process included five steps: EG preheating for 20 minutes, Argon gas flushing for 1 minutes, $AgNO_3$ injection within 5 minutes, PVP injection within 10 minutes, and reaction mixture heating for 2 hours. They reported that the most important factors controlling the morphology and yield of AgNWs are the reaction temperature and $AgNO_3$/PVP ratio [118]. Liu et al. reported a modified polyol process for AgNW synthesis with sharp end by controlling the AgNW growth, oxidative etching, and PVP passivation rates occurring at the tip of AgNW for scanning tunneling microscopy and tip-enhanced Raman spectroscopy applications [119]. Inose et al. also used a water-mediated polyol process to synthesize pencil-like sharp AgNWs by adding an appropriate amount of pure water (0.2–0.4 ($v/v$), %) in the conventional polyol synthesis [120]. Wang et al. introduced AgCl particles (reaction products between NaCl and $AgNO_3$) as seeds for heterogeneous nucleation in a modified polyol process. The amount and reaction time of AgCl as well as reaction temperature were adjusted to synthesize uniform AgNWs with small diameters of about 52 nm and aspect ratios above 1000 [121]. Li et al. introduced a modified fast (30 minutes) polyol synthesis process by finding the optimum conditions to synthesize AgNWs with diameters of $53 \pm 9$ nm, lengths of $31 \pm 7$ $\mu$m, and aspect ratio of 584.9 [122]. Andrew et al. introduced a solution-based low temperature method to synthesize AgNWs and to functionalize their surfaces by either displacement or adsorption. They showed that the adsorption of a luminescent polymer or PVP thiol displacement can be used to functionalize AgNWs. Characterization demonstrated polymer inhomogeneity on the AgNW surfaces and noninteracting polymer excitons [123]. Lee et al. introduced a successive multiple growth (SMG) polyol process in which AgNWs produced in a first synthesis are used as seeds to grow very long AgNWs. They showed that this process can be repeated up to seven times to produce extremely high aspect ratio (1000–3000) AgNWs [7]. Jiu et al. utilized a salt-assisted hydrothermal process to synthesize AgNWs by using PVP not only as a polymeric capping agent but also as a reducing agent in deionized water (DIW) in an autoclave [88]. Hua et al. introduced a successive multistep process to produce ultrathick AgNWs. This was achieved through the initial formation of thin AgNWs as seeds for growth of thick AgNWs [124]. Yang et al. reported a water-involved synthesis of AgNWs by a rapid and scalable heterogeneous nucleation process. They proposed that the addition of small amounts of water with an optimal ratio to the reducing agent of 0.25% plays an essential role in obtaining a high yield of AgNWs [73]. Zhao et al. reported a water-assisted polyol process to increase the aspect ratio of AgNWs and demonstrated the effect of a proper amount of water in promoting and facilitating the charge transfer process as transfer of electrons are easier in polar solvents [125]. Lee et al. utilized a polyol process in the presence of propylene glycol (PG) as a solvent and a reducing agent, PVP as a capping agent, and 1-butyl-3-methylimidazolium chloride (BMIM-Cl) as a growth controller [96]. Moon et al. synthesized AgNWs with glycerol/-DIW as a solvent and a reducing agent in a polyol process [126]. Lee et al. reported the synthesis of ultrathin AgNWs with a high aspect ratio around 1000 by a polyol process under high pressure reaction conditions. They showed that high pressure can enhance the rate of nucleation and consequently decrease the AgNW diameter [127]. Abbasi et al. tried cobalt chloride ($CoCl_2$) as a salt mediator or growth-promoting additive in the presence of an optimum ratio of glycerol/water (G/W) as a solvent to synthesize AgNWs at high rates with good morphology control [109]. Junaidi et al. introduced a polyol synthesis using polyvinyl alcohol (PVA) as a capping agent and a stabilizer without adding any salt mediator [69]. Patarroyo et al. introduced a novel high yield green silver nanorod (AgNR) synthesis in the presence of tannic acid as an assistance to nucleate decahedral seeds needed for the monodisperse AgNP production [128].

Recently, Liu et al. also introduced the use of glycerol as a more stable and stronger solvent and a reducing agent containing three hydroxyl groups compared to EG for synthesis of thin and uniform AgNWs. Glycerol can be heated to a higher temperature due to its higher boiling point of 290°C compared to the EG boiling point of 197°C. They synthesized AgNWs up to 10–20 $\mu$m in length and 40–50 nm in diameter without addition of salt mediators, chlorides, and template salts by autoclaving mixtures at 197°C for 9 hr. The autoclave step prevents the oxidization of glycerol in air and consequently formation of acrolein and light-yellow polymer [129]. Li et al. synthesized AgNWs as long as 160 $\mu$m with 40–85 nm diameter with glycerol as a solvent and a reducing agent and heating at 150°C [130]. Jang et al. synthesized AgNWs as long as 65 $\mu$m with an aspect ratio up to 1500 in a tetrabutylammonium dichlorobromide (TBADCB) salt-based polyol synthesis process in which the wire diameter can be controlled by the TBADCB/$AgNO_3$ molar ratio and length can be controlled by mechanical stirring (unidirectional axial stirring) and reaction temperature. In this process, TBADCB, an organic halide with high thermal stability, acted as a soft template and ionic halogen salt containing an ammonium cation and a $BrCl_2^-$ anion [131]. Wei et al. introduced a facile polyol synthesis of segmented

AgNWs through end-to-end self-connection of twinned crystals of neighboring rods or wires with an average dimeter of 66 nm [132]. Tang et al. studied a novel modified AgNW synthesis process to control and reduce the high activity defects of synthesized AgNWs through an etching process in which a locally uneven ligand distribution is required to provide more ligand molecules in the nucleation step and less in the growth step. They showed that the AgNWs synthesized in this etching process have fewer straight defects with similar morphology to pentatwinned structures compared to the AgNWs synthesized via a nonetching route [133]. Xi et al. recently used ethylene glycol (EG) and diethylene glycol (DG) as the combined solvents and reducing agent to synthesize ultrathin AgNWs in a large-scale polyol process. They showed that adjustment of the ratio between these two solvents and reducing agents can control their reduction activity and viscosity. They produced AgNWs with 100 nm diameters in the presence of EG and decreased the diameter to ~35 nm using a EG/DG ratio of 4/1 to 3/2 [134]. Rekha et al. recently reported the synthesis of silver nanorods (AgNRs) by a modified seed-mediated method at room temperature [135]. Niu et al. used a modified polyol process with the addition of benzoin to synthesize AgNW with diameters as small as 13 nm and aspect ratios of up to 3000. They also controlled the temperature in the course of the reaction by forming AgCl and AgBr at room temperature and then increasing the temperature to 150°C or 160°C, depending on the desired diameter, while controlling the stirring rate [136]. Zhabg et al. used a polyol process with high molecular weight PVP and $FeCl_3$ as a capping agent and a salt mediator, respectively, to produce a high aspect ratio (length up to 220 $\mu$m) of AgNWs at relatively low temperature (130°C) and long reaction time (8 hr). For the first time, they used filter cloths for purification and to separate short nanowires, AgNRs, and AgNPs produced as byproducts [137]. Chen et al. devised a modified polyol process using both stirred and stagnant conditions during the synthesis process and combined that with a heating process. They increased the temperature over 15-20 minutes up to 180°C while purging the reaction solution with Nitrogen. This was followed by 10 minutes at temperature of 170°C while stirring but without Nitrogen purging. After 10 minutes of stirring, the reaction was brought to completion after one hour at the stagnant condition to produce AgNW with diameters of about 21 nm and lengths of up to about 20 $\mu$m. They also introduced a novel water-based purification method along with a small amount (5 ppm) of surfactant such as fluorocarbon surfactant as the purifying agent [138]. Yi et al. used a microwave-assisted technique in the presence of NaBr to control the morphology and size of the synthesized nanostructures as well as to reduce the reaction time from hours to minutes by controlling the NaBr concentration, and microwave time and power that can provide different reaction energies and consequently different reaction rates [139]. Xu et al. utilized a modified polyol process to synthesize very long AgNW (~220 $\mu$m) by mixing two different molecular weights (58,000 and 360,000) of PVP as a capping agent. The solution was prepared at room temperature and transferred to a heat transfer bath at 130°C. The solution was first stirred just 10 minutes and then left unstirred for 3.5 hr [49]. Sim et al. introduced the formation of AgNWs without addition of an organic capping agent and a stabilizer such as PVP by using small amounts of NaCl and $Fe(NO_3)_3$ at a low temperature of 110°C for a long reaction time of 15 hr without stirring [140].

In a study by Hemmati et al., the polyol process based on the method introduced by Xia's research group was used [6]. The reactor volume was scaled up twenty times for application to conductive inks adaptable for the screen printing process [9]. They performed a parametric study on the polyol synthesis of AgNWs to find the most important parameters that control the yield of AgNWs compared to other Ag nanostructures. They investigated the effect of several parameters such as temperature, reagent concentration, PVP MW, rate of stirring, and sonication time for $AgNO_3$ solution preparation. Based on this parametric study, it was found that four parameters (temperature, $AgNO_3$ concentration, PVP concentration, and $CuCl_2$ concentration) are the most important factors affecting AgNW yield (percentage of AgNWs in respect to other Ag nanostructures). A design of experiment (DoE) procedure was used to investigate the simultaneous effect of these parameters on the AgNW yield and to optimize synthesis to maximize AgNW yield [141].

Table 1 shows a summary of the reaction conditions such as reaction time and temperature, reagent precursor, additive and salt mediator, reducing agent, morphology and dimensions of the Ag nanostructures, and the characterization techniques used in several studies of the polyol synthesis of AgNWs.

*3.7. Polyol Flow and Continuous Synthesis of AgNWs.* There are a few studies regarding the polyol synthesis of AgNWs in flow reactors to achieve better control of morphology and to scale up the process with high quality, high yield, and high aspect ratio relative to batch reactors. Gottesman et al. utilized a millifluidic reactor to synthesize AgNWs at high yield (92%) by optimizing the reaction conditions at an elevated temperature of 198°C close to the solvent (EG) boiling point and in the absence of any salt mediator. They found that the best morphology can be obtained at 30 min reaction time with a nanowire length in the range of 2-50 $\mu$m and average length of ~10 $\mu$m and diameter of 71 nm ± 2 [143]. Espinosa et al. synthesized five grams of AgNW using both batch and flow methods. They utilized a 1/4-inch stainless steel tube reactor equipped with the HPLC pump for the flow synthesis of AgNW using EG, $AgNO_3$, PVP, and $CuCl_2$ as the solvent and reducing agent, silver precursor, capping agent, and salt mediator, respectively, at temperature of 152°C. They reported flow synthesis of AgNW with lengths of 10-20 $\mu$m and thicknesses of 50-100 nm [64]. Yun et al. utilized a trapped tubular flow reactor for polyol AgNW synthesis by using EG, PVP/sodium dodecyl sulfate (SDS), $AgNO_3$, and NaBr as the solvent and reducing agent, capping agent, Ag precursor, and seeding agent, respectively, at temperature of 160°C. They suggested that high-yield AgNW synthesis without defects can be attributed to the absence of excessive shearing that happens in a stirred batch reactor. They reported the synthesis of AgNW with the length of 30-80 $\mu$m and diameter of 80 nm [144]. Lau et al.

Table 1: Summary of the reaction conditions and specifications in several AgNW polyol syntheses.

| Regent precursor/capping agent | Reducing agent | Salt mediator | Reaction time, temperature/heating | Morphology & dimensions | Characterization techniques | Ref. |
|---|---|---|---|---|---|---|
| $AgNO_3$/PVP | EG | NaCl | 1 hr<br>170°C | NW<br>Diameter: 26 nm<br>Length: 1113 nm | TEM and UV-vis | [142] |
| $AgNO_3$/PVP | EG | — | 2 hr plus injection time for $AgNO_3$ (5 s) and PVP (10 min)<br>160°C | NW<br>Diameter: Average of 56 nm<br>Length: Average of 12 $\mu$m | SEM, TEM, HRTEM, XRD, UV-vis, and FTIR | [118] |
| $AgNO_3$/PVP | EG | TBADBC | 40 min at 25°C (stirring)<br>2 hr at 25°C (stagnant)<br>30 min at 120°C<br>Heating at 150/160/170°C | NW<br>Diameter: average of 16 nm<br>Length: average of 35 $\mu$m | FE-SEM, XRD, UV-vis, and EDX | [102] |
| $AgNO_3$/PVP | EG | NaCl, $CoCl_2$, $FeCl_3$, and $CrCl_3$ | 3 hr<br>160°C | NW<br>Diameter: ~80 nm<br>Length: 75-160 $\mu$m | XRD, SEM, and TEM | [101] |
| $PtCl_2$, $AgNO_3$/PVP | EG | — | 60 min<br>160°C | NW<br>Diameter: 30-40 nm<br>Length: ~50 $\mu$m | TEM, SEM, and UV-vis | [83] |
| $AgNO_3$/PVP | EG | CuCl, $CuCl_2$, $Cu(NO_3)_2$, and NaCl | 60-90 min<br>151.1°C | NW<br>Diameter: 100 nm<br>Length: 10-50 $\mu$m | TEM and SEM | [6] |
| $AgNO_3$, Pd decahedral seeds/PDDA | EG | — | 8 hr<br>200 °C | NR<br>Diameter: ~20 nm<br>Length: ~77 nm | TEM, EDX, UV-vis-NIR, and ATR-FTIR | [85] |
| $AgNO_3$ | EG | KBr, KOH, KCl, $Fe(NO_3)_3$, $PdCl_2$, $Na_2S$, and ascorbic acid | 2 hr<br>180°C | NW<br>Diameter: 30-450 nm | TEM, SEM, XRD, and UV-vis | [103] |
| $AgNO_3$/PVP | EG | — | 60 min<br>160°C | NW<br>Diameter: 60-100 nm<br>Length: 90 $\mu$m | SEM, CLSM, and NC-AFM | [123] |
| $AgNO_3$/PVP | EG | NaCl | 170°C | NW | SEM and XRD | [87] |
| $AgNO_3$/PVP (MW: 15,000) | EG | — | 150°C | NP (~60%)/NW (~40%)<br>*D*: ~120nm<br>*L*: ~3 $\mu$m | FE-SEM, TEM, XRD, UV-vis, and IR spectroscopy | [98] |
| $AgNO_3$/PVP (MW: 38,000) | | | | NP (~50%)/NW (~50%)<br>*D*: ~100 nm<br>*L*: ~3 $\mu$m | | |

Table 1: Continued.

| Regent precursor/capping agent | Reducing agent | Salt mediator | Reaction time, temperature/heating | Morphology & dimensions | Characterization techniques | Ref. |
|---|---|---|---|---|---|---|
| $AgNO_3$/PVP (MW: 58,000) | | | | NP (~10%)/NW (90%)<br>*D*: ~180 nm<br>*L*: ~8 $\mu$m | | |
| $AgNO_3$/PVP (MW: 200,000) | | | | NP (~5%)/NW (~95%)<br>*D*: ~120nm<br>*L*: ~8 $\mu$m<br>NW (~99%) | | |
| $AgNO_3$/PVP (MW: 800,000) | | | | *D*: ~100 nm<br>*L*: ~10 $\mu$m | | |
| $AgNO_3$/PVP | EG | NaCl | 3.5 min<br>Microwave heating | NW | TEM | [59] |
| $AgNO_3$/PVP | EG | $CuCl_2$ | 90 min<br>151.1°C | NW<br>Diameter: <150 nm<br>Length: 400-500 $\mu$m | SEM, HR-TEM, and XRD | [7] |
| $AgNO_3$/PVP | EG | — | 60 min<br>160°C | NW<br>Diameter: 100 nm<br>Length: 10 $\mu$m | FE-SEM, TEM, UV-vis, and XRD | [58] |
| $AgNO_3$ | PVP in DIW | $FeCl_3$,<br>NaCl, and $Na_2CO_3$ | 24 hr<br>150°C | NW<br>Diameter: 60 nm<br>Length: 5-20 $\mu$m | SEM, XRD, and UV-vis | [88] |
| $AgNO_3$/PVP | EG | $Na_2S$ | 150°C | NW<br>Diameter: 90 nm<br>Length: >10 $\mu$m | SEM, HRTEM, SAED, UV-vis, and XRD | [30] |
| $AgNO_3$/PVP | EG | $FeCl_3$ | 145°C | NW<br>Diameter: 72 nm<br>Length: tens of $\mu$m | TEM, XRD, and UV-vis | [89] |
| $AgNO_3$/PVP | EG | $(NH_4)_2CO_3$ | 60 min<br>160°C | NW<br>Diameter: ~100 nm<br>Length: 10-40 $\mu$m | SEM, HR-TEM, and SAED | [27] |
| $AgNO_3$/PVP | EG | $FeCl_3$ | 151°C (14°C/min) | NW<br>Diameter: 84 nm<br>Length: 20 $\mu$m | SEM, HR-TEM, and UV-vis | [92] |
| $AgNO_3$/PVP | EG | AgCl | 170°C | NW<br>Diameter: 10-50 nm<br>Length: 15-30 $\mu$m | SEM, TEM, EDS, XRD, and FTIR | [100] |

Table 1: Continued.

| Regent precursor/capping agent | Reducing agent | Salt mediator | Reaction time, temperature/heating | Morphology & dimensions | Characterization techniques | Ref. |
|---|---|---|---|---|---|---|
| $AgNO_3$/PVP | EG | NaCl<br>NaBr | 1 hr<br>170°C | NW<br>Diameter: 20 nm<br>Length: 20 $\mu$m | SEM | [106] |
| $AgNO_3$/PVP | Glycerol/DIW | NaCl | 210°C (8°C/min) | NW<br>Diameter: 60-90 nm<br>Length: 8-12 $\mu$m | SEM, TEM, UV-vis | [73] |
| $AgNO_3$/PVP | PG | BMIM-Cl | 24 hr<br>90°C | NW<br>Diameter: 45 nm<br>Length: 25 $\mu$m | SEM, LSM, and XRD | [99] |
| $AgNO_3$/PVP | EG | — | 30 min<br>160°C | NW<br>Diameter: 100-300 nm<br>Length: 10-50 $\mu$m | SEM, TEM, and UV-vis | [93] |
| $AgNO_3$/PVP | EG | NaCl/KBr | 4 hr<br>120°C | NW<br>Diameter: 26 nm<br>Length: 21 $\mu$m | SEM and UV-vis | [107] |
| $AgNO_3$/PVP | EG | NaCl and KBr | 30 min<br>160-180°C | NW<br>Diameter: 200 nm<br>Length: 110 $\mu$m<br>NW<br>Diameter: 50 nm<br>Length: 80 $\mu$m | FEG-SEM and TEM | [115] |
| $AgNO_3$/PVP | EG | NaBr | 35 min<br>160°C | NW<br>Diameter: 20 nm<br>Length: 20 $\mu$m | TEM, HRTEM, and UV-vis | [108] |
| $AgNO_3$/PVP | EG | | 60 min<br>160°C | | FESEM and UV-vis | [65] |
| | | $CuSO_4 \cdot 5H_2O$ | | NPs and a few NRs | | |
| | | $Cu(NO_3)_2 \cdot 3H_2O$ | | NPs | | |
| | | KCl | | NPs and NWs | | |
| | | NaCl | | NPs and NWs | | |
| | | $FeCl_3 \cdot 6H_2O$ | | NPs and NWs | | |
| | | $CuCl_2 \cdot 2H_2O$ | | NWs and few NPs | | |
| | | HCl | | NWs and few NPs | | |
| $AgNO_3$/PVP | EG | $CuCl_2 \cdot 2H_2O$ | 30 min<br>160°C | NW<br>Diameter: 31-57 nm<br>Length: 50 $\mu$m | TEM and SEM | [66] |

Table 1: Continued.

| Regent precursor/capping agent | Reducing agent | Salt mediator | Reaction time, temperature/heating | Morphology & dimensions | Characterization techniques | Ref. |
|---|---|---|---|---|---|---|
| $AgNO_3$/PVP | EG | — | 40 min (3 steps) 160°C | NW Diameter: 1820 nm Length: 40 $\mu$m | SEM | [124] |
| $AgNO_3$/PVP | EG | $CuCl_2$ | 40 min 160°C | NW Diameter: 60-141 nm Length: average of 102 and longest of 268 $\mu$m | SEM and XRD | [67] |
| $AgNO_3$/PVP | Glycerol/DIW | NaCl | 45 min | NW Diameter: 45 nm Length: 200 $\mu$m | SEM | [126] |
| $AgNO_3$/PVP | EG | NaCl/KBr | 1 hr 160°C/(1000 psi (69 bar) of $N_2$) | NW Diameter: 16-22 nm Length: 20 $\mu$m | TEM and SEM | [127] |
| $AgNO_3$/PVP | G/W | $CoCl_2 \cdot 6H_2O$ | 40 min 160°C | NW Diameter: 196 nm Length: 12.46 $\mu$m | TEM, SEM, XRD, and XPS | [109] |
| $AgNO_3$/PVP | 1,2-propandiol and EG | | | NW | TEM, FESEM, XRD, and UV-vis | [68] |
| | | — | 90 min, 170°C | $D$ = 64 nm, $L$ = 12 $\mu$m | | |
| | | $FeCl_2$ | 60 min, 155°C | $D$ = 88 nm, $L$ = 12 $\mu$m | | |
| | | $AlCl_3$ | 120 min, 180°C | $D$ = 180-230 nm, $L$ = 20 $\mu$m | | |
| | | $FeCl_3$ | 30 min, 170°C | $D$ = 40-60 nm, $L$ = 7-10 $\mu$m | | |
| $AgNO_3$/PVA | EG | — | 90 min | NW Diameter: 190 ± 40 nm Length: 70 ± 20 $\mu$m | SEM, XRD, and UV-vis | [69] |
| $AgNO_3$/PVP | EG | — | 1 hr 160°C | NW Diameter: 40 nm Length: 10 $\mu$m | SEM and UV-vis | [74] |
| $AgNO_3$/PVP | EG | $CuCl_2$ | 90 min 150°C | NW Diameter: 102 nm Length: 3.2 $\mu$m | SEM | [9] |

Table 1: Continued.

| Regent precursor/capping agent | Reducing agent | Salt mediator | Reaction time, temperature/heating | Morphology & dimensions | Characterization techniques | Ref. |
|---|---|---|---|---|---|---|
| $AgNO_3$/PVP | Glycerol | — | 9 hr<br>150°C (autoclave) | NW<br>Diameter: 40-50 nm<br>Length: 10-20 $\mu$m | SEM, XRD, TEM, and UV-vis | [129] |
| $AgNO_3$/PVP | EG | NaCl and KBr | 3 hr<br>160°C | NW<br>Diameter: 20 nm<br>Length: 50 $\mu$m | FED-SEM, AFM, TEM, EDS, EDX, XRD, XPS, and UV-vis-NIR | [94] |
| $AgNO_3$/PVP | Glycerol | NaCl | 5 hr<br>150°C | NW<br>Diameter: 40-85 nm<br>Length: >100 $\mu$m | XRD, SEM, and UV-vis | [130] |
| $AgNO_3$/PVP | EG | $FeCl_3$ | 5 hr<br>130°C | NW<br>Diameter: 70-80 nm<br>Length: 10 $\mu$m | TEM | [110] |
| $AgNO_3$/PVP | EG | TBADCB | 30 min at 120°C<br>30 min at 170°C | NW<br>Diameter: 32 nm<br>Length: 65 $\mu$m | SEM, XRD, and SPS | [131] |
| $AgNO_3$/PVP | EG | NaCl | 2.5 hr<br>150°C | NW<br>Diameter: 66 nm<br>Length: tens of $\mu$m | XRD, SEM, TEM, and UV-vis | [132] |
| $AgNO_3$/PVP | EG | NaCl, $FeCl_3$, $Fe(NO_3)_3$, and $KNO_3$ | 6 hr<br>130°C | NW<br>Length: 14-40 $\mu$m | SEM, TEM, and UV-vis | [133] |
| $AgNO_3$/PVP (in presence of dilute HCl) | EG | — | 170-190°C | NW, NC, and NP | TEM and UV-vis | [95] |
| [PVP]/[$AgNO_3$] = 0.8/0.7 | | | | Micro and nanocube | | |
| [PVP]/[$AgNO_3$] = 0.8/0.1 | | | | NWs | | |
| [PVP]/[$AgNO_3$] = 0.8/0.45 | | | | NWs & NPs | | |
| $AgNO_3$/PVP | EG | NaCl, KBr | 1 hr<br>160°C | | SEM, TEM, EDS, EDX, XRD, XPS, and UV-vis | [111] |
| | | $AgNO_3$/NaCl/NaBr:<br>80/2/0 | | Diameter: 162.5 ± 21.8<br>Aspect ratio: 360<br>NW yield: 94% | | |
| | | 80/0/2 | | Diameter: 27.5 ± 7.6<br>Aspect ratio: 230<br>NW yield: 30% | | |
| | | 800/2/1 | | Diameter: 94.4 ± 11.5<br>Aspect ratio: 380<br>NW yield: 97% | | |

Table 1: Continued.

| Regent precursor/capping agent | Reducing agent | Salt mediator | Reaction time, temperature/heating | Morphology & dimensions | Characterization techniques | Ref. |
|---|---|---|---|---|---|---|
| | | 80/2/1 | | Diameter: 40.8 ± 6.9<br>Aspect ratio: 2100<br>NW yield: 90% | | |
| | | 16/2/1 | | Diameter: 29.0 ± 3.8<br>Aspect ratio: 1400<br>NW yield: 85% | | |
| $AgNO_3$/PVP | EG/DG | NaCl and KBr | 5 hr<br>145°C | NW<br>Diameter: 35 nm<br>Aspect ratio > 1000 | SEM, TEM, and XRD | [134] |
| $AgNO_3$/PVP | EG | $CuCl_2$ and KCl | 20-30 min<br>167°C | NW<br>Aspect ratio: 800 | SEM | [112] |
| $AgNO_3$/PVP | EG | NaCl and NaBr | 60 min<br>150°C | NW<br>Diameter: 16 nm<br>Aspect ratio up to 3000 | TEM, HRTEM, UV-vis, and XRD | [136] |
| | | NaBr | 60 min<br>160°C | NW<br>Diameter: 13 nm<br>Aspect ratio up to 3000 | | |
| $AgNO_3$/PVP | EG | NaCl and NaBr | 90 min<br>160°C | NW<br>Diameter: 20-50 nm<br>Length: 30-60 $\mu$m | SEM, TEN, and HRTEM | [113] |
| $AgNO_3$/PVP | EG | $MnCl_2$ and NaBr | 4 hr<br>120°C | NW<br>Diameter: 20-50 nm<br>Length: 4-7 to 20-34 $\mu$m | SEM, TEM, and XRD | [114] |
| $AgNO_3$/PVP | EG | $FeCl_3$ | 8 hr<br>130°C | NW<br>Diameter: ~ 55 nm<br>Length: ~ 220 $\mu$m | SEM, TEM, and HRTEM | [137] |
| $AgNO_3$/PVP | EG | NaCl and $Fe(NO_3)_3$ | 15 hr<br>110°C | NW<br>Diameter: 45 nm<br>Length: 40 $\mu$m | SEM, TEM, HRTEM, XRD, and UV-vis | [140] |

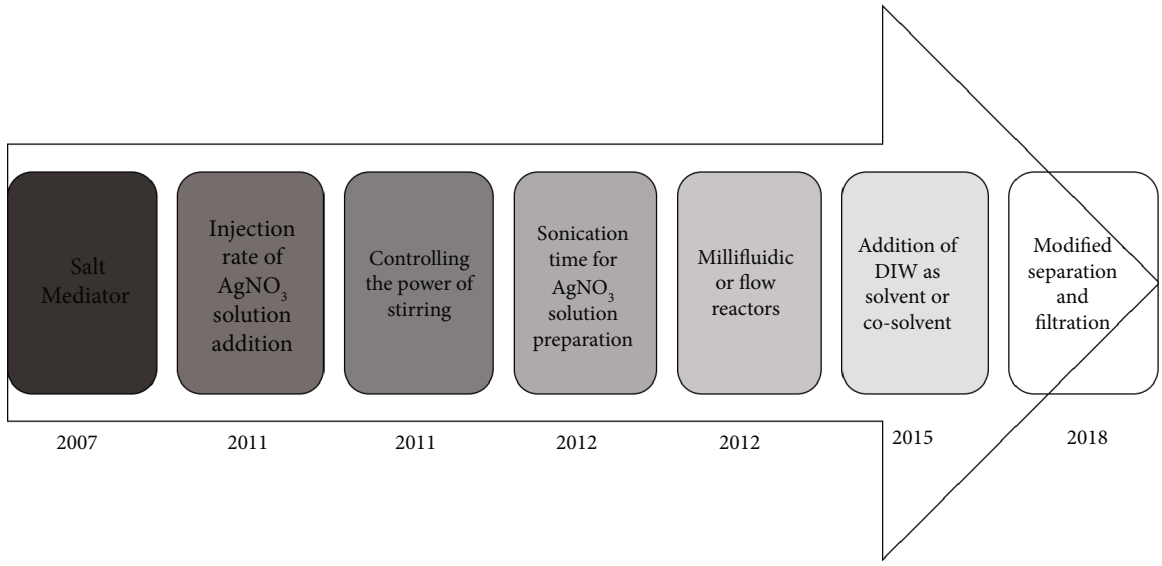


Figure 1: Timeline for the progresses in order to overcome the challenges in polyol synthesis of AgNWs.

utilized a novel segmented flow reactor consisting of a binary pump module, a reactor heater, and a 10 mL perfluoroalkoxy (PFA) reaction coil tubing to synthesize AgNW at 130°C with lengths up to 36.4 $\mu$m and diameters as small as 95 nm by controlling PVP MW. They showed that a higher PVP MW corresponding to longer PVP chain length led to a longer length and smaller diameter of the synthesized AgNWs [145].

Hemmati et al. in another study addressed the challenges in the polyol batch synthesis of AgNW such as low yield and low aspect ratio of AgNWs, presence of other nanostructures as byproducts, irregular morphology of the wires, and long reaction time. They introduced a millifluidic polyol synthesis of AgNWs at lower temperature compared to the batch process. They were able to achieve near 100% yield of high aspect ratio AgNWs in a continuous manner [146, 147].

From this overview of recent studies on the polyol synthesis of AgNWs, it is clear that the obstacles and challenges to control the morphology with a high aspect ratio have been overcome through methods such as introduction of a salt mediator, control of the injection rate of $AgNO_3$, optimization of sonication time for $AgNO_3$ solution preparation, control of stirring power, addition of DIW as a solvent or cosolvent, and application of millifluidic or flow reactors.

Figure 1 shows a timeline in which dark gray indicates a method that is well studied and light gray indicates processes in the early stage of their development, where work in the near future is likely to be centered. The corresponding starting year for each method is shown as well.

## 4. Reaction Mechanism of AgNW Polyol Synthesis

An understanding of the reaction mechanism and dynamics in the polyol synthesis of AgNW allows reaction optimization in terms of conditions such as temperature and reagent concentrations. To reach this goal, it is essential to know how different factors in the synthesis affect wire morphology, for instance, what is the mechanism to facilitate the growth of initially formed seeds to the wire shape by the anion and cation provided from a salt mediator and what are the kinetics behind the application of polymeric reagents as a capping agent, a stabilizer, or a growth director? Finally, the steps governing formation of AgNWs must be clarified.

Several studies used methods such as microscopic and spectroscopic characterizations (TEM, HRTEM, SEM, UV-vis, …) to assess the reaction mechanism. Schuette et al. utilized AgCl nanocubes of various sizes as heterogeneous nucleants to synthesize AgNW through the polyol process. As the AgNW diameter was almost independent of AgCl size, they showed that the nucleation event had little influence on AgNW diameter. Their kinetic investigation showed that AgNW length, diameter, and aspect ratio grow in parallel. Consequently, they showed that growth is limited by the rate of reduction through a surface-catalyzed reduction at which Ostwald ripening or aggregation of NPs are essential components of the growth mechanism [105]. Mao et al. used a self-seeding process and proposed a reaction mechanism based on the adsorption of PVP onto the {100} surface of the silver seeds confining growth to the {111} surface [58]. Lai et al. produced Ag/Ag homojunction NWs (HNWs) by an effective and simple solvothermal method and showed that the Ag/Ag HNW synthesis is sensitive to PVP concentration and reaction temperature [89]. Liu et al. utilized a $(NH_4)_2CO_3$-mediated polyol process instead of a conventional salt-mediated process for improvement of AgNW purity and showed that the synthesized AgNWs have rounded instead of faceted ends on the {111} crystal plane. They proposed that in the presence of PVP and $(NH_4)_2CO_3$, the initial multiple twinned particles (MTPs) with twin boundaries grow into AgNWs with rounded ends [104]. Murph et al. proposed that synthesis proceeds by a coarsening process through the oriented attachment mechanisms of the initial pentatwinned silver seeds as nucleation centers. They explained that the seeds are produced by the reduction of Ag ions in boiling water, with sodium hydroxide and sodium citrate as additives, and subsequently AgNWs are

produced. They performed molecular dynamic computations with an embedded atom method to compare with the experimental results [148]. Wu et al. developed a growth model based on their observation of coarsening and combination of Ag nanorods by syringe rate testing [93]. Whitcomb et al. evaluated the growth mechanism in a high-temperature polyol process through both potentiometric Ag ion measurements and incorporation of nitric oxide monitoring to clarify the crystal growth process during the reduction of Ag ions to metallic Ag. They concluded that the reduction of Ag ions and growth of AgNWs include a series of discrete phases, from AgCl precipitation to Ostwald ripening [149]. Wang et al. investigated the seeding protocol for high-concentration synthesis of AgNWs. Based on AgNW nucleation and growth behavior, they found a linear relation between nucleation and the $Ag^+$ and $Cl^-$ concentrations. Based on the proposed mechanism, they reported synthesis of high quality of AgNWs at which $Ag^+$ concentrations are twenty times higher than the previously reported polyol process. They also demonstrated control of AgNW diameter through the size of the AgCl seeds [150]. Abbasi et al. tried cobalt chloride ($CoCl_2$) as a salt mediator or a growth-promoting additive in the presence of an optimum ratio of glycerol/water (G/W) as solvent to synthesize AgNW not only in a rapid way but with ability to control the AgNW morphology as well. They also proposed a growth mechanism based on the AgCl formation monitoring, an important intermediate stage in generation of AgNWs [109]. Li et al. described a hydrothermal reaction mechanism similar to the polyol process in which pentagonal twinned silver seed crystals with $D_{5h}$ symmetry are produced and subsequently increase in diameter. The reaction requires a stationary solution and a relatively high temperature with high molecular weight PVP to produce long AgNWs [130]. Jang et al. proposed a four-step reaction mechanism including nucleation, cluster formation, seeding, and AgNW growth with assistance of PVP [131]. Wei et al. explained the reaction mechanism behind the formation of segmented AgNWs including the initial steps of formation of single nanowires with assistance of a salt mediator and a capping agent. They attributed the formation of segmented wires to the higher potential energy of the end atoms causing them to diffuse to the sides or attach end to end to reduce the surface chemical potential [132]. Tang et al. described a detailed reaction mechanism in the polyol process involving an etching effect. In this mechanism, the ligand concentration is higher in the nucleation step and lower in the growth step and maximizes the benefit of etching in the latter. The mechanism entails a transition from ligand-rich aggregates of PVP to an uneven ligand distribution with PVP deficiency. The reason is that the silver ions coordinate better with repeating units of PVP as a capping agent. With more silver ions released as the reaction continues, the restricting motion of PVP will limit its coordination with silver ions, which promotes etching [133]. Rui et al. introduced the application of electron trap distribution (ETD) to explain the growth mechanism of wires with different diameters and yields. They showed that by simultaneous application of NaCl and NaBr as salt mediators, $AgBr_{1-x}Cl_x$ would be formed as a mixed silver halide crystal with uniform EDT which is beneficial for the formation of high aspect ratio AgNWs. The $x$ value, defined as $x = [NaCl]/([NaCl] + [NaBr])$, controls the diameter and yield of AgNWs [111].

Hemmati et al. also showed that the growth mechanism includes three steps of reduction, nucleation, and growth by SEM characterization of nanostructures obtained at different stages of the reaction (every 15 minutes) as shown in Figure 2. This mechanism illustrates that the small silver nanoparticles start to dissolve, as they are not stable in the solution. In the presence of PVP acting as a capping agent that selectively adsorbs on {100} facets of the silver nanocrystals, 1D silver nanostructures begin to grow. The chloride ions provided by $CuCl_2$ form AgCl reducing the concentration of silver ions and releasing them slowly at the beginning of the reaction. The $Cu^{2+}$ is reduced to $Cu^+$ by EG and assists the growth of AgNWs by scavenging oxygen atoms from the surface of the silver seeds. Purging with Argon gas during the reaction also acts to remove oxygen. In summary, silver ion reduction, nucleation in the presence of salt mediator, and wire growth with assistance of PVP acting as a capping agent are the three main steps in the synthesis of AgNWs through the polyol synthesis process [9, 147]. A schematic illustration of the AgNW polyol reaction mechanisms and kinetics according to various studies is shown in Figures 3–6. All of these results regarding the polyol AgNW synthesis emphasize the necessity to precisely control reaction parameters such as temperature, salt mediator type and concentration, capping agent MW, and concentration to synthesize high-quality, high-aspect ratio AgNW with high yield.

## 5. Lessons from Polyol AgNW Synthesis toward Green and Sustainable AgNW Synthesis

Green noble nanoparticle syntheses utilizing natural precursors are of great interest because of cost effectiveness, facile reactions, less harmful feedstocks and procedures, and sustainability. These green technologies can be achieved by the application of green reagents including the reducing agent, solvent, and capping agent. Due to the need for environmentally friendly technologies for nanomaterial synthesis, a synergy between biotechnology and nanotechnology has led to consideration of biosynthesis of nanostructures. Taking advantage of biological materials in nanoparticle synthesis is one of the most promising approaches in modern nanoscience because the formation of nanostructures by organisms is a highly evolved and broad family of processes. Nowadays, green noble nanoparticle synthesis processes utilizing natural precursors are of great interest because they are cost effective, facile, benign, and sustainable. However, these new techniques should be optimized not only in terms of scale-up capability but also in product quality and performance. Although there are many published studies regarding the chemical synthesis of 1D metal nanostructures, there are comparatively few regarding green methods. For instance, Lin et al. used broth of Cassia fistula leaf as a reducing and capping agent to synthesize AgNWs with diameter of 50-60 nm and length up to tens of micrometers. Based on the FTIR characterization, they found that some water-

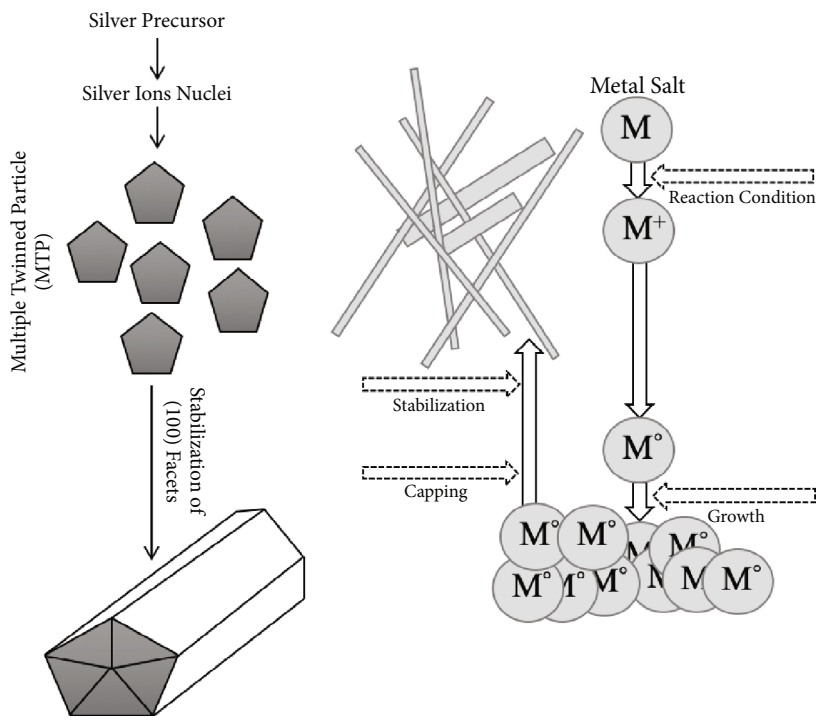


Figure 2: Schematic of the introduced silver nanowire growth mechanism of the polyol process [146].

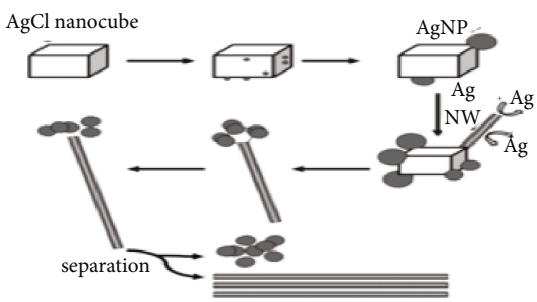


Figure 3: Heterogeneous nucleation and growth pathway for AgNWs (adapted with permission from [105]; Copyright 2014 American Chemical Society).

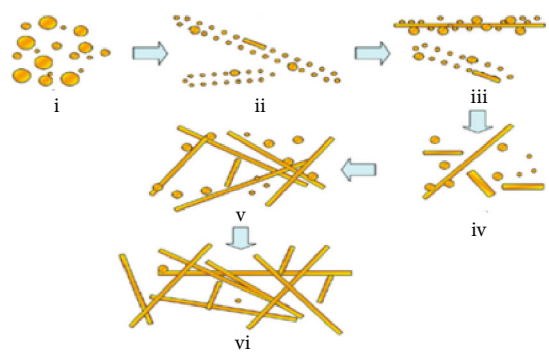


Figure 4: Schematic illustration of the coarsening mechanism via oriented attachment process for the evolution of silver into one-dimensional nanostructures (reprinted with permission from [148]; Copyright 2015 American Chemical Society).

soluble polyhydroxy components, such as alkaloids, flavonoids, and polysaccharose, were acting as capping ligands in AgNW formation. Based on the TEM images of the synthesized particles during the reaction, they found that the growth of AgNWs is due to the recrystallization of nanoparticles next to each other in a linear fashion rather than point-initiated growth of initially formed seeds [151]. Ma et al. utilized glucose to synthesize AgNWs for silver nanowire-silver nanoparticle-graphene nanosheet composite fabrication [152]. Jeevika et al. used clove oil (Syzygium aromaticum) that contains 81-95% phenols as a green reducing agent to synthesize AgNW in the diameter range of 30-80 nm with lengths of 2–5 $\mu$m at room temperature. They also showed that the size and morphology of the synthesized nanostructures are sensitive to $AgNO_3$ concentration [153]. In another study, Nadagouda et al. demonstrated synthesis of various morphologies of silver and palladium nanostructures including nanorods and nanowires using vitamin $B_2$ acting as both a reducing agent and a capping agent in various solvents such as water, isopropanol, acetone, and acetonitrile. They showed that the morphology and size of the resulting nanostructures depend on the solvent used for the preparation. For instance, nanorods are produced in water whereas thick nanowires are produced in isopropanol [154]. Wang et al. formed dendritic silver nanostructures (DSNs) using ascorbic acid as a reducing agent and clove oil as a capping agent under an ultrasound [155]. Flores-Gonzalez et al. used two different green teas: Mexican tea (Royal Tea, Mexico) and Korean tea (Boseong green tea), containing Camellia sinensis as a reducing agent in the presence of PVP at low concentration and MW of 40,000 to synthesize AgNW with diameter around 50 nm and length of

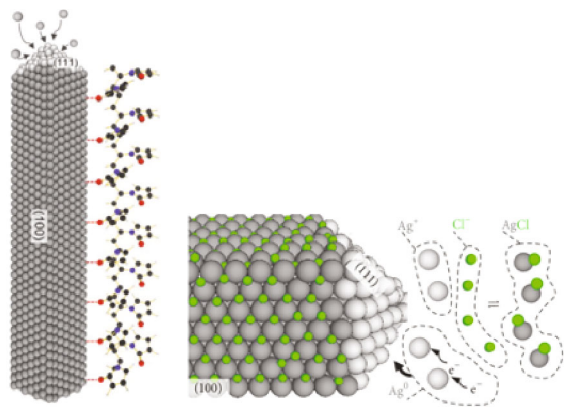


(a) (b)

Figure 5: (a) Schematic of wire formation. (b) Schematic for the effect of KCl on the wire formation (reproduced from [112] under the Creative Commons Attribution 4.0 International (CC BY 4.0) License).

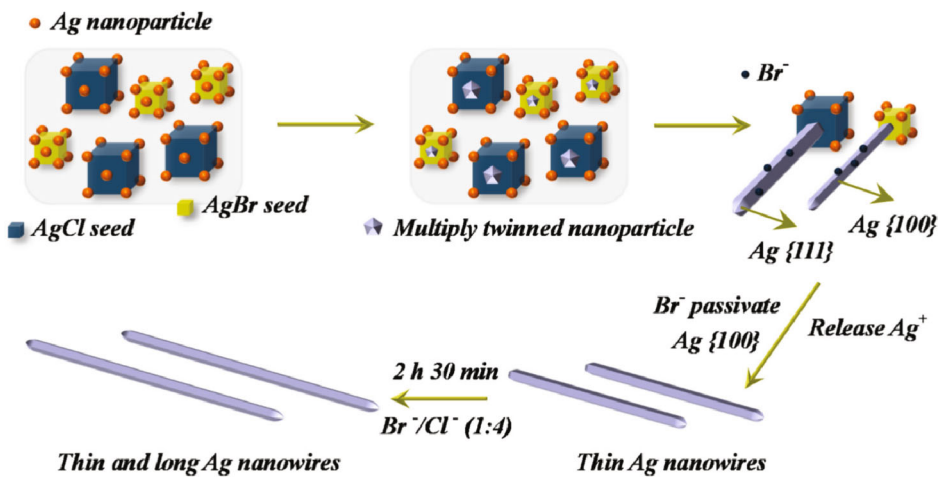


Figure 6: Schematic representation of the proposed formation mechanism of high aspect ratio AgNWs through the bromine ion- ($Br^-$-) assisted one-step synthesis method (reproduced from [166] under the Creative Commons Attribution 4.0 International (CC BY 4.0) License).

1.3 $\mu$m. They attributed the reduction ability of this green reducing agent due to the presence of epigallocatechin, epicatechin, epicatechin-3-gallate, and epigallocatechin-3-gallate (EGCG) [156]. Feiz Soleimani et al. synthesized different morphologies of silver nanostructures such as nanocubes, nanospheres, nanorices, and nanorods with blunt and sharp ends using medium molecular weight starch, glucose, and chitosan in acetic acid solution at different reaction conditions. They found that both chitosan and starch can selectively adsorb on {100} facets of initially formed silver seeds and facilitate the growth of AgNWs in the {111} direction as PVP does in the polyol process as a capping agent [157]. Recently, Dong synthesized single-crystal silver nanowires with lengths up to tens of micron and diameters of 50 nm utilizing tannin, a naturally occurring plant polyphenol, functioning as both reducing and stabilizing agents at temperatures of 45–55°C. They reported that a slow reaction rate favors anisotropic growth of nanowires and the reducing ability of tannin is due to oxidization of its hydroxyl groups. By FTIR characterization, they found that there is a remarkable change in the hydroxyl group during synthesis. Tannin exhibits a broad peak in the region of 3300–3500 $cm^{-1}$ corresponding to –OH groups. However, extremely weakened peaks were observed after AgNW synthesis, which shows the involvement of hydroxyl groups in the formation of the Ag nanowires [158].

Hemmati et al. recently showed that Maui Raw Turbinado brown sugar acts simultaneously as a reducing and capping agent in synthesis of 1D silver nanostructures at low temperature (25-50°C) [159].

## 6. Concluding Remarks and Future Directions

Based on the review of studies of polyol synthesis of AgNWs, there have been much investigation and substantial progress in batch synthesis of AgNWs by the polyol process. Most of these synthesis methods are carried out on small scales and are designed for optimization, parametric study, or

mechanistic investigation of the reaction mechanism. The challenges in batch synthesis of AgNWs on large scales include difficult reaction control resulting in batch to batch variations and production of morphologies other than AgNWs resulting in low yield. Synthesis of AgNWs is normally time consuming and the final cost of available commercial products is high. The polyol flow synthesis in the millifluidic reactor overcomes these challenges through mixing control in small volumes in a continuous manner. Continuous polyol synthesis of AgNWs is scalable and can produce a high yield of AgNWs in large volume continuously. Moreover, the green chemistry synthesis of nanoparticles has recently gained much attention raising the possibility of alternative energy efficient, safe, and environmentally benign paths to nanomaterial synthesis. Nowadays, the need for sustainable development regarding the environment has stimulated research on green synthesis [12]. As a result, a synergy between biotechnology and nanotechnology as biosynthesis of nanostructures is inevitable and taking advantage of biological materials in nanoparticle synthesis is one of the most promising approaches in modern nanoscience [13, 160]. Therefore, the strategy of utilizing the reducing capabilities of green reducing agents directly in nanomaterial synthesis known as green chemistry synthesis of nanomaterials has great advantages in 1D metal nanostructure synthesis [161]. There are a few studies regarding small-scale green synthesis of AgNWs utilizing various green reducing agents and capping agents such as clove oil and vitamin $B_2$ [153, 154].

Future research in the area of polyol synthesis of AgNWs is expected to emphasize large-scale polyol millifluidic synthesis of AgNWs in large volume continuously and in high yield to dramatically reduce cost. In addition, a primary goal will be to take advantage of green and millifluidic synthesis to develop a millifluidic green synthesis of AgNWs using water as solvent for biodegradability and low toxicity. Chemical nanoparticle synthesis from metal salts in most current processes involves harsh chemicals, surfactants, and additives. On the other hand, green synthesis is aimed at applying natural extracts as a reducing agent with inherent growth termination, stabilization, and capping characteristics [162–164]. However, these new techniques should be optimized not only in terms of scale-up but also with respect to product quality and performance. Moreover, future research is expected to focus on optimization of the both polyol millifluidic and green millifluidic synthesis of AgNWs with respect to the millifluidic reactor parameters such as residence time, temperature, and reagent injection rates. The objective is a large scale, smart, green, inexpensive, environmentally friendly, and continuous process for AgNW synthesis on the foundation of the chemical synthesis methods reviewed in this study. Finally, *in situ* X-ray adsorption spectroscopy (XAS) is a versatile technique that provides an opportunity to investigate the reaction dynamic and mechanism of AgNW growth in a millifluidic reactor to further control their morphology, size distribution, and crystal structures. In future research, both *in situ* XAS characterization and millifluidic reactor design hold promise for probing the reaction mechanisms and dynamics of nanostructure synthesis at the atomic level [165].

## Conflicts of Interest

The authors declare that they have no conflicts of interest.

## References


[1] S. K. Batabyal, C. Basu, A. R. Das, and G. S. Sanyal, "Green chemical synthesis of silver nanowires and microfibers using starch," *Journal of Biobased Materials and Bioenergy*, vol. 1, no. 1, pp. 143–147, 2007.

[2] S. Hemmati, D. P. Barkey, and N. Gupta, "Rheological behavior of silver nanowire conductive inks during screen printing," *Journal of Nanoparticle Research*, vol. 18, no. 8, pp. 1–11, 2016.

[3] M. S. Dresselhaus, Y. M. Lin, O. Rabin, M. R. Black, and G. Dresselhaus, *Nanowires*, Material Review in Press, 2003.

[4] J. Zhao, C. Buia, J. Han, and J. P. Lu, "Quantum transport properties of ultrathin silver nanowires," *Nanotechnology*, vol. 14, no. 5, pp. 501–504, 2003.

[5] V. Rodrigues, J. Bettini, A. R. Rocha, L. G. C. Rego, and D. Ugarte, "Quantum conductance in silver nanowires: Correlation between atomic structure and transport properties," *Physical Review B*, vol. 65, no. 15, 2002.

[6] K. E. Korte, S. E. Skrabalak, and Y. Xia, "Rapid synthesis of silver nanowires through a CuCl- or CuCl2-mediated polyol process," *Materials Chemistry*, vol. 18, no. 4, pp. 437–441, 2008.

[7] J. H. Lee, P. Lee, D. Lee, S. S. Lee, and S. H. Ko, "Large-Scale Synthesis and Characterization of Very Long Silver Nanowires via Successive Multistep Growth," *Crystal Growth & Design*, vol. 12, no. 11, pp. 5598–5605, 2012.

[8] X. Tang and M. Tsuji, "Syntheses of Silver Nanowires in Liquid Phase," in *Nanowires Science and Technology*, Nicoleta Lupu, Ed., InTech, 2010, http://www.intechopen.com/books/nanowires-science-and-technology/syntheses-of-silver-nanowires-in-liquid-phase.

[9] S. Hemmati, D. P. Barkey, N. Gupta, and R. Banfield, "Synthesis and Characterization of Silver Nanowire Suspensions for Printable Conductive Media," *ECS Journal of Solid State Science and Technology*, vol. 4, no. 4, pp. P3075–P3079, 2015.

[10] D. A. Dinh, K. N. Hui, K. S. Hui, J. Singh, P. Kumar, and W. Zhou, "Silver Nanowires: A Promising Transparent Conducting Electrode Material for Optoelectronic and Electronic Applications," *Reviews in Advanced Sciences and Engineering*, vol. 2, no. 4, pp. 324–345, 2013.

[11] B. Wiley, Y. Sun, and Y. Xia, "Synthesis of Silver Nanostructures with Controlled Shapes and Properties," *Accounts of Chemical Research*, vol. 40, no. 10, pp. 1067–1076, 2007.

[12] S. Basu, P. Maji, and J. Ganguly, "Rapid green synthesis of silver nanoparticles by aqueous extract of seeds of Nyctanthes arbor-tristis," *Applied Nanoscience*, vol. 6, no. 1, pp. 1–5, 2016.

[13] M. Parveen, F. Ahmad, A. M. Malla, and S. Azaz, "Microwave-assisted green synthesis of silver nanoparticles from Fraxinus excelsior leaf extract and its antioxidant assay," *Applied Nanoscience*, vol. 6, no. 2, pp. 267–276, 2016.

[14] V. Kumar, D. Bano, S. Mohan, D. K. Singh, and S. H. Hasan, "Sunlight-induced green synthesis of silver nanoparticles using aqueous leaf extract of _Polyalthia longifolia_ and its antioxidant activity," *Materials Letters*, vol. 181, pp. 371–377, 2016.

[15] S. Chairam and E. Somsook, "Facile, versatile and green synthesis of silver nanoparticles by mung bean starch and their catalytic activity in the reduction of 4-nitrophenol," *Chiang Mai Journal of Science*, vol. 43, no. 3, pp. 609–619, 2016.

[16] K. Jyoti and A. Singh, "Green synthesis of nanostructured silver particles and their catalytic application in dye degradation," *Journal of Genetic Engineering and Biotechnology*, vol. 14, no. 2, pp. 311–317, 2016.

[17] K. Jia, H. Shou, P. Wang, X. Zhou, and X. Liu, "Controlled synthesis of silver nanostructures stabilized by fluorescent polyarylene ether nitrile," *Applied Surface Science*, vol. 377, pp. 180–183, 2016.

[18] B. Khodashenas and H. R. Ghorbani, "Synthesis of silver nanoparticles with different shapes," *Arabian Journal of Chemistry*, 2015.

[19] M. Zargar, K. Shameli, G. R. Najafi, and F. J. Farahani, "Plant mediated green biosynthesis of silver nanoparticles using Vitex negundo L. extract," *Journal of Industrial and Engineering Chemistry*, vol. 20, pp. 4169–4175, 2014.

[20] M. Noroozi, A. Zakaria, M. M. Moksin, Z. A. Wahab, and A. Abedini, "Green Formation of Spherical and Dendritic Silver Nanostructures under Microwave Irradiation without Reducing Agent," *International Journal of Molecular Sciences*, vol. 13, no. 7, pp. 8086–8096, 2012.

[21] R. S. Jones, R. R. Draheim, and M. Roldo, "Silver Nanowires: Synthesis, Antibacterial Activity and Biomedical Applications," *Applied Sciences*, vol. 8, p. 673, 2018.

[22] S. Kaviya, J. Santhanalakshmi, and B. Viswanathan, "Green Synthesis of Silver Nanoparticles UsingPolyalthia longifolia-Leaf Extract along with D-Sorbitol: Study of Antibacterial Activity," *Journal of Nanotechnology*, vol. 2011, 5 pages, 2011.

[23] J. Tang, M. Yu, T. Jiang, E. Wang, C. Ge, and Z. Chen, "A green approach for the synthesis of silver dendrites and their superior SERS performance," *Optik*, vol. 136, pp. 244–248, 2017.

[24] P. Gnanaprakasam and T. Selvaraju, "Green synthesis of self assembled silver nanowire decorated reduced graphene oxide for efficient nitroarene reduction," *RSC Advances*, vol. 4, pp. 24518–24525, 2014.

[25] B. Wu, A. Heidelberg, J. J. Boland, J. E. Sader, Sun, and Li, "Microstructure-Hardened Silver Nanowires," *Nano Letters*, vol. 6, no. 3, pp. 468–472, 2006.

[26] S. Narayanan, G. Cheng, Z. Zeng, Y. Zhu, and T. Zhu, "Strain Hardening and Size Effect in Five-fold Twinned Ag Nanowires," *Nano Letters*, vol. 15, no. 6, pp. 4037–4044, 2015.

[27] V. K. R. Rao, V. K. Abhinav, P. S. Karthik, and S. P. Singh, "Conductive silver inks and their applications in printed and flexible electronics," *RSC Advances*, vol. 5, no. 95, pp. 77760–77790, 2015.

[28] T. Zhang, Y. J. Song, X. Y. Zhang, and J. Y. Wu, "Synthesis of Silver Nanostructures by Multistep Methods," *Sensors*, vol. 14, no. 4, pp. 5860–5889, 2014.

[29] C. Preston, Z. Fang, J. Murray et al., "Silver nanowire transparent conducting paper-based electrode with high optical haze," *J. Mater. Chem. C*, vol. 2, no. 7, pp. 1248–1254, 2014.

[30] L. Zhang, B. Wang, G. Zhu, and X. Zhou, "Synthesis of silver nanowires as a SERS substrate for the detection of pesticide thiram," *Spectrochimica Acta Part A: Molecular and Biomolecular Spectroscopy*, vol. 133, pp. 411–416, 2014.

[31] L. Wang, X. Gao, L. Jin, Q. Wu, Z. Chen, and X. Lin, "Amperometric glucose biosensor based on silver nanowires and glucose oxidase," *Sensors and Actuators B: Chemical*, vol. 176, pp. 9–14, 2013.

[32] X. Cao, S. Liu, Q. Feng, and N. Wang, "Silver nanowire-based electrochemical immunoassay for sensing immunoglobulin G with signal amplification using strawberry-like ZnO nanostructures as labels," *Biosensors & Bioelectronics*, vol. 49, pp. 256–262, 2013.

[33] S. Yao and Y. Zhu, "Wearable multifunctional sensors using printed stretchable conductors made of silver nanowires," *Nanoscale*, vol. 6, no. 4, pp. 2345–2352, 2014.

[34] B. U. Hwang, J. H. Lee, T. Q. Trung et al., "Transparent Stretchable Self-Powered Patchable Sensor Platform with Ultrasensitive Recognition of Human Activities," *ACS Nano*, vol. 9, no. 9, pp. 8801–8810, 2015.

[35] J. Wang, J. Jiu, M. Nogi et al., "A highly sensitive and flexible pressure sensor with electrodes and elastomeric interlayer containing silver nanowires," *Nanoscale*, vol. 7, no. 7, pp. 2926–2932, 2015.

[36] F. Lin, S. Yao, M. McKnight, Y. Zhu, and A. Bozkurt, "Silver nanowire based wearable sensors for multimodal sensing," in *2016 IEEE Topical Conference on Biomedical Wireless Technologies, Networks, and Sensing Systems (BioWireleSS)*, pp. 55–58, Austin, TX, USA, January 2016.

[37] L. Hu, H. S. Kim, J.-Y. Lee, P. Peumans, and Y. Cui, "Scalable Coating and Properties of Transparent, Flexible, Silver Nanowire Electrodes," *ACS Nano*, vol. 4, no. 5, pp. 2955–2963, 2010.

[38] J. Y. Lee, S. T. Connor, Y. Cui, and P. Peumans, "Solution-Processed Metal Nanowire Mesh Transparent Electrodes," *Nano Letters*, vol. 8, no. 2, pp. 689–692, 2008.

[39] G. Y. Margulis, M. G. Christoforo, D. Lam et al., "Spray Deposition of Silver Nanowire Electrodes for Semitransparent Solid-State Dye-Sensitized Solar Cells," *Advanced Energy Materials*, vol. 3, no. 12, pp. 1657–1663, 2013.

[40] J. Liang, L. Li, K. Tong et al., "Silver Nanowire Percolation Network Soldered with Graphene Oxide at Room Temperature and Its Application for Fully Stretchable Polymer Light-Emitting Diodes," *ACS Nano*, vol. 8, no. 2, pp. 1590–1600, 2014.

[41] H. G. Cheong, R. E. Triambulo, G. H. Lee, I. S. Yi, and J. W. Park, "Silver Nanowire Network Transparent Electrodes with Highly Enhanced Flexibility by Welding for Application in Flexible Organic Light-Emitting Diodes," *ACS Applied Materials & Interfaces*, vol. 6, no. 10, pp. 7846–7855, 2014.

[42] X. Z. Xiang, W. Y. Gong, M. S. Kuang, and L. Wang, "Progress in application and preparation of silver nanowires," *Rare Metals*, vol. 35, no. 4, pp. 289–298, 2016.

[43] J. Wang, J. Jiu, T. Araki et al., "Silver Nanowire Electrodes: Conductivity Improvement Without Post-treatment and Application in Capacitive Pressure Sensors," *Nano-Micro Letters*, vol. 7, no. 1, pp. 51–58, 2015.

[44] B. Sciacca, J. van de Groep, A. Polman, and E. C. Garnett, "Solution-Grown Silver Nanowire Ordered Arrays as Transparent Electrodes," *Advanced Materials*, vol. 28, no. 5, pp. 905–909, 2016.

[45] B. R. Yang, G. S. Liu, S. J. Han et al., "Coating, patterning, and transferring processes of silver nanowire for flexible display and sensing applications," *Journal of the Society for Information Display*, vol. 24, no. 4, pp. 234–240, 2016.

[46] J. L. Tian, H. Y. Zhang, and H. J. Wang, "Preparation and Properties of Silver Nanowire-Based Transparent Conductive

Composite Films," *Journal of Electronic Materials*, vol. 45, no. 6, pp. 3040–3045, 2016.

[47] L. Bormann, F. Selzer, N. Weiß, D. Kneppe, K. Leo, and L. Müller-Meskamp, "Doped hole transport layers processed from solution: Planarization and bridging the voids in non-continuous silver nanowire electrodes," *Organic Electronics*, vol. 28, pp. 163–171, 2016.

[48] A. B. V. K. Kumar, C. W. Bae, L. Piao, and S. H. Kim, "Silver nanowire based flexible electrodes with improved properties: High conductivity, transparency, adhesion and low haze," *Materials Research Bulletin*, vol. 48, no. 8, pp. 2944–2949, 2013.

[49] F. Xu, W. Xu, B. Mao et al., "Preparation and cold welding of silver nanowire based transparent electrodes with optical transmittances >90% and sheet resistances <10 ohm/sq," *Journal of Colloid and Interface Science*, vol. 512, pp. 208–218, 2018.

[50] L. Graham, G. Collins, J. D. Holmes, and R. D. Tilley, "Synthesis and catalytic properties of highly branched palladium nanostructures using seeded growth," *Nanoscale*, vol. 8, no. 5, pp. 2867–2874, 2016.

[51] F. Fiévet, S. Ammar-Merah, R. Brayner et al., "The polyol process: a unique method for easy access to metal nanoparticles with tailored sizes, shapes and compositions," *Chemical Society Reviews*, vol. 47, no. 14, pp. 5187–5233, 2018.

[52] Q. Shen, Q. Min, J. Shi et al., "Morphology-Controlled Synthesis of Palladium Nanostructures by Sonoelectrochemical-Method and Their Application in Direct Alcohol Oxidation," *The Journal of Physical Chemistry C*, vol. 113, no. 4, pp. 1267–1273, 2009.

[53] S. P. Chandran, M. Chaudhary, R. Pasricha, A. Ahmad, and M. Sastry, "Synthesis of Gold Nanotriangles and Silver Nanoparticles Using Aloe vera Plant Extract," *Biotechnology Progress*, vol. 22, no. 2, pp. 577–583, 2006.

[54] S. Fahad, H. Yu, L. Wang et al., "Recent progress in the synthesis of silver nanowires and their role as conducting materials," *Journal of Materials Science*, vol. 54, no. 2, pp. 997–1035, 2019.

[55] Z. Zhang, W. Shen, J. Xue et al., "Recent advances in synthetic methods and applications of silver nanostructures," *Nanoscale Research Letters*, vol. 13, no. 1, p. 18, 2018.

[56] P. Zhang, I. Wyman, J. Hu et al., "Silver nanowires: Synthesis technologies, growth mechanism and multifunctional applications," *Materials Science and Engineering: B*, vol. 223, pp. 1–23, 2017.

[57] F. Fievet, J. P. Lagier, and M. Figlarz, "Preparing Monodisperse Metal Powders in Micrometer and Submicrometer Sizes by the Polyol Process," *MRS Bulletin*, vol. 14, no. 12, pp. 29–34, 1989.

[58] H. Mao, J. Feng, X. Ma, C. Wu, and X. Zhao, "One-dimensional silver nanowires synthesized by self-seeding polyol process," *Journal of Nanoparticle Research*, vol. 14, no. 6, pp. 1–15, 2012.

[59] N. V. Nghia, N. N. K. Truong, N. M. Thong, and N. P. Hung, "Synthesis of Nanowire-Shaped Silver by Polyol Process of Sodium Chloride," *International Journal of Materials and Chemistry*, vol. 2, no. 2, pp. 75–78, 2012.

[60] Y. J. Song, M. Wang, X. Y. Zhang, J. Y. Wu, and T. Zhang, "Investigation on the role of the molecular weight of polyvinyl pyrrolidone in the shape control of high-yield silver nanospheres and nanowires," *Nanoscale Research Letters*, vol. 9, no. 1, p. 17, 2014.

[61] K. S. Chou and Y. S. Lai, "Effect of polyvinyl pyrrolidone molecular weights on the formation of nanosized silver colloids," *Materials Chemistry and Physics*, vol. 83, no. 1, pp. 82–88, 2004.

[62] M. R. Johan, N. A. K. Aznan, S. T. Yee et al., "Synthesis and Growth Mechanism of Silver Nanowires through Different Mediated Agents (CuCl2and NaCl) Polyol Process," *Journal of Nanomaterials*, vol. 2014, Article ID 105454, 7 pages, 2014.

[63] A. Habib, *Optimization of conditions for the synthesis of silver nanowire*, WISE Summer Programs, 2006.

[64] N. Espinosa, R. R. Sondergaard, M. Jorgensen, and F. C. Krebs, "Flow synthesis of silver nanowires for semitransparent solar cell electrodes: a life cycle perspective," *ChemSusChem*, vol. 9, no. 8, pp. 893–899, 2016.

[65] Q. Zhu, Z. Zhang, Z. Sun, B. Cai, and W. Cai, "Importance of cations and anions from control agents in the synthesis of silver nanowires by polyol method," *Applied Physics A: Materials Science & Processing*, vol. 122, no. 6, pp. 1–7, 2016.

[66] S. Wang, Y. Tian, S. Ding, and Y. Huang, "Rapid synthesis of long silver nanowires by controlling concentration of $Cu^{2+}$ ions," *Materials Letters*, vol. 172, pp. 175–178, 2016.

[67] S. Wang, Y. Tian, S. Ding, and C. Wang, "The role of chloride ions in rapid synthesis of ultra-long silver nanowires for flexible electrodes," *Materials Research Express*, vol. 3, no. 7, 2016.

[68] M. T. Satoungar, H. Azizi, S. Fattahi, M. K. Mehrizi, and H. Fallahi, "Effect of different mediated agents on morphology and crystallinity of synthesized silver nanowires prepared by polyol process," *Journal of Nanomaterials*, vol. 2016, Article ID 4354136, 8 pages, 2016.

[69] Junaidi, M. Yunus, Harsojo, E. Suharyadi, and K. Triyana, "Effect of Stirring rate on The Synthesis Silver Nanowires using Polyvinyl Alcohol as A Capping Agent by Polyol Process," *International Journal on Advanced Science, Engineering and Information Technology*, vol. 6, no. 3, 2016.

[70] P. Nalawade, P. Mukherjee, and S. Kapoor, "Biosynthesis, characterization and antibacterial studies of silver nanoparticles using pods extract of Acacia auriculiformis," *Spectrochimica Acta Part A: Molecular and Biomolecular Spectroscopy*, vol. 129, pp. 121–124, 2014.

[71] M. Gnanadesigan, M. Anand, S. Ravikumar et al., "Biosynthesis of silver nanoparticles by using mangrove plant extract and their potential mosquito larvicidal property," *Asian Pacific Journal of Tropical Medicine*, vol. 4, no. 10, pp. 799–803, 2011.

[72] Z. Yang, H. Qian, H. Chen, and J. N. Anker, "One-pot hydrothermal synthesis of silver nanowires via citrate reduction," *Journal of Colloid and Interface Science*, vol. 352, no. 2, pp. 285–291, 2010.

[73] C. Yang, Y. Tang, Z. Su, Z. Zhang, and C. Fang, "Preparation of Silver Nanowires via a Rapid, Scalable and Green Pathway," *Journal of Materials Science & Technology*, vol. 31, no. 1, pp. 16–22, 2015.

[74] G. X. Chen, Y. Y. Chen, Y. Y. Cui, Q. F. Chen, T. Chen, and Y. Yang, "Morphology-controlled fabrication of nano Ag/poly (vinyl pyrrolidone) composites and their effect on electric conductive properties of UV ink," *Materials Technology*, vol. 31, no. sup1, pp. 17–22, 2016.

[75] A. K. Shukla and S. Iravani, *Nanoscience in Food and Agriculture 1*, Springer International Publishing, Switzerland, 2016.

[76] G. Suresh, P. H. Gunasekar, D. Kokila et al., "Green synthesis of silver nanoparticles using _Delphinium denudatum_ root extract exhibits antibacterial and mosquito larvicidal activities," *Spectrochimica Acta Part A: Molecular and Biomolecular Spectroscopy*, vol. 127, pp. 61–66, 2014.

[77] V. Kathiravan, S. Ravi, and S. Ashokkumar, "Synthesis of silver nanoparticles from Melia dubia leaf extract and their in vitro anticancer activity," *Spectrochimica Acta Part A: Molecular and Biomolecular Spectroscopy*, vol. 130, pp. 116–121, 2014.

[78] S. Y. Lee and M. T. Harris, "Surface modification of magnetic nanoparticles capped by oleic acids: Characterization and colloidal stability in polar solvents," *Journal of colloid and interface science*, vol. 293, no. 2, pp. 401–408, 2006.

[79] A. K. Manocchi, N. E. Horelik, B. Lee, and H. Yi, "Simple, Readily Controllable Palladium Nanoparticle Formation on Surface-Assembled Viral Nanotemplates," *Langmuir*, vol. 26, no. 5, pp. 3670–3677, 2010.

[80] Y. Sun and Y. Xia, "Shape-Controlled Synthesis of Gold and Silver Nanoparticles," *Science*, vol. 298, no. 5601, pp. 2176–2179, 2002.

[81] Y. Sun, B. Mayers, T. Herricks, and Y. Xia, "Polyol Synthesis of Uniform Silver Nanowires: A Plausible Growth Mechanism and the Supporting Evidence," *Nano Letters*, vol. 3, no. 7, pp. 955–960, 2003.

[82] Y. Sun, Y. Yin, B. T. Mayers, T. Herricks, and Y. Xia, "Uniform Silver Nanowires Synthesis by Reducing AgNO3 with Ethylene Glycol in the Presence of Seeds and Poly(Vinyl Pyrrolidone)," *Chemistry of Materials*, vol. 14, no. 11, pp. 4736–4745, 2002.

[83] Y. Sun, B. Gates, B. Mayers, and Y. Xia, "Crystalline Silver Nanowires by Soft Solution Processing," *Nano Letters*, vol. 2, no. 2, pp. 165–168, 2002.

[84] S. E. Skrabalak, B. J. Wiley, M. Kim, E. V. Formo, and Y. Xia, "On the Polyol Synthesis of Silver Nanostructures: Glycolaldehyde as a Reducing Agent," *Nano Letters*, vol. 8, no. 7, pp. 2077–2081, 2008.

[85] M. Luo, H. Huang, S. I. Choi et al., "Facile Synthesis of Ag Nanorods with No Plasmon Resonance Peak in the Visible Region by Using Pd Decahedra of 16 nm in Size as Seeds," *ACS Nano*, vol. 9, no. 10, pp. 10523–10532, 2015.

[86] N. T. X. Minh, Q. T. Anh, B. T. M. Thu et al., "Effects of Synthesis Conditions on the Formation and Morphology of Silver nanowire," *Vietnam Journal of Science and Technology*, vol. 56, no. 2A, pp. 111–117, 2018.

[87] S. Coskun, B. Aksoy, and H. E. Unalan, "Polyol Synthesis of Silver Nanowires: An Extensive Parametric Study," *Crystal Growth & Design*, vol. 11, no. 11, pp. 4963–4969, 2011.

[88] J. Jiu, T. Tokuno, M. Nogi, and K. Suganuma, "Synthesis and application of Ag nanowires via a trace salt assisted hydrothermal process," *Journal of Nanoparticle Research*, vol. 14, no. 7, pp. 1–11, 2012.

[89] X. Lai, X. Feng, M. Zhang et al., "Large-scale synthesis and surface plasmon resonance properties of angled silver/silver homojunction nanowires," *Journal of Nanoparticle Research*, vol. 16, no. 3, pp. 1–11, 2014.

[90] Z. Kaili, D. Yongguo, and C. Shimin, "Facile One-Pot Polyol Method for the Synthesis of Uniform Size Silver Nanowires," *Journal of Nanoscience and Nanotechnology*, vol. 16, no. 1, pp. 480–488, 2016.

[91] Z. Liu, S. Tian, J. Yang et al., "Sulfur ion-induced shape evolution of Ag nanocrystals by microwave-assisted polyol process," *Materials Letters*, vol. 164, pp. 647–650, 2016.

[92] G. H. Lim, S. J. Lee, I. Han et al., "Polyol synthesis of silver nanostructures: Inducing the growth of nanowires by a heat-up process," *Chemical Physics Letters*, vol. 602, pp. 10–15, 2014.

[93] W.-H. Wu, H.-Y. Chuang, and S. L.-c. Hsu, "Synthesis and mechanism of template-free growth of silver nanowires via syringes," *Journal of Materials Research*, vol. 31, no. 1, pp. 109–116, 2016.

[94] M. B. Gebeyehu, T. F. Chala, S. Y. Chang, C. M. Wu, and J. Y. Lee, "Synthesis and highly effective purification of silver nanowires to enhance transmittance at low sheet resistance with simple polyol and scalable selective precipitation method," *RSC advances*, vol. 7, no. 26, pp. 16139–16148, 2017.

[95] A. K. Srivastava, P. Awasthi, S. Kanojia et al., "Synthesis of Silver Nanostructures and their Application in Highly Sensitive SERS Sensors," *Defence Science Journal*, vol. 68, no. 1, p. 98, 2017.

[96] A. Amirjani, P. Marashi, and D. H. Fatmehsari, "Effect of $AgNO_3$ addition rate on aspect ratio of $CuCl_2$-mediated synthesized silver nanowires using response surface methodology," *Colloids and Surfaces A: Physicochemical and Engineering Aspects*, vol. 444, pp. 33–39, 2014.

[97] L. Sonntag, F. Eichler, N. Weiß et al., "Influence of the average molar mass of poly(N-vinylpyrrolidone) on the dimensions and conductivity of silver nanowires," *Physical Chemistry Chemical Physics*, vol. 21, no. 18, pp. 9036–9043, 2019.

[98] J.-J. Zhu, C.-X. Kan, J.-G. Wan, M. Han, and G.-H. Wang, "High-Yield Synthesis of Uniform Ag Nanowires withHigh Aspect Ratios by Introducing the Long-Chain PVP in an Improved Polyol Process," *Journal of Nanomaterials*, vol. 2011, 7 pages, 2011.

[99] H. S. Lee, Y. W. Kim, J. E. Kim et al., "Synthesis of dimension-controlled silver nanowires for highly conductive and transparent nanowire films," *Acta Materialia*, vol. 83, pp. 84–90, 2015.

[100] T. L. Yang, C. T. Pan, Y. C. Chen et al., "Synthesis and fabrication of silver nanowires embedded in PVP fibers by near-field electrospinning process," *Optical Materials*, vol. 39, pp. 118–124, 2015.

[101] B. Zhang, R. Dang, Q. Cao, P. Zhao, K. Chen, and H. Meng, "High-Yield Synthesis of Long Silver Nanowires via Chromic Chloride and a Stable Reaction Environment," *Journal of Nanomaterials*, vol. 2019, 8 pages, 2019.

[102] X. Yuan, H. Yang, Y. Li et al., "Synthesis of Silver Nanowires by Using Tetrabutyl Ammonium Dibromochloride as the Auxiliary for Low-Haze Flexible Transparent Conductive Films," *Langmuir*, vol. 35, no. 36, pp. 11829–11835, 2019.

[103] C. Chen, L. Wang, G. Jiang et al., "Study on the synthesis of silver nanowires with adjustable diameters through the polyol process," *Nanotechnology*, vol. 17, no. 15, pp. 3933–3938, 2006.

[104] S. Liu, B. Sun, J. G. Li, and J. Chen, "Silver nanowires with rounded ends: ammonium carbonate-mediated polyol synthesis, shape evolution and growth mechanism," *CrystEngComm*, vol. 16, no. 2, pp. 244–251, 2014.

[105] W. M. Schuette and W. E. Buhro, "Polyol Synthesis of Silver Nanowires by Heterogeneous Nucleation; Mechanistic

Aspects Influencing Nanowire Diameter and Length," *Chemistry of Materials*, vol. 26, no. 22, pp. 6410–6417, 2014.

[106] B. Li, S. Ye, I. E. Stewart, S. Alvarez, and B. J. Wiley, "Synthesis and Purification of Silver Nanowires To Make Conducting Films with a Transmittance of 99%," *Nano Letters*, vol. 15, no. 10, pp. 6722–6726, 2015.

[107] K. Zhang, Y. Du, and S. Chen, "Sub 30 nm silver nanowire synthesized using KBr as co-nucleant through one-pot polyol method for optoelectronic applications," *Organic Electronics*, vol. 26, pp. 380–385, 2015.

[108] R. R. da Silva, M. Yang, S.-I. Choi et al., "Facile synthesis of sub-20 nm silver nanowires through a bromide-mediated polyol method," *ACS Nano*, vol. 10, no. 8, pp. 7892–7900, 2016.

[109] N. M. Abbasi, L. Wang, H. Yu et al., "Glycerol and Water Mediated Synthesis of Silver Nanowires in the Presence of Cobalt Chloride as Growth Promoting Additive," *Journal of Inorganic and Organometallic Polymers and Materials*, vol. 26, no. 3, pp. 680–690, 2016.

[110] S. Zhao, Q. Wang, and Z. Qu, "Controlled Synthesis of Uniform Silver Nanowires via a Simple Polyol Process," *IOP Conference Series: Materials Science and Engineering*, vol. 301, p. 012014, 2018.

[111] Y. Rui, W. Zhao, D. Zhu et al., "Understanding the Effects of NaCl, NaBr and Their Mixtures on Silver Nanowire Nucleation and Growth in Terms of the Distribution of Electron Traps in Silver Halide Crystals," *Nanomaterials*, vol. 8, no. 3, p. 161, 2018.

[112] M. Bobinger, V. Dergianlis, M. Becherer, and P. Lugli, "Comprehensive Synthesis Study of Well-Dispersed and Solution-Processed Metal Nanowires for Transparent Heaters," *Journal of Nanomaterials*, vol. 2018, Article ID 7304807, 13 pages, 2018.

[113] T. N. Trung, V. K. Arepalli, R. Gudala, and E. T. Kim, "Polyol synthesis of ultrathin and high-aspect-ratio Ag nanowires for transparent conductive films," *Materials Letters*, vol. 194, pp. 66–69, 2017.

[114] B. Lei, J. Wang, Y. Du, and K. Zhang, "Controlling the size of silver nanowires through one-pot polyol method with trace halide and its effect on kinetic process," *Materials Research Express*, vol. 4, no. 7, 2017.

[115] L. J. Andrés, M. F. Menéndez, D. Gómez et al., "Rapid synthesis of ultra-long silver nanowires for tailor-made transparent conductive electrodes: proof of concept in organic solar cells," *Nanotechnology*, vol. 26, no. 26, p. 265201, 2015.

[116] A. Amirjani, P. Marashi, and D. H. Fatmehsari, "The effect of agitation state on polyol synthesis of silver nanowire," *International Nano Letters*, vol. 6, no. 1, pp. 41–44, 2016.

[117] J. Lu, D. Liu, and J. Dai, "Preparation of highly conductive silver nanowires for electrically conductive adhesives," *Journal of Materials Science: Materials in Electronics*, vol. 30, no. 16, pp. 15786–15794, 2019.

[118] S. Fahad, H. Yu, L. Wang et al., "Synthesis of silver nanowires with controlled diameter and their conductive thin films," *Journal of Materials Science: Materials in Electronics*, vol. 30, no. 14, pp. 12876–12887, 2019.

[119] Q. Liu, S. Kim, X. Ma et al., "Ultra-sharp and surfactant-free silver nanowire for scanning tunneling microscopy and tip-enhanced Raman spectroscopy," *Nanoscale*, vol. 11, no. 16, pp. 7790–7797, 2019.

[120] T. Inose, S. Toyouchi, G. Lu et al., "Water-mediated polyol synthesis of pencil-like sharp silver nanowires suitable for nonlinear plasmonics," *Chemical Communications*, vol. 55, no. 77, pp. 11630–11633, 2019.

[121] H. Wang, Y. Wang, and X. Chen, "Synthesis of uniform silver nanowires from AgCl seeds for transparent conductive films via spin-coating at variable spin-speed," *Colloids and Surfaces A: Physicochemical and Engineering Aspects*, vol. 565, pp. 154–161, 2019.

[122] W. Li, Y. He, J. Xu, W. Wang, Z. Zhu, and H. Liu, "Preparation of Ag NWs and Ag NWs@PDMS stretchable sensors based on rapid polyol method and semi-dry process," *Journal of Alloys and Compounds*, vol. 803, pp. 332–340, 2019.

[123] P. Andrew and A. Ilie, "Functionalised Silver Nanowire Structures," *Journal of Physics: Conference Series*, vol. 61, pp. 36–40, 2007.

[124] J. Hua, F. Wu, F. Fan, W. Wang, Z. Xu, and F. Li, "Synthesis and surface plasmonic properties of ultra-thick silver nanowires," *Journal of Physics: Condensed Matter*, vol. 28, no. 25, p. 254005, 2016.

[125] W. Zhao, S. S. Wang, H. T. Cao et al., "An eco-friendly water-assisted polyol method to enhance the aspect ratio of silver nanowires," *RSC Advances*, vol. 9, no. 4, pp. 1933–1938, 2019.

[126] H. Moon, P. Won, J. Lee, and S. H. Ko, "Low-haze, annealing-free, very long Ag nanowire synthesis and its application in a flexible transparent touch panel," *Nanotechnology*, vol. 27, no. 29, p. 295201, 2016.

[127] E.-J. Lee, Y.-H. Kim, D. K. Hwang, W. K. Choi, and J.-Y. Kim, "Synthesis and optoelectronic characteristics of 20 nm diameter silver nanowires for highly transparent electrode films," *RSC Advances*, vol. 6, no. 14, pp. 11702–11710, 2016.

[128] J. Patarroyo, A. Genç, J. Arbiol, N. G. Bastús, and V. Puntes, "One-pot polyol synthesis of highly monodisperse short green silver nanorods," *Chemical Communications*, vol. 52, no. 73, pp. 10960–10963, 2016.

[129] B. Liu, H. Yan, S. Chen et al., "Stable and Controllable Synthesis of Silver Nanowires for Transparent Conducting Film," *Nanoscale Research Letters*, vol. 12, no. 1, p. 212, 2017.

[130] Y. Li, S. Guo, H. Yang, Y. Chao, S. Jiang, and C. Wang, "One-step synthesis of ultra-long silver nanowires of over 100 $\mu$m and their application in flexible transparent conductive films," *RSC Advances*, vol. 8, no. 15, pp. 8057–8063, 2018.

[131] H. W. Jang, B. Y. Hwang, K. W. Lee, Y. M. Kim, and J. Y. Kim, "Controlling the size of silver nanowires produced by a tetrabutylammonium dichlorobromide salt-based polyol process: Kinetics of silver crystal growth," *AIP Advances*, vol. 8, no. 2, 2018.

[132] Y. Wei, Q.-l. Zhang, H.-j. Wan, Y.-n. Zhang, S.-w. Zheng, and Y. Zhang, "A facile synthesis of segmented silver nanowires and enhancement of the performance of polymer solar cells," *Physical Chemistry Chemical Physics*, vol. 20, no. 27, pp. 18837–18843, 2018.

[133] L. Tang, J. Zhang, L. Dong et al., "Coating-free, air-stable silver nanowires for high-performance transparent conductive film," *Nanotechnology*, vol. 29, no. 37, p. 375601, 2018.

[134] W. Xi, R. Ma, H. Wang, Z. Gao, W. Zhang, and Y. Zhao, "Ultrathin Ag Nanowires Electrode for Electrochemical Syngas Production from Carbon Dioxide," *ACS Sustainable Chemistry & Engineering*, vol. 6, no. 6, pp. 7687–7694, 2018.

[135] C. R. Rekha, V. U. Nayar, and K. G. Gopchandran, "Synthesis of highly stable silver nanorods and their application as SERS substrates," *Journal of Science: Advanced Materials and Devices*, vol. 3, no. 2, pp. 196–205, 2018.

[136] Z. Niu, F. Cui, E. Kuttner et al., "Synthesis of Silver Nanowires with Reduced Diameters Using Benzoin-Derived Radicals to Make Transparent Conductors with High Transparency and Low Haze," *Nano Letters*, vol. 18, no. 8, pp. 5329–5334, 2018.

[137] Y. Zhang, J. Guo, D. Xu, Y. Sun, and F. Yan, "One-Pot Synthesis and Purification of Ultralong Silver Nanowires for Flexible Transparent Conductive Electrodes," *ACS Applied Materials & Interfaces*, vol. 9, no. 30, pp. 25465–25473, 2017.

[138] G. Chen, L. Bi, Z. Yang, L. Chen, G. Wang, and C. Ye, "Water-Based Purification of Ultrathin Silver Nanowires toward Transparent Conductive Films with a Transmittance Higher than 99%," *ACS Applied Materials & Interfaces*, vol. 11, no. 25, pp. 22648–22654, 2019.

[139] Z. Yi, X. Xu, X. Tan et al., "Microwave-assisted polyol method rapid synthesis of high quality and yield Ag nanowires," *Surface & Coatings Technology*, vol. 327, pp. 118–125, 2017.

[140] H. Sim, S. Bok, B. Kim et al., "Organic-Stabilizer-Free Polyol Synthesis of Silver Nanowires for Electrode Applications," *Angewandte Chemie International Edition*, vol. 55, no. 39, pp. 11814–11818, 2016.

[141] S. Hemmati and D. P. Barkey, "Parametric Study, Sensitivity Analysis, and Optimization of Polyol Synthesis of Silver Nanowires," *ECS Journal of Solid State Science and Technology*, vol. 6, no. 4, pp. P132–P137, 2017.

[142] S. H. Mirjalili, M. R. Nateghi, and F. Kalantari-Fotooh, "Preparation of silver nanowire/expanded polytetrafluoroethylene and polypropylene nanocomposites via all solution process method for antibacterial applications," *The Journal of The Textile Institute*, vol. 110, no. 12, pp. 1–9, 2019.

[143] R. Gottesman, A. Tangy, I. Oussadon, and D. Zitoun, "Silver nanowires and nanoparticles from a millifluidic reactor: application to metal assisted silicon etching," *New Journal of Chemistry*, vol. 36, no. 12, pp. 2456–2459, 2012.

[144] H. Yun, D. Seo, M. Lee, S. Kwon, and L. Park, "Effective Synthesis and Recovery of Silver Nanowires Prepared by Tapered Continuous Flow Reactor for Flexible and Transparent Conducting Electrode," *Metals*, vol. 6, no. 1, p. 14, 2016.

[145] K. S. Lau, S. X. Chin, S. T. Tan et al., "Silver nanowires as flexible transparent electrode: Role of PVP chain length," *Journal of Alloys and Compounds*, vol. 803, pp. 165–171, 2019.

[146] S. Hemmati, D. P. Barkey, L. Eggleston, B. Zukas, N. Gupta, and M. Harris, "Silver Nanowire Synthesis in a Continuous Millifluidic Reactor," *ECS Journal of Solid State Science and Technology*, vol. 6, no. 4, pp. P144–P149, 2017.

[147] S. Hemmati, *Doctoral Dissertation*, University of New Hampshire Scholars' Repository, 2016.

[148] S. E. H. Murph, C. J. Murphy, A. Leach, and K. Gall, "A Possible Oriented Attachment Growth Mechanism for Silver Nanowire Formation," *Crystal Growth & Design*, vol. 15, no. 4, pp. 1968–1974, 2015.

[149] D. R. Whitcomb, A. R. Clapp, P. Buhlmann, J. C. Blinn, and J. Zhang, "New Perspectives on Silver Nanowire Formation from Dynamic Silver Ion Concentration Monitoring and Nitric Oxide Production in the Polyol Process," *Crystal Growth & Design*, vol. 16, no. 4, pp. 1861–1868, 2016.

[150] C. Wang, B. Cheng, H. Zhang et al., "Probing the seeded protocol for high-concentration preparation of silver nanowires," *Nano Research*, vol. 9, no. 5, pp. 1532–1542, 2016.

[151] L. Lin, W. Wang, J. Huang et al., "Nature factory of silver nanowires: Plant-mediated synthesis using broth of _Cassia fistula_ leaf," *Chemical Engineering Journal*, vol. 162, no. 2, pp. 852–858, 2010.

[152] H. Ma, J. Zeng, S. Harrington et al., "Hydrothermal Fabrication of Silver Nanowires-Silver Nanoparticles-Graphene Nanosheets Composites in Enhancing Electrical Conductive Performance of Electrically Conductive Adhesives," *Nanomaterials*, vol. 6, no. 6, p. 119, 2016.

[153] A. Jeevika and D. R. Shankaran, "Seed-free synthesis of 1D silver nanowires ink using clove oil (Syzygium Aromaticum) at room temperature," *Journal of Colloid and Interface Science*, vol. 458, pp. 155–159, 2015.

[154] M. N. Nadagouda and R. S. Varma, "Green Synthesis of Ag and Pd Nanospheres, Nanowires, and Nanorods Using Vitamin B2: Catalytic Polymerisation of Aniline and Pyrrole," *Journal of Nanomaterials*, vol. 2008, Article ID 782358, 8 pages, 2008.

[155] H. Wang, W. Xing, J. Chen, G. Liu, and G. Xu, *Journal of Materials Science: Materials in Electronics*, vol. 28, no. 8, pp. 6152–6158, 2017.

[156] M. Flores-González, M. Talavera-Rojas, E. Soriano-Vargas, and V. Rodríguez-González, "Practical mediated-assembly synthesis of silver nanowires using commercialCamellia sinensisextracts and their antibacterial properties," *New Journal of Chemistry*, vol. 42, no. 3, pp. 2133–2139, 2018.

[157] F. F. Soleimani, T. Saleh, S. A. Shojaosadati, and R. Poursalehi, "Green Synthesis of Different Shapes of Silver Nanostructures and Evaluation of Their Antibacterial and Cytotoxic Activity," *BioNanoScience*, vol. 8, no. 1, pp. 72–80, 2018.

[158] L. Dong, "One pod synthesis of single-crystal silver nanowires for selective detection of Pb(II)," *Micro & Nano Letters*, vol. 14, no. 2, pp. 137–141, 2019.

[159] S. Hemmati, E. Retzlaff-Roberts, C. Scott, and M. T. Harris, "Artificial Sweeteners and Sugar Ingredients as Reducing Agent for Green Synthesis of Silver Nanoparticles," *Journal of Nanomaterials*, vol. 2019, Article ID 9641860, 16 pages, 2019.

[160] H. R. Rajabi, H. Deris, and H. S. Faraji, "A facile and green biosynthesis of silver nanostructures by aqueous extract of Suaeda acuminata after microwave assisted extraction," *Nanochemistry Research*, vol. 1, no. 2, pp. 177–182, 2016.

[161] B. Keita, T. Liu, and L. J. Nadjo, "Synthesis of remarkably stabilized metal nanostructures using polyoxometalates," *Journal Materials Chemistry*, vol. 19, no. 1, pp. 19–33, 2009.

[162] N. Visaveliya and J. M. Köhler, "A self-seeding synthesis of Ag microrods of tuned aspect ratio: ascorbic acid plays a key role," *Nanotechnology*, vol. 24, no. 34, p. 345604, 2013.

[163] Z. Hosseinidoust, M. Basnet, T. G. M. van de Ven, and N. Tufenkji, "One-pot green synthesis of anisotropic silver nanoparticles," *Environmental Science: Nano*, vol. 3, no. 6, pp. 1259–1264, 2016.

[164] I. Hussain, N. B. Singh, A. Singh, H. Singh, and S. C. Singh, "Green synthesis of nanoparticles and its potential application," *Biotechnology Letters*, vol. 38, no. 4, pp. 545–560, 2016.

[165] K. S. Krishna, C. V. Navin, S. Biswas et al., "Millifluidics for Time-resolved Mapping of the Growth of Gold Nanostructures," *Journal of the American Chemical Society*, vol. 135, no. 14, pp. 5450–5456, 2013.

[166] Y. Li, X. Yuan, H. Yang, Y. Chao, S. Guo, and C. Wang, "One-Step Synthesis of Silver Nanowires with Ultra-Long Length and Thin Diameter to Make Flexible Transparent Conductive Films," *Materials*, vol. 12, no. 3, p. 401, 2019.

Hindawi
Journal of Nanomaterials
Volume 2020, Article ID 5641063, 12 pages
https://doi.org/10.1155/2020/5641063

*Research Article*

# Enhancing Charge Transfer and Photoelectric Characteristics for Organic Solar Cells

**Xiaofei Wang,[1] Weiwei Pei,[2] and Yuanzuo Li[1]**

[1]*College of Science, Northeast Forestry University, Harbin, 150040 Heilongjiang, China*
[2]*College of Science, Jiamusi University, 154001 Heilongjiang, China*

Correspondence should be addressed to Yuanzuo Li; yzli@nefu.edu.cn

Received 2 July 2019; Revised 19 September 2019; Accepted 11 October 2019; Published 26 February 2020

Guest Editor: Scott L. Wallen



The main purpose of this work is to analyze the effect of steric hindrance on the photoelectric performance of three different donor sensitizers (ZHG5, ZHG6, and ZHG7) by molecular theory simulation engineering. Photoelectric physical and photoelectric chemical parameters are investigated by means of frontier molecular orbital, global reactivity descriptors, optical absorption properties, fluorescent lifetime, charge density difference, and influence of external electric field. The results showed that the performance of the quinoxaline sensitizer was deteriorated by gradually increasing the steric hindrance to auxiliary donors. The optical properties of the hybridization of cir-coronene graphene quantum dot (GR) with the three dyes have been revealed, and the results show that graphene quantum dots can indeed improve the optical properties of solar cells. In addition, nine new molecules were designed by inserting six functional groups; it is found that inserting -CN in the acceptor part of the molecular structure is beneficial to the performance of the sensitizer.

## 1. Introduction

Energy is the driving force for the development of human society. However, due to the depletion of fossil energy, human society is facing an energy crisis. Therefore, the development and utilization of clean energy are particularly important. Solar cells have many advantages, such as clean and pollution-free, low cost, and renewable and have gradually become a hot research object. Since the advent of dye-sensitized solar cells (DSSCs) in 1991, high-performance sensitizers have been a hot topic among researchers [1]. The common dye-sensitized solar cells are mainly composed of five parts: transparent conductive optical (TCO) glass, transparent nanocrystalline semiconductor thin films (photoanode), photoactive layer (dye and electrolyte solution without photoanode), redox electrolyte, and counter electrode (photocathode), which forms the sandwich's structure [2, 3]. As a core component of dye-sensitized solar energy, the photoactive layer of different components directly affects the performance of the cells. As the filling material of the photoactive layer, the sensitizer can be divided into two types: metal sensitizer and nonmetal sensitizer. Nonmetallic sensitizer and polymers have the advantages of nonpollution, stability and well performance, which can be used as a potential candidate in the field of optoelectronics [4, 5].

The diversity of sensitizers has always been a research hotspot in the field of DSSCs, and the performance of sensitizers represented by D-$\pi$-A type structure is particularly outstanding, which has been unanimously recognized by the academic community [6–8]. Xu et al. [9] synthesized a new sensitizer with D-$\pi$-A structure and applied it to the modified photoanode and found that the photoanode with 3D inverse opal nanostructure was more favorable to the photoelectric properties of DSSC. Huang and his collaborators [10] synthesized two novel $\pi$-conjugated moieties that could be part of $\pi$-bridge for the construction of D-$\pi$-A-configured photosensitizers for DSSC applications. The results demonstrated that lateral $\pi$-conjugated expansion can improve device performance better than the linear $\pi$-conjugated extension. Duerto and his collaborators [11] synthesized four new sensitizers for DSSCs with a *tert*-butyldimethylsilylether in order to test their physical

and photovoltaic properties. The experimental results verify that the performance of the device is greatly improved when thiophene is inserted into the $\pi$-conjugated bridge part.

Many achievements have been made in the research on the performance of sensitizers in experiments, and the theoretical part has been widely used with the improvement of the density functional theory (DFT) technology [12–16]. In addition, graphene quantum dots have also been studied theoretically and experimentally as fillers of photosensitive layers [17, 18]. Dong et al. [19] used DFT to investigate the tentative mechanism of the intramolecular electron and hole separation process at the quantum chemical level. The results implied that electrons are injected from QDs@GR nanomaterials into the cir-coronene graphene quantum dot and transition along with graphene sheet through $\pi^*$ orbitals to achieve interfacial separation of electron-hole. Gao and coworkers [20] used theoretical and experimental methods to simulate the optical properties of four sensitizers and cir-coronene graphene quantum dot nanocomposites. The results demonstrate that the optical properties of all the nanocomposites have enhanced compared with those of isolated sensitizers. Li et al. [21] used the method of quantum chemistry calculation to simulate a series of sensitizers with rigid fused $\pi$-conjugated bridge. The calculated results indicate that reducing the aromaticity of the $\pi$-conjugated bridge can promote intramolecular electron delocalization and enhance the electronic injection at the Dye/$TiO_2$ interface.

In this work, based on the research results of Chen and his collaborators [22], we used the method of quantum chemistry to further analyze how the steric hindrance affects the performance of the sensitizer (ZHG5, ZHG6, and ZHG7). In addition, sensitizers ZHG6 and ZHG7 were synthesized by adding auxiliary donors based on the molecular structure of ZHG5. The photophysical and photochemical characteristics of three sensitizers in tetrahydrofuran (THF) were simulated. Meanwhile, the optical properties of cir-coronene graphene quantum dot (we use GR to indicate the cir-coronene graphene quantum dot mentioned below) hybridization with ZHG5, ZHG6, and ZHG7 have been revealed. Subsequently, nine new molecules based on the molecular structure of ZHG5 have been designed to study the optical characteristics of sensitizers and the interface electron injection from the photoactive layer to semiconductors.

## 2. Computational Details

The DFT [23, 24] and TD-DFT [25–27] were used to analyze the ground-state and excited-state performance of the sensitizers. Moreover, the optimized geometries and frontier molecular orbitals of dyes were simulated by using B3LYP/6-31g(d) [28–30]. In order to make the theoretical simulation results more convincing, the functional used in the excited state needs to be screened. Based on sensitizer ZHG5, the UV-Vis absorption spectra simulated by six functionals (Cam-B3LYP, $\omega$B97X, PBEPBE, MPW1PW91, LC-$\omega$PBE, and B3LYP [31–36]) were compared with the experimental spectra. Functional Cam-B3LYP, whose performance was closest to the experimental results, was selected for subsequent calculation of the properties of excited states, and the results of the simulation are summarized in Table S1. Meanwhile, the excited-state properties of all sensitizers were calculated in THF solution by means of the conductor polarizable continuous model (C-PCM) [37].

In addition, adiabatic electron-transfer time ($\tau_2$) and rate ($k_{\mathrm{ET}}$) from sensitizers to semiconductor were simulated in THF solution. The electron-transfer time could be calculated by the following formula [38, 39]:

$$\hbar\Gamma = \sum_{\mathrm{i}} p_i |\varepsilon_i - E_{\mathrm{LUMO}}|, \tag{1}$$

$$\tau(\mathrm{fs}) = \frac{658}{\hbar\Gamma}\ (\mathrm{meV}), \tag{2}$$

where $\hbar\Gamma$ is the broadening width, $p_i$ and $\varepsilon_i$ represent the adsorbate part of $i$th molecular orbital for the sensitizer and its corresponding molecular orbital energy, and $E_{\mathrm{LUMO}}$ is the sum of the energies of the adsorbate in the unoccupied orbitals. All the theoretical results were obtained by Gaussian 09 [40].

## 3. Results and Discussion

*3.1. Spatial Structures.* The geometry structures of three investigated sensitizers ZHG5, ZHG6, and ZHG7 were optimized in tetrahydrofuran (THF) solution without symmetry constraint, and their spatial structures are available in Figure 1 and Scheme 1. With the donor part based on ZHG5, a benzene ring was inserted into the auxiliary donor portion of ZHG5 as a secondary electron-donating group, so we get sensitizer ZHG6. Based on the structure of ZHG6, a 2-(4-ethylhexyloxy)naphthalene ($D_2{}^*$) as the steric hindrance was inserted into the auxiliary donor group and we get molecule ZHG7. Some dihedral angles for all the optimized structures are summarized in Table 1. The interfacial angles ($\theta_1$) between the donor and auxiliary donor for three dyes are -34.03°, -34.23°, and 33.28°, respectively. The twisted angles ($\theta_2$) between the donor section and the $\pi$-conjugation part for three dyes are 43.88°, 43.83°, and 39.77°, respectively, which means that the juncture section is distorted. Combining previous research in this area, we conclude that the donor portion of the dye molecule has a distorted structure; it inhibits the intermolecular $\pi$-$\pi$ aggregation on the semiconductor films. The $\pi$-spacers show good coplanarity with the acceptor unit with the dihedral angles ($\theta_3$) less than 1.8° in the three dyes. Thus, the $\pi$-bridges make excellent $\pi$-conjugation with the acceptor part, which facilitates for ICT and red shift of absorbance range. The dihedral angle $\theta_4$ between two benzene rings is unique to dye ZHG7, and its value is 82.05°. This approximately right-angled two $D_2$ planar structure indicates the existence of a steric hindrance effect by donor T-type stacking interaction, which results in the distortion of two structures that should be coplanar.

*3.2. Frontier Molecular Orbital (FMO) Analysis.* The molecular orbitals' transition ability can be reflected by the orbitals' energy levels. The calculated energy levels are shown in Table 2 and Figure 2. In addition, FMOs and charge density difference (CDD) of ZHG5, ZHG6, and ZHG7 are presented

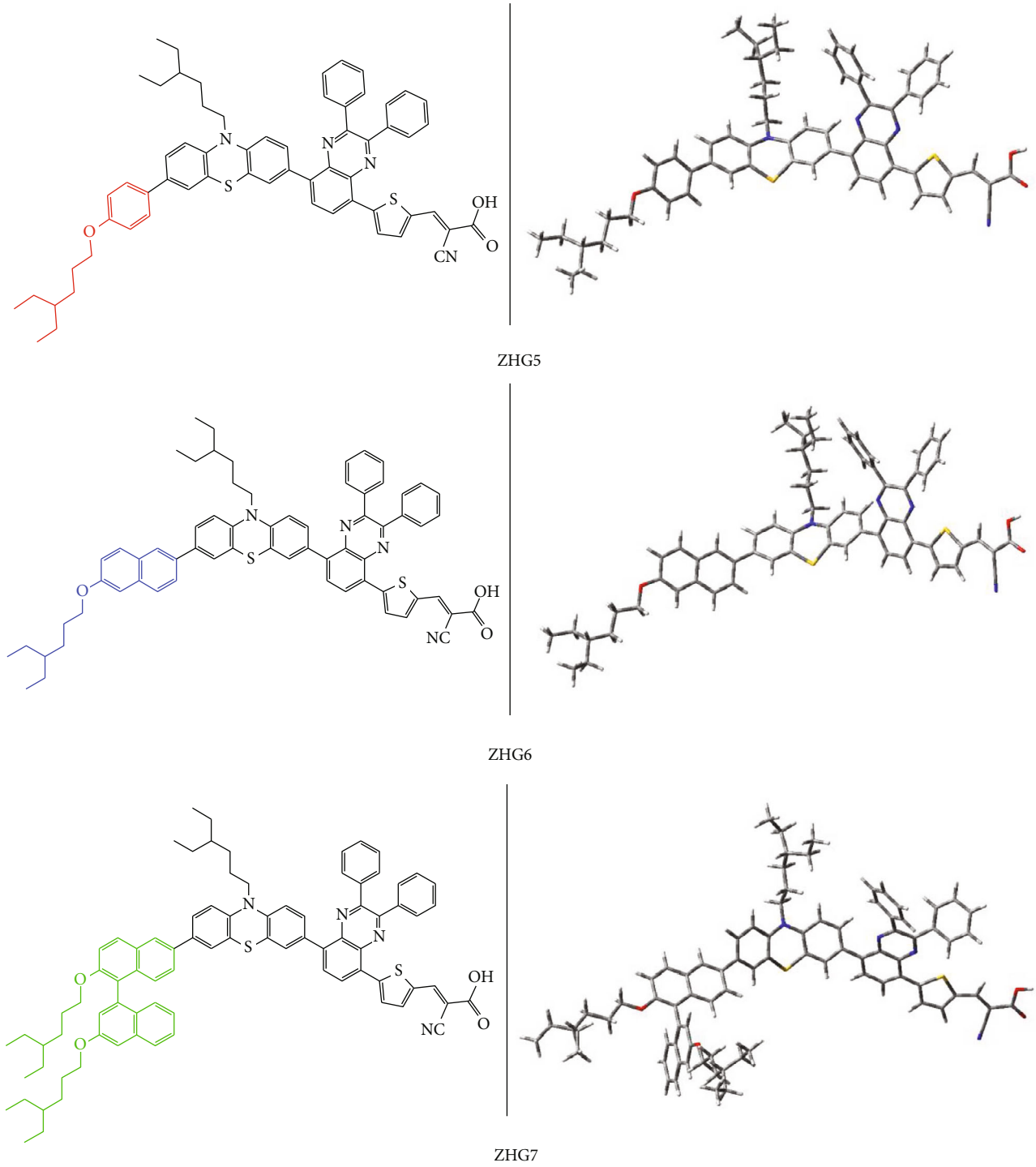


Figure 1: Chemical structures of ZHG5, ZHG6, and ZHG6.

in Figure 3. The energy levels of sensitizers need to meet the levels of $I^-/I_3^-$ couple and $TiO_2$ conducting band edge. LUMO levels of the sensitizer are laying above the conduction band of the titanium dioxide (-4.0 eV) [41], demonstrating that electrons can be transferred easily from the excited-state sensitizer to semiconductor. The HOMO levels of the sensitizer are under the redox potential of $I_3^-/I^-$ electrolyte (-4.6 eV) [42], which indicates that the electron-deprived sensitizers can quickly replenish the lost electrons from the electrolyte. For ZHG5, the electron densities at HOMO are mainly occupied in the donor and auxiliary parts (see Figure 3). The electron densities aggregate the acceptor section at LUMO. The CDD can directly reflect the difference of electron density between the ground state and the first excited state. In Figure 3, the green (red) sections represent the negative (positive) electron density. As sensitizer ZHG5 is stimulated by light, electrons are transferred from the donor section to the acceptor moiety. As the acceptor group of the sensitizer

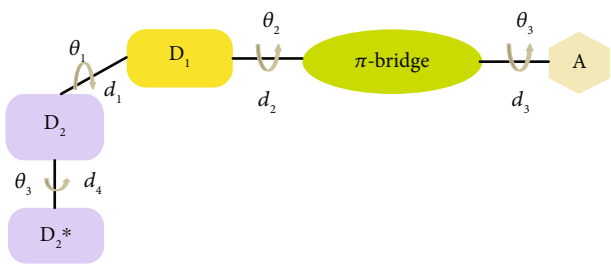


Scheme 1: Brief structure of D–D–$\pi$–A dyes ($\theta_1$–$\theta_4$ represent the dihedral angle; $d_1$–$d_4$ represent the bond length; $D_2{}^*$ represents the 2-(4-ethylhexyloxy)naphthalene).

Table 1: Selected bond lengths and dihedral angles based on the optimized geometries of the three dyes in THF solution.

| | ZHG5 | ZHG6 | ZHG7 |
|---|---|---|---|
| | Bond length (Å) | | |
| $d_1$ | 1.483 | 1.483 | 1.482 |
| $d_2$ | 1.478 | 1.478 | 1.478 |
| $d_3$ | 1.425 | 1.424 | 1.425 |
| $d_4$ | —— | —— | 1.498 |
| | Dihedral angle (°) | | |
| $\theta_1$ | -34.03 | -34.23 | 33.28 |
| $\theta_2$ | 43.88 | 43.83 | 39.77 |
| $\theta_3$ | 1.73 | 1.54 | 1.36 |
| $\theta_4$ | —— | —— | 82.05 |

Table 2: Energy levels and energy gaps of all the investigated dyes and its complexes in solvent (eV).

| | $H$ | $L$ | $\Delta_{H-L}$ |
|---|---|---|---|
| ZHG5 | -4.94 | -2.89 | 2.05 |
| ZHG6 | -4.95 | -2.89 | 2.06 |
| ZHG7 | -4.96 | -2.89 | 2.07 |
| ZHG5/GR | -4.94 | -2.97 | 1.97 |
| ZHG6/GR | -4.96 | -2.97 | 1.99 |
| ZHG7/GR | -4.96 | -2.97 | 1.99 |

is easily adsorbed on the semiconductor substrate, the electron transfer from the photosensitive layer to the photoanode is facilitated. The electron distributions of ZHG6 at the HOMO and LUMO are similar to those of ZHG5. As sensitizer ZHG7 is stimulated by light, intramolecular charge transfer occurs.

Table 2 shows that HOMO energy levels in investigated sensitizers is ZHG5 > ZHG6 > ZHG7, and the order of energy gaps is ZHG7 > ZHG6 > ZHG5, which indicates that the insertion of the benzene ring and 2-(4-ethylhexyloxy)-naphthalene as steric hindrance caused the HOMO level of the photosensitizer to decrease, and it is not conducive to absorption spectrum bathochromic shift. The insertion of these functional groups into molecules leads to an increase in the energy gap, which is not conducive to photoexcitation.

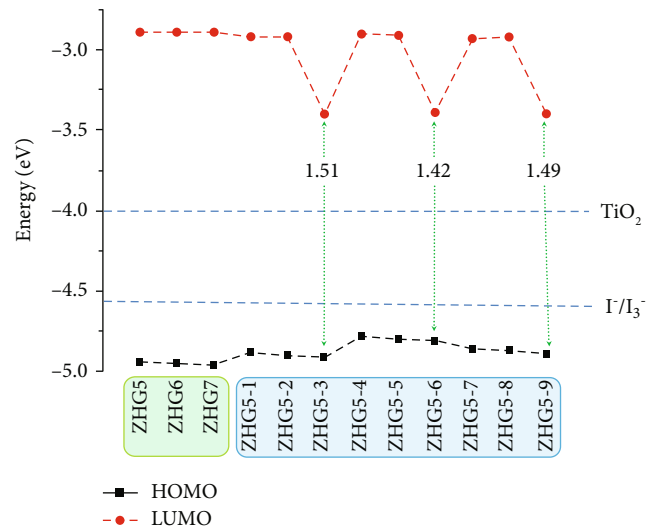


Figure 2: Molecular orbital energies and energy gaps of the molecules.

This may be the reason for the degradation of the overall performance of sensitizers, so the simulation results are in line with the experimental conclusions.

*3.3. Global Reactivity Descriptors.* On the basis of Koopmans' theorem [43–45], different global reactivity descriptors, i.e., electronegativity ($\chi$), hardness ($\eta$), softness ($S$), chemical potential ($\mu$) and electrophilicity index ($\Delta$E), are computed by means of the energies of ionization potential (IP) and electron affinity (EA). The smaller ionization potentials are favorable for electron transfer to semiconductor substrate, and the larger electron affinities inhibit electron transfer from photo-anode to photosensitive layer. The electron affinities of the three sensitizers had no obvious changes. From Table 3, the ionization potentials are 4.813 eV, 4.826 eV, and 4.827 eV for ZHG5, ZHG6, and ZHG7, which is indicating that sensitizer ZHG5 is more efficient at injecting electrons into the semiconductor substrate.

Moreover, the total molecular energies ($E_{TOTAL}$), chemical hardness ($\eta$), chemical softness ($S$), and electrophilicity index ($\Delta$E) of the three dyes in a solvent phase were calculated. As shown in Table 3, chemical hardness is a measure of electron transfer resistance, and the results show that ZHG5 is 3.316 eV, which is the lowest value relative to ZHG6 (3.328 eV) and ZHG7 (3.330 eV). Chemical potential can reflect the ability of photosensitive molecules to transfer electrons to an equilibrium state after photoexcitation, it can be seen from Table 3 that the escaping ability of ZHG5 is strongest. The electrophilicity index is the property of a molecule to obtain electrons from the environment or to provide electrons to the environment. All three molecules have a negative electrophilicity index, which means all three dyes have the ability to provide electrons to the environment.

*3.4. Optical Characteristics.* The UV-Visible absorption spectra were simulated via TD-DFT in THF solvent. The wavelength of the maximum molar extinction coefficient

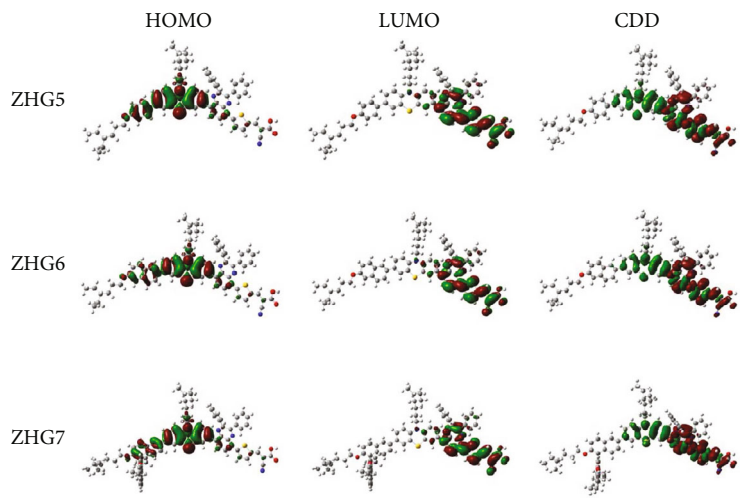


Figure 3: The molecular orbitals HOMO (left), LUMO (middle), and charge density difference (right) between the excited- and ground-state diagrams of three original molecules.

Table 3: Ionization potentials (IP), electron affinities (EA), electronegativity ($\chi$), hardness ($\eta$), softness ($S$/eV$^{-1}$), chemical potential ($\mu$), electrophilicity index ($\Delta$E), and total molecular energies ($E_{\mathrm{TOTAL}}$/Hartree) of ZHG5, ZHG6, and ZHG7 (eV).

| | ZHG5 | ZHG6 | ZHG7 |
|---|---|---|---|
| IP | 4.813 | 4.826 | 4.827 |
| EA | 2.995 | 2.996 | 2.995 |
| $\chi$ | 6.311 | 6.324 | 6.325 |
| $\eta$ | 3.316 | 3.328 | 3.330 |
| $S$ | 0.726 | 0.725 | 0.725 |
| $\mu$ | -3.904 | -3.911 | -3.911 |
| $\Delta$E | -1.818 | -1.830 | -1.832 |
| $E_{\mathrm{TOTAL}}$ | -3639.847 | -3793.493 | -4567.906 |

($\lambda_{\mathrm{abs}}$) and maximum oscillator strengths ($f$) were listed in Table 4 and Table S2. In addition, the absorption spectra of the three molecules are displayed in Figure 4. For ZHG5, the $\lambda_{\mathrm{abs}}$ and $f$ of the first excited state are 452.36 nm and 1.450. Compared with ZHG5, the $\lambda_{\mathrm{abs}}$ simulated by ZHG6 is 451.50 nm and an oscillator of 1.499. In addition, the $\lambda_{\mathrm{abs}}$ of ZHG7 is 452.00 nm with the oscillator of 1.516. The simulated UV-Vis absorption spectrum curves agree with the experimental data, and it can be seen that the addition of auxiliary donor does not change the absorption property of the sensitizer.

The fluorescence performance of the sensitizer can reflect whether the sensitizer can be used as the photosensitive layer of DSSC. When the fluorescence lifetime of the molecule is long, the excited state of the electron lasts for a long time, which is conducive to electron transfer. The emission characteristics are affected by many factors, such as the molar extinction coefficient, the vertical emission energy, and the simulated data are summarized in Table 5. The wavelengths of the wavelength of fluorescence emission peak ($\lambda_{\mathrm{em}}$) are higher (~120 nm) than those of the wavelengths of the maximum molar extinction coefficient ($\lambda_{\mathrm{abs}}$) for the three dyes.

Moreover, the fluorescence lifetime of the sensitizers can be derived by the following formula [46]:

$$\tau = \frac{c^3}{2(E_{\mathrm{flu}})^2 f}, \tag{3}$$

here, $f$ represents the oscillator of the fluorescence spectrum. $c$ stands for the velocity of light and $E_{\mathrm{flu}}$ means the vertical emission energy. $\tau$ is the fluorescence lifetime. The $\tau$ of the three sensitizers in S1 state is shown in Table 5, and it can be seen that the fluorescence lifetime of the sensitizers decreases with the increase of the auxiliary donor group. The specific relationship between molecules is ZHG5 (3.00 ns) > ZHG6 (2.93 ns) > ZHG7 (2.91 ns), which indicates that sensitizer ZHG5 is more suitable to be the photosensitive layer of DSSC than the other two sensitizers.

*3.5. External Electric Field Analysis.* Electron transfer is affected by the electric field, and the appropriate direction and intensity of the electric field can enhance the electron transfer of the sensitizer to the semiconductor, so it is particularly necessary to simulate the optical properties of sensitizers in the electric field. The external electric field of different strengths ($F = 0$, $5 \times 10^{-4}$, $10 \times 10^{-4}$, $15 \times 10^{-4}$, $20 \times 10^{-4}$, $25 \times 10^{-4}$, and $30 \times 10^{-4}$ au) along the $x$-axis (The direction of the donor to the acceptor) was applied to the three sensitizers. Since the oxygen-containing group can be easily anchored to the semiconductor substrate, the direction of the external electric field is perpendicular to the semiconductor substrate [47, 48]. The energy levels and gaps of the three sensitizers in the applied electric field of different intensities are summarized in Table S3. Comparing with the HOMO energy level without the intensity of the external electric field (-4.94 eV for ZHG5), it can be found that when the applied external electric field intensity is between 0 and $15 \times 10^{-4}$ au, the energy level increases with the increase of the external electric field. In addition, the LUMO level and energy gap decrease as the

Table 4: The calculated transition properties of ZHG5, ZHG6, and ZHG7 in THF via TD-DFT/Cam-B3LYP/6-31G(d).

| Dyes | State | $E$ (eV) | $\lambda_{abs}$ (nm) | Contribution MO | Strength ($f$) | Experiment (nm) |
|---|---|---|---|---|---|---|
| ZHG5 | S1 | 2.74 | 452.36 | (51.7%) H ⟶ L | 1.450 | 471 |
| | S2 | 3.28 | 377.97 | (34.4%) H-1 ⟶ L | 0.198 | |
| | S3 | 3.60 | 335.51 | (14.9%) H-8 ⟶ L | 0.290 | |
| ZHG6 | S1 | 2.75 | 451.50 | (49.6%) H ⟶ L | 1.499 | 466 |
| | S2 | 3.28 | 377.44 | (35.3%) H-2 ⟶ L | 0.178 | |
| | S3 | 3.70 | 335.44 | (21.9%) H-9 ⟶ L | 0.054 | |
| ZHG7 | S1 | 2.74 | 452.00 | (49.0%) H ⟶ L | 1.516 | 472 |
| | S2 | 3.29 | 377.16 | (41.0%) H-3 ⟶ L | 0.182 | |
| | S3 | 3.70 | 335.53 | (11.5%) H-11 ⟶ L | 0.051 | |

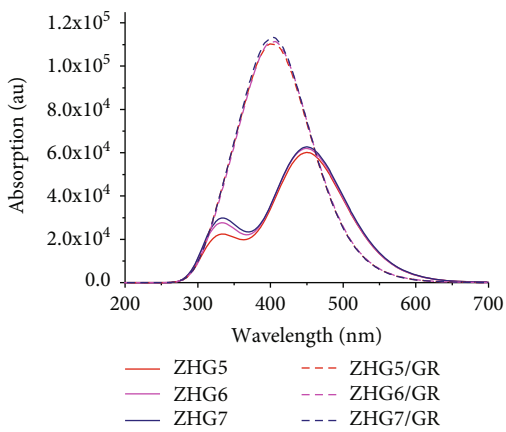


Figure 4: The UV-Vis absorption spectra of three isolated molecules and Dye/GR complexes in solvent.

Table 5: Emission properties of dyes ZHG5, ZHG6, and ZHG7.

| Dye | State | $E_{flu}$ (eV)/$\lambda_{em}$ (nm) | $f$ | $\tau_1$ (ns) | Contribution MO |
|---|---|---|---|---|---|
| ZHG5 | S1 | 2.18/569 | 1.6163 | 3.00 | H ⟶ L/76.7% |
| ZHG6 | S1 | 2.18/568 | 1.6565 | 2.93 | H ⟶ L/76.1% |
| ZHG7 | S1 | 2.18/568 | 1.6674 | 2.91 | H ⟶ L/75.8% |

external electric field increases. Not only that, when the electric field intensity is greater than $15 \times 10^{-4}$, there is no regularity in the change of the molecular energy level. For ZHG6, when the external electric field strength is $5 \times 10^{-4}$ au, the HOMO value is very small and resulting in a large energy gap. Besides, the LUMO and energy gap all decrease with the increase of the $F$, and the HOMO decreases as the $F$ increases. When the $F$ is greater than $20 \times 10^{-4}$ au, the HOMO is greater than -4.6 eV, indicating that the $F$ is appropriate between 0 and $20 \times 10^{-4}$ au. In addition, it is worth noting that the HOMO energy level can be adjusted by controlling the strength of the applied $F$, so as to affect whether DSSC works properly. According to this principle, the sensitizer can be designed as a nonlinear optical switch controlled by the electric field. For ZHG7, the variation trend of energy gap and energy level in the external electric field is the same as that of ZHG5.

The optical properties of the three sensitizers in electric fields of different intensities are shown in Figure 5 and Table S4. For three molecules, the absorption peak red shifts as the strength of the external electric field increases, and the oscillator strength of S1 decreases as the external electric field increases. By means of the absorption spectrum, it can be found that the absorption interval of dye in the visible region increases with the increase of the external electric field intensity, which is favorable for the sensitizer to be excited by light.

*3.6. Molecular Electrostatic Potential (MEP).* In order to examine the differential mutagenicities among three dyes, the molecular electrostatic potential (MEP) was calculated, and the results are shown in Figure 6. The MEP maps can directly reflect the reaction area of nucleophilic attack and electrophilic attack on molecules, and the different colors at the surface represent the different values of MEP. The electrostatic potential is in increasing order red < pink < buff < -palegreen < mazarine. The color gradient of electrostatic potential ranges from -0.06 au (red) to 0.06 au (mazarine). The MEP maps of all sensitizers showed that the hydrogen atom with hydroxyl groups in the acceptor had the highest positive potential compared with other parts of the molecule, indicating the preferred site for nucleophilic attack. The relatively negative potential regions are observed on nitrogen atom with the cyano group and oxygen atom with the carbonyl group in the acceptor part, which is the preferred area of electrophilic attack. It can be seen from the MEP maps that both nucleophilic attack and electrophilic attack are concentrated in the acceptor part of the sensitizers, indicating that the acceptor parts are the unstable region for three dyes. Therefore, the graphene quantum dot can be inserted in the acceptor parts to simulate the optical properties of the doped graphene on the device.

*3.7. Properties of Dye/Graphene (Dye/GR) Complex.* In order to prevent the $sp^2$ hybridization network structure of graphene from being destroyed by the chemical functionalization of graphene oxide, inhibition of graphene oxidation has been applied to the preparation of Dye/GR nanomaterials. The cir-coronene graphene with $D_{6h}$ planar reticular structure was adopted as the quantum dot for anchoring sensitizers. The C-C single bond is formed between the sensitizer

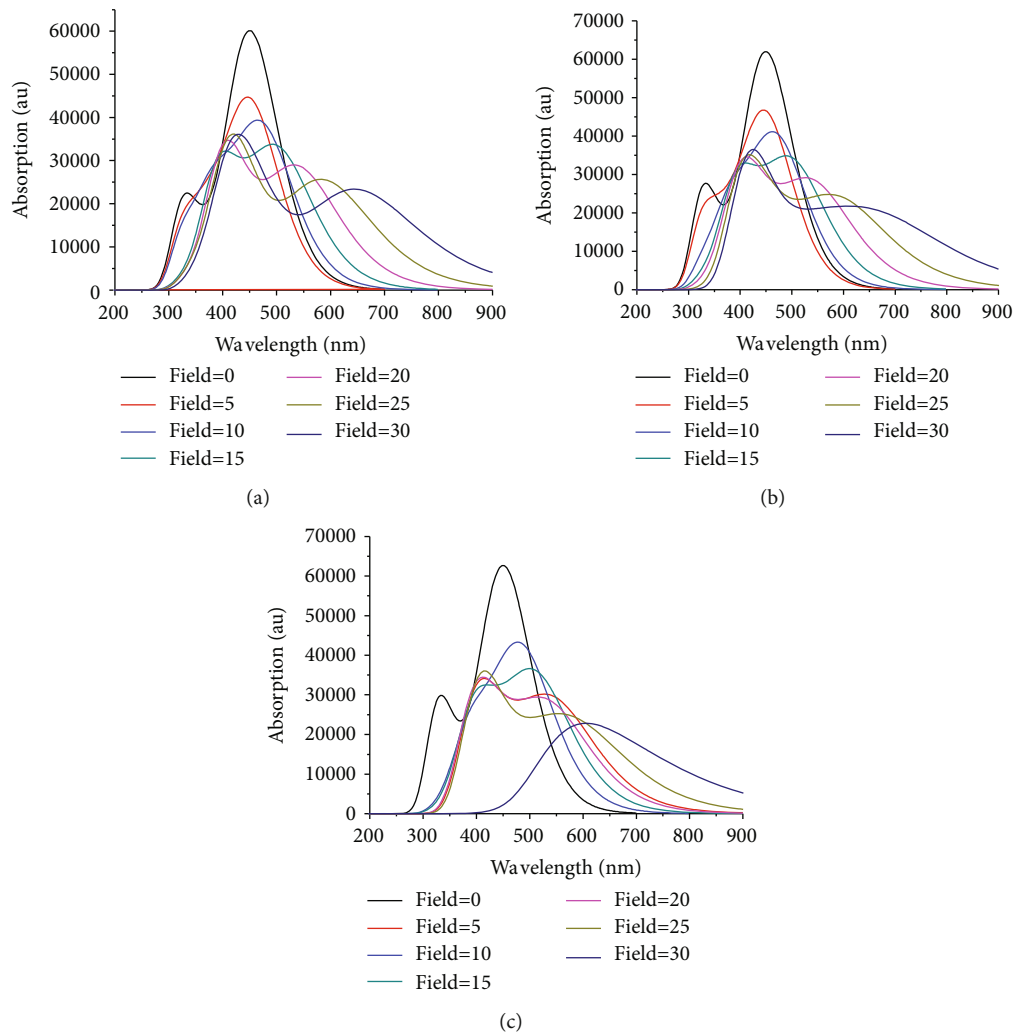


Figure 5: Simulated absorption spectra of three molecules under different electric field intensities ($\times 10^{-4}$ au): (a) ZHG5, (b) ZHG6, (c) ZHG7.

molecules and quantum dots through dehydration and condensation. The C-C bonds formed between the three sensitizers and the quantum dots range from 1.498 to 1.499 Å. This is a stable state compared to the length of the C-C bonds in the molecule (1.39-1.55 Å).

The energy levels and energy gaps of Dye/GR are given in Table 2. As can be seen from the chart, the HOMO level of the complex did not change significantly after the sensitizer was hybrid with graphene quantum dots, but the LUMO levels of the three complexes decreased to different degrees, which leads to a smaller gap, and which facilitates the transition of the molecular orbital.

The frontier molecular orbitals and optical properties are plotted in Figure S1, Figure 4 and Table S5. Table S5 shows that the oscillator intensity reaches its maximum when the molecular orbitals are transferred from HOMO-3 to LUMO, indicating that S2 is analyzed in detail. For ZHG5/GR, the maximum absorption peak in S2 state is 470.85 nm, which is red shifted about 18 nm compared with the isolated sensitizer. Moreover, the oscillator strength of the sensitizer doped with graphene quantum dots also rises to 2.248, which is very beneficial to the light capture efficiency. In the excited-state S2, electrons are photoexcited from HOMO-3 to LUMO. On HOMO-3, the electron densities are distributed over the entire molecule, except for the second donor and graphene quantum dot. Moreover, the electron densities are occupied in the acceptor moiety of complex in the LUMO orbital.

The $\lambda_{abs}$ of the S2 for ZHG6/GR is 470.90 nm, and the $f$ is 2.295. Compared with molecule ZHG6, the absorption peak of ZHG6/GR was red shifted about 19 nm. This excited-state electron has a transition from HOMO-2 to LUMO. In HOMO-2, the electron densities are distributed on graphene quantum dots. Besides, the electron densities are distributed among the acceptor part of the complex in LUMO. For ZHG7/GR, the $\lambda_{abs}$ in S2 is 469.95 nm, and the $f$ is 2.288, with the electron having a transition from HOMO-2 orbital to LUMO orbital in this state. For ZHG7, the $\lambda_{abs}$ of ZHG7/GR was red shifted about 17.95 nm. In this excited state, the transition of electron density is similar to that of complex ZHG6/GR. As can be seen from the optical properties of the three complexes, the energy gaps of the complexes were significantly reduced after the graphene quantum dots were doped. At the same time, the molar

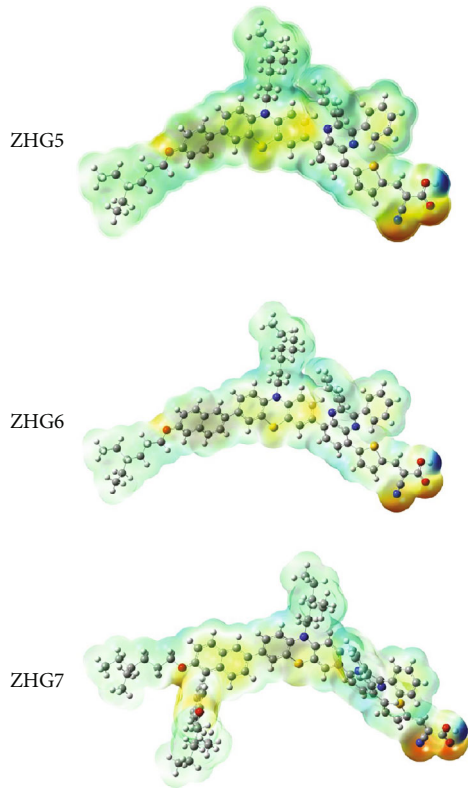


Figure 6: Molecular electrostatic potential plots of dyes ZHG5, ZHG6, and ZHG7 under uniform standards, where the red color depicts negative (electron-rich) regions (the preferred areas of electrophilic attack) and blue color depicts positive (electron-poor) regions (which preferred areas of nucleophilic attack).

extinction coefficients were also significantly increased, and the absorption spectrums were also significantly red shift. The simulation results evidenced that graphene quantum dot filling system compared with an isolated sensitizer is more advantageous to the optical performance of DSSCs.

*3.8. Designed Molecules.* The molar extinction coefficient, energy gap, fluorescence lifetime, and global reactivity descriptors of ZHG5 are better than those of ZHG6 and ZHG7. Based on the optimized spatial structure of ZHG5, nine sensitizers were designed by insertion of different functional groups (-OH, $-NH_2$, $-OCH_3$, $-CF_3$, -F, and -CN). The structural formulas for the nine design sensitizers are presented in Figure 7, where the -OH, $-NH_2$, and $-OCH_3$ groups are inserted into the donor portion, and the $-CF_3$, -F, and -CN groups are inserted into the acceptor section.

The energy gaps and FMOs of the nine designed dye sensitizers are shown in Figure 2 and Figure S2, and the detailed data are summarized in Table S6. The HOMO energy level of the nine designed dyes is generally higher than that of the original molecule ZHG5, and the LUMO energy level decreased obviously (see Table 2). Therefore, compared with ZHG5, the energy gap of the nine designed molecules is reduced, in which ZHG5-3, ZHG5-6, and ZHG5-9 are decreased significantly. The optical properties of nine designed dyes are shown in Figure S3 and Table S7.

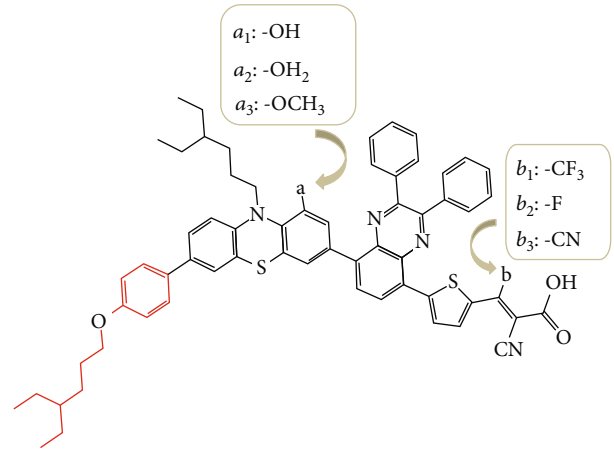


Figure 7: Chemical structures of the nine designed molecules, where ZHG5 − 1 = ZHG5 + $a_1$ + $b_1$, ZHG5 − 2 = ZHG5 + $a_1$ + $b_2$, ZHG5 − 3 = ZHG5 + $a_1$ + $b_3$, ZHG5 − 4 = ZHG5 + $a_2$ + $b_1$, ZHG5 − 5 = ZHG5 + $a_2$ + $b_2$, ZHG5 − 6 = ZHG5 + $a_2$ + $b_3$, ZHG5 − 7 = ZHG5 + $a_3$ + $b_1$, ZHG5 − 8 = ZHG5 + $a_3$ + $b_2$, and ZHG5 − 9 = ZHG5 + $a_3$ + $b_3$.

Compared to molecular ZHG5, the molar extinction coefficients of the designed molecules are generally reduced, and the absorption spectra of ZHG5-3, ZHG5-6, and ZHG5-9 show an obvious red shift.

In addition, in order to make the simulation results of the optical properties of the designed molecules more accurate, the sensitizers are anchored to the semiconductor and the properties of Dye/$TiO_2$ complexes are analyzed [49, 50]. The sensitizer molecules and $TiO_2$ are linked by a Ti-O single bond. The energy gaps and optical parameters of the nine complexes and ZHG5 are summarized in Table 6 and Table S6. The FMOs and absorption spectrum are available in Figures 8 and 9. By means of semiconductor anchoring, the simulation results can be more reliable and convincing. Therefore, the simulation results that the optical properties of ZHG5-3, ZHG5-6 and ZHG5-9 were better than the other six design molecules were verified again, and the optical properties of the sensitizers can be improved by inserting -CN into the acceptor part of the molecule ZHG5.

The adiabatic interface electron transfer theory is used to simulate the electron transfer from the sensitizer to the semiconducting band. By using the developed Newns-Anderson approach [51–54], the interfacial electron transfer (IET) time ($\tau_2$) from sensitizers to a semiconductor can be simulated, and the detailed data are listed in Table 6. From Table 6, it can be found that the interfacial electron injection time of the designed molecules are in the same order of femtosecond.

## 4. Conclusion

In summary, the effects of steric hindrance and graphene quantum dots on the optical properties of DSSC were simulated by theoretical calculation. The results indicate that the donor part of ZHG5 was inserted into benzene ring and 2-(4-ethylhexyloxy)naphthalene as space steric hindrance caused the energy gap and ionization energy were increased,

Table 6: Calculated optical properties and interfacial electron-transfer time $\tau_2$ (fs) of the ZHG5/$TiO_2$ and Dye/$TiO_2$ complexes on S1 state.

| Dyes | $E$ (eV) | $\lambda_{abs}$ (nm) | Contribution MO | Strength ($f$) | $\tau_2$ |
|---|---|---|---|---|---|
| ZHG5/$TiO_2$ | 2.59 | 478.48 | (37.65%) H ⟶ L | 1.740 | 5.2 |
| ZHG5-1/$TiO_2$ | 2.70 | 459.58 | (35.10%) H ⟶ L + 1 | 1.300 | 5.1 |
| ZHG5-2/$TiO_2$ | 2.60 | 478.20 | (47.76%) H ⟶ L | 1.613 | 4.7 |
| ZHG5-3/$TiO_2$ | 2.25 | 551.13 | (51.73%) H ⟶ L | 1.543 | 6.3 |
| ZHG5-4/$TiO_2$ | 2.56 | 484.71 | (25.30%) H ⟶ L | 1.338 | 4.4 |
| ZHG5-5/$TiO_2$ | 2.56 | 484.11 | (50.21%) H ⟶ L | 1.532 | 4.7 |
| ZHG5-6/$TiO_2$ | 2.21 | 559.92 | (55.41%) H ⟶ L | 1.480 | 5.5 |
| ZHG5-7/$TiO_2$ | 2.54 | 487.58 | (37.13%) H ⟶ L + 1 | 1.367 | 4.4 |
| ZHG5-8/$TiO_2$ | 2.59 | 479.27 | (48.80%) H ⟶ L | 1.581 | 4.6 |
| ZHG5-9/$TiO_2$ | 2.25 | 552.03 | (52.70%) H ⟶ L | 1.524 | 5.7 |

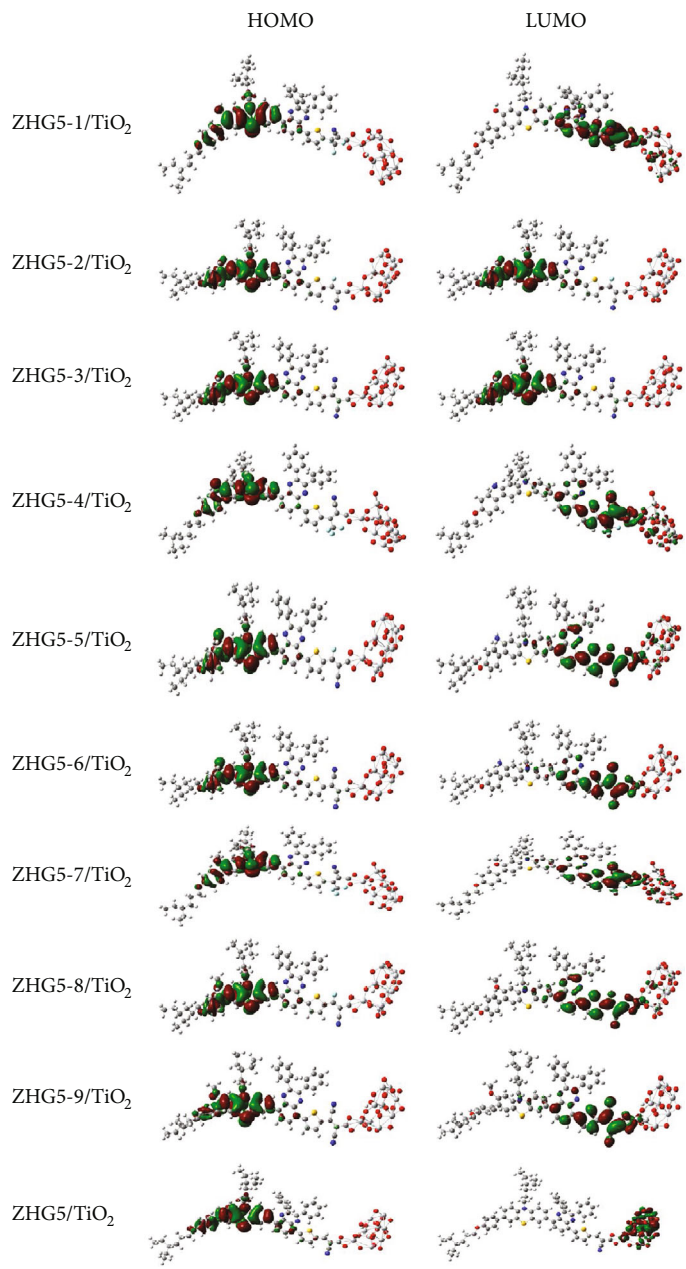


Figure 8: Selected frontier molecular orbitals of the designed Dye/$TiO_2$ and ZHG5/$TiO_2$ complexes in solvent.

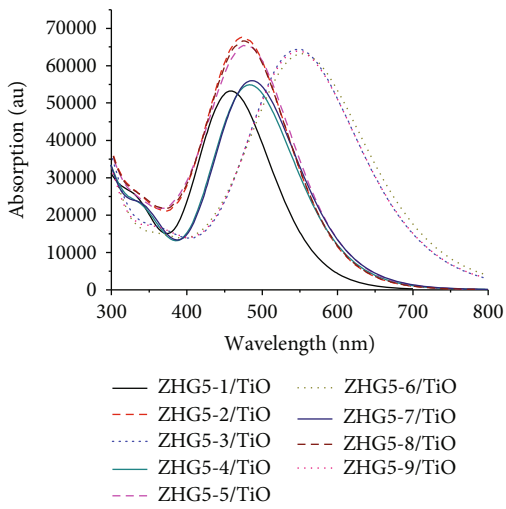


Figure 9: Simulated UV-Vis spectra of the designed Dye/$TiO_2$ complexes in solvent.

and the fluorescence lifetime was reduced, which was not conducive to electron transfer and excited-state duration. This indicates that the steric hindrance effect is caused by the excessive size of the donor part, which is unfavorable to the overall performance of the sensitizer. Based on the analysis of the molecular electrostatic potential, a graphene quantum dot is anchored in the acceptor part with high electron activity, and it is found that the energy gaps of the Dye/GR complexes are reduced and the molar extinction coefficients are generally increased, which indicates that the sensitizer can improve the photoelectric properties of the device after anchoring graphene. The nine molecules were designed by inserting functional groups based on the molecular structure of ZHG5. The results showed that the improvement to the photoelectric properties of the molecules was the most obvious when -CN was inserted into the acceptor of the sensitizer. In addition, molecular dynamics of IET of the designed molecules were simulated, and the results showed that the dynamic transfer process of the designed molecules reached the femtosecond level, which was beneficial to the electron injection efficiency and short-circuit current.

## Data Availability

The data used to support the findings of this study are available from the corresponding author upon request.

## Conflicts of Interest

The authors declare no conflict of interest.

## Acknowledgments

This work was supported by the National Natural Science Foundation of China (Grant Nos. 11974152 and 11404055), the Fundamental Research Funds for the Heilongjiang Postdoctoral Grant (LBH-Z15002), Fundamental Research Funds for China Postdoctoral Science Foundation (2016M590270), the Fundamental Research Funds for the Central Universities (2572018BC24) and the Heilongjiang Provincial Youth Science Foundation (QC2013C006).

## Supplementary Materials

Table S1: experimental absorption peak, calculated absorption peaks with corresponding oscillator strengths of the dye ZHG5 in dichloromethane by using different functionals via TD-DFT/6-31G(d) method (nm). Table S2: the calculated transition properties of ZHG5, ZHG6 and ZHG7 in THF via TD-DFT/Cam-B3LYP/6-31G(d). Table S3: energy levels and energy gaps of the dyes in different external electric field (×10-4 au), in which H and L represent HOMO and LUMO, respectively (eV). Table S4: calculated transition energies and oscillator strengths of ZHG5, ZHG6, and ZHG7 in electric field (×10-4 au), in which H and L represent HOMO and LUMO, respectively. Table S5: the calculated transition properties of ZHG5/GR, ZHG6/GR, and ZHG7/GR in THF via TD-DFT/Cam-B3LYP/6-31G(d). Table S6: the calculated transition properties of the nine designed dyes and ZHG5 in solvent (eV). Table S7: the calculated transition properties of the nine designed molecules in solvent (eV). Figure S1: the frontier molecular orbits and charge density difference (right) between the excited- and ground-state diagrams of ZHG5/GR, ZHG6/GR, and ZHG7/GR. Figure S2: FMO diagrams of the designed molecules. Figure S3: simulated UV-Vis spectra of ZHG5 and nine designed molecules in solvent: (a) ZHG5, ZHG5-1, ZHG5-2, and ZHG5-3; (b) ZHG5, ZHG5-4, ZHG5-5, and ZHG5-6; (c) ZHG5, ZHG5-7, ZHG5-8, and ZHG5-9. *(Supplementary Materials)*

## References

[1] B. O'Regan and M. Grätzel, "A low-cost, high-efficiency solar cell based on dye-sensitized colloidal $TiO_2$ films," *Nature*, vol. 353, no. 6346, pp. 737–740, 1991.

[2] G. di Carlo, A. O. Biroli, F. Tessore, S. Caramori, and M. Pizzotti, "$\beta$-Substituted $Zn^{II}$ porphyrins as dyes for DSSC: A possible approach to photovoltaic windows," *Coordination Chemistry Reviews*, vol. 358, pp. 153–177, 2018.

[3] J. D. Roy-Mayhew and I. A. Aksay, "Graphene materials and their use in dye-sensitized solar cells," *Chemical Reviews*, vol. 114, no. 12, pp. 6323–6348, 2014.

[4] M. Daniels, F. de Jong, K. Kennes et al., "Promising Molecules for Optoelectronic Applications: Synthesis of 5,10-Dihydrobenzo[a ]indolo[2,3-c ]carbazoles by Scholl Reaction of 1,2-Bis(indol-2-yl)benzenes," *European Journal of Organic Chemistry*, vol. 2018, no. 34, pp. 4683–4688, 2018.

[5] X. D. Wang, C. H. Yao, F. Wang, and Z. D. Li, "Cellulose-based nanomaterials for energy applications," *Small*, vol. 13, no. 42, p. 1702240, 2017.

[6] J. Zhang, H. C. Zhu, R. L. Zhong, L. Wang, and Z. M. Su, "Promising heterocyclic anchoring groups with superior adsorption stability and improved IPCE for high-efficiency noncarboxyl dye sensitized solar cells: a theoretical study," *Organic Electronics*, vol. 54, pp. 104–113, 2018.

[7] X. L. Shi, Y. H. Yang, L. H. Wang, and Y. Z. Li, "Introducing asymmetry induced by benzene substitution in a rigid fused $\pi$ spacer of D–$\pi$–A-Type solar cells: a computational

investigation," *Journal of Physical Chemistry C*, vol. 123, no. 7, pp. 4007–4021, 2019.

[8] X.-F. Zang, Z.-S. Huang, H.-L. Wu et al., "Molecular design of the diketopyrrolopyrrole-based dyes with varied donor units for efficient dye-sensitized solar cells," *Journal of Power Sources*, vol. 271, pp. 455–464, 2014.

[9] L. Xu, C. Aumaitre, Y. Kervella et al., "Increasing the efficiency of organic dye-sensitized solar cells over 10.3% using locally ordered inverse opal nanostructures in the photoelectrode," *Advanced Functional Materials*, vol. 28, no. 15, p. 1706291, 2018.

[10] L. Huang, P. Ma, G. Deng et al., "Novel electron-deficient quinoxalinedithienothiophene- and phenazinedithienothiophene-based photosensitizers: The effect of conjugation expansion on DSSC performance," *Dyes and Pigments*, vol. 159, pp. 107–114, 2018.

[11] I. Duerto, E. Colom, J. M. Andrés-Castán et al., "DSSCs based on aniline derivatives functionalized with a *tert* -butyldimethylsilyl group and the effect of the $\pi$-spacer," *Dyes and Pigments*, vol. 148, pp. 61–71, 2018.

[12] C. Chitpakdee, S. Jungsuttiwong, T. Sudyoadsuk, V. Promarak, N. Kungwan, and S. Namuangruk, "Modulation of $\pi$-spacer of carbazole-carbazole based organic dyes toward high efficient dye-sensitized solar cells," *Spectrochimica Acta Part A: Molecular and Biomolecular Spectroscopy*, vol. 174, pp. 7–16, 2017.

[13] Y. Li, X. Li, J. Qi, and Y. Xu, "Tunable optoelectronic properties of D-A-$\pi$-A type dyes by altering auxiliary acceptor position and atomic electronegativity," *Journal of Molecular Liquids*, vol. 287, p. 110883, 2019.

[14] P. H. Ren, C. F. Sun, Y. Shi, P. Song, Y. H. Yang, and Y. Z. Li, "Global performance evaluation of solar cells using two models: from charge-transfer and recombination mechanisms to photoelectric properties," *Journal of Materials Chemistry C*, vol. 7, no. 7, pp. 1934–1947, 2019.

[15] M. Xie, F. Q. Bai, J. J. Wang, Y. Q. Zheng, and Z. Y. Lin, "Theoretical investigations on the unsymmetrical effect of $\beta$-link Zn-porphyrin sensitizers on the performance for dye-sensitized solar cells," *Physical Chemistry Chemical Physics*, vol. 20, no. 5, pp. 3741–3751, 2018.

[16] X. Y. Jin, L. B. Sun, D. Y. Li, C. L. Wang, and F. Q. Bai, "Efficiency difference between furan- and thiophene-based D–$\pi$–A dyes in DSSCs explained by theoretical calculations," *RSC Advances*, vol. 8, no. 52, pp. 29917–29923, 2018.

[17] B. Mandal, S. Sarkar, and P. Sarkar, "Theoretical studies on understanding the feasibility of porphyrin-sensitized graphene quantum dot solar cell," *The Journal of Physical Chemistry C*, vol. 119, no. 6, pp. 3400–3407, 2015.

[18] B. Rajbanshi and P. Sarkar, "Optimizing the photovoltaic properties of CdTe quantum dot–porphyrin nanocomposites: a theoretical study," *The Journal of Physical Chemistry C*, vol. 120, no. 32, pp. 17878–17886, 2016.

[19] C. Dong, X. Li, P. Jin, W. Zhao, J. Chu, and J. Qi, "Intersubunit electron transfer (IET) in quantum dots/graphene complex: what features does IET endow the complex with?," *The Journal of Physical Chemistry C*, vol. 116, no. 29, pp. 15833–15838, 2012.

[20] F. Gao, C. L. Yang, M. S. Wang, X. G. Ma, and W. W. Liu, "Theoretical studies on the possible sensitizers of DSSC: Nanocomposites of graphene quantum dot hybrid phthalocyanine/-tetrabenzoporphyrin/tetrabenzotriazaporphyrins/*cis*-tetrabenzodiazaporphyrins/tetrabenzomonoazaporphyrins and their Cu-metallated macrocycles," *Spectrochimica Acta Part A: Molecular and Biomolecular Spectroscopy*, vol. 195, pp. 176–183, 2018.

[21] P. Li, Z. Wang, C. Song, and H. Zhang, "Rigid fused $\pi$-spacers in D–$\pi$–a type molecules for dye-sensitized solar cells: a computational investigation," *Journal of Materials Chemistry C*, vol. 5, no. 44, pp. 11454–11465, 2017.

[22] S.-G. Chen, H.-L. Jia, X.-H. Ju, and H.-G. Zheng, "The impact of adjusting auxiliary donors on the performance of dye-sensitized solar cells based on phenothiazine D-D-$\pi$-A sensitizers," *Dyes and Pigments*, vol. 146, pp. 127–135, 2017.

[23] P. Hohenberg and W. Kohn, "Inhomogeneous electron gas," *Physical Review*, vol. 136, no. 3B, pp. B864–B871, 1964.

[24] W. Kohn and L. J. Sham, "Quantum density oscillations in an inhomogeneous electron gas," *Physical Review*, vol. 137, no. 6A, pp. A1697–A1705, 1965.

[25] E. K. U. Gross and W. Kohn, "Local density-functional theory of frequency-dependent linear response," *Physical Review Letters*, vol. 55, no. 26, pp. 2850–2852, 1985.

[26] M. E. Casida, C. Jamorski, K. C. Casida, and D. R. Salahub, "Molecular excitation energies to high-lying bound states from time-dependent density-functional response theory: characterization and correction of the time-dependent local density approximation ionization threshold," *The Journal of Chemical Physics*, vol. 108, no. 11, pp. 4439–4449, 1998.

[27] A. D. Becke, "Density-functional exchange-energy approximation with correct asymptotic behavior," *Physical Review A*, vol. 38, no. 6, pp. 3098–3100, 1988.

[28] A. D. Becke, "Density-functional thermochemistry. III. The role of exact exchange," *The Journal of Chemical Physics*, vol. 98, no. 7, pp. 5648–5652, 1993.

[29] C. Lee, W. Yang, and R. G. Parr, "Development of the Colle-Salvetti correlation-energy formula into a functional of the electron density," *Physical Review B Condensed Matter*, vol. 37, no. 2, pp. 785–789, 1988.

[30] W. Li, F. Q. Bai, J. Chen, J. Wang, and H. X. Zhang, "Planar amine-based dye features the rigidified O-bridged dithiophene $\pi$-spacer: A potential high-efficiency sensitizer for dye-sensitized solar cells application," *Journal of Power Sources*, vol. 275, pp. 207–216, 2015.

[31] T. Yanai, D. P. Tew, and N. C. Handy, "A new hybrid exchange-correlation functional using the Coulomb-attenuating method (CAM-B3LYP)," *Chemical Physics Letters*, vol. 393, no. 1–3, pp. 51–57, 2004.

[32] J. P. Perdew, K. Burke, and M. Ernzerhof, "Generalized gradient approximation made simple," *Physical Review Letters*, vol. 77, no. 18, pp. 3865–3868, 1996.

[33] Y. Tawada, T. Tsuneda, S. Yanagisawa, T. Yanai, and K. Hirao, "A long-range-corrected time-dependent density functional theory," *The Journal of Chemical Physics*, vol. 120, no. 18, pp. 8425–8433, 2004.

[34] O. A. Vydrov and G. E. Scuseria, "Assessment of a long-range corrected hybrid functional," *The Journal of Chemical Physics*, vol. 125, no. 23, p. 234109, 2006.

[35] J.-D. Chai and M. Head-Gordon, "Systematic optimization of long-range corrected hybrid density functionals," *The Journal of Chemical Physics*, vol. 128, no. 8, p. 084106, 2008.

[36] C. Adamo and V. Barone, "Exchange functionals with improved long-range behavior and adiabatic connection methods without adjustable parameters: the mPW and mPW1PW models," *The Journal of Chemical Physics*, vol. 108, no. 2, pp. 664–675, 1998.

[37] V. Barone and M. Cossi, "Quantum calculation of molecular energies and energy gradients in solution by a conductor solvent model," *The Journal of Physical Chemistry A*, vol. 102, no. 11, pp. 1995–2001, 1998.

[38] D. M. Newns, "Self-consistent model of hydrogen Chemisorption," *Physics Review*, vol. 178, no. 3, pp. 1123–1135, 1969.

[39] R. A. Marcus and N. Sutin, "Electron transfers in chemistry and biology," *Biochimica et Biophysica Acta*, vol. 811, no. 3, pp. 265–322, 1985.

[40] M. J. Frisch, G. W. Trucks, H. B. Schlegel et al., *Gaussian ~09 Revision D.01*, Gaussian, Inc., Wallingford, CT, USA, 2009.

[41] M. Grätzel, "Photoelectrochemical cells," *Nature*, vol. 414, no. 6861, pp. 338–344, 2001.

[42] L.-J. He, W. Wei, J. Chen, R. Jia, J. Wang, and H.-X. Zhang, "The effect of D–[De–$\pi$–A]n (n = 1, 2, 3) type dyes on the overall performance of DSSCs: a theoretical investigation," *Journal of Materials Chemistry C*, vol. 5, no. 30, pp. 7510–7520, 2017.

[43] R. G. Pearson, "Absolute electronegativity and hardness: application to inorganic chemistry," *Journal of Organic Chemistry*, vol. 27, no. 4, pp. 734–740, 1988.

[44] Z. Z. Sun, Q. S. Li, P. P. Sun, and Z. S. Li, "Probing the regeneration process of triphenylamine-based organic dyes in dye-sensitized solar cells," *Journal of Power Sources*, vol. 276, pp. 230–237, 2015.

[45] R. Gayathri, "An experimental and theoretical investigation of the electronic structure and photoelectrical properties of 1, 4-diacetoxy-2-methylnaphthalene for DSSC application," *Journal of Molecular Structure*, vol. 1166, pp. 63–78, 2018.

[46] I. Litani-Barzilai, V. Bulatov, V. V. Gridin, and I. Schechter, "Detector based on time-resolved ion-induced voltage in laser multiphoton ionization and laser-induced fluorescence," *Analytica Chimica Acta*, vol. 501, no. 2, pp. 151–156, 2004.

[47] K. E. Lee, M. A. Gomez, S. Elouatik, and G. P. Demopoulos, "Further understanding of the adsorption mechanism of N719 sensitizer on anatase TiO2 films for DSSC applications using vibrational spectroscopy and confocal Raman imaging," *Langmuir*, vol. 26, no. 12, pp. 9575–9583, 2010.

[48] H. C. Zhu, C. F. Li, Z. H. Fu, S. S. Wei, X. F. Zhu, and J. Zhang, "Increasing the open-circuit voltage and adsorption stability of squaraine dye binding onto the $TiO_2$ anatase (1 0 1) surface via heterocyclic anchoring groups used for DSSC," *Applied Surface Science*, vol. 455, pp. 1095–1105, 2018.

[49] A. Irfan, A. R. Chaudhry, S. Muhammad, and A. G. Al-Sehemi, "Exploring the potential of boron-doped nanographene as efficient charge transport and nonlinear optical material: a first-principles study," *Journal of Molecular Graphics*, vol. 75, pp. 209–219, 2017.

[50] S. H. Li, C. R. Zhang, L. H. Yuan et al., "The role of electronic donor moieties in porphyrin dye sensitizers for solar cells: electronic structures and excitation related properties," *Journal of Renewable and Sustainable Energy*, vol. 9, no. 5, 2017.

[51] J. P. Muscat and D. M. Newns, "Chemisorption on metals," *Progress in Surface Science*, vol. 9, no. 1, pp. 1–43, 1978.

[52] Y. M. Hailu, M. T. Nguyen, and J. C. Jiang, "Effects of the terminal donor unit in dyes with D-D-$\pi$-A architecture on the regeneration mechanism in DSSCs: a computational study," *Physical Chemistry Chemical Physics*, vol. 20, no. 36, pp. 23564–23577, 2018.

[53] Y. C. Li, J. Y. Liu, D. X. Liu, X. Li, and Y. L. Xu, "D-A-$\pi$-A based organic dyes for efficient DSSCs: A theoretical study on the role of $\pi$-spacer," *Computational Materials Science*, vol. 161, pp. 163–176, 2019.

[54] N. Wazzan and A. Irfan, "Theoretical study of triphenylamine-based organic dyes with mono-, di-, and tri-anchoring groups for dye-sensitized solar cells," *Organic Electronics*, vol. 63, pp. 328–342, 2018.

Hindawi
Journal of Nanomaterials
Volume 2020, Article ID 7915878, 13 pages
https://doi.org/10.1155/2020/7915878

*Research Article*

# ZIF-67/*g*-$C_3N_4$-Modified Electrode for Simultaneous Voltammetric Determination of Uric Acid and Acetaminophen with Cetyltrimethylammonium Bromide as Discriminating Agent

**Huynh Truong Ngo,[1,2] Le Thi Hoa,[1] Nguyen Tan Khanh,[3] Tran Thi Bich Hoa,[1] Tran Thanh Tam Toan,[1] Tran Xuan Mau,[1] Nguyen Hai Phong,[1] Ho Sy Thang,[4] and Dinh Quang Khieu[1]**

[1]*University of Sciences, Hue University, 530000, Vietnam*
[2]*Department of Food Safety and Hygiene, Thua Thien Hue 530000, Vietnam*
[3]*University of Medicine and Pharmacy, Hue University, 530000, Vietnam*
[4]*Office of Graduate Affairs, Dong Thap University, 870000, Vietnam*

Correspondence should be addressed to Ho Sy Thang; hsthang@dthu.edu.vn and Dinh Quang Khieu; dqkhieu@hueuni.edu.vn

Received 4 September 2019; Revised 31 December 2019; Accepted 8 January 2020; Published 27 January 2020

Academic Editor: Alexander Pyatenko



In the present paper, the ZIF-67/*g*-$C_3N_4$ composite was synthesized and utilized as a modifier for a glassy carbon electrode for the simultaneous voltammetric determination of uric acid (URA) and acetaminophen (ACE) with cetyltrimethylammonium bromide (CTAB) as a discriminating agent. The composite was characterized using X-ray diffraction, scanning electron microscopy, transmission electron microscopy, X-ray photoelectron spectroscopy, and nitrogen adsorption/desorption isotherms. The obtained ZIF-67/*g*-$C_3N_4$ composite exhibits good textural properties (specific surface area: 75 $m^2 \cdot g^{-1}$) and is stable in water with a pH range of 3 to 10. The ZIF-67/*g*-$C_3N_4$-modified electrode combined with CTAB as a discriminating agent possesses excellent catalytic electrochemistry towards URA and ACE with well-defined electrochemical responses. The electrochemical kinetics study is also addressed. The linear relation of the oxidation peak current of URA and ACE and the concentration ranging from 0.2 $\mu$M to 6.5 $\mu$M provide a detection limit of 0.052 $\mu$M for URA and 0.053 $\mu$M for ACE. The proposed method is well-suited to simultaneously analyze URA and ACE in human urine with comparable results with HPLC.

## 1. Introduction

Uric acid (denoted as URA) is a heterocyclic compound with formula $C_5H_4N_4O_3$, which is the primary end product of purine metabolism. A high URA level in the blood can indicate the presence of numerous diseases and/or physiological disorders. A high concentration of URA in the urine and blood is observed in patients suffering from diseases such as gout and hyperuricaemia [1]. Acetaminophen (denoted as ACE) with formula $C_8H_9NO_2$, also known as paracetamol, is an effective pain killer used to relieve pains related to many parts of the body [2]. An ACE overdose can cause toxic metabolite accumulation, which may cause serious hepatotoxicity and nephrotoxicity [3].

Today, the speed, selectivity, sensibility, low detection limits, low cost, and *in situ* operation of electroanalytical techniques have been considered as the robust approaches to analyze organic or inorganic traces, especially in pharmaceutical compounds. Uric acid and ACE, as well as dopamine and ascorbic acid, exhibit the redox behaviour at similar potentials. The simultaneous detection of these compounds is sometimes difficult because of interfering overlapping effects. Employing separation steps such as chromatography can sometimes overcome this drawback, but it is usually an

expensive option. Therefore, the search for simple, inexpensive, sensitive, and accurate analytical approaches for the simultaneous detection of URA and ACE would be necessary. There exist two approaches to overcome these issues in electrochemical analysis: (i) using an electrode modified with hybrid nanomaterials to improve the interaction of electrospecies and electrode and subsequently increase the peak-peak separation of analytes and electrochemical signals. Phong et al. [4] studied the simultaneous determination of ascorbic acid, paracetamol, and caffeine using an electrochemically rGO-modified electrode. Kutluay and Aslanoglu [5] reported the selective determination of ACE in the presence of ascorbic acid, dopamine, and uric acid using a glassy carbon electrode modified with multiwalled carbon nanotubes. (ii) The second approach is to use the surfactants as a discriminating agent to promote the peak-peak separation. Surfactants are amphiphilic molecules that contain a hydrophilic group at the one end and a hydrophobic group at the other. Below the critical micelle concentration on the solid-liquid interface, the surfactants form a bilayer or hemimicelle structures [6, 7]. These special structures initiate the interface properties of the electrodes and consequently act as discriminating agents to enhance the resolution of electrodes when the voltammetric peaks of two oxidation or reduction species occur at similar potentials. Alarcón-Angeles et al. [8] reported using sodium dodecyl sulfate as a discriminating agent for the electrochemical determination of dopamine in the presence of ascorbic acid. Liu et al. [9] studied the selective determination of dopamine in the presence of ascorbic acid using cetyltrimethylammonium bromide (denoted as CTAB) as a masking agent.

Recently, graphitic carbon nitride ($g$-$C_3N_4$), which is a polymeric layered material, structurally analogous to graphene, has emerged as a prospective material for use in electrochemistry [10, 11]. Besides its thermal and chemical stability, graphitic carbon nitride possesses metal-free and multiple structural defects, tunable electronic structure, mechanical stability, and high electrical conductivity [12]. Zeolitic imidazolate frameworks (ZIFs) are a subclass of metal-organic frameworks (MOFs). ZIFs are topologically isomorphic with zeolites. They are formed from tetrahedral metal ions (e.g., Zn and Co) connected by imidazolate linkers [13]. ZIF-67 with isostructural SOD zeolitic topology is formed from cobalt ions and 2-methylimidazole. ZIF-67 has a porous structure, a large surface area, and a big amount of active sites, and therefore, it is applied to several fields such as as a catalyst, for separation, and for adsorption [14, 15]. However, ZIF-67 has poor stability and low electrical conductivity. This limits its application in electrochemistry. Combining the advantageous features of both ZIF-67 and $g$-$C_3N_4$, one can manufacture versatile materials for electrochemistry and other potential applications. Recently, Meng et al. [16] reported ZIF-67/$g$-$C_3N_4$ as an efficient photocatalyst for $CO_2$ reduction. To the best of our knowledge, little is known about the use of ZIF-67/$g$-$C_3N_4$ as an electrode modifier in the electrochemical analysis.

Responding to this gap of knowledge, this article presents the synthesis of the ZIF-67/$g$-$C_3N_4$ composite using the ultrasound/microwave-assisted approach. Then, the composite was employed as a modifier to develop a novel electrode for the simultaneous determination of URA and ACE with CTAB as a discriminating agent.

## 2. Experimental

*2.1. Materials.* Melamine ($C_3H_6N_6$, 99%), cobaltous nitrate hexahydrate ($Co(NO_3)\cdot 6H_2O$, 99%), 2-methylimidazole ($CH_3C_3H_2N_2H$, 99%), uric acid ($C_5H_4N_4O_3$, >99%), acetaminophen ($CH_3CONHC_6H_4OH$, >99%), and cetyltrimethylammonium bromide (denoted as CTAB, $CH_3(CH_2)_{15}N(Br)(CH_3)_3$, >98%), sodium hydroxide (NaOH, ≥97%), hydrochloric acid (HCl, 37%), glucose ($C_6H_{12}O_6$, ≥99%), sucrose ($C_{12}H_{22}O_{11}$, ≥99%), sodium oxalate ($Na_2C_2O_4$, ≥99%), sodium nitrate ($NaNO_3$, ≥99%), calcium chloride ($CaCl_2$, ≥98%), potassium sulfate ($K_2SO_4$, ≥98%), ammonium sulfate ($(NH_4)_2SO_4$, ≥99%), and potassium bicarbonate ($KHCO_3$, ≥99%) were obtained from Merck & Co., Germany. Phosphoric acid ($H_3PO_4$, 85%), acetic acid ($CH_3COOH$, ≥99.8%), and boric acid ($H_3BO_3$, 99%) were purchased from Daejung Co., Korea. A Britton-Robinson buffer (denoted as BR-BS) is used for the pH range from 2 to 10. It was prepared by mixing equal volumes of 0.04 M $H_3BO_3$ (2.04 g/100 mL), 0.04 M $H_3PO_4$ (2.8 mL of 85% $H_3PO_4$/100 mL), and 0.04 M $CH_3COOH$ (2.3 mL of glacial $CH_3COOH$/100 mL) that has been adjusted to the desired pH with 0.2 M NaOH or 0.2 M HCl. The stock solution of $1 \times 10^{-2}$ M URA and $1 \times 10^{-2}$ M ACE was prepared daily. Standard solutions were prepared by diluting the stock solution with the BR-BS.

*2.2. Apparatus.* X-ray diffraction (XRD) analysis was performed on a D8 Advance Bruker anode X-ray diffractometer with Cu K$\alpha$ ($\lambda = 1.5406$ Å) radiation. Nitrogen adsorption/-desorption isotherms were performed using a Micromeritics 2020 volumetric adsorption analyzer system. Samples were degassed by heating under vacuum at 180°C for 3 hours. The specific surface area of the samples was calculated using the Brunauer-Emmett-Teller (BET) model. X-ray photoelectron spectroscopy (XPS) was recorded on a Shimadzu Kratos AXIS ULTRA DLD spectrometer equipped with a Theta Probe ARXPS System (Thermo Fisher Scientific, UK). The peak fitting was performed by CasaXPS software. The transmission electron microscopy (TEM) and scanning electron microscopy (SEM) images were collected using a JEOL JEM-2100F (USA) and an SEM JMS-5300LV (USA), respectively. Electrochemical measurements were performed using a CPA-HH5 Computerized Polarography Analyzer (Vietnam). Voltammetric measurements were performed using a glassy carbon electrode (GCE, 2.8 mm diameter) or a ZIF-67/$g$-$C_3N_4$-modified GCE (ZIF-67/$C_3N_4$-GCE) as a working electrode, an Ag/AgCl/3 M KCl as a reference electrode, and a platinum foil auxiliary electrode.

High-performance liquid chromatography (HPLC) was also used to determine the concentration of URA and ACE. The measurements were performed on a Shimadzu 2030 HPLC system with the following parameters: UV-vis detector ($\lambda = 275$ nm) and C18 ($250 \times 4$ mm; 5 $\mu$m) chromatographic column; mobile phase: mixture of phosphate buffer

pH 2.3/acetonitrile (35/65 *v*/*v*); flow rate of 1.5 mL·min$^{-1}$; and injection volume: 5 mL.

*2.3. ZIF-67/g-$C_3N_4$ Preparation.* *g*-$C_3N_4$ was synthesized according to the reference [17]. Briefly, melamine (10 g) was placed into a crucible with a cover under ambient pressure. Then, it was heated to 550°C for 4 h in nitrogen, and a yellow *g*-$C_3N_4$ powder was obtained. $Co(NO_3)\cdot 6H_2O$ (2 mM) and 2-methylimidazole (2 mM) were completely dissolved in ethanol (15 mL) separately. 36 mg *g*-$C_3N_4$ was added into the cobaltous nitrate solution at ambient temperature and treated with ultrasound for 1 hour. Then, the 2-methylimidazole solution was added to the suspension of *g*-$C_3N_4$ and cobalt nitrate. Next, the mixture was placed into a microwave device and irradiated for 15 minutes, resulting in a light purple precipitate (ZIF-67/*g*-$C_3N_4$). Finally, the precipitate was washed with ethanol three times and dried at 80°C in air.

*2.4. Preparation of Electrodes.* A glassy carbon electrode (GCE) (2.8 mm diameter) was polished using 0.05 mm alumina slurry and rinsed thoroughly with distilled water. The electrode was then purified under ultrasonic agitation in ethanol for 5 min. 2 milligrams of ZIF-67/*g*-$C_3N_4$ was dispersed in 1 mL methanol under ultrasonic agitation for 60 min, resulting in a homogeneous purple suspension. 5 $\mu$L of ZIF-67/*g*-$C_3N_4$ suspension was dropped on the electrode surface. Then, the modified electrode was then dried at ambient temperature to obtain a ZIF-67/*g*-$C_3N_4$/GCE.

*2.5. Electrochemical Measurements.* The electrochemical measurements of URA and ACE were performed using cyclic voltammetry (CV) and differential pulse voltammetry (DPV). The DPVs were recorded in the potential range from −100 mV to 600 mV at ambient temperature with the pulse amplitude of 50 mV in all cases.

*2.6. Real Sample Determination.* Three samples of human urine were used to test the method. In detail, 1.0 mL of the urine sample was spiked with URA and ACE and mixed with 1.0 mL of BS buffer solution to produce a 2.0 mL test solution. 150 $\mu$M CTAB was added. The proposed DPV method was applied to the determination of URA and ACE in the spiked solution.

## 3. Results and Discussion

*3.1. Characterization of Materials.* The ZIF-67/*g*-$C_3N_4$ composite was synthesized through mixing *g*-$C_3N_4$ with the Co (II)/imidazole solution in ethanol under the ultrasonic and microwave irradiation. The resulting solids were investigated using XRD analysis (Figure 1(a)). All characteristic peaks of ZIF-67 (Figure 1(a)) are indexed according to the simulated XRD pattern of ZIF-67 from the database (CCDC671073). As for $C_3N_4$ (Figure 1(b)), two characteristic diffraction peaks of the tetragonal phase for *g*-$C_3N_4$ appear at $2\theta = 13.4°$ and 27.5° corresponding to the crystal plane of (100) and (002), respectively, and are indexed according to JCPDS 87-1526 [18]. In the XRD pattern of ZIF-67/*g*-$C_3N_4$ (Figure 1(c)), all the characteristic peaks of *g*-$C_3N_4$ and ZIF-67 are reduced significantly but still clearly observed. During ultrasonic treatment, *g*-$C_3N_4$ could split into the small clusters of *g*-$C_3N_4$, and thus, its crystal structure practically collapses. Therefore, the XRD diffractions of *g*-$C_3N_4$ are not observed in Figure 1(c). The textural properties of *g*-$C_3N_4$, ZIF-67, and the composite were characterized using nitrogen adsorption/desorption isotherms. As represented in Figure 1(d), all the samples illustrate a type IV isotherm with an H3 hysteresis loop according to IUPAC classification. $S_{BET}$ of *g*-$C_3N_4$ is 5 m$^2\cdot$g$^{-1}$, while ZIF-67 exhibits a large $S_{BET}$ of 1,330 m$^2\cdot$g$^{-1}$ due to its highly ordered and uniform structure. It is worth noting that the specific surface area of ZIF-67/*g*-$C_3N_4$ increases significantly ($S_{BET} = 75$ m$^2\cdot$g$^{-1}$) compared with that of pure *g*-$C_3N_4$. The large specific surface area results in the efficient adsorption of analytes during the electrochemical process.

The morphologies of the resulting samples are investigated with SEM and TEM. The TEM image of *g*-$C_3N_4$ (Figure 2(a)) exhibits nanorods with 50 nm diameters, while the morphology of ZIF-67 consists of uniform polyhedrons of 134.2 ± 5.6 nm in size (counted for 140 particles) (Figure 2(b)). It is possible that the bonding of $Co^{2+}$ to N in g-$C_3N_4$ is less strong than that in 2-methylimidazole. Therefore, $Co^{2+}$ cations first coordinate with the nitrogen atoms from g-$C_3N_4$, and while 2-methylimidazole (MI) is added, it reacts with N to form ZIF-67 particles of around 10-20 nm which are highly dispersed on the *g*-$C_3N_4$ matrix as shown in Figure 3(c). The synthesis of ZIF-67 concurrently with *g*-$C_3N_4$ may suppress the growth of ZIF-67 crystals. Consequently, its size is rather small compared with that of ZIF-67 synthesized without *g*-$C_3N_4$.

To determine the chemical composition and the elemental state of ZIF-67/*g*-$C_3N_4$, its XPS was performed (Figure 4). As can be seen in Figure 4(a), the composite mainly consists of C, N, and Co with binding energy at around 285, 400, and 795 eV, respectively. In the N1s core level spectrum (Figure 4(b)), two peaks at 399.03 and 400.9 eV are assigned to the sp$^2$-bonded nitrogen and $\pi$ excitation of *g*-$C_3N_4$, respectively [19, 20]. In the C1s core level spectrum (Figure 4(c)), the four deconvoluted peaks appear at 284.78, 285.36, 287.24, and 288.78 eV. These peaks can be assigned to C–C sp$^2$ (284.78 eV) and C–C sp$^3$ (287.24 eV) in imidazole [21, 22], sp$^2$-bonded carbon (288.78 eV) in aromatic rings of *g*-$C_3N_4$ (N–C=N), and the C–C coordination of the surface adventitious carbon (285.36 eV) [12]. For the Co2p core level spectrum (Figure 4(d)), the duplex of Co2p appears at 779.85 eV for $Co2p_{3/2}$ with a satellite peak at 783.94 eV and at 795.71 eV for $Co2p_{1/2}$ with a satellite peak at 801.14 eV. The main peak-satellite peak separation is narrow at about ~4 and ~5.4 eV for $Co2p_{3/2}$ and $Co2p_{1/2}$, respectively. The difference between the main peaks and the satellites is an important characteristic of the oxidation state of the cobalt ion. A narrow separation of about 4~6 eV (found in our study) is typical for Co (II), whereas a larger difference of about 9~10 eV is often found in Co (III) [23]. Therefore, the Co ions in ZIF-67/*g*-$C_3N_4$ are divalent.

The stability of the electrode modifier in different acidic media is critical for the application in the electrochemical analysis. In the present study, the ZIF-67/*g*-$C_3N_4$ composite

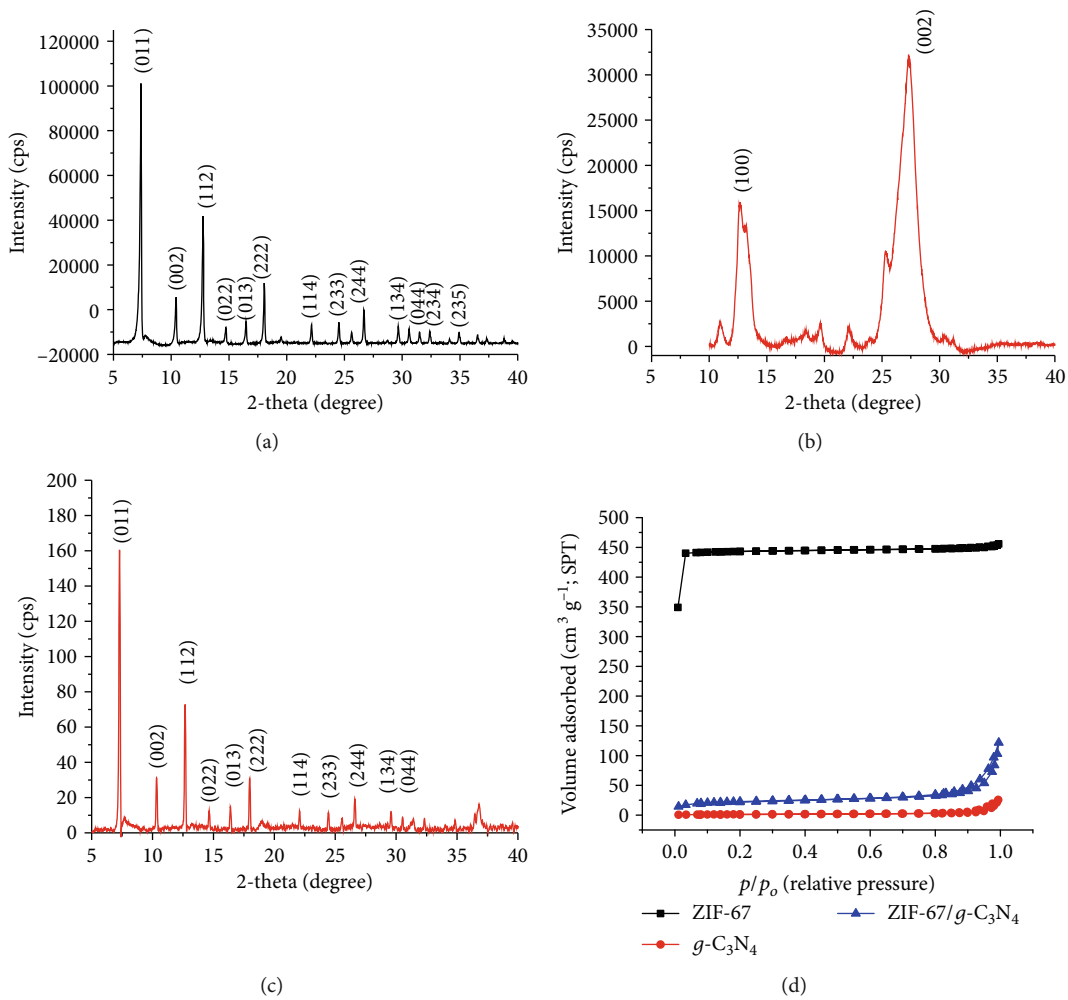


Figure 1: XRD patterns of (a) ZIF-67, (b) $g$-$C_3N_4$, and (c) ZIF-67/$g$-$C_3N_4$ and (d) nitrogen adsorption/desorption isotherms of ZIF-67, $g$-$C_3N_4$, and ZIF-67/$g$-$C_3N_4$.

was immersed in water with pH ranging from 1 to 11 for 10 hours (Figure 5). The stability of the composite was assessed via XRD measurement. At low pH (pH 1), the intensity of diffractions of this sample is reduced or even disappeared compared with the original ZIF-67/$g$-$C_3N_4$, and those of the samples at pH = 3 ÷ 12 seem slightly changeable, indicating that the composite is stable in aqueous solutions in this pH range.

*3.2. Electrochemical Behaviour.* Figure 6(a) represents the CVs at bare GCE, $g$-$C_3N_4$/GCE, ZIF-67/GCE, and ZIF-67-$g$-$C_3N_4$/GCE electrodes. As seen in the figure, the oxidation of URA and ACE occurs at similar potentials, and as a result, these two peaks are overlapped. However, the peaks are resolved significantly at the modified electrodes. The peak-to-peak separation is 0.10 V, 0.07 V, and 0.11 V for $g$-$C_3N_4$/GCE, ZIF-67/GCE, and ZIF-67/$g$-$C_3N_4$/GCE, respectively. The intensity of the oxidation peak for URA and ACE at ZIF-67/$g$-$C_3N_4$-GCE is 3.06 and 3.11 times as high as that at $g$-$C_3N_4$/GCE and 2.21 and 2.35 times as high as that at ZIF-67/GCE. These figures reveal that ZIF-67-$g$/$C_3N_4$ significantly promotes the electron transfer and, thus, oxidation of URA and ACE.

The peak current depends on the ZIF-67/$g$-$C_3N_4$ amount modified on the electrode surface (Figure 6(b)). ZIF-67/$g$-$C_3N_4$ enhances analyte adsorption. As a result, the peak current increases and reaches the maximum at the volume of the suspension of around 4 $\mu$L. Further increase of ZIF-67/$g$-$C_3N_4$ leads to a decrease in peak current because a thicker layer of adsorbed ZIF-67/$g$-$C_3N_4$ could reduce the electrical conductivity.

*3.2.1. Effect of CTAB.* The effects of CTAB concentration on the peak-to-peak separation of URA and ACE were performed by recording CVs of a series of solutions containing $C_{URA} = C_{ACE} = 0.5$ mM and various concentrations of CTAB (Figure 7(a)). As can be seen from Figure 7(b), the peak-to-peak separation ($\Delta E$) increases with CTAB concentration and peaks at 150 $\mu$M CTAB ($\Delta E = 0.18$ V). Further increasing CTAB concentration leads to a slight reduction of $\Delta E$. It is worth noting that the oxidation potential of ACE at 0.25 V seems to be constant, while the oxidation potential

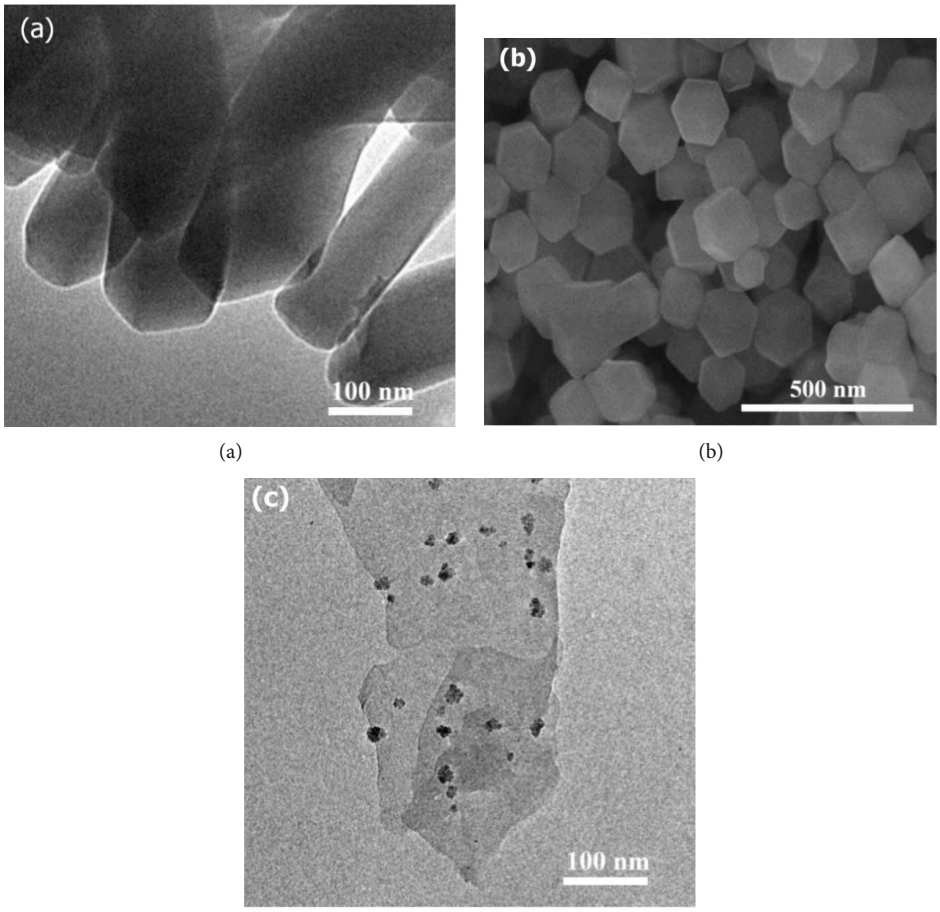


(a) (b)

(c)

Figure 2: (a) TEM of $g$-$C_3N_4$; (b) SEM of ZIF-67; (c) TEM of ZIF-67/$g$-$C_3N_4$.

of URA shifts to less positive values with increasing CTAB concentration. The possible reason would be that CTAB molecules aggregate on the surface of the modified electrode to form micelles for discriminating ACE from URA. The concentration of 150 $\mu$M for CTAB is suitable for further experiments.

*3.2.2. Effect of pH.* The CV curves at ZIF-67/$g$-$C_3N_4$-GCE were measured in the pH range from 7 to 10 (Figure 3(a)). The peak potential, $E_p$, reduces as pH increases, indicating that protons are involved in the redox processes (Figure 3(b)). The peak current, $I_p$, increases with pH and peaks at pH = 9. Further increase in pH causes a negligible change in the peak current (Figure 3(c)).

The anodic peak potential corresponds well to pH ranging from 7 to 10 with high correlation coefficients ($r = 0.985$ and 0.999) (Equations (1) and (2)):

$$E_{p,URA} = (0.34 \pm 0.03) + (-0.030 \pm 0.004) \times \text{pH}, r = 0.985, \quad (1)$$

$$E_{p,ACE} = (0.74 \pm 0.01) + (-0.056 \pm 0,001) \times \text{pH}, r = 0.999. \quad (2)$$

The slope of the oxidation peak potential of ACE vs. pH is 0.056 V/pH, which is very close to the theoretical value of 0.059 V/pH, corresponding to the equal number of protons and electrons in the redox process. The electrochemical oxidation of URA proceeding by a 2e/2 proton mechanism to yield a diimine is nowadays well established. Meanwhile, the value of 0.030 V/pH deviates significantly from the theoretical value of 0.0599 V/pH and is about its half, indicating that the electrode process is more complex in the studied pH and the number of transferred electrons may be twice as much as that of protons.

*3.2.3. Effect of Scan Rate.* Important information about the electrochemical mechanism can be derived from the relationship between the voltammetric signals ($E_p$ and $I_p$) and the scan rate (denoted as $v$). In the present study, the $E_p$ and $I_p$ dependence on the scan rate was investigated by using CVs (Figure 8(a)). If the electrooxidation reaction is reversible, $E_p$ is independent on $v$ and vice versa. As can be seen from Figure 8(a), the peak potential increases with the scan rate. Therefore, the electron transfer in the URA and ACE electrooxidation is irreversible [24].

The linear plots of $I_p$ vs. the square root of the scan rate ($v^{1/2}$) were established to assess whether the electrooxidation

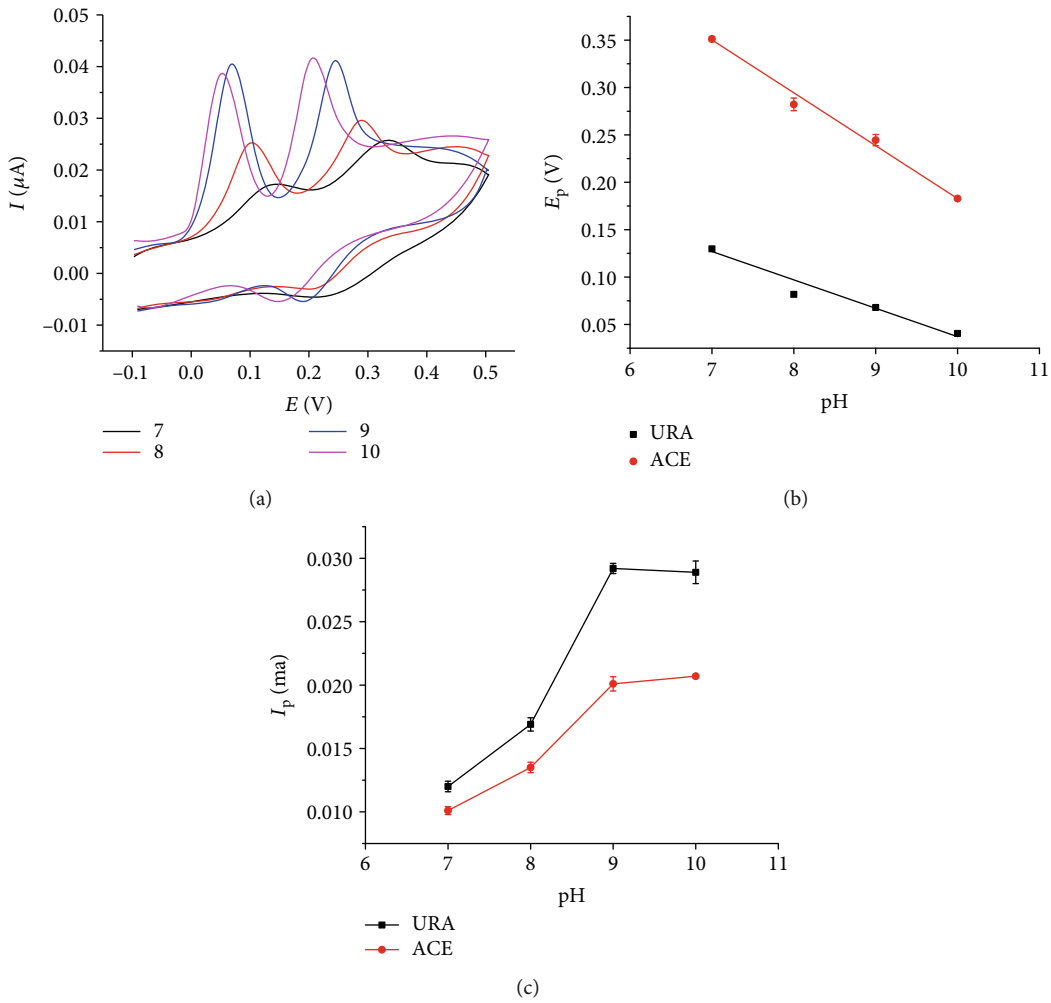


Figure 3: (a) CVs recording at ZIF-67/$C_3N_4$-GCE in 0.1 M BR-BS pH = 7 ÷ 10 containing equal concentrations of 0.5 mM URA, ACE, and 150 $\mu$M CTAB; (b) the plot of $E_p$ vs. pH; (c) the plot of $I_p$ vs. pH.

reaction is an adsorption-controlled or diffusion-controlled process (Figure 8(b)). If the linear plot of $I_p$ vs. $v^{1/2}$ passes the origin, this process is controlled by diffusion; otherwise, it is an adsorption-controlled process [24]. The linear regression equations of $I_p$ vs. $v^{1/2}$ are expressed as follows:

$$\begin{aligned} I_{p,URA} &= (-0.160 \pm 0.033) + (0.100 \pm 0.006) \times v^{1/2}, \\ &\quad r = 0.995, p < 0.001, \\ I_{p,ACE} &= (-0.023 \pm 0.019) + (0.091 \pm 0.011) \times v^{1/2}, \\ &\quad r = 0.979, p = 0.004. \end{aligned} \tag{3}$$

The linear relation of $I_{p,URA}$ and $I_{p,ACE}$ vs. $v^{1/2}$ is statistically significant ($r = 0.997 \div 0.999$, $p < 0.05$). The number in the parentheses represents the 95% confidence interval. The intercepts do not pass the origin because the 95% confidence interval for the intercept does not contain 0 (varying from −0.041 to −0.004 for ACE and from −0.072 to −0.006 for URA). This indicates that the electrode process of the URA and ACE electrooxidation is controlled by adsorption.

The linear regression equations of $E_p$ vs. ln $v$ are as follows:

$$\begin{aligned} E_{p,URA} &= 0.112 + 0.026 \times \ln v, r = 0.984, \\ E_{p,ACE} &= 0.290 + 0.027 \times \ln v, r = 0.984. \end{aligned} \tag{4}$$

According to the Laviron theory [25], the relation of $E_p$ vs. ln $v$ can be expressed as Equation (5) in an irreversible system:

$$E_p = E^0 - \frac{RT}{(1-\alpha)nF} \ln \frac{RTK_s}{(1-\alpha)nF} + \frac{RT}{(1-\alpha)nF} \ln v, \tag{5}$$

where $\alpha$ is the electron transfer coefficient, $R$ is the universal constant (8.314 J/mol·K) at 298 K, and $F$ is the Faraday constant (96,500 C·mol$^{-1}$). The slope of the line of $E_p$ vs. ln $v$ provides the value of $(1-\alpha) \times n$ for ACE and URA being 0.95 and 0.99, respectively (Figure 8(c)). It is assumed that the value of $\alpha$ is 0.5. Then, the value of $n$ is 1.9 for ACE and 1.98 for URA. Therefore, the equal number of electrons

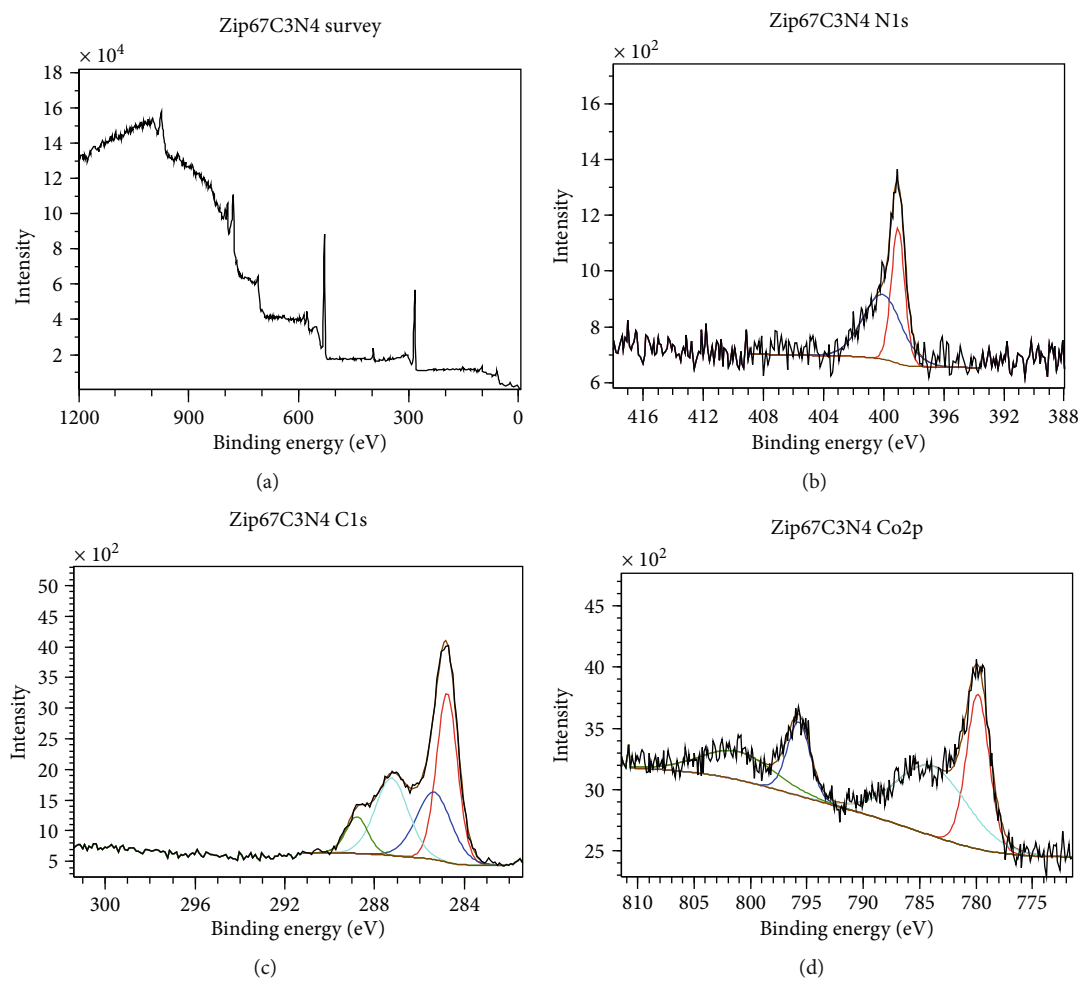


Figure 4: XPS spectra of ZIF-67/$g$-$C_3N_4$: (a) survey spectrum; (b) N1s XPS spectrum; (c) C1s XPS spectrum; (d) Co2p XPS spectrum.

transferred is 2 for ACE. This means that two electrons and two protons are involved in the ACE oxidation to form N-acetyl-p-quinone-imine [26] at the modified electrodes. In the case of URA, the ratio of the number of protons and transferred electrons is not equal to one and involves less protons than electrons, e.g., two electrons and one proton. Although the mechanism of URA at the modified electrode is nuclear, this could be explained as the inference due to uncertainties introduced by the close proximity of voltammetric peak to the background discharge probably due to oxidation undergoing deprotonation or the adsorption of oxidation products blocking the electrode at the studied pH.

The favorable signal-promoting effect indicates that CTAB enhances the discriminating peak current of ACE and URA. In this aspect, ZIF-67/$g$-$C_3N_4$ plays an important role in promoting the electron transfer rates of ACE and URA and brings out excellent electrocatalytic activity towards the *redox* reactions. Because ZIF-67 comprises imidazole rings of the $sp^2$-conjugated bond ($\pi$–$\pi$ interaction), the $\pi$–$\pi$ stacking interaction between the phenyl structures of URA and ACE and the three-dimensional imidazolate structure of ZIF-67/$g$-$C_3N_4$ favors the adsorption on the modified electrode surface. The coordination of the nitrogen atoms in the analytes with Co (II) ions attracts ACE and URA to the modified electrode surface. In addition, $g$-$C_3N_4$ facilitates electron mobility in the redox reaction. In addition, the CTAB as a discriminating agent is also contributed to the well-defined separation of electrochemical signals. Therefore, the combination of these effects promotes the transfer of electrons and results in enhancing voltammetric signals. The oxidation mechanism for ACE and URA at the modified electrodes is proposed in Figure 9.

*3.3. Interference Study.* Interferents commonly existent in biological samples include glucose, sucrose, oxalate, $CaCl_2$, $(NH_4)_2SO_4$, $NaNO_3$, $KHCO_3$, and $K_2SO_4$. Table 1 presents the tolerance limits of eight interferents. The tolerance limit, $C_{tol}$, is the concentration of the interferent that raises a relative error (RE) of 5% in the determination of 0.5 $\mu$M URA or 0.5 $\mu$M ACE. The findings show that the interference of inorganic salts is insignificant. However, some organic compounds, such as glucose, interfere but only at high concentrations. This indicates that the proposed method is likely to be free from common interferents in biological samples.

*3.4. Long-Term Stability, Repeatability, and Linear Range.* The long-term stability of the electrochemical response is of special interest for automatic monitoring of biological

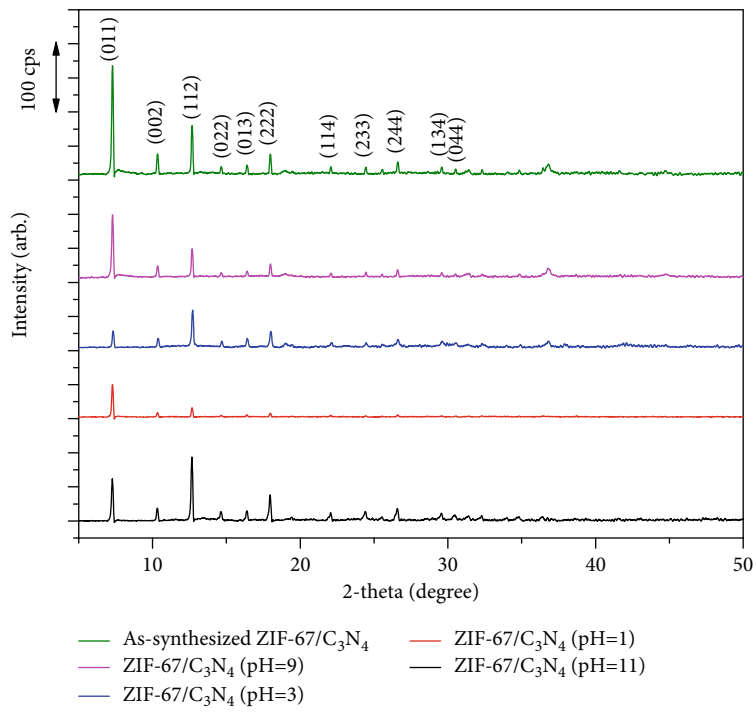


Figure 5: The stability of ZIF-67/$g$-$C_3N_4$ in water with different pH.

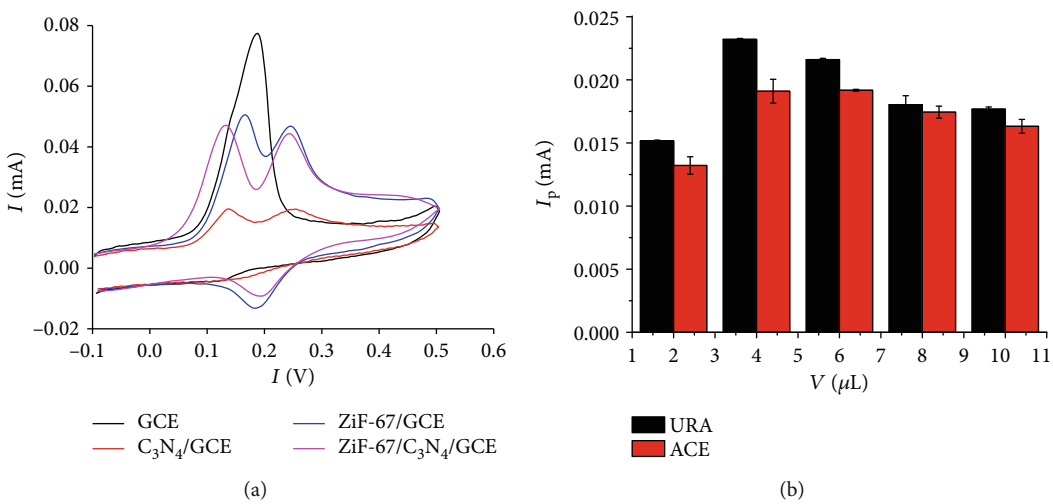


Figure 6: (a) CVs at different electrodes in 0.1 M BR-BS pH 9 containing equal concentrations of 0.5 mM URA and ACE; (b) effect of ZIF-67/$g$-$C_3N_4$ amount on anodic peak current.

analytes. Hence, the response of ZIF-67/g-$C_3N_4$ was performed for a ten-day period by immersing the electrode in a solution of spiked water with 0.1 M BR-BS pH 9 containing 150 $\mu$M CTAB, 0.2 $\mu$M URA, and 0.2 $\mu$M ACE (10 measurements were performed during the working-day period). The electrode was stored in the buffer solution between each analysis. The changes of average $I_p$ versus time are presented in Figure 10. The RSDs (relative standard deviations) of $I_p$ for URA and ACE were 7.72 and 7.02%, respectively, using the same electrode for all the measurements. These values were lower than $1/2RSD_H$ [27] indicating that the proposed DP-ASV method exhibits high stability.

The repeatability of the DP-ASV responses was evaluated by using a RSD for nine consecutive determinations of $5 \times 10^{-7}$ M URA and $5 \times 10^{-7}$ M ACE. The RSD of URA and ACE is 1.03 and 1.52, which is lower than $1/2RSD_{Hozit}$, indicating that the modified electrode shows good stability. The stability of the ZIF-67/$g$-$C_3N_4$-modified electrode was also tested by leaving the electrode in a desiccator under atmospheric conditions for 10 days. The DP-ASV peak currents

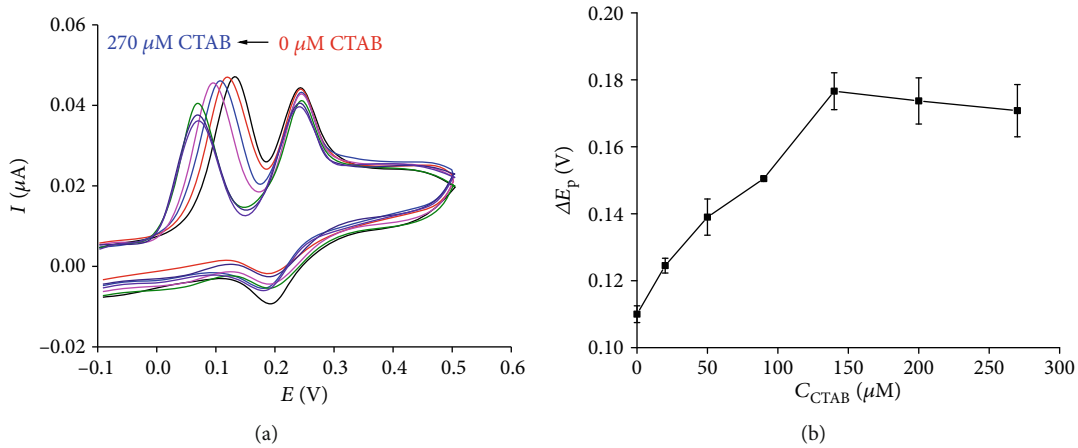


Figure 7: (a) CVs at ZIF-67/$g$-$C_3N_4$/GCE in 0.1 M BR-BS containing $C_{URA} = C_{ACE} = 0.5$ mM and various concentrations of CTAB; (b) peak-to-peak separation as a function of CTAB concentration.

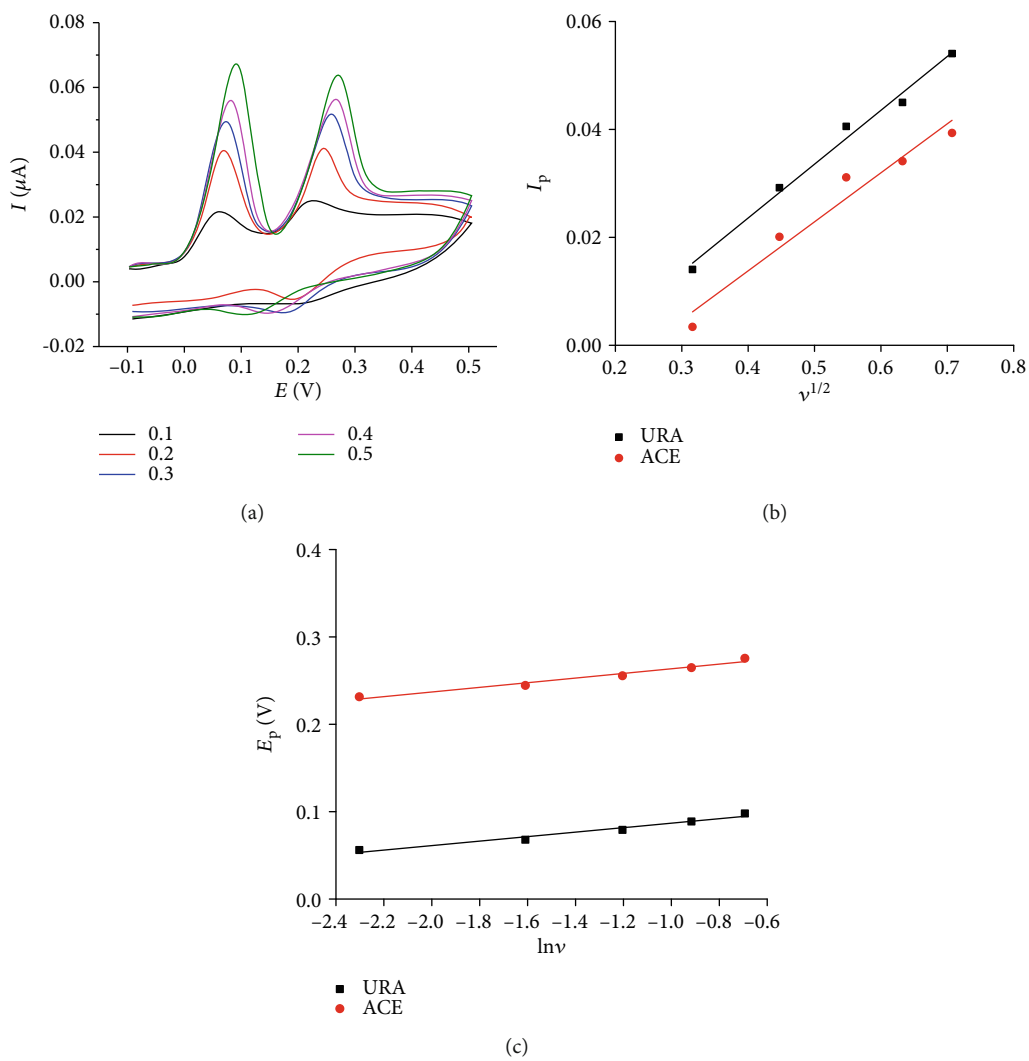


Figure 8: Scan rate dependence of peak potential and peak current (a); the linear plots of $I_p$ vs. $\nu^{1/2}$ (b); $E_p$ vs. ln $\nu$ (c); $C_{CTAB} = 150 \times 10^{-6}$ M and $C_{URA} = C_{ACE} = 0.5 \times 10^{-3}$ M in BR-BS buffer 0.1 M, pH 9.

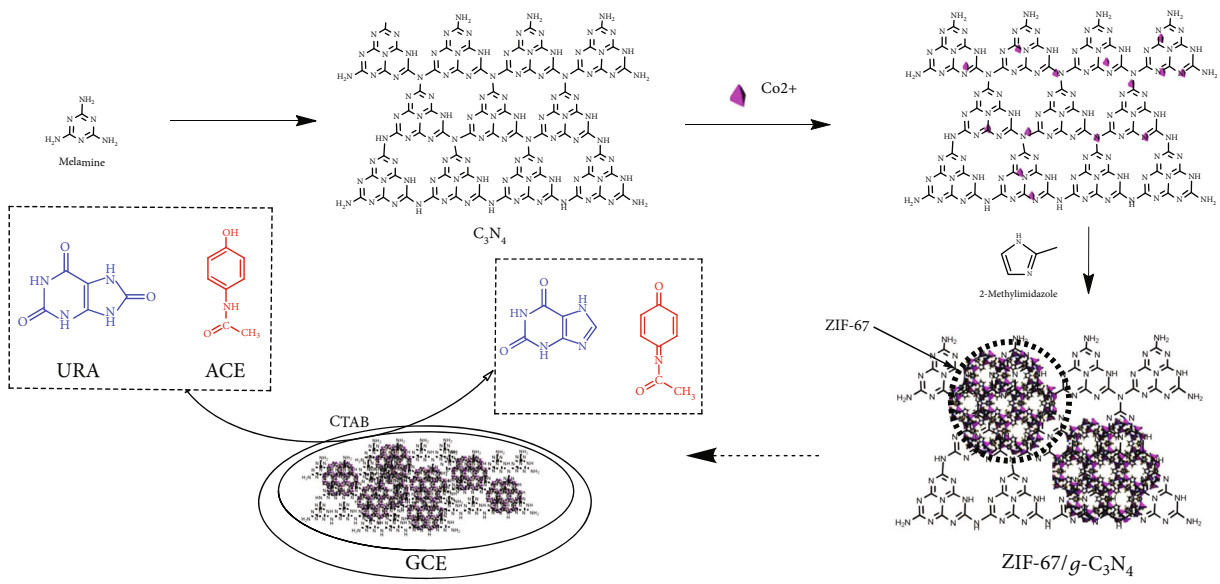


Figure 9: Proposed mechanism of URA and ACE oxidation at the ZIF-67/$g$-$C_3N_4$-modified electrode.

Table 1: Tolerance limits of interferents, $C_{tot}$ ($5{\cdot}10^{-7}$ M URA or $5{\cdot}10^{-7}$ M URA in 0.1 M BR-BS pH 9 and 150 $\mu$M CTAB).

| Interfering substances | $C_{tot}$ ($\mu$M) URA (0.5 $\mu$M) | RE (%) | ACE (0.5 $\mu$M) | RE (%) |
|---|---|---|---|---|
| Glucose | 75 | −4.55 | 75 | 4.9 |
| Sucrose | 75 | −4.30 | 75 | 4.99 |
| Oxalate | 75 | −4.79 | 150 | 4.85 |
| $NaNO_3$ | 150 | −4.92 | 150 | 4.86 |
| $CaCl_2$ | 100 | 2.49 | 100 | −3.40 |
| $K_2SO_4$ | 150 | 4.2 | 150 | −3.1 |
| $(NH_4)_2SO_4$ | 100 | −3.26 | 100 | 4.38 |
| $KHCO_3$ | 150 | −4.32 | 150 | 3.19 |

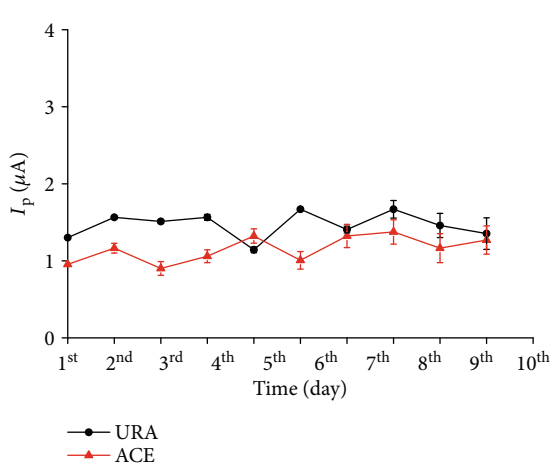


Figure 10: Long-term stability test for a ten-day period.

for $5 \times 10^{-7}$ M URA and $5 \times 10^{-7}$ M ACE decrease by less than 4.61 and 4.90%, respectively. The high stability of the ZIF-67/$g$-$C_3N_4$-modified electrode contributed to its high mechanical strength and high stability in water, making it a potential for practical applications.

The detection of each compound in the presence of the other was conducted. Figure 11(a) shows the DPV curves recorded when adding URA or ACE and keeping the other constant. The anodic peak current increases linearly ($I_{p,URA} = 0.09 + 5.69C_{URA}$, $r = 0.995$) with the concentration of URA from 0.02 to 0.65 $\mu$M in the presence of ACE with the limit detection (LOD) of 0.055 $\mu$M (Figure 11(b)). A similar behaviour is observed with the detection of ACE ($I_{p,ACE} = 0.15 + 5.63C_{ACE}$, $r = 0.997$) in the same concentration range with the detection limit of 0.056 $\mu$M (Figures 11(c) and 11(d)). Figure 12(a) represents the DP-DVS curves recorded for the simultaneous addition of URA and ACE in the concentration range between 0.02 and 0.65 $\mu$M. The plots of $I_{p,URA}$ and $I_{p,ACE}$ vs. the URA and ACE concentrations are shown in Figure 12(b). The linear regression equations are $I_{p,URA} = 0.06 + 5.81C_{URA}$, $r = 0.998$, and $I_{p,ACE} = 0.14 + 5.84 C_{ACE}$, $r = 0.999$. The LODs of URA and ACE are 0.052 $\mu$M and 0.053 $\mu$M, respectively. The similarity in LOD of URA and ACE in the mixture and as an individual infers that no remarkable interference due to the oxidation of the compounds occurs.

The linear regression equations of the peak current vs. the analyte concentration are expressed as follows:

$$I_{p,URA} = (0.06 \pm 0.05) + (5.82 \pm 0.03) \times C_{URA}, r = 0.998,$$
$$I_{p,ACE} = (0.14 \pm 0.04) + (5.84 \pm 0.11) \times C_{ACE}, r = 0.999. \quad (6)$$

In the range from 0.02 to 0.65 $\mu$M for URA and ACE, the LODs of URA and ACE are 0.052 $\mu$M and 0.053 $\mu$M,

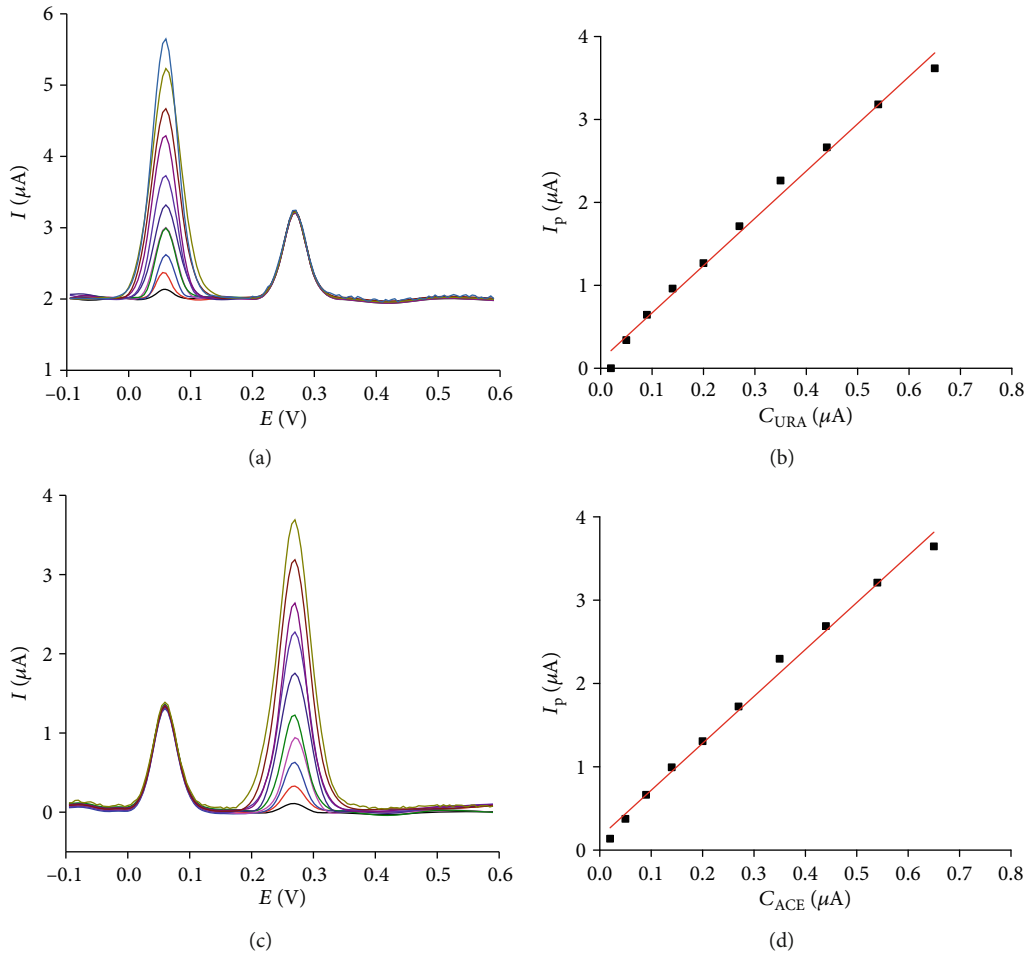


Figure 11: Differential pulse voltammetric responses at ZIF-67/$g$-$C_3N_4$-GCE in 0.1 M BR-BS pH 9 containing (a) 150 $\mu$M CTAB and 0.2 $\mu$M ACE; the URA concentration varying from 0.02 to 0.65 $\mu$M; (b) plot of anodic peak current as a function of URA concentration; (c) 150 $\mu$M CTAB, 0.2 $\mu$M URA; the ACE concentration varying from 0.02 to 0.65 $\mu$M; (d) plot of anodic peak current as a function of ACE concentration.

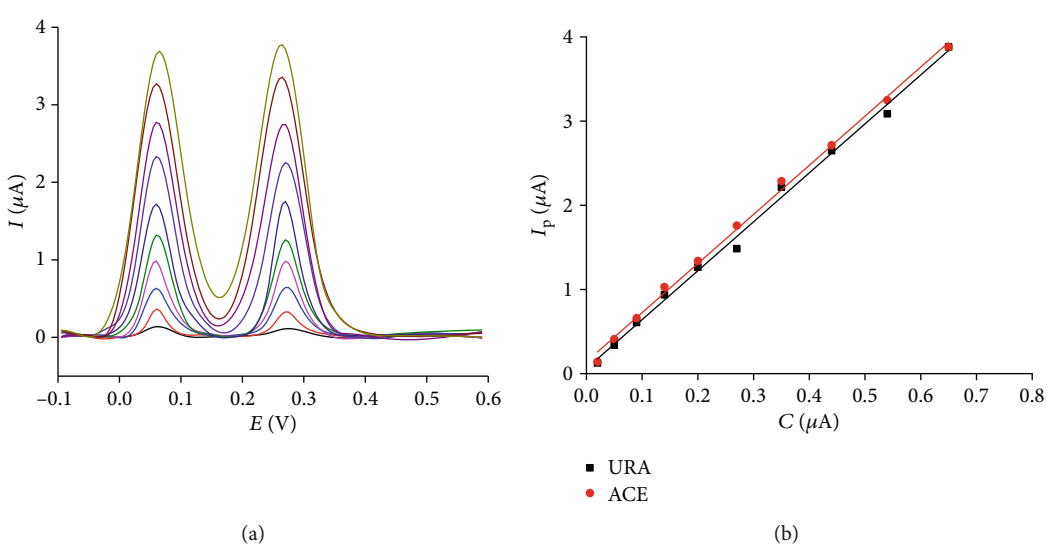


Figure 12: (a) DPVs recorded at ZIF-67/$g$-$C_3N_4$/GCE in 0.2 BR-BS pH 9 containing equal concentrations varying from 0.2 to 6.5 $\mu$M; (b) plot of anodic peak current as a function of analyte concentration.

Table 2: Comparison of some LOD and linear range of different modified electrodes for the determination of URA and ACE.

| Electrode | Linear range ($\mu$M) (URA/ACE) | LOD ($\mu$M) URA | LOD ($\mu$M) ACE | Reference |
|---|---|---|---|---|
| Ionic liquid/CNT/chitosan-CGE | (2–450)/(1–400) | 0.34 | 0.24 | [28] |
| Thiol functional ferrocene derivative stabilized Au NP/carbon dot nanocomposite coupling with graphene-GCE | (0.6–9.2)/(0.5–46) | 0.2 | 0.1 | [29] |
| SWCNT/chitosan/ionic liquid nanocomposite-GCE | (3–320)/(2–200) | 0.27 | 0.11 | [30] |
| MCNT/chitosan composite-GCE | (10–400)/(2–250) | 0.4 | 0.16 | [31] |
| ZIF-67/$g$-$C_3N_4$-GCE | **(0.2–6.5)/(0.2–6.5)** | **0.052** | **0.053** | **The present study** |

Notes: MCNT: multiwalled carbon nanotube; SWCNT: single-walled carbon nanotube; GCE: glassy carbon electrode.

Table 3: URA and ACE detection in urine samples obtained using the proposed method and HPLC.

| Sample | Analytes | Added ($\mu$M) | Found[a] ($\mu$M) | Rev. (%) | HPLC ($\mu$M) |
|---|---|---|---|---|---|
| Urine #1 | URA | 0 | 22.69 | 99.4 | —[a] |
| | | 10 | 32.63 | | 32.77 |
| | ACE | 0 | 0 | 96.7 | — |
| | | 10 | 9.67 | | 9.81 |
| Urine #2 | URA | 0 | 26.11 | 97.8 | — |
| | | 10 | 35.89 | | 35.92 |
| | ACE | 0 | 0 | 98.0 | — |
| | | 10 | 9.80 | | 9.85 |
| Urine #3 | URA | 0 | 25.03 | 96.9 | — |
| | | 10 | 34.72 | | 34.81 |
| | ACE | 0 | 0 | 104.0 | — |
| | | 10 | 10.4 | | 9.80 |

[a]No analysis.

respectively. Table 2 shows the ability of the ZIF-67/$g$-$C_3N_4$ electrode for the URA and ACE determination compared with other reported electrodes. The present electrode has a much lower limit of detection for the determination of URA and ACE in comparison with most modified materials.

The ZIF-67/$g$-$C_3N_4$-modified electrode was utilized in the real sample analysis. Urine samples were collected from three healthy volunteers. The DPV results of the urine samples were obtained for URA and ACE in the BS solution, to which 10 $\mu$L of a URA and ACE stock solution was spiked to an electrochemical cell without any preliminary pretreatment. The amount of URA and ACE in the samples was determined with the calibration method using DPV and is presented in Table 3. The recovery of the proposed method varies in the acceptable range of 90–110%. The URA and ACE level in the samples was also tested using HPLC for comparison. The paired-sample $t$-test with $\alpha = 0.05$ shows that there is no significant difference between the DPV proposed method and HPLC ($t(5) = 0.215$; $p = 0.839$). This suggests that the proposed method enables to determine the URA and ACE level in the human urine with satisfactory results.

## 4. Conclusions

ZIF-67/$g$-$C_3N_4$ was synthesized using the ultrasonic-assisted approach. The obtained material exhibits a large specific surface area and high stability in pH ranging of 3 to 12. The ZIF-67/$g$-$C_3N_4$ electrode shows high stability and reproducibility in repetitive measurements. The proposed method provides satisfactory results for the detection of uric acid and acetaminophen in human urine. The method is time-competitive, easy to perform, highly stable, and sensitive with high detectability. All these features suggest that the proposed method is a potential candidate for practical applications.

## Data Availability

The data used to support the findings of this study are available from the corresponding authors upon request.

## Conflicts of Interest

The authors declare that they have no conflicts of interest.

## Acknowledgments

This research is funded by Vietnam National Foundation for Science and Technology Development (NAFOSTED) under grant number 104.06-2018.15.

## References

[1] J. M. Zen, J. J. Jou, and G. Ilangovan, "Selective voltammetric method for uric acid detection using pre-anodized Nafion-coated glassy carbon electrodes," *Analyst*, vol. 123, no. 6, pp. 1345–1350, 1998.

[2] R. M. De Carvalho, R. S. Freire, S. Rath, and L. T. Kubota, "Effects of EDTA on signal stability during electrochemical detection of acetaminophen," *Journal of Pharmaceutical and Biomedical Analysis*, vol. 34, no. 5, pp. 871–878, 2004.

[3] F. L. Martin and A. E. M. McLean, "Comparison of paracetamol-induced hepatotoxicity in the rat in vivo with progression of cell injury in vitro in rat liver slices," *Drug and Chemical Toxicology*, vol. 21, no. 4, pp. 477–494, 1998.

[4] N. H. Phong, T. T. T. Toan, M. X. Tinh, T. N. Tuyen, T. X. Mau, and D. Q. Khieu, "Simultaneous voltammetric determination of ascorbic acid, paracetamol, and caffeine using electrochemically reduced graphene-oxide-modified electrode,"

*Journal of Nanomaterials*, vol. 2018, Article ID 5348016, 15 pages, 2018.

[5] A. Kutluay and M. Aslanoglu, "An electrochemical sensor prepared by sonochemical one-pot synthesis of multi-walled carbon nanotube-supported cobalt nanoparticles for the simultaneous determination of paracetamol and dopamine," *Analytica Chimica Acta*, vol. 839, pp. 59–66, 2014.

[6] J. F. Rusling, "Controlling electrochemical catalysis with surfactant microstructures," *Accounts of Chemical Research*, vol. 24, no. 3, pp. 75–81, 1991.

[7] R. Vittal, H. Gomathi, and K. J. Kim, "Beneficial role of surfactants in electrochemistry and in the modification of electrodes," *Advances in Colloid and Interface Science*, vol. 119, no. 1, pp. 55–68, 2006.

[8] G. Alarcón-Angeles, S. Corona-Avendaño, M. Palomar-Pardavé, A. Rojas-Hernández, M. Romero-Romo, and M. T. Ramírez-Silva, "Selective electrochemical determination of dopamine in the presence of ascorbic acid using sodium dodecyl sulfate micelles as masking agent," *Electrochimica Acta*, vol. 53, no. 6, pp. 3013–3020, 2008.

[9] S. Q. Liu, W. H. Sun, and F. T. Hu, "Graphene nano sheet-fabricated electrochemical sensor for the determination of dopamine in the presence of ascorbic acid using cetyltrimethylammonium bromide as the discriminating agent," *Sensors and Actuators B: Chemical*, vol. 173, pp. 497–504, 2012.

[10] Y. Hou, J. Li, Z. Wen, S. Cui, C. Yuan, and J. Chen, "N-doped graphene/porous g-$C_3N_4$ nanosheets supported layered-$MoS_2$ hybrid as robust anode materials for lithium-ion batteries," *Nano Energy*, vol. 8, pp. 157–164, 2014.

[11] Z. Meng, Y. Xie, T. Cai, Z. Sun, K. Jiang, and W. Q. Han, "Graphene-like g-$C_3N_4$ nanosheets/sulfur as cathode for lithium-sulfur battery," *Electrochimica Acta*, vol. 210, pp. 829–836, 2016.

[12] L. Tan, J. Xu, X. Zhang, Z. Hang, Y. Jia, and S. Wang, "Synthesis of g-$C_3N_4$/$CeO_2$ nanocomposites with improved catalytic activity on the thermal decomposition of ammonium perchlorate," *Applied Surface Science*, vol. 356, pp. 447–453, 2015.

[13] G. Lu and J. T. Hupp, "Metal-organic frameworks as sensors: a ZIF-8 based Fabry-Pérot device as a selective sensor for chemical vapors and gases," *Journal of the American Chemical Society*, vol. 132, no. 23, pp. 7832-7833, 2010.

[14] L. Yang, L. Yu, M. Sun, and C. Gao, "Zeolitic imidazole framework-67 as an efficient heterogeneous catalyst for the synthesis of ethyl methyl carbonate," *Catalysis Communications*, vol. 54, pp. 86–90, 2014.

[15] P. M. Usov, C. McDonnell-Worth, F. Zhou, D. R. MacFarlane, and D. M. D'Alessandro, "The electrochemical transformation of the zeolitic imidazolate framework ZIF-67 in aqueous electrolytes," *Electrochimica Acta*, vol. 153, pp. 433–438, 2015.

[16] Y. Meng, L. Zhang, H. Jiu et al., "Construction of g-$C_3N_4$/ZIF-67 photocatalyst with enhanced photocatalytic $CO_2$ reduction activity," *Materials Science in Semiconductor Processing*, vol. 95, pp. 35–41, 2019.

[17] N. Tian, H. Huang, and Y. Zhang, "Mixed-calcination synthesis of $CdWO_4$/g-$C_3N_4$ heterojunction with enhanced visible-light-driven photocatalytic activity," *Applied Surface Science*, vol. 358, pp. 343–349, 2015.

[18] Y. He, J. Cai, T. Li et al., "Efficient degradation of RhB over $GdVO_4$/g-$C_3N_4$ composites under visible-light irradiation," *Chemical Engineering Journal*, vol. 215-216, pp. 721–730, 2013.

[19] M. Tahir, C. Cao, N. Mahmood et al., "Multifunctional g-C3N4Nanofibers: a template-free fabrication and enhanced optical, electrochemical, and photocatalyst properties," *ACS Applied Materials & Interfaces*, vol. 6, no. 2, pp. 1258–1265, 2014.

[20] Q. Xu, C. Jiang, B. Cheng, and J. Yu, "Enhanced visible-light photocatalytic $H_2$-generation activity of carbon/g-$C_3N_4$ nanocomposites prepared by two-step thermal treatment," *Dalton Transactions*, vol. 46, no. 32, pp. 10611–10619, 2017.

[21] Y. Zheng, Y. Jiao, Y. Zhu et al., "Hydrogen evolution by a metal-free electrocatalyst," *Nature Communications*, vol. 5, no. 1, pp. 1–8, 2014.

[22] X. Yan, L. Tian, M. He, and X. Chen, "Three-dimensional crystalline/amorphous Co/$Co_3O_4$ core/shell nanosheets as efficient electrocatalysts for the hydrogen evolution reaction," *Nano Letters*, vol. 15, no. 9, pp. 6015–6021, 2015.

[23] D. Barreca, C. Massignan, S. Daolio et al., "Composition and microstructure of cobalt oxide thin films obtained from a novel cobalt (II) precursor by chemical vapor deposition," *Chemistry of Materials*, vol. 13, no. 2, pp. 588–593, 2001.

[24] A. J. Bard and L. J. Falkner, *Electrochemical Methods: Fundamentals and Applications*, vol. 60, Wiley, New York, NY, USA, 2001.

[25] E. Laviron, "General expression of the linear potential sweep voltammogram in the case of diffusionless electrochemical systems," *Journal of Electroanalytical Chemistry*, vol. 101, no. 1, pp. 19–28, 1979.

[26] S. A. Kumar, C. F. Tang, and S. M. Chen, "Electroanalytical determination of acetaminophen using nano-$TiO_2$/polymer coated electrode in the presence of dopamine," *Talanta*, vol. 76, no. 5, pp. 997–1005, 2008.

[27] W. Horwitz and R. Albert, "The concept of uncertainty as applied to chemical measurements," *Analyst*, vol. 122, no. 6, pp. 615–617, 1997.

[28] S. Kianipour and A. Asghari, "Room temperature ionic liquid/multiwalled carbon nanotube/chitosan-modified glassy carbon electrode as a sensor for simultaneous determination of ascorbic acid, uric acid, acetaminophen, and mefenamic acid," *IEEE Sensors Journal*, vol. 13, no. 7, pp. 2690–2698, 2013.

[29] L. Yang, N. Huang, Q. Lu et al., "A quadruplet electrochemical platform for ultrasensitive and simultaneous detection of ascorbic acid, dopamine, uric acid and acetaminophen based on a ferrocene derivative functional Au NPs/carbon dots nanocomposite and graphene," *Analytica Chimica Acta*, vol. 903, pp. 69–80, 2016.

[30] M. Afrasiabi, S. Kianipour, A. Babaei, A. A. Nasimi, and M. Shabanian, "A new sensor based on glassy carbon electrode modified with nanocomposite for simultaneous determination of acetaminophen, ascorbic acid and uric acid," *Journal of Saudi Chemical Society*, vol. 20, pp. S480–S487, 2016.

[31] A. Babaei, D. J. Garrett, and A. J. Downard, "Selective simultaneous determination of paracetamol and uric acid using a glassy carbon electrode modified with multiwalled carbon nanotube/chitosan composite," *Electroanalysis*, vol. 23, no. 2, pp. 417–423, 2011.

Hindawi
Journal of Nanomaterials
Volume 2019, Article ID 9151979, 9 pages
https://doi.org/10.1155/2019/9151979

*Research Article*

# Preparation of $Ga_{0.25}Zn_{4.67}S_{5.08}$ Microsphere by Ultrasonic Spray Pyrolysis and Its Photocatalytic Disinfection Performance under Visible Light

**Tuo Yan**,[1,2] **Jianhui Huang**,[2,3] **Jinhong Bi**,[1] **Liyan Xie**,[2,4] **and Huimin Huang**[1]

[1]*College of Environment & Resources, Fuzhou University, Fuzhou 350108, China*
[2]*College of Environmental & Biological Engineering, Putian University, Putian 351100, China*
[3]*Fujian Provincial Key Laboratory of Ecology-Toxicological Effects & Control for Emerging Contaminants, Putian 351100, China*
[4]*Key Laboratory of Ecological Environment and Information Atlas, Fujian Provincial University, Putian 351100, China*

Correspondence should be addressed to Jianhui Huang; owenhuang95@163.com

Received 2 September 2019; Accepted 2 December 2019; Published 23 December 2019

Academic Editor: Sesha Srinivasan



The $Ga_{0.25}Zn_{4.67}S_{5.08}$ catalysts were prepared by ultrasonic spray pyrolysis with thiourea as a precursor. The crystal structure, optical properties, specific surface area, chemical composition, surface morphology, and internal structure of the prepared samples were characterized by XRD, UV-Vis DRS, BET, XPS, SEM, and TEM, respectively. The disinfection performance and the main active species of the synthesized catalysts under visible light irradiation were investigated with *E. coli* K12. The study results indicate that $Ga_{0.25}Zn_{4.67}S_{5.08}$ prepared at 400°C exhibited the best antibacterial performance with complete kill of *E. coli* K12 within 4 h. The antibacterial performance of the prepared sample is also higher than that prepared by the hydrothermal method. The result of the radical trapping experiment indicates that the photogenerated holes play a dominant role in the disinfection process.

## 1. Introduction

Various pathogenic bacteria living in waters have always been the greatest threat to human health. The statistic data show that millions of people were disabled or die because of bacteria every year [1]. Traditional sterilization techniques include chemical sterilization and ultraviolet (UV) disinfection. Among them, the chemical disinfection method uses strong oxidants such as liquid chlorine, sodium hypochlorite, chloramine, chlorine dioxide, or ozone, which has an efficient sterilization effect and effectively protects people's drinking water safety. However, liquid chlorine and sodium hypochlorite can increase the risk of disinfection by-product (DBP) formation [2, 3]. Chloramine disinfection may form carcinogenic nitrosamines and nitrite substances by reacting with nitrates and inorganic salts. Chlorine dioxide and chlorite may be produced during chlorine dioxide disinfection, causing blood erythrocyte damage and limiting oxygen transport [4]. Ozone disinfection has high energy consumption and may oxide some aqueous organic substances to form carboxylic acids, formaldehyde, ketones, and other carcinogenic and genetic toxic by-products [5].

The UV disinfection method can rapidly achieve the effect of sterilization and disinfection by damaging the molecular structure of microbial DNA or RNA without producing DBPs [6]. However, some bacteria, such as spores, fungal spores, Mycobacterium tuberculosis, and Bacillus subtilis, are highly resistant to ultraviolet light. In addition, some bacteria have the ability of self-repair or resurrection, so the sterilization is not durable. These problems limit the further popularization of UV disinfection [7]. Except for those mentioned above, the heavy metal ions such as $Ag^+$ were also reported to have superior ability in cell killing; however, the high toxicity limits their application in disinfection [8].

Therefore, it is urgent to develop an economical, safe, and efficient disinfection technology for microbial inactivation in water [9].

In recent years, photocatalytic sterilization technology with photocatalyst as the core has attracted more and more attention due to its advantages of direct utilization and conversion of sunlight, high efficiency, stability, and no by-product formation [10]. Some traditional semiconductor materials such as $TiO_2$ and ZnS have the ability of photocatalytic sterilization. However, these semiconductors are hampered by a large intrinsic band gap. Based on the above limitation, enormous efforts, such as doping and heterojunction construction, have been investigated to broaden the visible light response [11–14], but the photocatalytic efficiency was still not obviously enhanced, which greatly limited their practical application. Therefore, it is imperative to develop a new type of high-efficiency photocatalyst to make up for the shortcomings of traditional materials. Recent series of studies have shown that ternary sulfides such as $Cu_3SbS_3$ [15], $ZnIn_2S_4$ [16], $Cu_2Mo_6S_8$ [17], and $CuS_xSe_{1-x}$ [18] are highly attractive due to their low cost, excellent electrical properties, and nonlinear optical properties. Particularly, their physicochemical properties can be facile regulated by adjusting the composition of each element, making them stand out among many new photocatalysts [19]. The literature reports that $Ga_2S_3$ is an effective optoelectronic material; however, its wide band gap ($E_g$ = 3.4 eV) limits the application of visible light [20]. Therefore, a new ternary sulfide photocatalyst with an adjustable and optimized band structure can be obtained by introducing new metal elements in the crystal phase structure of $Ga_2S_3$.

At present, the preparation methods of ternary sulfides mainly include the hydrothermal method [21], electrochemical method [22], and microwave-assisted method [23]. Most of these methods need high temperature, high pressure, or external template to control the morphology; thus, it is difficult to be widely used. In recent years, it has been reported that the ultrasonic spray pyrolysis (USP), which can be carried out under ambient pressure with no template, serves as a novel preparation method for photocatalyst. It mainly includes atomization of the solution by means of an atomizer and the physicochemical reaction of the droplets under heating conditions [24]. The catalyst particles with a high specific surface can be obtained by USP, and the photocatalytic efficiency can be significantly improved compared to conventional preparation methods.

In this study, a novel ternary sulfide photocatalyst $Ga_{0.25}Zn_{4.67}S_{5.08}$ was prepared using USP. The effect of reaction conditions on the $Ga_{0.25}Zn_{4.67}S_{5.08}$ was studied, and their photocatalytic activities were evaluated using bacterial disinfection under visible light irradiation.

## 2. Experimental Section

*2.1. Catalyst Preparation.* The $Ga_{0.25}Zn_{4.67}S_{5.08}$ photocatalyst was prepared by a USP method. All chemicals used for synthesis were of analytical grade and used without further purification. In a typical process, 0.297 g $Ga(NO_3)_3{\cdot}XH_2O$, 0.511 g $Zn(NO_3)_3{\cdot}6H_2O$, and 0.761 g $CH_4N_2S$ were added into 150 mL distilled water under vigorous stirring to form a transparent solution. Ultrapure water was used in all the experiments. The solution was nebulized at 1.7 MHz ± 10% (YUYUE402AI, Shanghai) and then carried by air with different flow rates from 2 to 10 L·min$^{-1}$ through a quartz tube surrounded by a furnace thermostated at 400~900°C. The quartz reaction tube with the diameter of 5.0 cm had a long length of 60 cm [25]. The products were collected in a percolator with ultrapure water and then separated by centrifugation and washed thoroughly with ethanol and ultrapure water. The products were finally dried under a vacuum at 60°C overnight. For comparison, the $Ga_{0.25}Zn_{4.67}S_{5.08}$ were prepared by a modified hydrothermal method according to the previous study [11].

*2.2. Characterization.* The X-ray diffraction (XRD) pattern with a scan rate of 0.05° was recorded on a Shimadzu 6100 Advance X-ray diffractometer with Cu K$\alpha$ radiation in the $2\theta$ range from 20° to 60°. Scanning electron microscopy (SEM, SU8000) was used to characterize morphology of the obtained products. Transmission electron microscopy (TEM) study was carried out on a FEI Titan G2 60-300 electron microscopy instrument. The UV-Vis diffuse reflectance spectra (UV-Vis DRS) were performed on a UV-Vis spectrophotometer (Varian, Cary 500, Palo Alto, CA, USA) with $BaSO_4$ as the reference sample in these measurements. The Brunauer-Emmett-Teller (BET) specific surface areas and porosities of the sample were carried out by using the ASAP 2020 equipment (Micromeritics, Atlanta, GA, USA). X-ray photoelectron spectroscopy (XPS) measurements were performed on a PHI Quantum 2000 XPS system (Physical Electronics, Portland, OR, USA); all the binding energies were calibrated to the C 1s peak at 284.8 eV of the surface adventitious carbon. Photocurrent was measured by an electrochemical workstation (Multi Autolab M20) in a three-electrode system with a working electrode, a Pt sheet counter electrode, and a standard Ag/AgCl reference electrode containing 0.2 mol·L$^{-1}$ $Na_2SO_4$ solution as the electrolyte.

*2.3. Photocatalytic Antibacterial Tests.* The experiments of photocatalytic disinfection were carried out by using a 300 W Xe lamp with a UV cutoff filter (800 nm ≥ $\lambda$ ≥ 420 nm) as the light source. All glassware and 0.9% saline were autoclaved at 121°C for 20 min before the experiments. Typically, 10 mg of nanocrystal powder was mixed with 50 mL saline in the quartz cell, followed by the addition to 1 mL of the suspension containing *E. coli* cells. The suspension was stirred in darkness for 1 h to achieve adsorption equilibrium of viruses on the photocatalyst. Then, at different time intervals, 0.1 mL of the reaction mixture was collected and immediately diluted with sterilized saline for a serial dilution. Following that, 0.1 mL of the diluted solution was spread uniformly on nutrient agar and incubated at 37°C for 12 h; the number of viable cells was counted. The survival rate was estimated by the following equation: survival rate% = $(N_T/N_0) \times 100\%$, where $N_0$ and $N_T$ are the numbers of viable cells in darkness and after photocatalytic reaction with photocatalysts, respectively.

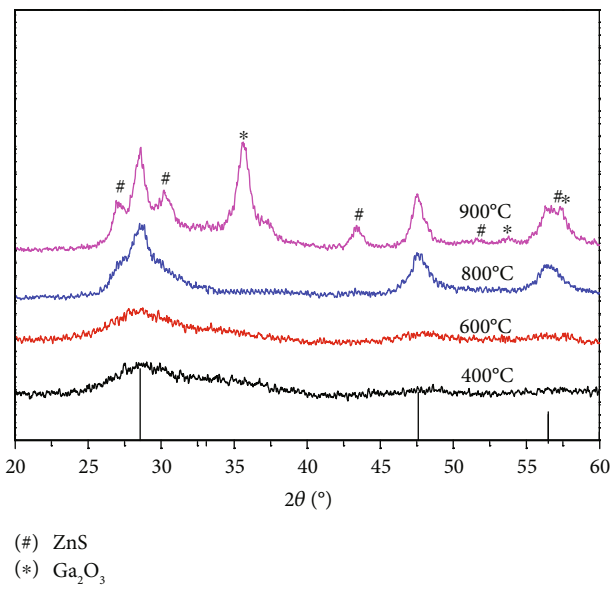


Figure 1: XRD patterns of $Ga_{0.25}Zn_{4.67}S_{5.08}$ prepared at different temperatures.

## 3. Result and Discussion

The X-ray powder diffraction analysis result is shown in Figure 1. The diffraction peaks at 28.6°, 47.6°, and 56.5° correspond to the (111), (220), and (311) planes of the cubic structure of $Ga_{0.25}Zn_{4.67}S_{5.08}$ (JCPDS card 49-1626), respectively. Among all of the peaks, the diffraction peak at (111) gradually becomes more intense and narrow with pyrolysis temperature, suggesting an increasing degree of crystallinity [26, 27]. At the same time, these synthesized samples prepared at 400°C and 600°C have a wide diffraction peak, indicating that the samples have smaller crystals and possibly improved the catalytic efficiency. The average grain sizes calculated by the Scherrer equation of the samples prepared at 400, 600, and 800°C are 1.03, 1.32, and 3.18 nm, respectively [28]. Nevertheless, when the temperature rises to 900°C, there are some possible $Ga_2O_3$ and ZnS impurity diffraction peaks in the XRD pattern, which may be due to the oxidation and decomposition of $Ga_{0.25}Zn_{4.67}S_{5.08}$ caused by high temperature.

Figures 2(a)–2(c) show the SEM images of the samples fabricated at 400°C and 800°C, respectively. It can be seen from Figure 2(a) that the samples were composed of well-defined spherical microspheres, and their diameters are approximately distributed between 100 nm and 1200 nm. By comparing with Figures 2(b) and 2(c), it can be found that there is a rough surface of the sample prepared at 400°C, which will increase the specific surface area and the active sites in the photocatalytic process, eventually leading to the enhancement of photocatalytic activity. When the temperature was raised to 800°C, the surface of the particles becomes relatively smooth. This can be ascribed to the increase of grain size under high temperature, and the surface roughness gradually decreases.

The spherical and porous structures of the as-prepared $Ga_{0.25}Zn_{4.67}S_{5.08}$ sample were further confirmed by TEM. The TEM images in Figures 2(d)–2(f) illustrate that the $Ga_{0.25}Zn_{4.67}S_{5.08}$ sample has porous structured microspheres and was built by the aggregation of plenty of nanoparticles. This structure will be beneficial to increase the specific surface area and the surface active sites of the catalyst. By enabling more contacts of the pollutant molecules with the catalysts, the performance in the photocatalytic process is thus improved. The composition of the product was confirmed by EDX analysis (Figure 2(g)), proving the presence of Ga, Zn, and S in the as-prepared sample.

On the basis of the above results, an illustration of the possible three-stage formation mechanism of $Ga_{0.25}Zn_{4.67}S_{5.08}$ microspheres was suggested (Scheme 1). First, the solution was atomized into aerosol under ultrasonic conditions. The aerosols were then carried by air through the quartz tube surrounded by a furnace. Subsequently, the droplets were rapidly vaporized under high temperature, while the thiourea in the aerosol also decomposes quickly and produces $H_2S$. The produced $H_2S$ rapidly reacted with the metal precursor to form ternary sulfide submicrospheres, while the mass and heat transfer were accelerated under gasification conditions. As the droplets were further evaporated and concentrated, the particle size gradually reduced to the obtained spherical particles.

The optical absorption properties of $Ga_{0.25}Zn_{4.67}S_{5.08}$ calcined at different temperatures were characterized by diffuse reflectance UV-Vis spectra (DRS) in the range of 200~800 nm as shown in Figure 3(a). All the samples display remarkable absorption in the visible region. Besides, the blue shift of the absorption band edge can be observed when the preparation temperature decreases from 900°C to 400°C. The blue shift of the adsorption edge with the decrease in preparation temperature is mainly due to the quantum confinement effect [26]. The energy band gap ($E_g$) of the sample can be calculated by the formula $\alpha h\nu = A(h\nu - E_g)^n$ [29]. The band gaps of the catalysts prepared at 400, 600, 800, and 900°C are calculated to be 2.21, 2.52, 2.45, and 2.29 eV, respectively, which indicates that the synthesized samples can respond well to visible light.

The chemical states of elements for the $Ga_{0.25}Zn_{4.67}S_{5.08}$ prepared at 600°C were examined by XPS analysis. The wide scan XPS spectrum (Figure 4(a)) reveals that the predominant elements are C, O, S, Zn, and Ga. Among these elements, S, Zn, and Ga elements are from the prepared composites, while C and O elements are from the XPS instrument itself and the adsorbed hydroxyl groups, respectively. The high-resolution spectra of the Ga 2p with two characteristic peaks at 1117.8 eV and 1144.6 eV corresponded to the $2p_{3/2}$ and $2p_{1/2}$ levels (Figure 4(b)), suggesting the existence of $Ga^{3+}$ species [30]. As shown in Figure 4(c), the two peaks at the binding energies of 161.4 eV and 162.6 eV can be attributed to the $2p_{3/2}$ and $2p_{1/2}$ levels of $S^{2-}$ [31]. The binding energies of two major peaks at 1021.0 eV and 1044.0 eV ascribed to Zn $2p_{3/2}$ and for $2p_{1/2}$, respectively (Figure 4(d)), in accordance with $Zn^{2+}$ in $Ga_{0.25}Zn_{4.67}S_{5.08}$ [32]. These results further indicate that $Ga_{0.25}Zn_{4.67}S_{5.08}$ can be successfully synthesized via USP.

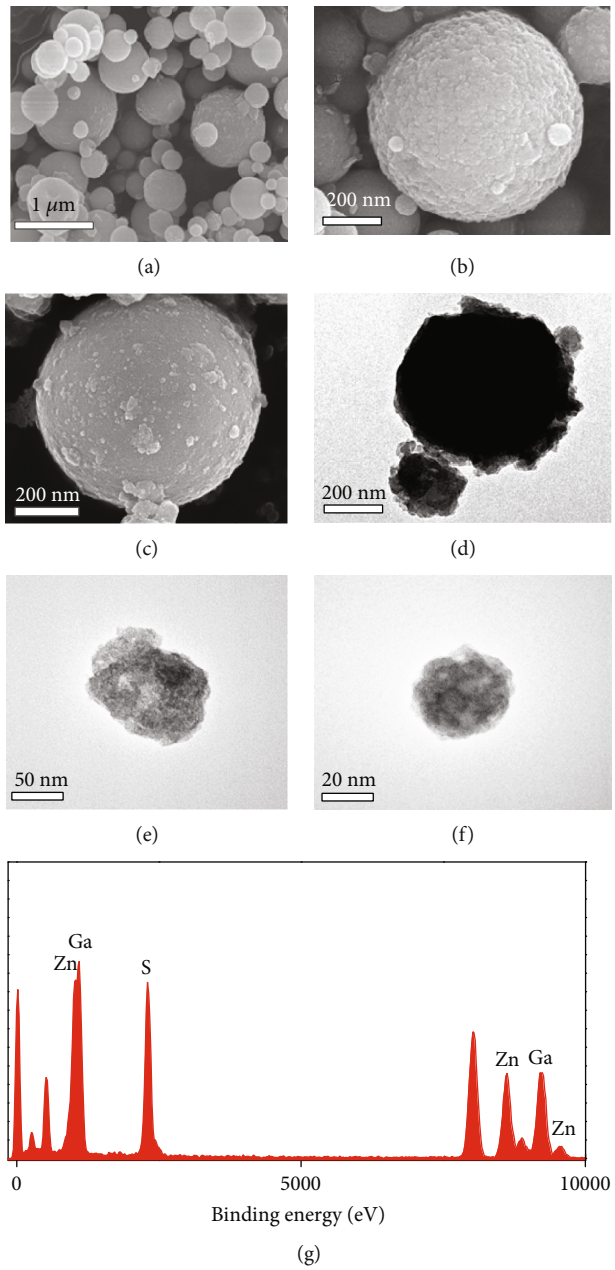


Figure 2: SEM images, TEM image, and energy dispersive spectrum of $Ga_{0.25}Zn_{4.67}S_{5.08}$ at different temperatures: (a, b) 400°C SEM images; (c, f) 800°C SEM images; (d, e) 400°C TEM images; (g) 400°C EDX spectrum.

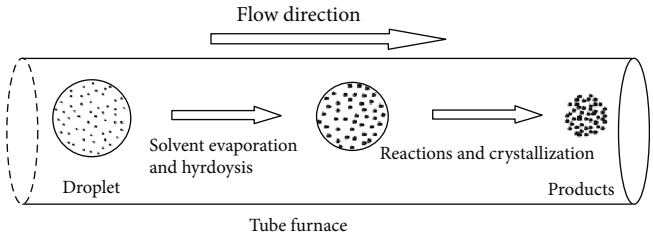


Scheme 1: Schematic diagram of the formation of $Ga_{0.25}Zn_{4.67}S_{5.08}$ microsphere.

The nitrogen adsorption-desorption isotherms and pore size distribution curve of the as-prepared samples were depicted in Figure 5. As shown in Figure 5(a), the physical adsorption isotherms of all the samples show the typical type IV isotherms with H3 hysteresis loop. The pore size obtained from the desorption branch of the isotherms exhibits a

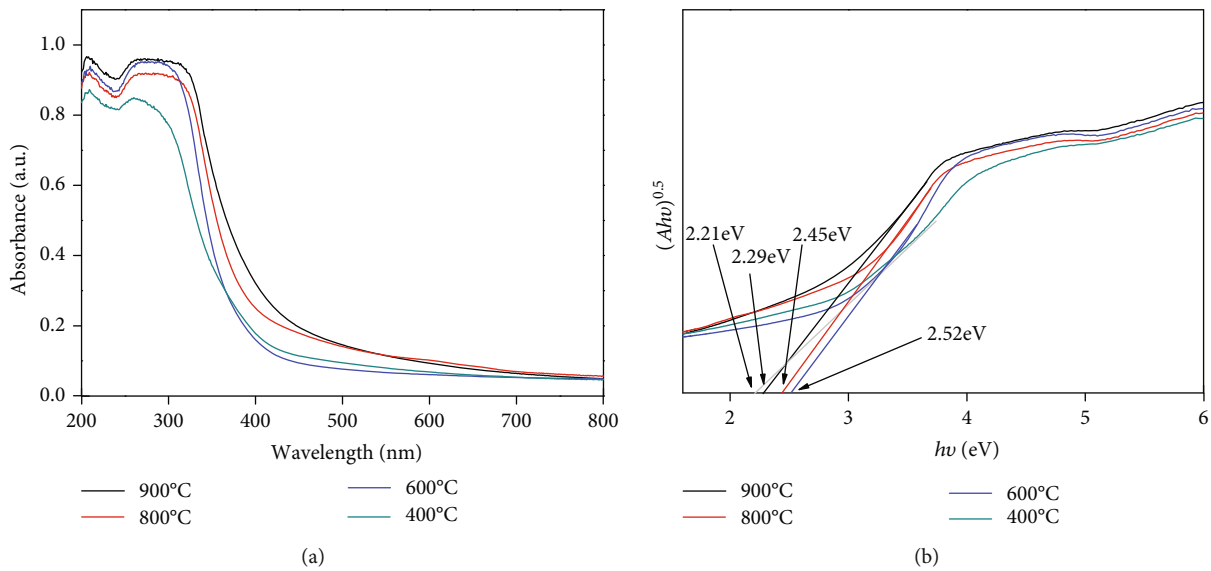


Figure 3: (a) Diffuse reflectance UV-Vis spectra of $Ga_{0.25}Zn_{4.67}S_{5.08}$ prepared at different temperatures; (b) the plot of the transformed Kubelka-Munk function versus the energy of light.

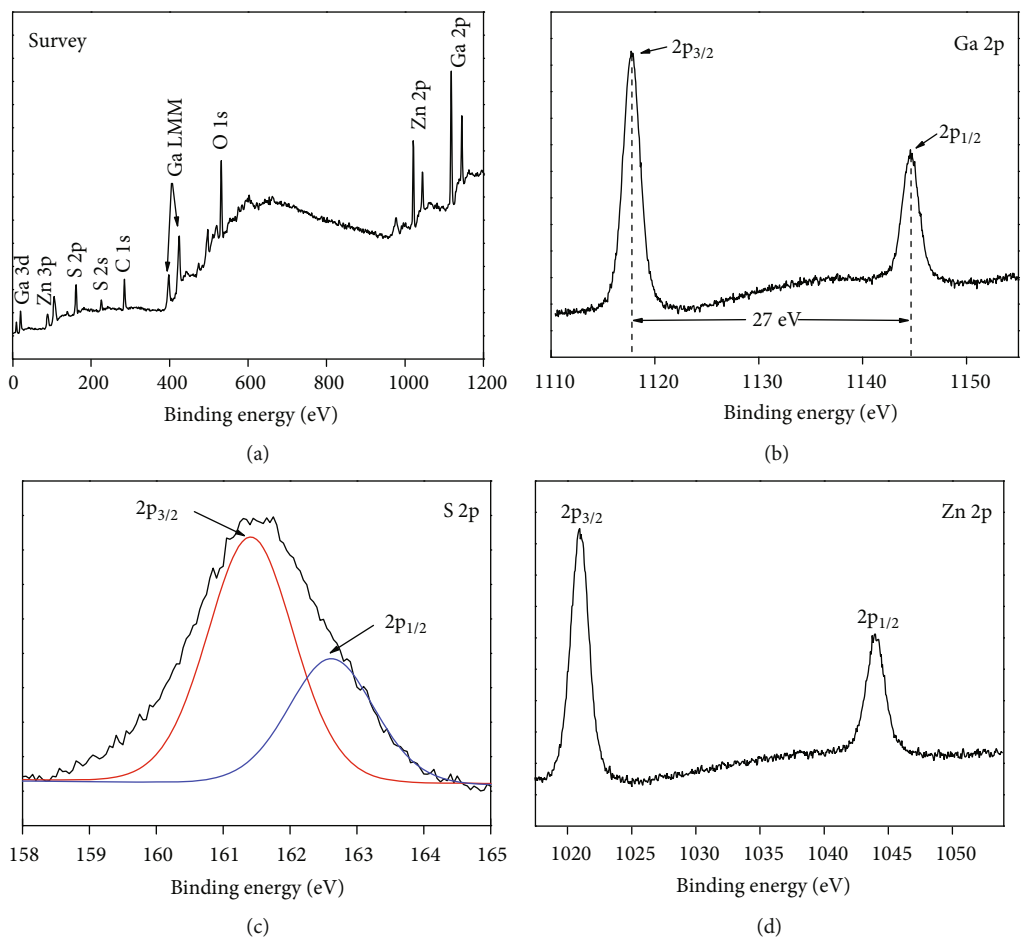


Figure 4: XPS spectra of catalyst prepared at 600°C: (a) the wide spectrum; (b) Ga 2p; (c) S 2p; (d) Zn 2p.

narrow distribution in the range of from 2 to 10 nm (Figure 5(b)), indicating the mesoporous nature of the as-prepared sample [33]. The porous structures with high specific surface areas could adsorb more active species and reactants on its surface and provide efficient transport pathways for the reactants and products during the photocatalytic

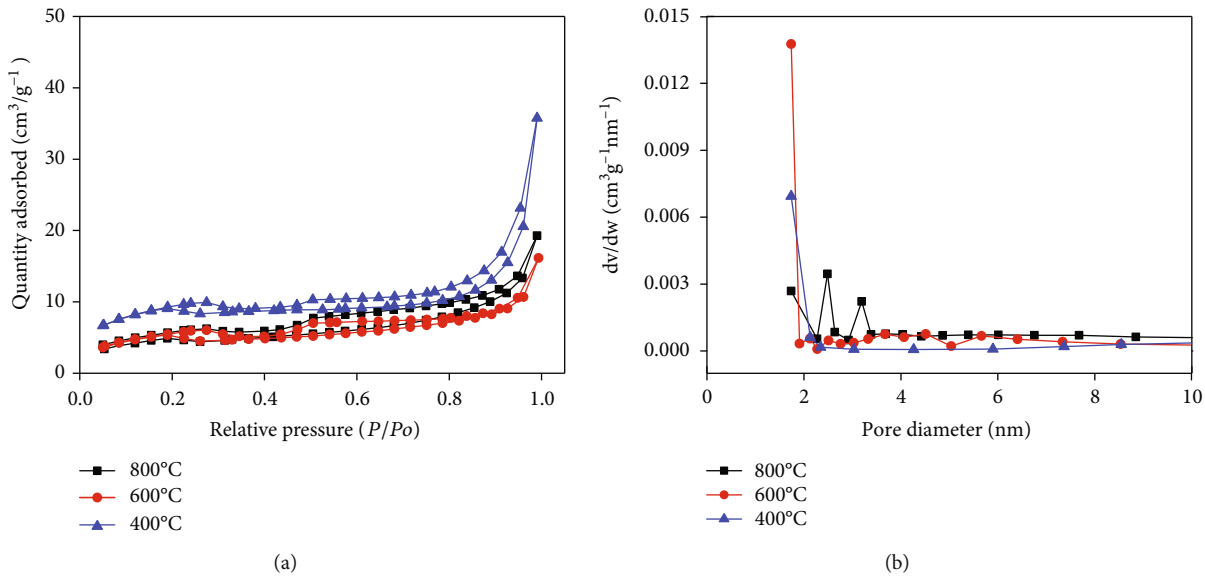


Figure 5: (a) $N_2$ adsorption-desorption isotherms; (b) pore size distribution curves of catalysts prepared at different temperatures.

Table 1: Porous properties of catalysts prepared at different temperatures.

| Temperature (°C) | $d$ (nm) | Pore size (nm) | Surface area ($m^2 \cdot g^{-1}$) | Pore volume ($cm^3 \cdot g^{-1}$) |
|---|---|---|---|---|
| 400 | 1.03 | 13.85 | 25.76 | 0.05 |
| 600 | 1.32 | 7.69 | 13.91 | 0.02 |
| 800 | 3.18 | 7.40 | 14.00 | 0.03 |

process, thus accelerating the photocatalytic reaction rate. The BET surface areas of the $Ga_{0.25}Zn_{4.67}S_{5.08}$ prepared at 400, 600, and 800°C were 25.76, 13.91, and 14.00 $m^2 \cdot g^{-1}$, respectively (Table 1). The catalyst prepared at 400°C possesses the highest specific surface area and the largest average pore size of 13.85 nm, compared with that of samples prepared at 600°C and 800°C at 7.69 and 7.40 nm, respectively.

Efficient charge separation is also an important factor affecting photocatalytic performance [34]. The photocurrent response as a useful method to evaluate the charge separation was tested. As shown in Figure 6, all samples have great photoelectric performance, manifesting that they could respond to visible light. Obviously, photocurrent generation was shown to be affected by the calcined temperature. Notably, the photocurrent of the sample obtained at 400°C is higher than that of the samples obtained at 600°C and 800°C, which could be ascribed to the fact that the sample obtained at 400°C has a larger specific surface area and more surface active sites. As a result, much more photogenerated electrons and holes can be produced. The photocurrent density generated by the 800°C sample was higher than that of the 600°C sample, which can be ascribed to the fact that the sample prepared at higher temperature has a higher crystallinity. The higher crystallinity may decrease the electron-hole pair recombination rate and lead to higher photocurrent density. The falling edges also show that the lifetime of the photogenerated carriers of the samples prepared at 400°C is much longer than that of 600°C and 800°C, which indicates that the

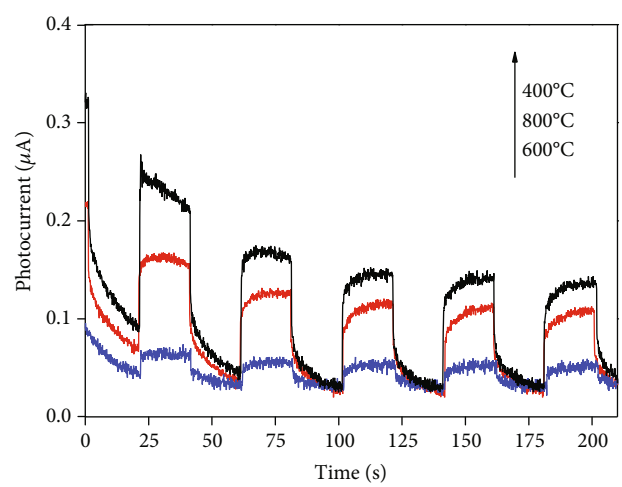


Figure 6: Photocurrent of $Ga_{0.25}Zn_{4.67}S_{5.08}$ prepared at different temperatures.

recombination of carriers of the samples prepared at 400°C is much lower than that of 600°C and 800°C. This is also benefit to photocatalytic performance.

The photocatalytic performances of the as-prepared $Ga_{0.25}Zn_{4.67}S_{5.08}$ samples with different temperatures were evaluated by measuring the survival rate of *E. coli* under visible light irradiation. As shown in Figure 7, no evident loss of survival rate was observed in the dark, indicating negligible toxicity of the photocatalyst. For the light control

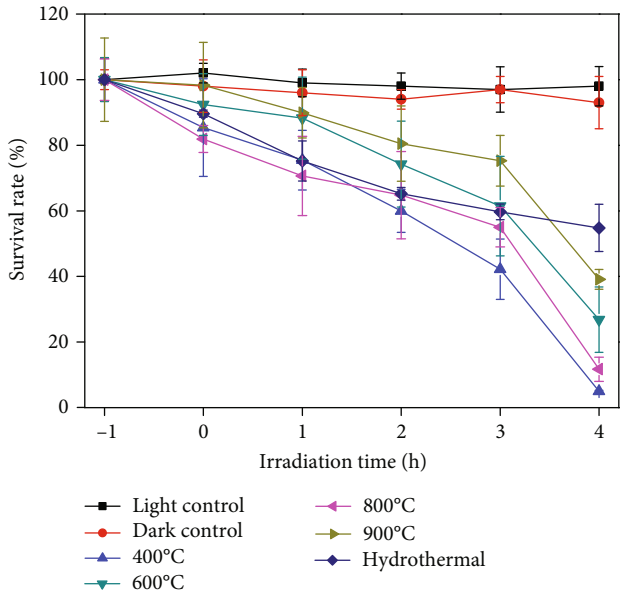


Figure 7: Disinfection efficiencies of $Ga_{0.25}Zn_{4.67}S_{5.08}$ prepared at different temperatures and hydrothermal method.

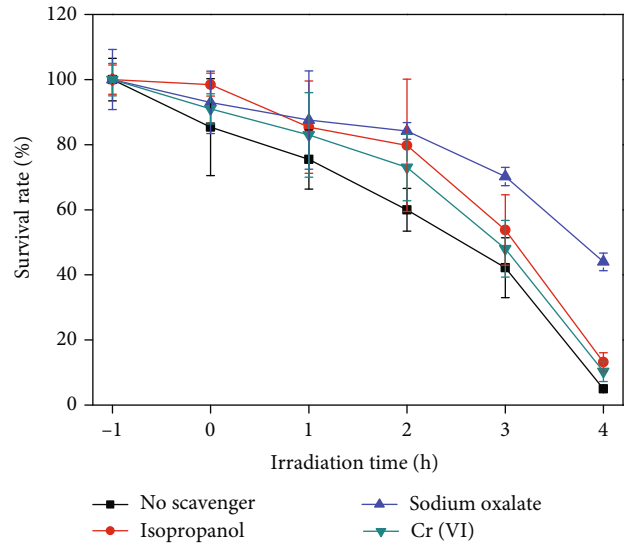


Figure 8: Disinfection efficiencies of catalysts in the presence of different sacrificial agents.

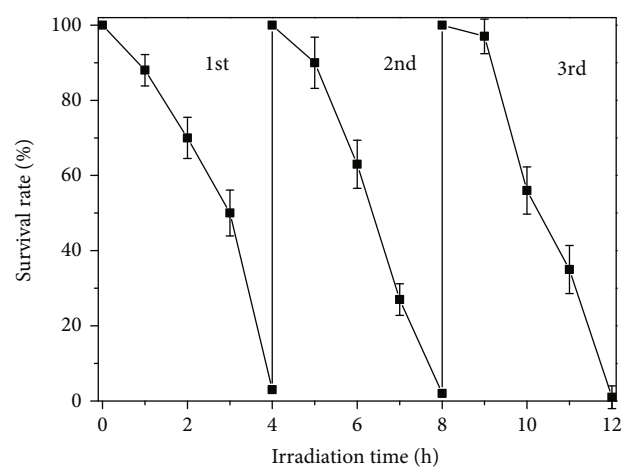


Figure 9: Stability of $Ga_{0.25}Zn_{4.67}S_{5.08}$ prepared at 400°C under visible light irradiation.

experiment, the test was performed without photocatalyst under the irradiation of visible light. The survival rate is stable which indicates the *E. coli* cannot be killed by visible light under the present condition. For the photocatalytic test, the suspension was stirred in darkness for 1 h to achieve adsorption equilibrium of the cells on the photocatalyst. As observed, all samples prepared by USP have greater bactericidal performance, compared to the sample prepared by the hydrothermal method. Under the presence of $Ga_{0.25}Zn_{4.67}S_{5.08}$ (400°C), nearly all bacteria cannot survive after 4 h of visible light irradiation, while the survival rate of other samples (600°C and 800°C) was only 27% and 12%, respectively. The bacterial suspension after the reaction was cultured for 96 h under dark reaction, and no change in the colony of *E. coli* was observed, indicating that the bacteria were indeed killed by the photocatalytic sterilization process, rather than simply suppressed. The higher photocatalytic performance of $Ga_{0.25}Zn_{4.67}S_{5.08}$ (400°C) can be ascribed to its larger specific surface area and more active sites.

It is well known that active groups such as $^{\bullet}OH$, $e^-$, and $h^+$ attack the bacterial cells during the reaction, eventually causing the decomposition of the cell wall [1]. In order to further explore which active substance played a decisive role in the photocatalytic sterilization process, different kinds of radical scavengers were added to a series of identical photocatalytic reaction systems. For example, sodium oxalate (0.5 mM as $h^+$ quencher), Cr (VI) (0.05 mM as $e^-$ quencher), and isopropanol (0.5 mM as OH quencher) are added to the different batches of the $Ga_{0.25}Zn_{4.67}S_{5.08}$ photocatalytic system, respectively, to capture $h^+$, $e^-$, and $^{\bullet}OH$ and to ensure that the scavengers under the concentration will not have any toxicity to *E. coli* [35]. As shown in Figure 8, the bacterial survival rate of photocatalytic systems added with isopropanol or Cr (VI) is almost the same with the system without a trapping agent, suggesting that $^{\bullet}OH$ and $e^-$ are not the main active substances in the photocatalytic sterilization, whereas when sodium oxalate was added as the hole trapping agent, the survival rate of bacteria reached 45% after irradiation for 4 h, suggesting that $h^+$ oxidation was the dominant radical for the photocatalytic disinfection.

The stability of the samples was evaluated by successive cycles of the photocatalytic sterilization process. As shown in Figure 9, the results indicate that the photocatalytic activity of the sample did not decrease significantly even after three successive cycles. These results indicate that $Ga_{0.25}Zn_{4.67}S_{5.08}$ microspheres possess excellent photocatalytic stability during the photocatalytic application.

Based on the above experimental and characterization results, a possible photocatalytic mechanism for disinfection by $Ga_{0.25}Zn_{4.67}S_{5.08}$ microspheres was proposed and displayed in Figure 10. Under the visible light irradiation, the hole and electron pairs are generated and separated; then,

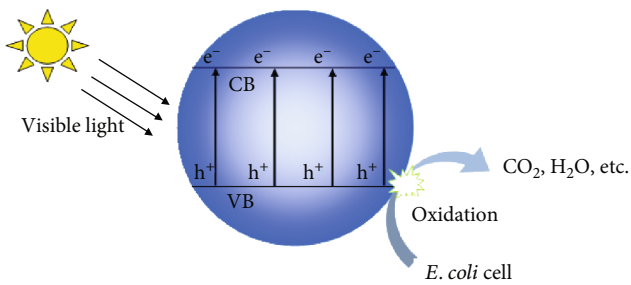


Figure 10: Proposed mechanism for disinfection over $Ga_{0.25}Zn_{4.67}S_{5.08}$ under visible light irradiation.

the holes directly reacted with the cells adsorbed and produce inorganic matters.

## 4. Conclusion

In summary, $Ga_{0.25}Zn_{4.67}S_{5.08}$ microspheres were synthesized by the USP process without adding template. The visible light photocatalytic antibacterial results indicate that the temperature of pyrolysis plays a dominant role in the disinfection process. On the basis of the DRS and BET, as well as the photocurrent, the superior photocatalytic activity of $Ga_{0.25}Zn_{4.67}S_{5.08}$ prepared at 400°C was ascribed to the narrowed band gap, the high specific surface areas, and more photogenerated holes. We believe that this study shed light on engineering other novel porous structured photocatalysts for low-cost water disinfection.

## Data Availability

The data used to support the findings of this study are available from the corresponding author upon request.

## Conflicts of Interest

The authors declare that they have no conflicts of interest.

## Acknowledgments

This work was supported by the Natural Science Foundation of Fujian Province (Grant No. 2016J05042), the Putian Science and Technology Bureau Project (2016S1001), and the Putian University Research Innovation Project (2018ZP03 and 2018ZP07) and the Putian University Research Project (2018048).

## References

[1] Y. Zhang, C. Lin, Q. Lin et al., "CuI-BiOI/Cu film for enhanced photo-induced charge separation and visible- light antibacterial activity," *Applied Catalysis B: Environmental*, vol. 235, pp. 238–245, 2018.

[2] Y. Wang, L. Lin, B. B. Li, M. H. Huang, B. B. Li, and L. Chen, "Preparation of hierarchical microsphere BiOBr catalyst and its photocatalytic disinfection performance under visible light," *Biotechnology Bulletin*, vol. 32, no. 8, pp. 242–248, 2016.

[3] M. G. Muellner, E. D. Wagner, K. McCalla, S. D. Richardson, Y. T. Woo, and M. J. Plewa, "Haloacetonitriles vs. regulated haloacetic acids: are nitrogen-containing DBPs more toxic?," *Environmental Science & Technology*, vol. 41, no. 2, pp. 645–651, 2007.

[4] H. Yu, S. Chen, X. Quan, and Z. Zhang, "The mechanism, materials and reactors of photocatalytic disinfection in water and wastewater treatment," *Progress in Chemistry*, vol. 29, no. 9, pp. 1030–1041, 2017.

[5] B. E. Logan and M. Elimelech, "Membrane-based processes for sustainable power generation using water," *Nature*, vol. 488, no. 7411, pp. 313–319, 2012.

[6] C. M. Zhang, Y. H. Miao, Q. P. Zhang, and H. Xu, "Effects of chlorination and ultraviolet disinfection on antibiotic resistance of fecal coliforms in secondary settling tank effluent of municipal wastewater treatment plant," *Research of Environmental Sciences*, vol. 27, no. 4, pp. 422–426, 2014.

[7] L. Jia, H. Xiangfeng, S. Jie, and W. Zhichao, "Controlling photo-reactivation of bacteria inactivated by UV disinfection," *Environmental Pollution & Control*, vol. 29, no. 11, pp. 841–843, 2007.

[8] T. V. M. Sreekanth, P. C. Nagajyothi, P. Muthuraman et al., "Ultra-sonication-assisted silver nanoparticles using _Panax ginseng_ root extract and their anti-cancer and antiviral activities," *Journal of Photochemistry and Photobiology B-Biology*, vol. 188, pp. 6–11, 2018.

[9] J. H. Huang, W. T. Lin, L. Y. Xie, and J. Q. Chen, "Construction of graphitic carbon nitride-bismuth oxyiodide layered heterostructures and their photocatalytic antibacterial performance," *Environmental Science*, vol. 38, no. 9, pp. 3979–3986, 2017.

[10] H. L. Tan, R. Amal, and Y. H. Ng, "Alternative strategies in improving the photocatalytic and photoelectrochemical activities of visible light-driven $BiVO_4$: a review," *Journal of Materials Chemistry A*, vol. 5, no. 32, pp. 16498–16521, 2017.

[11] B. Poornaprakash, U. Chalapathi, S. V. P. Vattikuti et al., "Enhanced fluorescence efficiency and photocatalytic activity of ZnS quantum dots through Ga doping," *Ceramics International*, vol. 45, no. 2, pp. 2289–2294, 2019.

[12] B. Poornaprakash, U. Chalapathi, S. V. Prabhakar Vttikuti, M. S. Pratap Reddy, and S. H. Park, "Pristine and Sm-doped ZnS quantum dots: structural, optical, luminescence, magnetic, and photocatalytic properties," *Chalcogenide Letters*, vol. 16, no. 2, pp. 49–55, 2019.

[13] S. V. P. Vattikuti, C. Byon, and S. Jeon, "Enhanced photocatalytic activity of ZnS nanoparticles loaded with $MoS_2$ nanoflakes by self-assembly approach," *Physica B: Condensed Matter*, vol. 502, pp. 103–112, 2016.

[14] B. Poornaprakash, U. Chalapathi, P. T. Poojitha, S. V. P. Vattikuti, and S.-H. Park, "Co-doped ZnS quantum dots: structural, optical, photoluminescence, magnetic, and photocatalytic properties," *Journal of Superconductivity and Novel Magnetism*, pp. 1–6, 2019.

[15] N. Bouaniza, N. Hosni, and H. Maghraoui-Meherzi, "Structural and optical properties of $Cu_3SbS_3$ thin film deposited by chemical bath deposition along with the degradation of methylene blue," *Surface and Coatings Technology*, vol. 333, pp. 195–200, 2018.

[16] Y. Chen, R. Huang, D. Chen et al., "Exploring the different photocatalytic performance for dye degradations over hexagonal $ZnIn_2S_4$ microspheres and cubic $ZnIn_2S_4$ nanoparticles," *ACS Applied Materials & Interfaces*, vol. 4, no. 4, pp. 2273–2279, 2012.

[17] X. Hong, Q. Liu, J. Iocozzia et al., "Needle-leaf-like Cu2Mo6S8Films for highly efficient visible-light photocatalysis," *Particle & Particle Systems Characterization*, vol. 35, no. 1, article 1700302, 2018.

[18] M. A. Yewale, A. K. Sharma, D. B. Kamble, C. A. Pawar, S. S. Potdar, and S. C. Karle, "Electrochemical synthesis of $CuS_xSe_{1-x}$ thin film for supercapacitor application," *Journal of Alloys and Compounds*, vol. 754, pp. 56–63, 2018.

[19] Q. Liu, X. Hong, X. Zhang et al., "Hierarchical $Cu_2S$ nanorods with different crystal phases for asymmetrical supercapacitors and visible-light photocatalysis," *Dalton Transactions*, vol. 47, no. 42, pp. 15189–15196, 2018.

[20] I. Caraman, S. Evtodiev, D. Untila et al., "Optical and photoelectric properties of planar structures obtained by thermal annealing of Ga2S3Plates in Zn vapors," *physica status solidi (a)*, vol. 214, no. 12, article 1700808, 2017.

[21] M. Gusain, A. Dubey, M. Das, and S. K. Singh, "Facial surfactant-free hydrothermal synthesis of $MoS_2$ microflower and its effect in electrochemical properties," *Journal of Solid State Chemistry*, vol. 274, pp. 58–63, 2019.

[22] S. Z. Werta, O. K. Echendu, and F. B. Dejene, "Optical and morphological studies of electrodeposited CdS thin film grown at different deposition times from acetate precursor," *ECS Journal of Solid State Science and Technology*, vol. 8, no. 2, pp. P112–P118, 2019.

[23] C. Nethravathi, R. Ragesh Nath, J. T. Rajamathi, and M. Rajamathi, "Microwave-assisted synthesis of porous aggregates of CuS nanoparticles for sunlight photocatalysis," *ACS Omega*, vol. 4, no. 3, pp. 4825–4831, 2019.

[24] A. A. G. Santiago, L. X. Lovisa, P. N. Medeiros et al., "Fast and simultaneous doping of $Sr_{0.9\text{-}x\text{-}y\text{-}z}Ca_{0.1}In_2O_4$:(xEu(3+), yTm(3+), zTb(3+)) superstructure by ultrasonic spray pyrolysis," *Ultrasonics Sonochemistry*, vol. 56, pp. 14–24, 2019.

[25] N. Gajić, Ž. Kamberović, Z. Anđić, J. Trpčevská, B. Plešingerova, and M. Korać, "Synthesis of tribological $WS_2$ powder from $WO_3$ prepared by ultrasonic spray pyrolysis (USP)," *Metals*, vol. 9, no. 3, p. 277, 2019.

[26] J. Huang, W. Lin, and J. Chen, "Synthesis of CdIn $_{**2**}$ S $_{**4**}$ Microsphere and Its Photocatalytic Activity for Azo Dye Degradation," *The Scientific World Journal*, vol. 2014, Article ID 241234, 6 pages, 2014.

[27] L. Lin, W. Ren, C. Wang, A. M. Asiri, J. Zhang, and X. Wang, "Crystalline carbon nitride semiconductors prepared at different temperatures for photocatalytic hydrogen production," *Applied Catalysis B: Environmental*, vol. 231, pp. 234–241, 2018.

[28] M. A. Subhan, P. C. Saha, P. Sarker, and M. al-Mamun, "Photoluminescence and enhanced visible light driven photocatalysis studies of $MoO_3$·CuO·ZnO nanocomposite," *Research on Chemical Intermediates*, vol. 44, no. 10, pp. 6311–6326, 2018.

[29] P. Li, H. Hu, J. Xu et al., "New insights into the photoenhanced electrocatalytic reduction of carbon dioxide on $MoS_2$-rods/$TiO_2$ NTs with unmatched energy band," *Applied Catalysis B: Environmental*, vol. 147, pp. 912–919, 2014.

[30] Y. Pan, L. Wang, S. Li, D. W. Gao, and X. W. Han, "Preparation and characterization of Co and $Ga_2O_3$-codoped ZnS and ZnSe bulk ceramics," *RSC Advances*, vol. 7, no. 80, pp. 50928–50934, 2017.

[31] C. Zeng, H. Huang, T. Zhang, F. Dong, Y. Zhang, and Y. Hu, "Fabrication of heterogeneous-phase solid-solution promoting band structure and charge separation for enhancing photocatalytic $CO_2$ reduction: a case of $Zn_XCa_1$-$XIn_2S_4$," *ACS Applied Materials & Interfaces*, vol. 9, no. 33, pp. 27773–27783, 2017.

[32] S. Y. Chae, S. J. Park, S. G. Han et al., "Enhanced photocurrents with ZnS passivated Cu(In,Ga)(Se,S)2Photocathodes synthesized using a nonvacuum process for solar water splitting," *Journal of the American Chemical Society*, vol. 138, no. 48, pp. 15673–15681, 2016.

[33] J. Liu, S. Zhang, and H. Zhao, "Fabricating visible-light photoactive 3D flower-like BiOCl nanostructures via a one-step solution chemistry method at room temperature," *Applied Surface Science*, vol. 479, pp. 247–252, 2019.

[34] W. H. Zhang, Q. H. Ji, H. C. Lan, and J. Li, "Preparation of $ZnTiO_3$/$TiO_2$ photocatalyst and its mechanism on photocatalytic degradation of organic pollutants," *Environmental Science*, vol. 40, no. 2, pp. 693–700, 2019.

[35] W. Wang, Y. Yu, T. An et al., "Visible-light-driven photocatalytic inactivation of E. coli K-12 by bismuth vanadate nanotubes: bactericidal performance and mechanism," *Environmental Science & Technology*, vol. 46, no. 8, pp. 4599–4606, 2012.

Hindawi
Journal of Nanomaterials
Volume 2019, Article ID 6316094, 12 pages
https://doi.org/10.1155/2019/6316094

*Research Article*

# Impact of AgNPs on Seed Germination and Seedling Growth: A Focus Study on Its Antibacterial Potential against *Clavibacter michiganensis* subsp. *michiganensis* Infection in *Solanum lycopersicum*

**Asma Noshad**,[1,2] **Crispin Hetherington**,[1] **and Mudassar Iqbal**[2]

[1]*Department of Chemistry, nCHREM & Centre for Analysis and Synthesis, Lund University, SE-22100 Lund, Sweden*
[2]*Dept. of Agricultural Chemistry, The University of Agriculture, Peshawar, 25130 KPK, Pakistan*

Correspondence should be addressed to Asma Noshad; asma.noshad@chem.lu.se

Received 23 August 2019; Accepted 29 October 2019; Published 3 December 2019

Guest Editor: Ganga Ram



This study investigated the effect of biogenic AgNPs on seed germination and seedling growth of *Solanum lycopersicum*. Treatment with silver nanoparticles (AgNPs) showed a significantly high germination rate and seedling growth compared to untreated seeds. Furthermore, its bactericidal effect against bacterial pathogen *Clavibacter michiganensis* subsp. *michiganensis* (*cmm*) infection in *Solanum lycopersicum* was also determined. Bacterial canker of tomato (BCT) caused by *cmm* results in reduced plant growth and production leading to considerable economic losses. Herein, fungal extracts of *T. harzianum* and *A. fumigatus* were used separately as a reducing agent to synthesize AgNPs of varying concentrations (0.088 mg/L, 0.176 mg/L, and 0.44 mg/L). Results suggested that the biosynthesized AgNPs not only worked as bactericide but also completely inhibited the incidence of *cmm* infection even at the lowest concentration of 0.088 mg/L under greenhouse conditions. Plants treated with AgNPs showed significantly enhanced growth parameters including plant height (cm), tomato yield/plant (g), fresh biomass (g), number of shoots/plant, root weight (g), and dry biomass (g). So, in order to reduce the toxic effects of chemical-based bactericides, biobased AgNPs are recommended, not only to control but also to prevent the bacterial infection in agriculture.

## 1. Introduction

Large doses of conventional chemical pesticides have resulted in the development of pest resistance and environmental contamination which are becoming one of the big challenges in agricultural industry. It has compelled research organizations to search for effective alternate (both in terms of cost and performance) plant protection pesticides. Integration of metal-based nanoparticles (NPs) in agriculture should be compatible with these requisites as they offer more efficient and eco-friendly alternates to conventional agricultural practices, e.g., nanopesticides, nanofertilizers, and nanosensors [1, 2]. Emergence of biobased nanopesticides which have a slow release formulation and are able to degrade active ingredients slowly proposes a hope of a more eco-friendly replacement to the chemical pesticides [3, 4]. In particular, fungal-based AgNPs could be the most feasible option due to their excellent antimicrobial potential for most of biomedical and industrial applications [4–6]. The focus of this study is to utilize beneficial fungi as they have several advantages over other microbes for many reasons; e.g., enzymes secreted by fungi play an important role in the synthesis of silver nanoparticles because of their ability to work both as reducing and stabilizing agents, but the detailed mechanism is still to be elucidated [7]. Previous studies highly recommend *A. fumigatus* for rapid biosynthesis of AgNPs effective against bacterial pathogens [8, 9]. Though the mechanism behind it is not yet well known, there exists a generally accepted mechanism. Extensive research needs to be carried out to conclude and generalize it.

Among the microbial syntheses of AgNPs, fungi are preferred due to

(i) excellent secretion of extracellular enzymes resulting in faster fabrication of AgNPs than chemical synthesis

(ii) involvement of NP synthesis in a cost- and time-effective manner

(iii) ease in isolating, culturing, processing, and storage

(iv) successful involvement in high-yield economy NPs

(v) nanoparticles by fungi being more stable with better monodisparity [7]

Myco-based fabrication of metal NPs is getting much research interest due to their extensive application in various sectors (Table 1).

This study was designed to synthesize and characterize AgNPs using 2 different fungal strains which is an economical, harmless, eco-friendly, and acceptable method. The fungal strains used were *T. harzianum* [11] and *A. fumigatus*. The biosynthesized AgNPs were subjected to *in vitro* screening for antibacterial efficacy against Gram-positive and Gram-negative bacteria. Based on the excellent outcome of *in vitro* antimicrobial potential, a greenhouse experiment was conducted to determine the effect of treatments on a control of *Clavibacter michiganensis* subsp. *michiganensis*. *cmm* is a bacterial pathogen responsible for bacterial canker of tomato (BCT) [20, 21] and a major production restraint, causing significant economic losses worldwide. Various biotic and abiotic stress factors contribute to this low yield; however, this study is focused on one of the biotic stress factors known as BCT. Lack of conventional resistance in tomato cultivars has made it very difficult to control it. So, the overarching aim of this study is to develop AgNPs through the green chemistry route with the ambition that these particles contribute some beneficial effects to the industrial agriculture in preventing and treating BCT. The synthesized AgNPs were characterized by UV-visible absorption spectra and X-ray diffraction (XRD) and confirmed by transmission electron microscope (TEM). The effect of pH on AgNPs during synthesis process and its stability behavior for six months were also kept under observation. It was also determined if the reduction process is an enzymatic reaction. Though it is not the first report to employ filamentous fungi *A. fumigatus* and *T. harzianum* for the extracellular synthesis of AgNPs, they are used for the first time to control the bacterial pathogen *cmm* which is considered under quarantine in Europe but still prevalent in many developing and underdeveloped countries. The production of antimicrobial compounds by the fungi *P. oligandrum* and *T. harzianum* highlights its importance [22].

## 2. Experimental

*2.1. Isolation and Culturing.* Pure cultures of *A. fumigatus* and *T. harzianum* were collected and reidentified at the Plant Pathology Dept. of the University of Agriculture, Peshawar. The obtained cultures were inoculated and grown using the protocol described by [11]. The experimental steps involved are as follows:

(i) Collection of fungal strains

(ii) Cultured or grown on nutrient medium

(iii) Exposure of the fungal filtrate solution to silver nitrate solution for the biosynthesis of AgNPs

(iv) Characterization process includes UV-Vis spectroscopy, TEM, energy-dispersive X-ray spectroscopy (EDX), and powder PXRD analysis

(v) *In vitro* antibacterial activity

(vi) Stability test for the synthesized AgNPs

(vii) Mechanism behind enzymatic reaction of AgNP synthesis

(viii) Effect of pH on AgNP synthesis

(ix) Seed germination and seedling growth test

(x) Screenhouse experiment to check the effect of synthesized AgNPs on *cmm* subsp. *michiganensis* control

*2.2. Statistical Analysis.* Origin Professional 8 (Microsoft, USA) software was used for statistical Gaussian approximation to find the full width at half maximum (FWHM). A completely randomized design CRD with 3 replications was used for the experiment. Calculation of one-way ANOVA, $P$ value $< 0.05$ is considered statistically significant.

The experimental steps involved in AgNP synthesis using the fungal source, their characterization, and antibacterial application *in vitro* as well in the greenhouse is presented in Figure 1. The explanation for each step is described with results in brief.

## 3. Results and Discussion

*3.1. Synthesis of AgNPs.* The prepared filtrate of each fungal isolate was brought in contact with $AgNO_3$ in 1 : 1 at 29°C. A robust colour change from yellow to brown was observed after 24 hours of the incubation period, indicating AgNP formation (Figures 2(a) and 2(b)). A sharp characteristic peak centered at ca. 422-429 nm and 425-4439 nm due to surface plasmon resonance SPR value in the visible region of the spectrum for *T. harzianum* and *A. fumigatus*, respectively (Figure 3). Increase in SPR value towards higher wavelength is proportional to the intensity of Ag in the reaction mixture, resulting in an increased number of AgNPs in the solution w.r.t. time [23]. The mechanism behind the synthesis of AgNPs involved bioreduction of silver ions to metallic silver ($Ag^{+2}$ to $Ag^0$), later on stabilized by the bioactive molecules present in the mycelial cells. During this process, toxic metal ions $Ag^{+2}$ are reduced to nontoxic AgNPs through the catalytic effect of the extracellular enzyme and metabolites secreted by fungi [24]. No colour change was observed in the control experiment when incubated under the same conditions (Figure 3). However, to justify that fungus-mediated AgNPs are the result of an enzymatic reaction, each of the fungal filtrate was boiled for 15 minutes to denature the proteins secreted by the fungi. This filtrate was used in the same

Table 1: Applications of AgNPs synthesized from different fungal strains.

| Nanoparticles | Fungi/yeasts | Application | References |
|---|---|---|---|
| | *A. niger* | Antibacterial activity, wound healing activity | [8] |
| | *Fusarium acuminatum* | Antibacterial properties against multidrug-resistant bacteria | [9] |
| | *F. oxysporum* | (i) Textile fabrics<br>(ii) Antibacterial properties against multidrug-resistant bacteria | [10] |
| | *Trichoderma harzianum* | Antibacterial properties against multidrug-resistant bacteria | [11] |
| | *Rhizopus stolonifer* | Antifungal activity | [12] |
| | *Penicillium oxalicum* | Catalytic activity | |
| Ag | *Penicillium* sp. | Antibacterial activity against MDR | [13] |
| | *F. solani* | Antibacterial effect by fungal process on cotton fabric | [14] |
| | *Pleurotus ostreatus*, *P. florida*, and *P. citrinopileatus* | Antimicrobial activity | [15] |
| | Alternaria alternata | Antifungal activity | [16] |
| | *A. clavatus* | Antimicrobial activity | |
| | *T. viride* | Vegetable and fruit preservation | [18] |
| | *Penicillium* sp. | Antibacterial properties against multidrug-resistant bacteria | [19] |

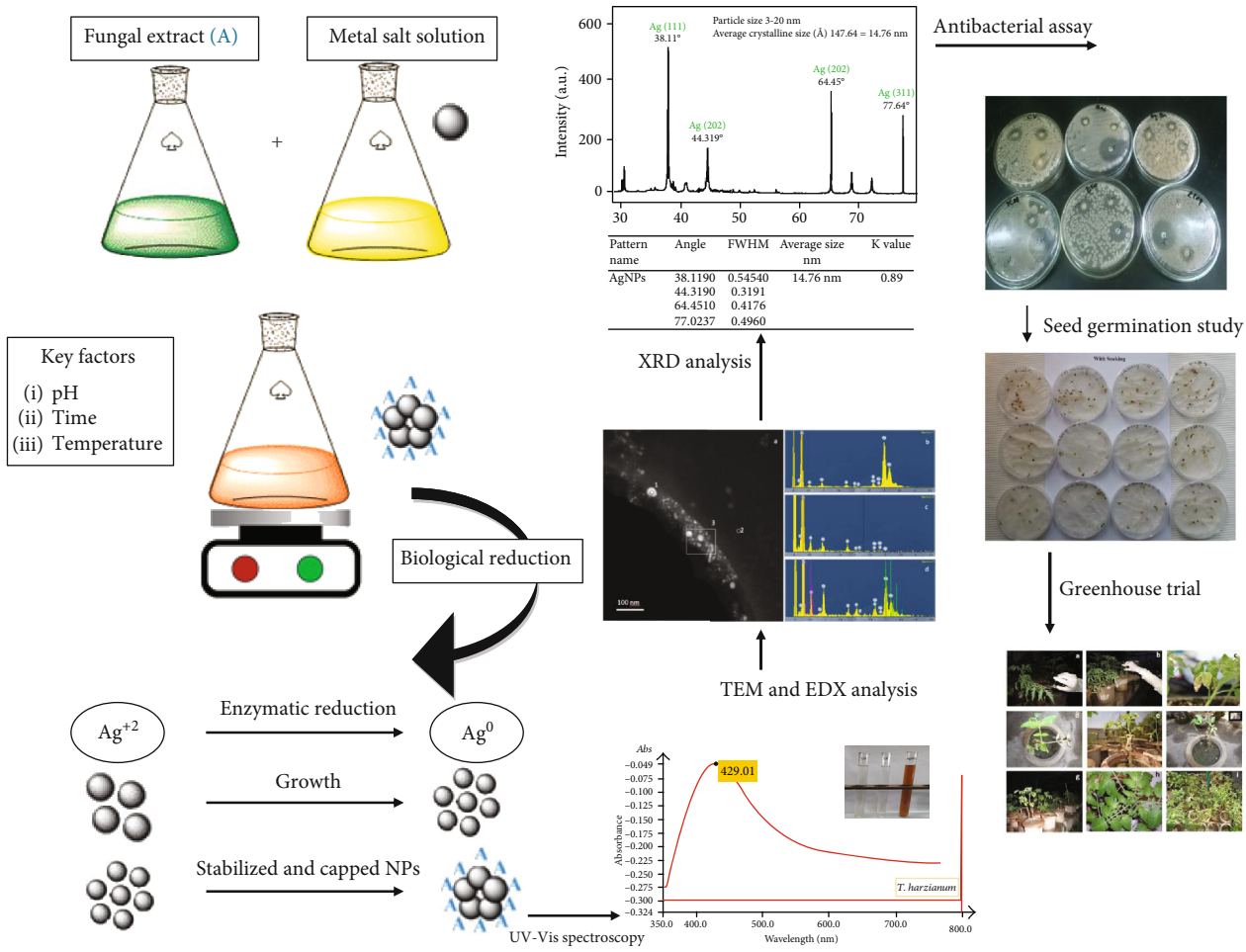


Figure 1: Graphical representation of experimental steps involved in the biological synthesis of AgNPs, characterization, and application.

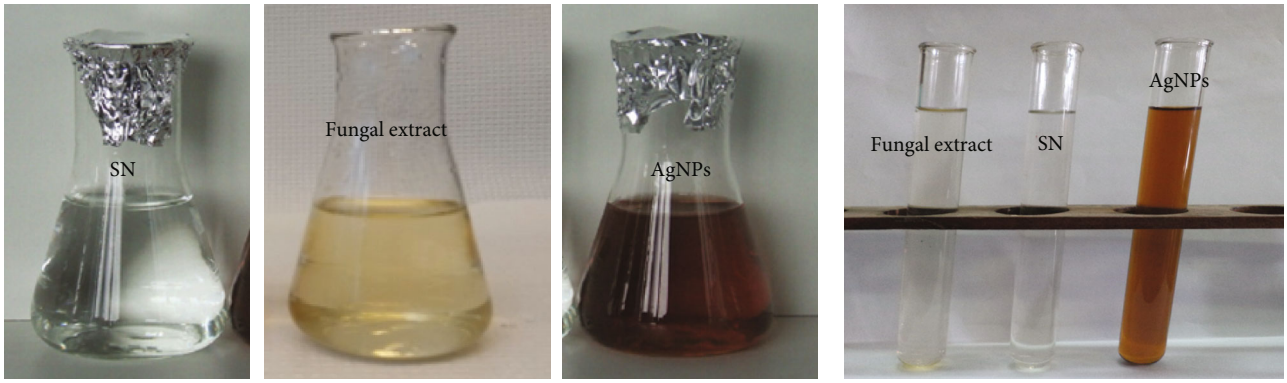


(a) (b)

Figure 2: Colour change from yellowish to dark brown after incubation signifying AgNPs formation. (a) fungla extract of *T. harzianum* treated with silver nitrate solution (SN) resulting in the formation of AgNPs (images reproduced with permission from Ref. [11]]. (b) fungla extract of *A. fumigatus* treated with silver nitrate solution (SN) resulting in the formation of *A. fumigatus*-mediated AgNPs.

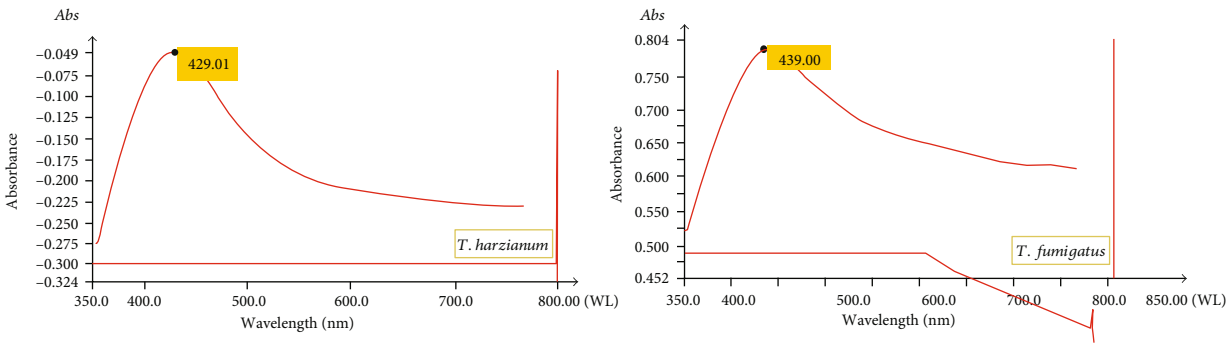


Figure 3: UV spectra for the solution mixture of fungal extract of *T. harzianum* and *A. fumigatus* mixed with $AgNO_3$ salt, showing absorbance peaks at 429.01 and 439 nm, respectively, while the downwards straight line indicates the UV spectrum for the boiled fungal extracts mixed with $AgNO_3$ salt, showing no absorbance peak for AgNPs, supporting the hypothesis of enzyme-based biosynthesis of AgNPs.

way as stated above for AgNP synthesis resulting in no colour change. The resultant reaction mixture was further confirmed for AgNP synthesis by a comparison of its spectra before and after its exposure to fungi as shown in Figure 3. The absorbance spectra for the reaction mixture showed no absorbance confirming that enzymes secreted from fungi are responsible for reducing $Ag^+$ into AgNPs. After the completion of the reaction, the solution was centrifuged at 10,000 rpm for 15 min, the supernatant was separated, and the settled material was dried under reduced pressure to obtain a solid material for characterization purposes.

*3.2. Stability Test.* To check the stability of the reaction mixture, it was kept at room temperature for six months and the absorption was monitored regularly. Our results confirmed that the solution mixture remains highly stable for six months with no evidence of aggregation of particles.

## 4. Effect of pH

Increase in pH has been observed for both samples until a stable SPR peak has been attained using UV-Vis spectroscopy as listed in Table 2. There was no noticeable change in the SPR value of the reaction mixture after 24 hours of the reaction demonstrating that the reaction came to equilibrium. Under low pH value, a pale white and yellow colour was observed which turned into dark brown with successive increase in pH of the reaction [25, 26]. Production of smaller and regular round-shaped AgNPs has been observed under high pH > 10 [26]. The pH values for the synthesized AgNPs on the selected PDB media were found to be in the range of 8.5-11.0.

For further details into the morphology and size of AgNPs, few drops of liquid suspension was coated on a carbon-coated copper grid and allowed to dry. The grid was then scanned employing HRTEM (JEOL 3000F). The obtained TEM image for AgNPs from both fungal samples displayed well-dispersed round-shaped AgNPs of 3-20 nm and 4-20 nm in size, respectively (Figures 4 and 5). TEM images revealed formation on the highest amount of AgNPs for *A. fumigatus* which is in agreement with the high intensity of the SPR value obtained for *A. fumigatus* also correlating with the earlier report of [27]. Thus, fungal species *A. fumigatus* is highly recommended for industrial-scale production of AgNPs. Energy-dispersive X-ray (EDX) analysis for both samples showed a high amount of AgNPs in the silver region confirming complete reduction of $Ag^+$ into AgNPs (Figures 4 and 5). Besides Ag, other weak signals for elements

Table 2: Presenting change in pH values along with UV-Vis peak data for the biogenic AgNPs from *T. harzianum* and *A. fumigatus*.

| Source | Reduction time | UV-Vis peak (nm) | Colour change | pH change |
|---|---|---|---|---|
| *T. harzianum* | 6-24 | 422-429 | Pale yellow-dark brown | 8.8-10.2 |
| *A. fumigatus* | 24 | 425-439 | Light yellow→dark brown | 8.0-11.5 |

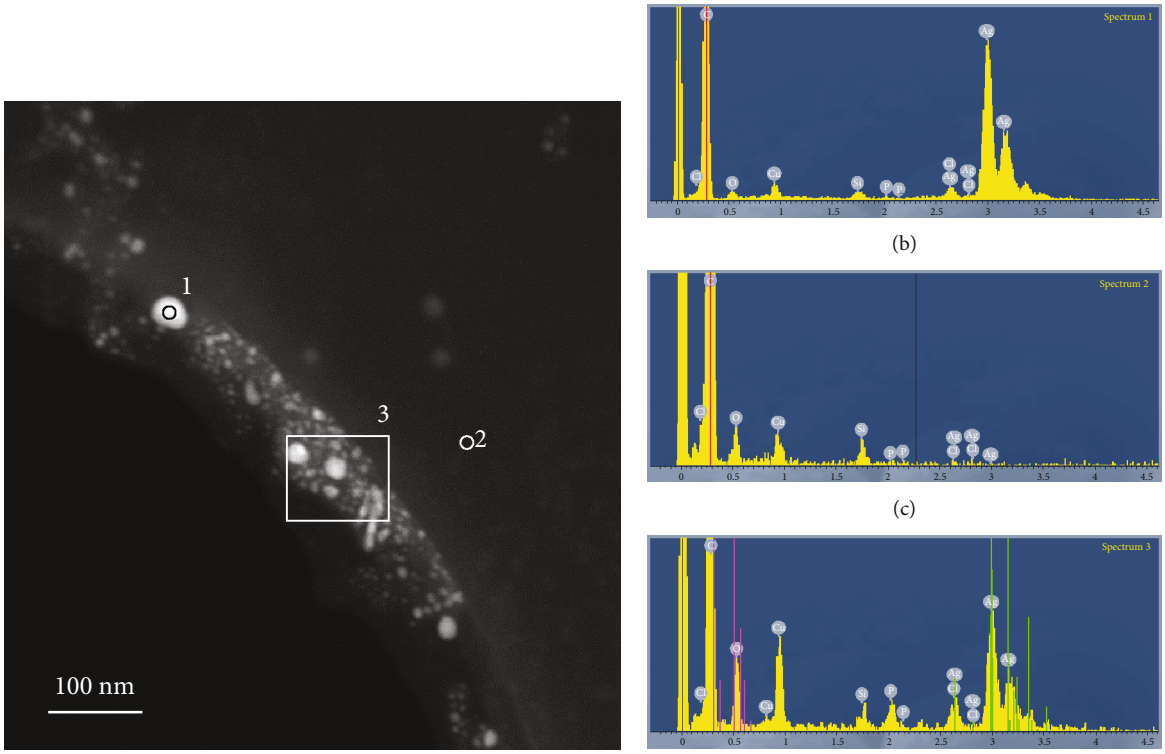


(a) (b) (c) (d)

Figure 4: STEM micrograph (a) of AgNPs obtained from the fungal mycelium of *T. harzianum* challenged with $AgNO_3$ solution and EDX spectra (b–d) from 3 areas. The EDX spectrum from area 3 is shown in (d) with green lines indicating positions of peaks for Ag. These lines are absent in the spectrum in (c) which is taken from the support film (figure reproduced with permission from Ref. [11]).

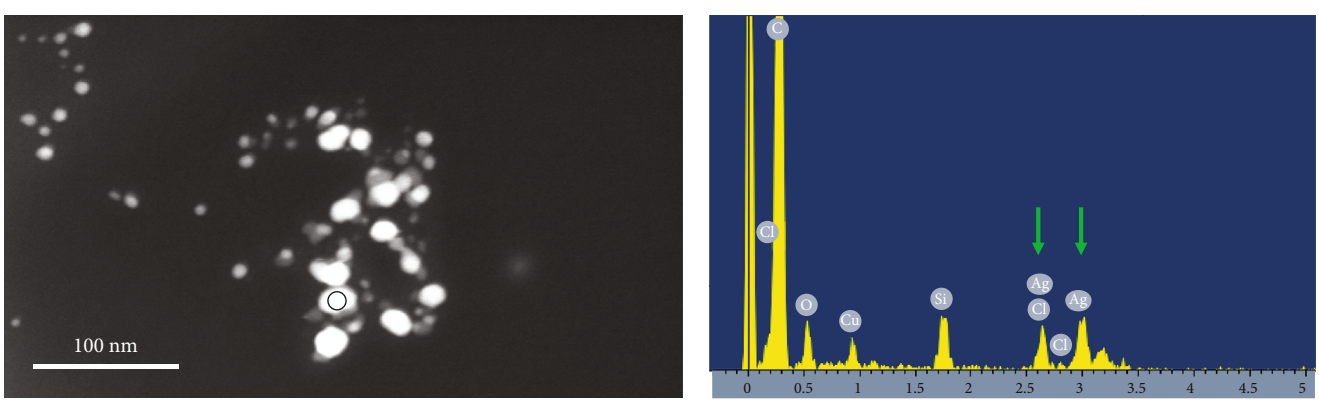


(a) (b)

Figure 5: STEM micrograph (a) of AgNPs from *A. fumigatus*. The circle on a nanoparticle indicates the location from which the EDX spectrum was taken (b). Green arrows point to the peaks at the energies (in keV) corresponding to Ag. Other peaks come from the support film and grid.

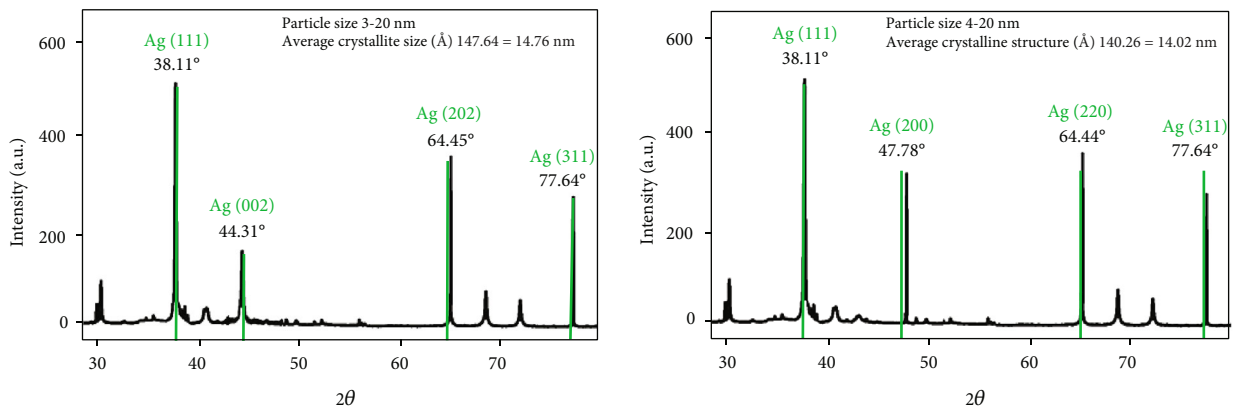


| Pattern name | Angle | FWHM | Average size (nm) | $K$ value |
|---|---|---|---|---|
| AgNPs | 38.1190 | 0.5454 | 14.76 nm | 0.89 |
| | 44.3190 | 0.3191 | | |
| | 64.4510 | 0.4176 | | |
| | 78.0237 | 0.4960 | | |

| Pattern name | Angle | FWHM | Average size (nm) | $K$ value |
|---|---|---|---|---|
| AgNPs | 38.1148 | 0.3578 | 14.02 nm | 0.89 |
| | 47.7831 | 0.4147 | | |
| | 64.4435 | 0.3348 | | |
| | 77.6438 | 0.4278 | | |

Figure 6: X-ray diffraction data for AgNPs fabricated from the reaction mixture of the $AgNO_3$ salt solution and fungal extract of *T. harzianum* and *A. fumigatus*.

including C, Cu, O, and Si were also identified due to the carbon-coated copper TEM grid used for sample deposition. SEAD measurements signify that the extracellular synthesis of AgNPs by *T. harzianum* and *A. fumigatus* produces highly crystalline AgNPs which is also in agreement with the XRD peak data.

The biosynthesized metal NPs were subjected to PXRD analysis for qualitative measurement (phase variety and crystal structure) using PXRD (STOE Stadi MP). XRD pattern for the synthesized AgNPs was recorded in a wide selection of Bragg angles $2\theta$ (30 to 80) operated at a voltage of 40 kV and current of 40 mA with a scan rate of 0.01°/s. The identified silver peaks were quite intense and comparably very sharp, indicating a high face-centered cubic (fcc) crystal structure of the AgNPs. X-ray diffraction peaks correspond to the (111) (002) (202) (311) and (111) (200) (220) (311) sets of lattice planes (Figure 6). The coherently diffracting crystallography domain sizes of 14.76 nm and 14.02 nm of the AgNPs are calculated from the width of the XRD peaks using the Scherrer formula [28]. Thus, the current XRD data infers that AgNPs synthesized from fungi could be effectively utilized for the green synthesis of round-shaped, crystal-structured, and well-defined dimension AgNPs.

## 5. Antimicrobial Effect of Biosynthesized AgNPs

The antibacterial assay of biogenic AgNPs was conducted using standard disc diffusion assay on nutrient agar media described by Noshad et al. [11]. The antibacterial potential for fungal-based AgNPs was evaluated against six bacterial strains including G+ve (*E. coli*, *Agrobacterium tumefaciens*, and *Xanthomonas campestris*) and G-ve (*Clavibacter michiganensis* subsp. *michiganensis*, *Streptococcus thermophilus*, and *Bacillus subtilis*). The synthesized AgNPs were applied in two different concentrations. A comparative study for AgNPs was made with $AgNO_3$ as the negative control and streptomycin solution as the positive control. The inoculated plates were incubated at 37°C for 24 h, and the inhibition zones were calculated using a caliper. All the experiments were carried out in triplicate recorded as the mean standard error (±SE). Compared to control treatments, excellent antimicrobial effect was observed for both samples (AgNPs) (Tables 3(a) and 3(b)). The synthesized biogenic AgNPs completely inhibited bacterial growth at all treated concentrations of 0.088 mg/L, 0.176 mg/L, and 0.44 mg/L. In Figures 7 and 8, it can be observed that the inhibition zones produced by AgNPs are comparable to a standard antibiotic (streptomycin) while being larger than the inhibition zones of control treatments, i.e., SN. Compared to bulk Ag, AgNPs possessed unique biological and physiochemical properties, making them the ideal antibacterial agent. Though the exact antibacterial mechanism of action is yet not understood, there exists a generally accepted mechanism, i.e., through release of $Ag^+$. Many reports suggested the importance of $Ag^+$ in enhanced antibacterial effect [29–32]. There exists a direct relation of the AgNP surface area to released $Ag^+$ concentration. AgNPs of the highest surface area will release the highest concentration of $Ag^+$ and vice versa. When AgNPs interact with a bacterial cell, they bind to the proteins in the cell membrane and penetrate into the cell. The released $Ag^+$ interacts with cellular structures such as respiratory enzymes and releases reactive oxygen species (ROS) resulting in apoptosis like DNA damage and cell death [33, 34].

Furthermore, it was also observed that the antimicrobial effect for both samples (AgNPs) was stronger against *cmm* subsp. *michiganensis*. So a greenhouse trial was planned to check the effect of AgNPs on the *cmm* control. For this purpose, a seed germination test was carried out first in the laboratory condition to see the impact of AgNPs on the seed germination rate, though several studies have reported varied influence of NPs on seed germination and root growth. For example, AgNPs had positive impact on the germination rate

Table 3

(a) Represents measurement for zone of inhibition (mm) for AgNPs from fungal filtrate of *A. fumigatus* against the listed microbial pathogens and comparative studies with different controls including streptomycin as the standard and silver nitrate (SN) as the blank

| Indicator bacteria | Zone of inhibition (mm ± SE) | | | | |
|---|---|---|---|---|---|
| | Streptomycin | AgNP 0.088 mg/L/disk | AgNP 0.176 mg/L/disk | AgNP 0.44 mg/L/disk | $AgNO_3$ |
| *C. michiganensis* | 1.16 ± 0.13 | 1.10 ± 0.10 | 1.14 ± 0.10 | 1.15 ± 0.10 | 0.86 ± 0.08 |
| *X. campestris* | 1.16 ± 0.13 | 0.96 ± 0.08 | 1.10 ± 0.10 | 1.10 ± 0.13 | 0.86 ± 0.08 |
| *E. coli* | 1.25 ± 0.10 | 1.06 ± 0.03 | 1.10 ± 0.08 | 1.10 ± 0.00 | 0.86 ± 0.08 |
| *S. thermophilus* | 1.36 ± 0.10 | 1.03 ± 0.13 | 1.03 ± 0.10 | 1.03 ± 0.11 | 0.86 ± 0.08 |
| *Ag. tumefaciens* | 1.13 ± 0.11 | 1.02 ± 0.05 | 1.06 ± 0.10 | 1.06 ± 0.08 | 0.86 ± 0.08 |
| *B. subtilis* | 1.26 ± 0.10 | 1.18 ± 0.10 | 1.20 ± 0.10 | 1.22 ± 0.03 | 0.86 ± 0.08 |

(b) Represents measurement for zone of inhibition (mm) for *T. harzianum*-mediated AgNPs against the listed microbial pathogens

| Indicator bacteria | Zone of inhibition (mm ± SE) | | | | |
|---|---|---|---|---|---|
| | Streptomycin | AgNP 0.088 mg/L/disk | AgNP 0.176 mg/L/disk | AgNP 0.44 mg/L/disk | $AgNO_3$ |
| *C. michiganensis* | 1.16 ± 0.13 | 0.93 ± 0.08 | 1.12 ± 0.08 | 1.16 ± 0.08 | 0.80 ± 0.01 |
| *X. campestris* | 1.12 ± 0.10 | 0.96 ± 0.12 | 1.06 ± 0.11 | 1.10 ± 0.08 | 0.80 ± 0.01 |
| *E. coli* | 1.46 ± 0.11 | 1.03 ± 0.08 | 1.16 ± 0.11 | 1.39 ± 0.08 | 0.80 ± 0.01 |
| *S. thermophilus* | 1.36 ± 0.03 | 1.08 ± 0.02 | 1.08 ± 0.03 | 1.30 ± 0.08 | 0.80 ± 0.01 |
| *Ag. tumefaciens* | 1.06 ± 0.08 | 0.73 ± 0.08 | 0.73 ± 0.08 | 1.00 ± 0.08 | 0.80 ± 0.01 |
| *B. subtilis* | 2.25 ± 0.03 | 1.26 ± 0.12 | 1.26 ± 0.03 | 2.15 ± 0.08 | 0.80 ± 0.01 |

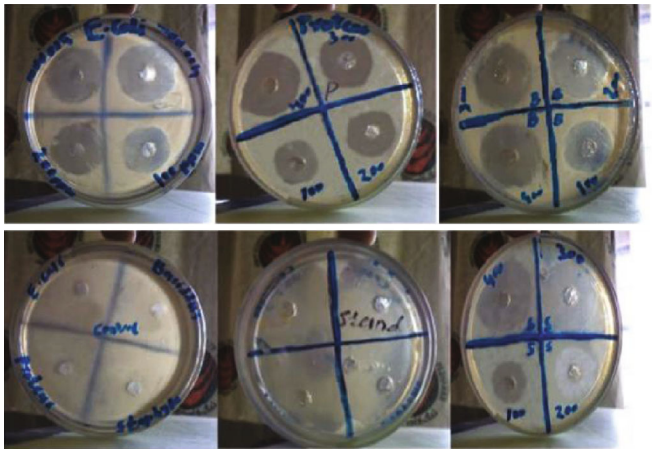

Figure 7: Antibacterial activity of biologically synthesized AgNPs from *T. harzianum* against G+ve (*E. coli, Agrobacterium tumefaciens*, and *Xanthomonas campestris*) and G-ve (*Clavibacter michiganensis* subsp. *michiganensis*, *Streptococcus thermophilus*, and *Bacillus subtilis*).

and seedling growth of *Pennisetum glaucum* [35]. $TiO_2$ NPs increased the seed germination rate of funnel seeds, and the same effect has been reported for ZnO NPs in cucumber [36]. In the case of corn, barley, and soybean, an enhanced germination rate has been documented using CNTs [36], though CNTs pose reduced seed germination in *L. sativum* [35]. Meanwhile, other investigations reported negative impact of CuO-based NPs on the seed germination rate of rice [37] while it had no effect on the seed germination rate of maize [38].

Results suggested that *S. lycopersicum* seeds treated with AgNPs resulted in a higher number of sprouted seeds in 3 to 12 days of germination, while in control treatments, the same effect has been observed on 14 to 18 days (Figure 9). Furthermore, compared to control treatments, increased length has been observed for AgNP-treated seedlings

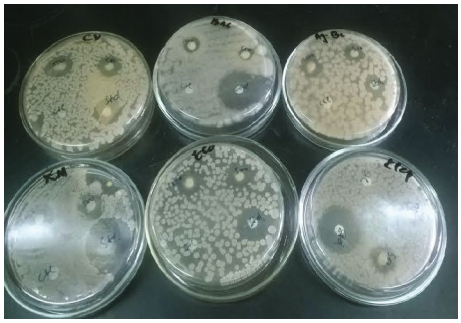

Figure 8: Antibacterial activity of biologically synthesized AgNPs from *A. fumigatus* against the Gram-positive and Gram-negative bacteria mentioned in Figure 7.

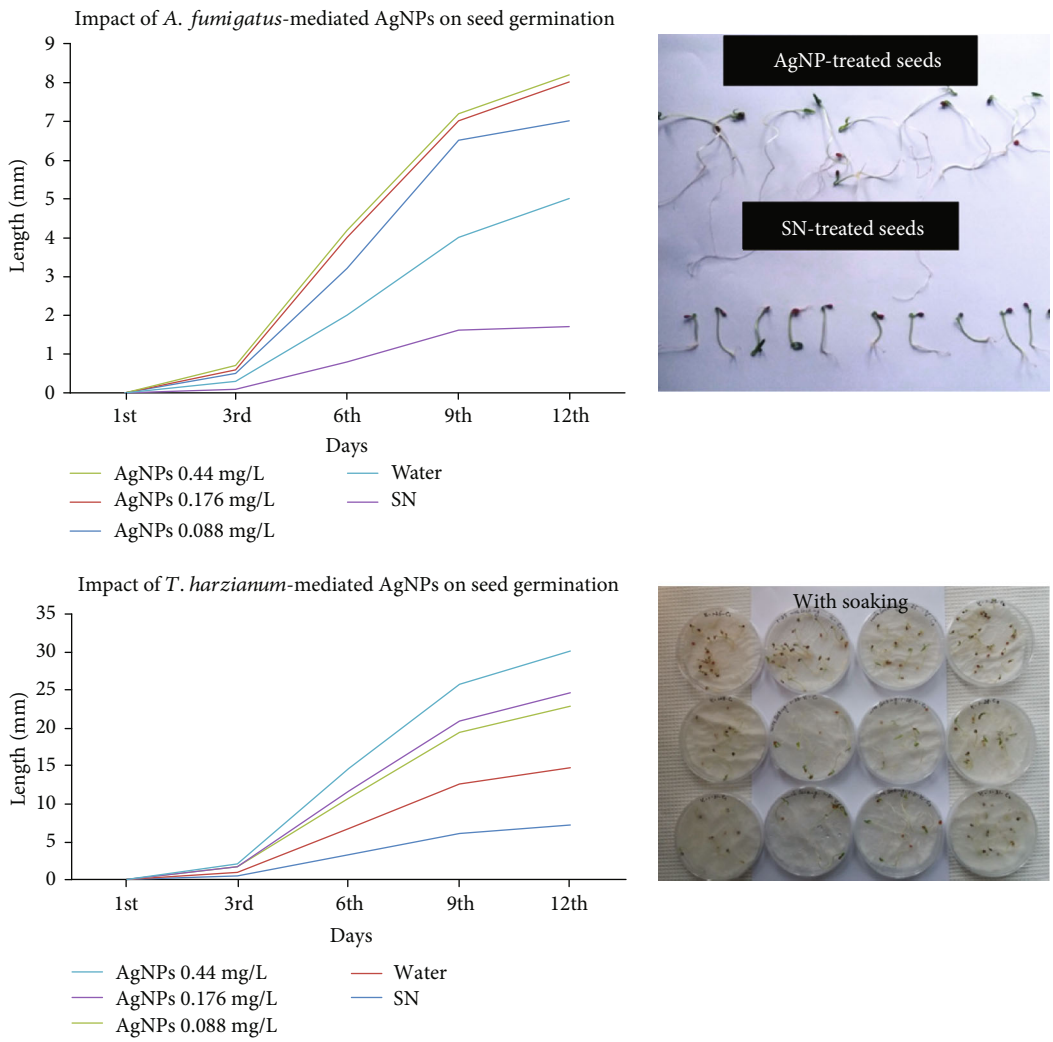


Figure 9: Graphical presentation for the impact of synthesized AgNPs on seed germination and seed growth. Panel (a) represents *A. fumigatus*-made AgNPs while (b) is for *T. harzianum*-made AgNPs. The inserted images (c) clearly demonstrate increased seedling length for AgNP-treated seedlings.

(Figure 9). The possible reason behind the enhanced seedling growth rate could be the efficient water and nutrient uptake by the treated seeds as AgNPs can penetrate through the seed coat and may activate the embryo. During penetration, AgNPs cause more new pores that remain helpful in carrying nutrients, efficiently leading to fast germination and growth rate [39]. $AgNO_3$ solution resulted in reduction in all observed growth parameters suggesting the toxic behavior

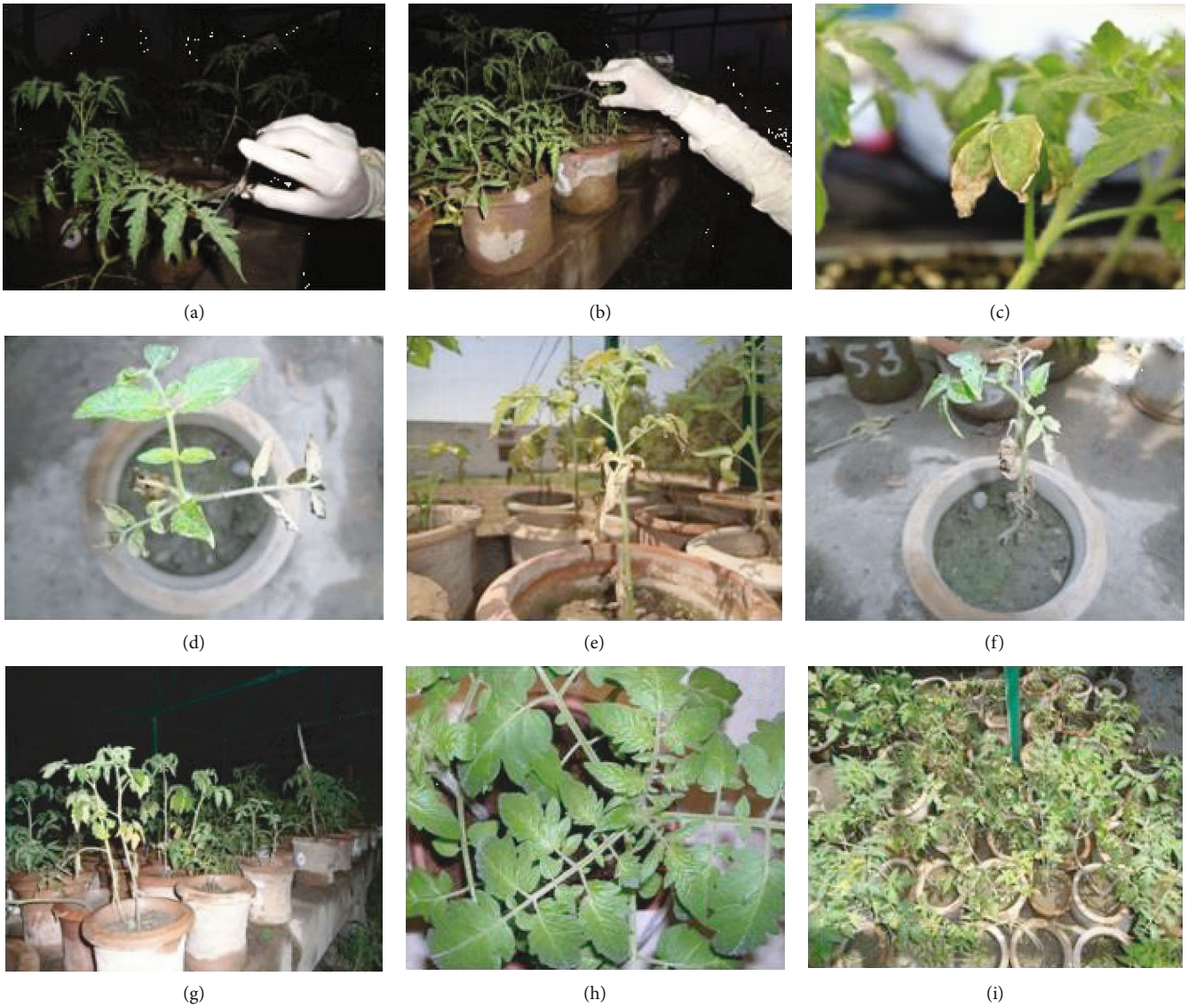


Figure 10: (a, b) shows inoculation of 6-week-old plants of tomato with *cmm* culture. (c, d) represents symptoms of BCT infection on tomato leaves upon artificial inoculation of *cmm*—appeared in control treatments only. (e, f) represents $AgNO_3$-treated plants—symptoms appeared and reduced growth of plants was also observed. Normal healthy growth was observed for AgNP-treated plants (g–i).

of a higher concentration of ionic silver to the plants, whereas only fungal extract had no measurable effect on the germination rate of *S. lycopersicum* seeds. It can be assumed here that stability of AgNPs with the fungal extract might be responsible for reducing its toxicity, also supported by [40]. The obtained outcome could be helpful to enhance the seed germination rate and seedling growth especially in dormant seeds. 6-week-old plants were transplanted (1 seedling/pot) to 15 cm diameter earthen pots. Each pot had 2 kg of standard commercial mix with slow release fertilizer. Different doses, i.e., 0.088 mg/L, 0.176 mg/L, and 0.44 mg/L, of AgNPs were mixed with the soil before transplanting seedlings. All of the plants were inoculated by clipping 3 inoculation sites per plant including 1 shoot per plant and the 2 youngest actively growing leaves per shoot and middle stem with scissors that had been dipped into *cmm* suspension. On the 7$^{th}$ week of the plant growth, plants were exposed to AgNPs weekly, once the symptoms appeared. Results demonstrated that compared to the control treatment, the biosynthesized AgNPs inhibited the growth of *cmm* completely (Figure 10). Importantly, application of the $AgNO_3$ solution alone resulted in reduced growth of plants which highly supports our assumption that the stability of AgNPs with the fungal extract might be responsible for reducing its toxicity in agreement with [40]. Compared to the control, all of the plant growth parameters including plant height (cm), tomato yield/plant (g), plant fresh biomass (g), number of shoots/plant, and plant dry biomass (g) showed significant healthy growth supporting the beneficial effect of biogenic AgNPs against the harmful effects of the bacterial pathogen *cmm* (Table 4).The

Table 4: Impact of AgNPs on disease incidence %, plant height, fresh biomass, dry biomass, and shoot per plant grown under screenhouse conditions.

| | Treatment | Plant height | Fresh biomass | Dry biomass | Shoot/plant | D.I.% |
|---|---|---|---|---|---|---|
| *T. harzianum*-made AgNPs | 0.088 mg/L | 65.2 ± 0.36 | 355.38 ± 1.26 | 76.79 ± 0.31 | 5.5 ± 0.33 | 31.47 |
| | 0.176 mg/L | 68.0 ± 0.33 | 375.32 ± 1.30 | 88.83 ± 0.39 | 6.0 ± 0.23 | 25.50 |
| | 0.44 mg/L | 72.8 ± 0.27 | 380.28 ± 0.91 | 90.07 ± 0.19 | 7.2 ± 0.23 | 22.61 |
| *A. fumigatus*-made AgNPs | 0.088 mg/L | 62.4 ± 0.69 | 360.00 ± 0.97 | 85.66 ± 0.45 | 5.8 ± 0.43 | 9.52 |
| | 0.176 mg/L | 64.6 ± 0.80 | 372.00 ± 0.91 | 90.30 ± 0.48 | 6.0 ± 0.27 | 7.14 |
| | 0.44 mg/L | 65.0 ± 0.33 | 382.80 ± 0.49 | 92.40 ± 0.43 | 7.5 ± 0.06 | 5.95 |
| | Streptomycin | 72.8 ± 0.79 | 381.60 ± 0.90 | 95.20 ± 0.72 | 7.6 ± 0.18 | 6 |
| | SN | 39.0 ± 0.66 | 105.20 ± 0.76 | 39.50 ± 0.51 | 2.4 ± 0.18 | 100 |
| | Water | 36.8 ± 0.27 | 159.40 ± 0.64 | 27.88 ± 0.31 | 2.4 ± 0.18 | 100 |

*in vitro* and screenhouse experiments remain successful against BCT control and showed a similar pattern of results as observed in seed germination and seedling growth.

## 6. Conclusion

Due to the antibiotic resistance profile, multidrug-resistant bacteria are developing which is becoming a severe problem. Use of broad-spectrum antibiotics to control it is more toxic, less effective, and more expensive [41]. So the researchers are attracted towards AgNPs, as there is much evidence suggesting that the use $Ag^+$ in the form AgNPs enhances the antibacterial activity many folds [42]. Thus, the results presented in this study are novel that could emerge as a better alternate to physical and chemical syntheses of AgNPs. The development of fungi-mediated AgNPs can overcome MDR bacteria, especially *cmm* subsp. *michiganensis* which is responsible for the bacterial canker of tomato. However, further studies are required to assess the toxicity level and possible side effects that may arise from the penetration ability of AgNPs.

## Data Availability

The data used to support the findings of this study are included within the article.

## Conflicts of Interest

The authors declare no conflict of interest.

## Acknowledgments

The authors are grateful to Lund University, Sweden, the Higher Education Commission-Pakistan, and the "Atomic Resolution Cluster"—a Research Infrastructure Fellow program of the Swedish Foundation for Strategic Research. I duly acknowledge Sven Lidin for providing the PXRD lab facility.

## References

[1] J. O. W. González, N. Stefanazzi, A. P. Murray, A. A. Ferrero, and B. F. Band, "Novel nanoinsecticides based on essential oils to control the German cockroach," *Journal of Pest Science*, vol. 88, no. 2, pp. 393–404, 2015.

[2] H. Chhipa and P. Joshi, "Nanofertilisers, nanopesticides and nanosensors in agriculture," in *Nanoscience in Food and Agriculture 1*, S. Ranjan, N. Dasgupta, and E. Lichtfouse, Eds., pp. 247–282, Springer, Champ, 2016.

[3] P. L. Kashyap, X. Xiang, and P. Heiden, "Chitosan nanoparticle based delivery systems for sustainable agriculture," *International Journal of Biological Macromolecules*, vol. 77, pp. 36–51, 2015.

[4] I. C. Hwang, T. H. Kim, S. H. Bang et al., "Insecticidal effect of controlled release formulations of etofenprox based on nanobio technique," *Journal of the Faculty of Agriculture, Kyushu University*, vol. 56, no. 1, pp. 33–40, 2011.

[5] J. J. Kim, "Nano silver chemotherapeutic agents and its applications," *International Journal of Chemical Engineering*, vol. 22, pp. 655–660, 2004.

[6] H. P. Borase, B. K. Salunke, R. B. Salunkhe et al., "Plant extract: a promising biomatrix for ecofriendly, controlled synthesis of silver nanoparticles," *Applied Biochemistry and Biotechnology*, vol. 173, no. 1, pp. 1–29, 2014.

[7] D. S. Balaji, S. Basavaraja, R. Deshpande, D. B. Mahesh, B. K. Prabhakar, and A. Venkataraman, "Extracellular biosynthesis of functionalized silver nanoparticles by strains of *Cladosporium cladosporioides* fungus," *Colloids and Surfaces B: Biointerfaces*, vol. 68, no. 1, pp. 88–92, 2009.

[8] A. K. Gade, P. Bonde, A. P. Ingle, P. D. Marcato, N. Durán, and M. K. Rai, "Exploitation of *Aspergillus niger* for synthesis of silver nanoparticles," *Journal of Biobased Materials and Bioenergy*, vol. 2, no. 3, pp. 243–247, 2008.

[9] A. Ingle, A. Gade, S. Pierrat, C. Sonnichsen, and M. Rai, "Mycosynthesis of silver nanoparticles using the fungus *Fusarium acuminatum* and its activity against some human pathogenic bacteria," *Current Nanoscience*, vol. 4, no. 2, pp. 141–144, 2008.

[10] S. U. Picoli, M. Durán, P. F. Andrade, and N. Duran, "Silver nanoparticles/silver chloride (Ag/AgCl) synthesized from *Fusarium oxysporum* acting against *Klebsiella pneumouniae* carbapenemase (KPC) and extended spectrum beta-lactamase (ESBL)," *Frontiers in Nanoscience and Nanotechnology*, vol. 2, no. 2, pp. 107–110, 2016.

[11] A. Noshad, M. Iqbal, L. Folkers et al., "Antibacterial effect of silver nanoparticles (AgNPs) synthesized from Trichoderma harzianum against Clavibacter michiganensis," *Journal of Nano Research*, vol. 58, pp. 10–19, 2019.

[12] V. Rathod, A. Banu, and E. Ranganath, "Biosynthesis of highly stabilized silver nanoparticles by *Rhizopus stolonifer* and their anti-fungal efficacy," *International Journal of Pharmacy and Biomedical Sciences*, vol. 2, no. 1, pp. 241–245, 2012.

[13] S. Honary, H. Barabadi, E. Gharaei-Fathabad, and F. Naghibi, "Green synthesis of copper oxide nanoparticles using *Penicillium aurantiogriseum*, *Penicillium citrinum* and *Penicillium waksmanii*," *Digest Journal of Nanomaterials and Biostructures*, vol. 7, no. 3, pp. 999–1005, 2012.

[14] M. El-Rafie, A. A. Mohamed, T. I. Shaheen, and A. Hebeish, "Antimicrobial effect of silver nanoparticles produced by fungal process on cotton fabrics," *Carbohydrate Polymers*, vol. 80, no. 3, pp. 779–782, 2010.

[15] A. Noshad, A. Noshad, M. Iqbal et al., "Aphidicidal potential of ethyl acetate extract from Pleurotus ostreatus," *Sarhad Journal of Agriculture*, vol. 31, no. 2, pp. 101–105, 2015.

[16] M. Gajbhiye, J. Kesharwani, A. Ingle, A. Gade, and M. Rai, "Fungus-mediated synthesis of silver nanoparticles and their activity against pathogenic fungi in combination with fluconazole," *Nanomedicine: Nanotechnology, Biology and Medicine*, vol. 5, no. 4, pp. 382–386, 2009.

[17] V. C. Verma, R. N. Kharwar, and A. Gange, "Biosynthesis of antimicrobial silver nanoparticles by the endophytic fungus *Aspergillus clavatus*," vol. 5, no. 1, pp. 33–40, 2010.

[18] Y. Qian, H. Yu, D. He et al., "Biosynthesis of silver nanoparticles by the endophytic fungus *Epicoccum nigrum* and their activity against pathogenic fungi," *Bioprocess and Biosystems Engineering*, vol. 36, no. 11, pp. 1613–1619, 2013.

[19] D. Singh, V. Rathod, S. Ninganagouda, J. Hiremath, A. K. Singh, and J. Mathew, "Optimization and characterization of silver nanoparticle by endophytic fungi *Penicillium* sp. isolated from *Curcuma longa* (turmeric) and application studies against MDR *E. coli* and S. *aureus*," *Bioinorganic Chemistry and Applications*, vol. 2014, Article ID 408021, 8 pages, 2014.

[20] D. L. Strider, "Bacterial canker of tomato caused by Corynebacterium michiganense; a literature review and bibliography," *North Carolina Agricultural Experiment Station Bulletin*, 1969.

[21] M. J. Davis, A. G. Gillaspie, A. K. Vidaver, and R. W. Harris, "*Clavibacter:* a new genus containing some phytopathogenic coryneform bacteria, including *Clavibacter xyli* subsp. *xyli* sp. nov., subsp. nov. and *Clavibacter xyli* subsp. *cynodontis* subsp. nov., pathogens that cause ratoon stunting disease of sugarcane and bermudagrass stunting disease," *International Journal of Systematic Bacteriology*, vol. 34, no. 2, pp. 107–117, 1984.

[22] M. E. Rateb, I. Hallyburton, W. E. Houssen et al., "Induction of diverse secondary metabolites in *Aspergillus fumigatus* by microbial co-culture," *RSC Advances*, vol. 3, no. 34, pp. 14444–14450, 2013.

[23] S. Sunkar and C. V. Nachiyar, "Biogenesis of antibacterial silver nanoparticles using the endophytic bacterium *Bacillus cereus* isolated from *Garcinia xanthochymus*," *Asian Pacific Journal of Tropical Biomedicine*, vol. 2, no. 12, pp. 953–959, 2012.

[24] K. Vahabi, G. A. Mansoori, and S. J. I. J. Karimi, "Biosynthesis of silver nanoparticles by fungus Trichoderma reesei (a route for large-scale production of AgNPs)," *Insciences Journal*, vol. 1, no. 1, pp. 65–79, 2011.

[25] J.-c. Qu, Y. P. Chang, Y. H. Ma et al., "A simple and sensitive colorimetric method for the determination of propafenone by silver nanoprobe," *Sensors and Actuators B: Chemical*, vol. 174, pp. 133–139, 2012.

[26] M. K. Alqadi, O. A. A. Noqtah, F. Y. Alzoubi, J. Alzouby, and K. Aljarrah, "pH effect on the aggregation of silver nanoparticles synthesized by chemical reduction," *Materials Science-Poland*, vol. 32, no. 1, pp. 107–111, 2014.

[27] K. Zomorodian, S. Pourshahid, A. Sadatsharifi et al., "Biosynthesis and characterization of silver nanoparticles by *Aspergillus* species," *BioMed Research International*, vol. 2016, Article ID 5435397, 6 pages, 2016.

[28] V. Petříček, M. Dušek, and L. Palatinus, "Crystallographic computing system JANA2006: general features," *Zeitschrift für Kristallographie - Crystalline Materials*, vol. 229, no. 5, pp. 345–352, 2014.

[29] X. Zhong, Y. Song, P. Yang et al., "Titanium surface priming with phase-transited lysozyme to establish a silver nanoparticle-loaded chitosan/hyaluronic acid antibacterial multilayer via layer-by-layer self-assembly," vol. 11, no. 1, Article ID e0146957, 2016.

[30] J.-C. Jin, X. J. Wu, J. Xu, B. B. Wang, F. L. Jiang, and Y. Liu, "Ultrasmall silver nanoclusters: Highly efficient antibacterial activity and their mechanisms," *Biomaterials Science*, vol. 5, no. 2, pp. 247–257, 2017.

[31] P. C. Lombardo, A. L. Poli, L. F. Castro, J. R. Perussi, and C. C. Schmitt, "Photochemical deposition of silver nanoparticles on clays and exploring their antibacterial activity," *ACS Applied Materials & Interfaces*, vol. 8, no. 33, pp. 21640–21647, 2016.

[32] T. Kim, G. B. Braun, Z. G. She, S. Hussain, E. Ruoslahti, and M. J. Sailor, "Composite Porous silicon–silver nanoparticles as theranostic antibacterial agents," *ACS Applied Materials & Interfaces*, vol. 8, no. 44, pp. 30449–30457, 2016.

[33] K. Zawadzka, K. Kądzioła, A. Felczak et al., "Surface area or diameter – which factor really determines the antibacterial activity of silver nanoparticles grown on TiO2coatings?," *New Journal Chemistry*, vol. 38, no. 7, pp. 3275–3281, 2014.

[34] U. Klueh, V. Wagner, S. Kelly, A. Johnson, and J. D. Bryers, "Efficacy of silver-coated fabric to prevent bacterial colonization and subsequent device-based biofilm formation," *Journal of Biomedical Materials Research*, vol. 53, no. 6, pp. 621–631, 2000.

[35] A. Parveen and S. Rao, "Effect of nanosilver on seed germination and seedling growth in *Pennisetum glaucum*," *Journal of Cluster Science*, vol. 26, no. 3, pp. 693–701, 2015.

[36] G. de la Rosa, M. L. López-Moreno, D. de Haro, C. E. Botez, J. R. Peralta-Videa, and J. L. Gardea-Torresdey, "Effects of ZnO nanoparticles in alfalfa, tomato, and cucumber at the germination stage: root development and X-ray absorption spectroscopy studies," *Pure and Applied Chemistry*, vol. 85, no. 12, pp. 2161–2174, 2013.

[37] A. K. Shaw and Z. J. C. Hossain, "Impact of nano-CuO stress on rice (*Oryza sativa* L.) seedlings," *Chemosphere*, vol. 93, no. 6, pp. 906–915, 2013.

[38] Z. Wang, X. Xie, J. Zhao et al., "Xylem- and phloem-based transport of cuo nanoparticles in maize (*Zea mays* L.)," vol. 46, no. 8, pp. 4434–4441, 2012.

[39] C. Srinivasan and R. Saraswathi, "Nano-agriculture—carbon nanotubes enhance tomato seed germination and plant growth," *Current science*, vol. 99, no. 3, pp. 274-275, 2010.

[40] J. Yasur and P. U. Rani, "Environmental effects of nanosilver: impact on castor seed germination, seedling growth, and plant

physiology," *Environmental Science and Pollution Research*, vol. 20, no. 12, pp. 8636–8648, 2013.

[41] G. F. Webb, E. M. C. D'Agata, P. Magal, and S. Ruan, "A model of antibiotic-resistant bacterial epidemics in hospitals," *Proceedings of the National Academy of Sciences of the United States of America*, vol. 102, no. 37, pp. 13343–13348, 2005.

[42] C. G. Gemmell, D. I. Edwards, A. P. Fraise et al., "Guidelines for the prophylaxis and treatment of methicillin-resistant *Staphylococcus aureus* (MRSA) infections in the UK," *Journal of Antimicrobial Chemotherapy*, vol. 57, no. 4, pp. 589–608, 2006.

Hindawi
Journal of Nanomaterials
Volume 2019, Article ID 3241968, 8 pages
https://doi.org/10.1155/2019/3241968

*Research Article*

# Preparation and Properties of Nanocellulose from *Miscanthus x giganteus*

**Valerii A. Barbash, Olha V. Yashchenko, and Olesia A. Vasylieva**

*Department of Ecology and Technology of Plant Polymers, Igor Sikorsky Kyiv Polytechnic Institute, Prospect Peremohy, 37 Kyiv 03056, Ukraine*

Correspondence should be addressed to Valerii A. Barbash; v.barbash@kpi.ua

Received 30 August 2019; Accepted 28 October 2019; Published 12 November 2019

Academic Editor: Sesha Srinivasan



*Miscanthus x giganteus* stalks were used to make organosolvent pulp and nanocellulose. The organosolvent miscanthus pulp (OMP) was obtained through thermal treatment in the mixture of glacial acetic acid and hydrogen peroxide at the first stage and the alkaline treatment at the second stage. Hydrolysis of the never-dried OMP was carried out by a solution of sulfuric acid with concentrations of 43% and 50% and followed by ultrasound treatment. Structural changes and the crystallinity index of OMP and nanocellulose were studied by SEM and FTIR methods. X-ray diffraction analysis confirmed an increase in the crystallinity of OMP and nanocellulose as a result of thermochemical treatment. We show that nanocellulose has a density of up to 1.6 g/cm$^3$, transparency up to 82%, and a crystallinity index of 76.5%. The AFM method showed that the particles of nanocellulose have a diameter in the range from 10 to 20 nm. A thermogravimetric analysis confirmed that nanocellulose films have a denser structure and lower mass loss in the temperature range of 320–440°C compared to OMP. The obtained nanocellulose films have high tensile strength up to 195 MPa. The nanocellulose obtained from OMP exhibits the improved properties for the preparation of new nanocomposite materials.

## 1. Introduction

Industrial developments, as well as changing consumption patterns associated with growing economies and prosperity, contribute to increasing demand for both renewable biological resources and nonrenewable stocks of minerals, metals, and fossil fuels. The limited reserves of mineral resources (oil, gas, and coal) determine the relevance of research in technologies for producing biodegradable materials from the renewable sources of raw materials [1]. Such renewable resources include raw plant materials, the products from the treatment of which have found wide use in various industries: chemical, pharmaceutical, paper, textile, electronic, and others [2, 3]. The main component of plant materials is cellulose, the most common biopolymer in nature. Cellulose is used for the production of nanocellulose and composite materials.

Nanocellulose is a new class of nanomaterials, which has unique properties, such as nanoscalability and biocompatibility and being a renewable and biodegradable material, that enable its use in many fields [4, 5]. Nanocellulose is used in optoelectronics, in the production of chemical current of sources and sorbents, for reinforcing and improving the thermal stability of polymeric and paper composites [6–8]. Nanocellulose has been incorporated into polymer matrices to produce reinforced composites of tenfold to hundredfold mechanical strength [9], as well as enhanced optical transparency [10]. These specific characteristics of nanocellulose reinforce mechanical properties of the polymer and improve the film's mechanical and/or barrier properties [11, 12].

Nanocellulose is obtained by acid hydrolysis and mechanical, oxidative, and enzymatic treatments of cellulose fibers [13–15]. The chemical method of hydrolysis of cellulose by acid solutions is the most common technique [16]. Usually, nanocellulose is obtained by acid hydrolysis of cellulosic materials from wood and nonwood plants. The main raw material used to produce cellulose on a worldwide scale is wood. The search for alternative sources of plant materials

continues to be a priority in countries where wood is scarce as a natural resource. Nonwood plants are a good candidate for an alternative source of such raw materials in the production of pulp.

In our previous works, we described the technology for obtaining nanocellulose from wheat straw [17], flax [18], and kenaf [19] and its properties. In the current work, we describe the conditions for obtaining nanocellulose from *Miscanthus x giganteus*, which is widely cultivated in Europe and the United States. Miscanthus giganteus (*Miscanthus x giganteus*) is a fast-growing perennial herb that grows in the European climatic zone, quite unpretentious and inexpensive to grow, with a high content of cellulose up to 49.7% [20]. Miscanthus is quite resistant to diseases, has frost resistance, and has rapid growth. The yield of miscanthus can reach 10-35 dry tons per hectare, and after a single planting, culture can be collected annually for 15-20 years [21]. Compared to wood, which requires about 10-12 years to fully mature, miscanthus requires a maximum of 3 years after planting to reach its peak dry biomass production which further showcases its potential as a viable source of raw materials. It is also one of the few plant species being dedicated to biomass cropping and is currently farmed in Europe and the United States primarily for use in electricity and heat generation (by combustion) as well as feedstock for biofuels. More recently, miscanthus has been expanded into other markets such as advanced materials and biobased products [22]. We characterize the organosolvent pulp obtained from the miscanthus using an environmentally safer method and the nanocellulose that can be obtained from it, and we also report on the properties of this nanocellulose.

## 2. Materials and Methods

*2.1. Raw Material and Chemicals.* We used the second-year miscanthus biomass as feedstock. The plant was grown in 2016-2017 in the grey-forest soil at the research field in Kyiv's vicinity. Miscanthus stalks were cleaned of leaves and nodes, crushed into particles of 5-7 mm in size and placed in a desiccator to maintain constant moisture and chemical composition. The chemical composition of miscanthus was determined according to TAPPI standards [23], namely, T 222 for lignin, T 257 for substances extracted with hot water, T 212 for substances extracted with 1% solution of NaOH, T 204 for substances extracted with alcohol-benzene solution, and T 211 to determine ash content and cellulose by the Kurschner-Hoffer method. All chemicals, including ice acetic acid, 35% hydrogen peroxide, NaOH, and sulfuric acid, were produced in Ukraine and used without further purification.

*2.2. Obtaining Pulp.* Cooking of miscanthus pulp was carried out in two stages. At the first stage, treatment of *Miscanthus x giganteus* in a mixture of glacial acetic acid and 35% hydrogen peroxide in a volume ratio of 70 : 30% at the liquid to solid ratio 10 : 1, at a temperature of $95 \pm 2^{\circ}$C for 30–240 min, was carried out. The cooking regime was determined in previous studies [17–19].

At the second stage, the alkaline treatment of obtained organosolvent miscanthus pulp (OMP) by solution of NaOH concentration of 7% for 15–240 min, at the liquid to solid ratio 12 : 1 at a temperature of $95 \pm 2^{\circ}$C, was carried out. The OMP after alkaline treatment was washed with hot distilled water to a neutral pH and was stored in sealed bags in a refrigerator for further research. The quality parameters of the obtained OMP samples we determined according to standard methods [23].

*2.3. Obtaining Nanocellulose.* Hydrolysis of the never-dried OMP was carried out by solution of sulfuric acid with concentrations of 43 and 50%, at the liquid to solid ratio 10 : 1, at temperatures of 40 and 60°C for 30–90 min, to obtain nanocellulose. The calculated amount of sulfate acid with the corresponding concentration was slowly added into the flask with the OMP suspension. Upon expiration of the reaction time, the hydrolysis was stopped by tenfold dilution with distilled water and cooling of the suspension to room temperature. The hydrolyzed nanocellulose was rinsed with distilled water three times by means of centrifugation at 4000 rev/min and subsequent dialysis until reaching neutral pH. Ultrasound treatment of nanocellulose with a concentration of 0.6% was performed using an ultrasound disintegrator UZDN-A (SELMI, Ukraine) with 22 kHz from 30 to 60 min. The nanocellulose suspension was placed in an ice bath to prevent overheating during treatment.

*2.4. Methods of Analyses.* The following instrumental methods of analysis of plant raw material, organosolvent miscanthus pulp, and nanocellulose have been used. The decrease of the cellulose particle size and the increase of its dispersity were assessed by measuring the changes in the dimensions of the miscanthus pulp. Scanning electron microscope (SEM) analysis was performed with a PEM–106I (SELMI, Ukraine) microscope to observe the morphology of OMP and nanocellulose films.

Topographical characterization of nanocellulose samples was assessed by atomic force microscopy (AFM). The measurements were done with a Si cantilever, operating in the tapping mode on the device Solver Pro M (NT-MDT, Russia). Details of the measurements are described in article [17].

X-ray diffraction patterns of the different cellulose samples were obtained by an Ultima IV diffractometer (Rigaku, Japan). Crystallinity index (CI) was used to calculate relative amount of crystalline material in the cellulose by the Segal method [24]: $\mathrm{CI} = (I_{200} - I_{\mathrm{am}})/I_{200} \times 100\%$, where $I_{200}$ is the intensity of (200) reflex about 23° and $I_{\mathrm{am}}$ is the intensity of amorphous scattering at 18.5°.

Electron absorption spectra of the nanocellulose films in UV, visible, and near-infrared regions were registered on a two-beam spectrophotometer 4802 (UNICO, USA) with a resolution of 1 nm.

The thermal degradation behavior of OMP, OMP after alkaline treatment, and nanocellulose samples was studied on a Q-1500D thermal analyzer (F. Paulik, J. Paulik, L. Erdey system, Hungary) from 25 to 600°C with a heating rate of $5^{\circ}\mathrm{C\,min^{-1}}$. The weight of samples was within 0.25

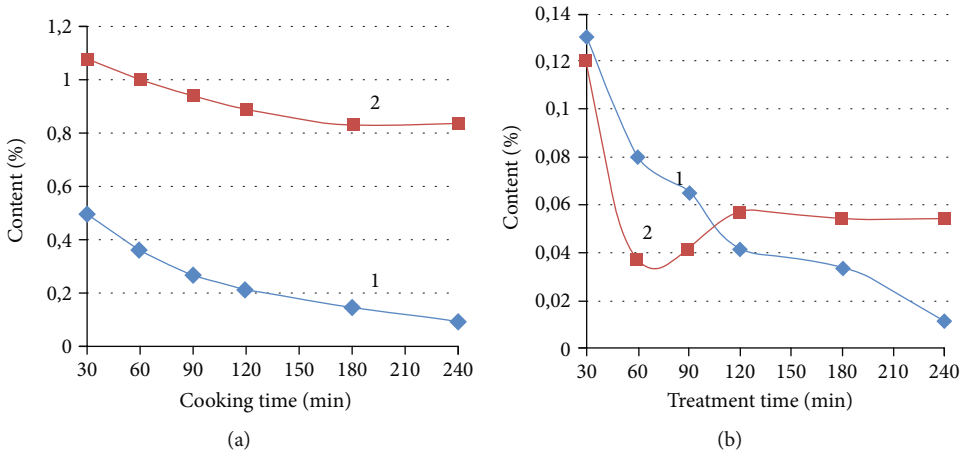


Figure 1: Properties of organosolvent miscanthus pulp after cooking (a) and alkaline treatment (b), % to a.d.r.m. 1: residual lignin; 2: ash content.

$\pm 0.01$ grams, reference substance—$\alpha$-corundum, crucible material—alund. Deviations of weight were registered and processed according to a program involving the use of computer technology.

Functional groups of OMP, OMP after alkaline treatment, and nanocellulose samples were analyzed using Fourier transform infrared spectrophotometer (FTIR Spectrometer "Tensor 37") in the range of 4000–500 $cm^{-1}$ with a resolution of 2 $cm^{-1}$.

The density of the nanocellulose films was determined in accordance with ISO 534:1988. Tensile strength of the nanocellulose films was measured at a controlled temperature of $23 \pm 1°C$ and humidity of $50 \pm 2\%$ according to ISO 527-1 as described in [17].

## 3. Results and Discussion

*3.1. Results of Cooking and Alkali Treatment.* Miscanthus stalks had the following chemical composition: 49.7% of cellulose; 27.7% of lignin; 1.8% of resins, fats, and waxes; 61.9% of pentosans; and 1.1% of mineral substances relative to absolutely dry raw material (a.d.r.m.). As can be seen from the chemical composition data, the miscanthus stalks according to the content of the main components—cellulose and lignin—correspond to softwood but contain more mineral substances than softwood and hardwood. The analysis of the content of the main components of miscanthus a priori allows us to conclude that this raw material can be considered to produce both pulp suitable for paper and cardboard and pulp for chemical processing, in particular, for the production of nanocellulose.

An increase in the cooking time from 30 to 240 minutes naturally leads to a decrease in the yield of pulp from 54.3% to 45.7% to a.d.r.m. Figure 1 shows the dependence of the content of lignin (1) and mineral substances (2) on the processing time.

As shown in Figure 1(a), the mineral content in the organosolvent miscanthus pulp after 90 minutes of cooking does not significantly decrease and remains in the range of 0.84-0.95% to a.d.r.m. Therefore, after 90 minutes of cooking, cellulose was used for its subsequent alkaline treatment in order to reduce the content of minerals and lignin in it. Figure 1(b) shows the dependence of contents of lignin (1) and mineral substances (2) in the pulp after the alkaline treatment. As a result of experiments, it was found that increasing the duration of the alkaline treatment from 30 to 240 minutes reduces the pulp yield from 72.3% to 51.0% to a.d.r.m. Subsequent alkaline treatment does not contribute to the extraction of minerals, but rather, the polysaccharides dissolve, the yield of pulp decreases, and, therefore, the percentage of ash increases. Therefore, to prepare nanocellulose from organosolvent pulp, we used 90-minute cooking and alkaline treatment for 60 minutes with a lignin content of 0.08% and mineral substances of 0.037% to a.d.r.m. Thus, carrying out peroxide cooking and alkaline treatment at low temperature ($96 \pm 1°C$) allows obtaining of cellulose with a high degree of whiteness (up to 85%) and low emissions of harmful substances into the environment.

*3.2. SEM Analysis.* The morphology structure of the samples of the miscanthus and organosolvent miscanthus pulp before and after alkaline treatment is shown in Figure 2.

The main components are xylem cells and phloem, which perform the conductive, mechanical, and storage functions in the stalks of plants. These include cells of tracheids, vessels, libriform, and parenchymal cells (Figure 2(a)). The presence of such cells is typical for different representatives of nonwood plant materials. The walls of miscanthus stalks consist of a network of longitudinal oval capillaries that provide access to the cooking solution to the cells. As a result of cooking, the miscanthus is exposed to thermochemical effects and the stalks are folded into separate short and wide fragments (Figure 2(b)). According to the SEM, the bulk of the pulp from miscanthus is made up of thin, ribbon fibers of different widths and lengths and can be single and joined to several pieces. The photographs confirm that in the process of thermochemical processing of plant materials, the size of the fibers decreases, primarily their width due to the removal of noncellulose plant components from them. Moreover, as can be seen from Figure 2(c), the fiber after intensive alkaline

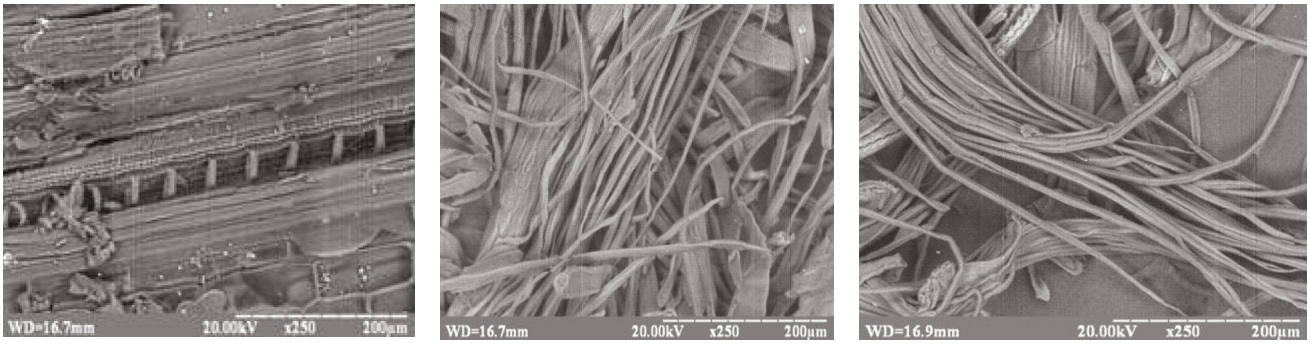


(a) (b) (c)

Figure 2: Scanning electron microscopy images of samples of the miscanthus stalks (a) and organosolvent miscanthus pulp before (b) and after alkaline treatment (c).

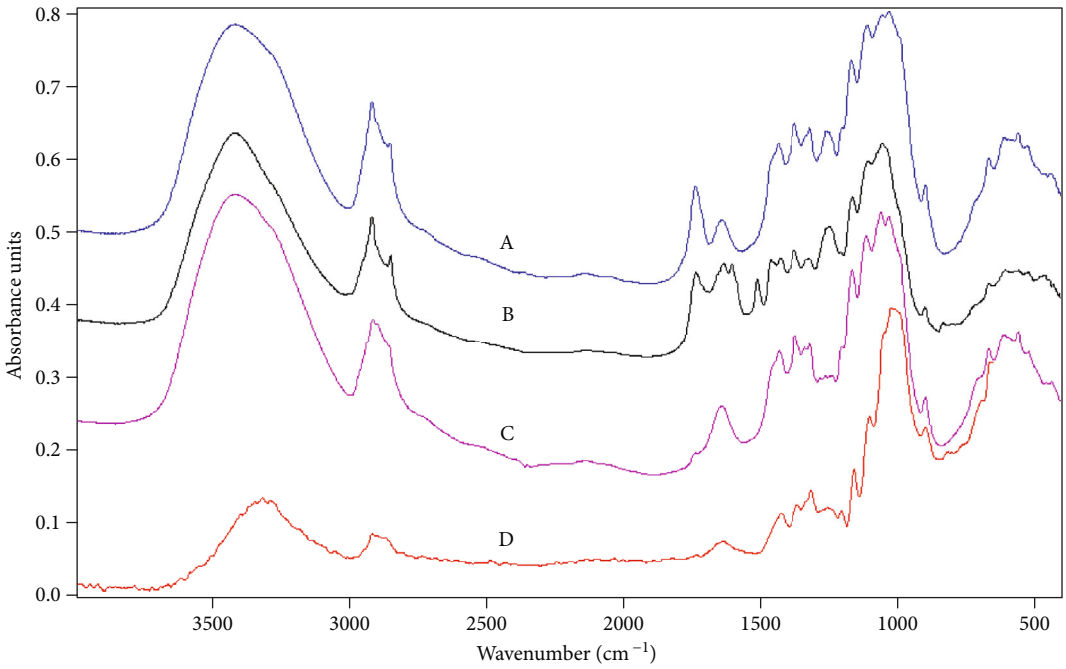


Figure 3: FTIR spectra of different samples: of miscanthus stalks (A), organosolvent miscanthus pulp before (B) and after alkaline treatment (C), and nanocellulose film (D).

treatment has a smooth surface, which indicates the relative chemical purity of the cellulose fibers.

*3.3. FTIR Analysis.* The extraction of noncellulosic components from organosolvent miscanthus pulp in the process of its thermochemical treatment was confirmed by infrared spectroscopy. Figure 3 shows the Fourier IR spectra of the miscanthus stalks, organosolvent miscanthus pulp before and after alkaline treatment, and the nanocellulose after hydrolysis.

All spectra are characterized by a wide bandwidth in the region of 3000–3800 cm$^{-1}$, which corresponds to stretching vibrations of hydroxyl groups included in intramolecular and intermolecular hydrogen bonds [24]. Spectra of miscanthus stalks and organosolvent miscanthus pulp before and after alkaline treatment have characteristic high-frequency bands, indicating the formation of intermolecular bonds. The band of nanocellulose in this region is characterized by low intensity, which indicates the formation of strong intermolecular bonds between the hydroxyl groups of the macromolecules of nanocellulose. The bands in the area of 3000–2800 cm$^{-1}$ correspond to the asymmetric and symmetric stretching vibrations of the methylene groups of the cellulose. Bands of stretching vibrations of double bonds lie in the region of 1500-1800 cm$^{-1}$. Vibration bands in the 1740 cm$^{-1}$ region indicate the presence of a carbonyl group characteristic of hemicelluloses. As can be seen from Figure 3, C, organosolvent cooking and subsequent alkaline treatment removes hemicelluloses from the cellulose composition. A decrease in the intensity of vibrations in the region of 1600 cm$^{-1}$, which is characteristic of aromatic compounds—residual lignin, indicates an almost complete

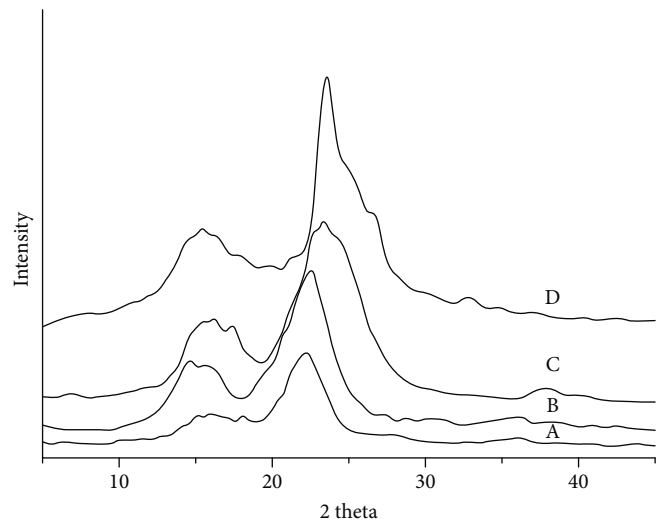


Figure 4: X-ray diffraction patterns of different cellulose samples: (A) miscanthus stalks, (B) organosolvent pulp, (C) OMP after alkaline treatment, and (D) nanocellulose after hydrolysis and sonication.

removal of lignin from plant materials and cellulose during their thermochemical treatments. The bands in the region of 1370 and 1430 $cm^{-1}$ are due to the deformation vibrations of the $CH_2$ groups, the band at 1160 $cm^{-1}$ is due to the asymmetric vibrations of the C–O bonds, while the band at 1060 $cm^{-1}$ corresponds to the vibrations of the C–O–C bridge of the glucopyranose ring of cellulose [25]. The increase of the intensity of the bands in the region of 1050, 1400, and 3400 $cm^{-1}$ demonstrates the efficiency of the removal of lignin and noncellulose components from the plant feedstock in the investigated sequence of thermochemical treatments.

*3.4. XRD Analysis.* The change in the ratio of amorphous and crystalline parts of OMP during its thermochemical and physical treatment was investigated by the XRD method. The analysis of X-ray diffraction patterns of miscanthus stalks (Figure 4, A), organosolvent miscanthus pulp (Figure 4, B), OMP after alkaline treatment (Figure 4, C), and nanocellulose after hydrolysis and sonication (Figure 4, D) was carried out.

The crystallinity index of miscanthus stalks was 65.8%; organosolvent pulp, 72.3%; OMP after alkaline treatment, 71.9%; and nanocellulose after hydrolysis and sonication, 76.7%. Thus, the results of X-ray diffraction analysis indicate an increase in the sample crystallinity in the process of their thermochemical and physical processing. This dependence is observed for cellulose from other representatives of nonwood and woody plant raw materials [17–19, 26, 27].

*3.5. Results of Hydrolysis.* We show the dependencies of the density, tensile strength, and transparency of nanocellulose films on the main technological parameters of the process for obtaining nanocellulose from organosolvent miscanthus pulp (Table 1). As can be seen from the data in Table 1, the hydrolysis of cellulose by solutions of sulfuric acid of different concentrations yields nanocellulose films of different quality. An increase in the quality of nanocellulose films improves with increasing sulfuric acid concentration, temperature, and duration of hydrolysis. An increase in the duration of ultrasonic treatment of suspension of nanocellulose obtained within one time of hydrolysis from 30 to 60 minutes increases the strength and transparency of nanocellulosic films. The highest values of quality indicators are the samples obtained at the maximum values of the studied technological parameters. The values of transparency of the films prepared in this study are higher than the transparency of the cellulose nanofiber films obtained from bleached kraft eucalyptus, acacia, and pine pulps reported previously (40–65%) [28].

The properties of obtained nanocellulose from OMP exhibit great potential in its application for the preparation of new nanocomposite materials, for example, for production in optoelectronic devices, as a reinforcing additive in the production of paper, cardboard, cement, etc.

Nanocellulose after hydrolysis and ultrasound treatment of OMP had homogeneous and stable nanocellulose suspension. The nature of stabilization of the colloidal suspension is explained by the presence of charged groups on the surface of the nanocellulose, which are formed by the interaction of cellulose with sulfuric acid due to the esterification reaction. The stability of nanocellulose suspensions is supported by images immediately after the preparation and after a prolonged storage time. There was no sedimentation of nanocellulose particles when stored at room temperature for an extended period of time (after 5 months of storage). Such stabilization of the nanocellulose suspension leads to the formation of films with a transparency of more than 80% in the visible spectral range, which is confirmed by the data of the article [29] and characteristic of nanocellulose from other plant raw materials [27].

*3.6. AFM Analyses.* Topographical characterization of organosolvent miscanthus nanocellulose by AFM and its 3D projection with definition of sample height is shown in Figure 5.

Figure 5(a) shows the lateral section of the miscanthus nanocellulose nanofibers, which form aggregates. The diameter of separate nanofibers is within the range from

Table 1: Dependencies of the parameters of nanocellulose films on the main technological parameters of the process of obtaining nanocellulose from organosolvent miscanthus pulp.

| Concentration $H_2SO_4$ (%) | Duration of hydrolysis (min) | Duration of ultrasonic treatment (min) | Quality of received films Density (g/cm$^3$) | Tensile strength (MPa) | Transparency (%) |
|---|---|---|---|---|---|
| Temperature 40°C | | | | | |
| | | 30 | 0.87/1.00 | 56.0/44.2 | 25.8/57.0 |
| | 30 | 45 | 1.04/1.08 | 58.3/54.1 | 40.6/64.2 |
| | | 60 | 1.05/1.12 | 80.0/66.7 | 41.8/67.0 |
| | | 30 | 1.04/1.12 | 54.5/50.0 | 30.3/51.1 |
| 43/50 | 60 | 45 | 1.08/1.15 | 59.3/66.1 | 43.3/67.0 |
| | | 60 | 1.16/1.22 | 77.7/83.3 | 52.769.7 |
| | | 30 | 1.09/1.15 | 70.7/77.5 | 42.7/59.9 |
| | 90 | 45 | 1.11/1.18 | 83.3/105.0 | 54.5/64.3 |
| | | 60 | 1.18/1.23 | 124.0/127.0 | 55.6/69.3 |
| Temperature 60°C | | | | | |
| | | 30 | 1.12/1.1 | 43.3/66.7 | 44.3/65.7 |
| | 30 | 45 | 1.22/1.23 | 57.5/70.7 | 52.0/75.6 |
| | | 60 | 1.26/1.28 | 60.4/75.0 | 70.7/76.3 |
| | | 30 | 1.15/1.33 | 55.5/78.0 | 68.6/68.7 |
| 43/50 | 60 | 45 | 1.23/1.37 | 60.0/80.6 | 65.3/70.9 |
| | | 60 | 1.32/1.42 | 62.0/88.0 | 74.4/80.8 |
| | | 30 | 1.04/1.45 | 44.4/115.0 | 38.5/75.7 |
| | 90 | 45 | 1.18/1.55 | 40.0/123.0 | 68.2/78.0 |
| | | 60 | 1.25/1.60 | 41.0/195.0 | 72.3/82.6 |

10 to 20 nm and possibly much less, since the image is obtained from fibers of nanocellulose located not in one layer. Therefore, we propose that the nanocellulose forms a film on the surface of the silicon substrate due to bonds between the molecules.

*3.7. TGA and DTA Analyses.* We also investigated the change in the thermal stability of samples of OMP, OMP after alkaline treatment, and nanocellulose films by the thermogravimetric analysis. Figure 6 shows the change of the thermal stability of OMP samples after cooking in peracetic acid (curve 1), of OMP after the alkaline treatment (curve 2), and of nanocellulose films after hydrolysis with 50% sulfuric acid and ultrasound treatment (curve 3).

As is shown in Figure 6, thermogravimetric curves of the studied samples have their own characteristics. So, in the temperature range from 50 to 90°C, the maximum weight loss (up to 12%) is observed for OMP, which is due to the evaporation of residual moisture from its fibers. When heating nanocellulose films to 240°C, and samples of OMP and OMP after alkaline treatment to 260°C, a slight (up to 3%) loss in mass is observed. In the process of further heating of the OMP and OMP samples after alkaline treatment to 340°C, up to 70% of their bulk is lost. Samples have a final degradation temperature of about 440°C for OMP and 500°C for OMP after alkaline treatment. For nanocellulose films, a smooth mass loss is observed in the temperature range 240–500° C, and the final decomposition is observed at a temperature of 540°C. It can be explained by the fact that during the chemical treatment and ultrasonic homogenization, a dense structure between pulp molecules is formed. The degradation behavior of the cellulose that underwent sulfuric acid hydrolysis was different from that of the initial cellulose and showed higher degradation temperature. The higher degradation temperature of the nanocellulose was due to the formation of a dense crystalline structure of the cellulose. These end chains started to decompose at the lower temperatures, as have been previously shown [30]. Our data also support previous findings that the sulfate groups, introduced during hydrolysis, can work as a flame retardant in such a way that they cause an increase in the char fraction [31].

## 4. Conclusions

Based on our work, *Miscanthus x giganteus* is a promising plant raw material for the production of organosolvent pulp, suitable for chemical processing, in particular, for the production of nanocellulose. Carrying out peroxide cooking and alkaline treatment at low temperature 96 ± 1°C allows obtaining organosolvent miscanthus pulp (OMP) with a high degree of whiteness up to 85% and low emissions of harmful substances into the environment. As a result of hydrolysis of never-dried cellulose with a solution of sulfuric acid with concentrations of 43 and 50% followed by ultrasonic treatment, nanocellulose was obtained. The structural changes and crystallinity degree of OMP and nanocellulose were studied by SEM and FTIR techniques. XRD analysis confirmed the increase of the degree of crystallinity of the

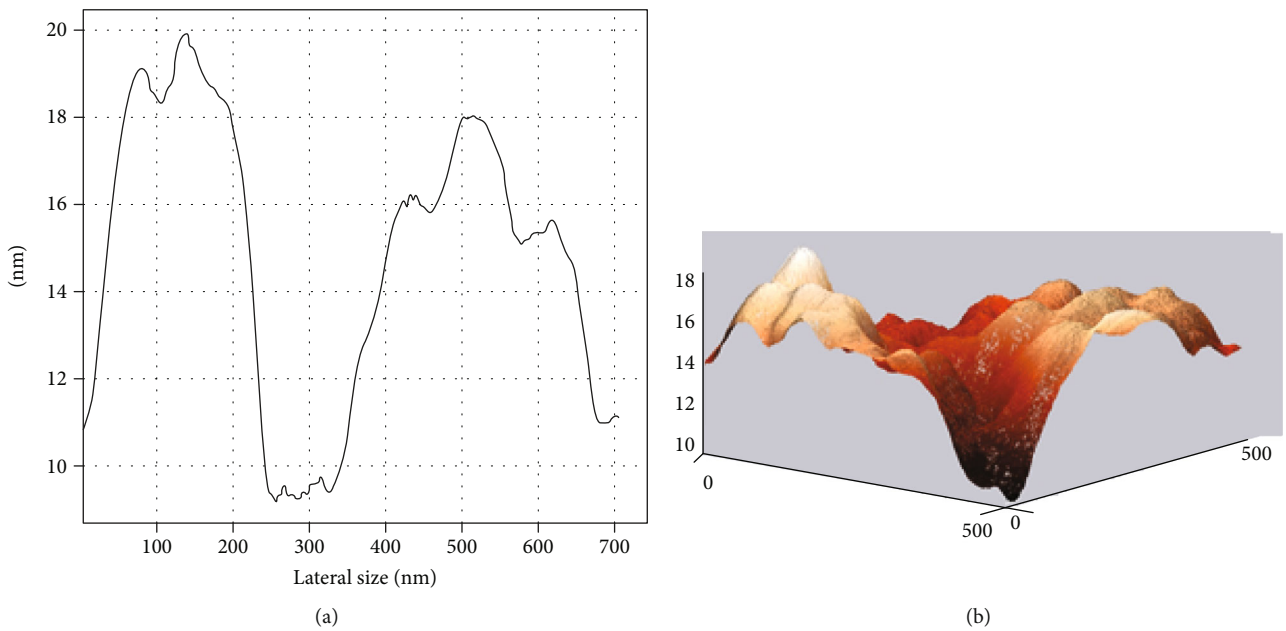


Figure 5: (a) The AFM images of the lateral size of the nanocellulose surface; (b) 3D projection with definition of sample height tapping mode.

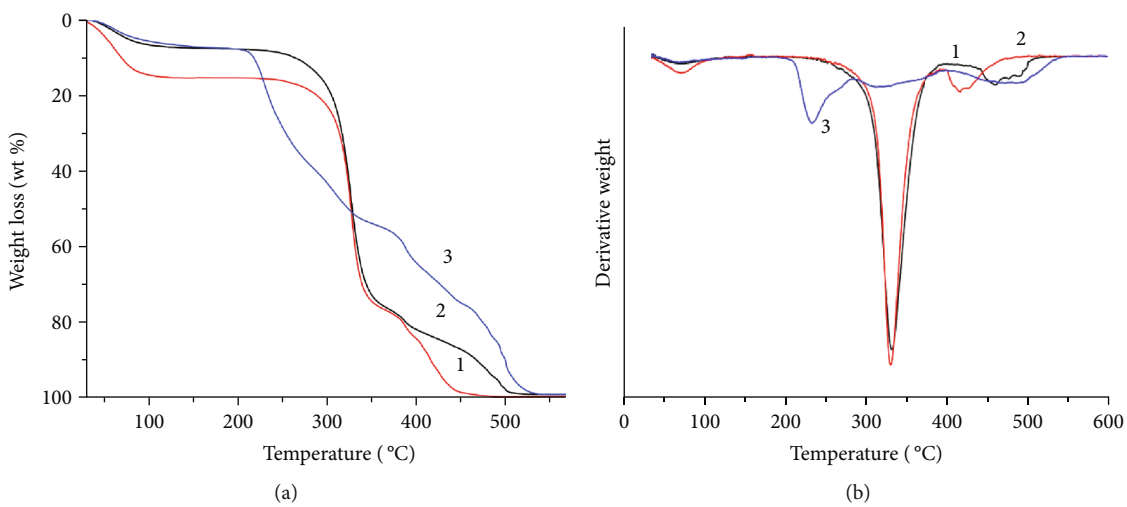


Figure 6: Gravimetric (a) and differential (b) curves of thermal analysis: (1) OMP, (2) OMP after alkaline treatment, and (3) nanocellulose film.

OMP and nanocellulose as a result of thermochemical treatment. We report that nanocellulose has a density up to 1.6 g/cm$^3$, transparency up to 82%, and crystallinity up to 76.5%. We observed using AFM microscopy that nanocellulose has a particle diameter in the range of 10 to 20 nm. Thermogravimetric analysis confirmed that nanocellulose films have a more dense structure and smaller mass loss in the temperature range of 320–440°C compared with OMP. Samples have a final degradation temperature of about 440°C for OMP and 500°C for OMP after alkaline treatment, but for nanocellulose films, the final decomposition is observed at a temperature of 540°C. The obtained nanocellulose films had high tensile strength up to 195 MPa. The properties of obtained nanocellulose from OMP exhibit great potential in its application for the preparation of new nanocomposite materials and can serve reinforcing additive in paper, cardboard, cement, etc.

## Data Availability

The XRD, FTIR, and TGA data used to confirm the results of this study are included in additional information files that are attached.

## Conflicts of Interest

The authors declare that they have no conflicts of interest.

## Acknowledgments

This work was financially supported by the Ministry of Education and Science of Ukraine.

## References

[1] R. Mülhaupt, "Green polymer chemistry and bio-based plastics: dreams and reality," *Macromolecular Chemistry and Physics*, vol. 214, no. 2, pp. 159–174, 2013.

[2] H. P. S. A. Khalil, A. H. Bhat, and A. F. I. Yusra, "Green composites from sustainable cellulose nanofibrils: a review," *Carbohydrate Polymers*, vol. 87, no. 2, pp. 963–979, 2012.

[3] Y. H. Jung, T.-H. Chang, H. Zhang et al., "High-performance green flexible electronics based on biodegradable cellulose nanofibril paper," *Nature Communications*, vol. 6, no. 1, 2015.

[4] B. Deepa, E. Abraham, N. Cordeiro et al., "Utilization of various lignocellulosic biomass for the production of nanocellulose: a comparative study," *Cellulose*, vol. 22, no. 2, pp. 1075–1090, 2015.

[5] K. Uetani, T. Okada, and H. T. Oyama, "Thermally conductive and optically transparent flexible films with surface-exposed nanocellulose skeletons," *Journal of Materials Chemistry C*, vol. 4, no. 41, pp. 9697–9703, 2016.

[6] C. Wang, H. Huang, M. Jia, S. Jin, W. Zhao, and R. Cha, "Formulation and evaluation of nanocrystalline cellulose as a potential disintegrant," *Carbohydrate Polymers*, vol. 130, pp. 275–279, 2015.

[7] S. Thiemann, S. J. Sachnov, F. Pettersson et al., "Cellulose-based ionogels for paper electronics," *Advanced Functional Materials*, vol. 24, no. 5, pp. 625–634, 2014.

[8] A. M. Adel, A. A. El-Gendy, M. A. Diab, R. E. Abou-Zeid, W. K. El-Zawawy, and A. Dufresne, "Microfibrillated cellulose from agricultural residues. Part I: papermaking application," *Industrial Crops and Products*, vol. 93, pp. 161–174, 2016.

[9] J. Luo, H. Chang, A. A. Bakhtiary Davijani et al., "Influence of high loading of cellulose nanocrystals in polyacrylonitrile composite films," *Cellulose*, vol. 24, no. 4, pp. 1745–1758, 2017.

[10] Y. Su, Y. Zhao, H. Zhang, X. Feng, L. Shi, and J. Fang, "Polydopamine functionalized transparent conductive cellulose nanopaper with long-term durability," *Journal of Materials Chemistry C*, vol. 5, no. 3, pp. 573–581, 2017.

[11] K.-Y. Lee, Y. Aitomäki, L. A. Berglund, K. Oksman, and A. Bismarck, "On the use of nanocellulose as reinforcement in polymer matrix composites," *Composites Science and Technology*, vol. 105, pp. 15–27, 2014.

[12] G. Siqueira, J. Bras, and A. Dufresne, "Cellulose whiskers versus microfibrils: influence of the nature of the nanoparticle and its surface functionalization on the thermal and mechanical properties of nanocomposites," *Biomacromolecules*, vol. 10, no. 2, pp. 425–432, 2009.

[13] I. A. Sacui, R. C. Nieuwendaal, D. J. Burnett et al., "Comparison of the properties of cellulose nanocrystals and cellulose nanofibrils isolated from bacteria, tunicate, and wood processed using acid, enzymatic, mechanical, and oxidative methods," *ACS Applied Materials & Interfaces*, vol. 6, no. 9, pp. 6127–6138, 2014.

[14] D. Y. Liu, G. X. Sui, and D. Bhattacharyya, "Synthesis and characterisation of nanocellulose-based polyaniline conducting films," *Composites Science and Technology*, vol. 99, pp. 31–36, 2014.

[15] T. S. Anirudhan, J. R. Deepa, and Binusreejayan, "Synthesis and characterization of multi-carboxyl-functionalized nanocellulose/nanobentonite composite for the adsorption of uranium(VI) from aqueous solutions: Kinetic and equilibrium profiles," *Chemical Engineering Journal*, vol. 273, pp. 390–400, 2015.

[16] J. Cruz and R. Fangueiro, "Surface modification of natural fibers: a review," *Procedia Engineering*, vol. 155, pp. 285–288, 2016.

[17] V. A. Barbash, O. V. Yaschenko, and O. M. Shniruk, "Preparation and properties of nanocellulose from organosolv straw pulp," *Nanoscale Research Letters*, vol. 12, no. 1, p. 241, 2017.

[18] V. Barbash, O. Yashchenko, and A. Kedrovska, "Preparation and properties of nanocellulose from peracetic flax pulp," *Journal of Scientific Research and Reports*, vol. 16, no. 1, pp. 1–10, 2017.

[19] V. A. Barbash, O. V. Yashchenko, and V. O. Opolsky, "Effect of hydrolysis conditions of organosolv pulp from kenaf fibers on the physicochemical properties of the obtained nanocellulose," *Theoretical and Experimental Chemistry*, vol. 54, no. 3, pp. 193–198, 2018.

[20] A. Płażek, F. Dubert, P. Kopeć et al., "*In vitro*-propagated *Miscanthus* × *giganteus* plants can be a source of diversity in terms of their chemical composition," *Biomass and Bioenergy*, vol. 75, pp. 142–149, 2015.

[21] N. Brosse, A. Dufour, X. Meng, Q. Sun, and A. Ragauskas, "Miscanthus: a fast-growing crop for biofuels and chemicals production," *Biofuels Bioproducts & Biorefining*, vol. 6, no. 5, pp. 580–598, 2012.

[22] E. Cudjoe, M. Hunsen, Z. Xue et al., "Miscanthus giganteus: a commercially viable sustainable source of cellulose nanocrystals," *Carbohydrate Polymers*, vol. 155, pp. 230–241, 2017.

[23] TAPPI, *Test Methods*, Georgia, Tappi Press, Atlanta, 2004.

[24] M. Poletto, H. O. Júnior, and A. Zattera, "Native cellulose: structure, characterization and thermal properties," *Materials*, vol. 7, no. 9, pp. 6105–6119, 2014.

[25] R. A. Ilyas, S. M. Sapuan, M. R. Ishak, and E. S. Zainudin, "Effect of delignification on the physical, thermal, chemical, and structural properties of sugar palm fibre," *BioResources*, vol. 12, no. 4, pp. 8734–8754, 2017.

[26] G. B. Paschoal, C. M. O. Muller, G. M. Carvalho, C. A. Tischer, and S. Mali, "Isolation and characterization of nanofibrillated cellulose from oat hulls," *Química Nova*, vol. 38, no. 4, pp. 478–482, 2015.

[27] V. A. Barbash, O. V. Yaschenko, S. V. Alushkin, A. S. Kondratyuk, O. Y. Posudievsky, and V. G. Koshechko, "The effect of mechanochemical treatment of the cellulose on characteristics of nanocellulose films," *Nanoscale Research Letters*, vol. 11, no. 1, p. 410, 2016.

[28] A. B. Fall, A. Burman, and L. Wagberg, "Cellulosic nanofibrils from eucalyptus,acacia and pine fibers," *Nordic Pulp & Paper Research Journal*, vol. 29, no. 1, pp. 176–184, 2014.

[29] A. B. Reising, R. J. Moon, and J. P. Youngblood, "Effect of particle alignment on mechanical properties of neat cellulose nanocrystal films," *Journal of Science & Technology for Forest Products and Processes*, vol. 2, no. 6, pp. 32–41, 2012.

[30] R. Hashaikeh and H. Abushammala, "Acid mediated networked cellulose: preparation and characterization," *Carbohydrate Polymers*, vol. 83, no. 3, pp. 1088–1094, 2011.

[31] M. Roman and W. Winter, "Effect of sulfate groups from sulfuric acid hydrolysis on the thermal degradation behavior of bacterial cellulose," *Biomacromolecules*, vol. 5, no. 5, pp. 1671–1677, 2004.

Hindawi
Journal of Nanomaterials
Volume 2019, Article ID 5198045, 16 pages
https://doi.org/10.1155/2019/5198045

*Research Article*

# Synthesis of Porous Octahedral ZnO/CuO Composites from Zn/Cu-Based MOF-199 and Their Applications in Visible-Light-Driven Photocatalytic Degradation of Dyes

**Tran Thanh Minh,[1] Nguyen Thi Thanh Tu,[2] Tran Thi Van Thi,[1] Le Thi Hoa,[1] Hoang Thai Long,[1] Nguyen Hai Phong,[1] Thong Le Minh Pham,[3] and Dinh Quang Khieu[1]**

[1]*University of Sciences, Hue University, 530000, Vietnam*
[2]*Institute for Environmental Science, Nguyen Tat Thanh University, 700000, Vietnam*
[3]*Institute of Research and Development, Duy Tan University, 550000, Vietnam*

Correspondence should be addressed to Dinh Quang Khieu; dqkhieu@hueuni.edu.vn

Received 22 June 2019; Revised 4 September 2019; Accepted 16 September 2019; Published 14 October 2019

Academic Editor: Sesha Srinivasan



In the present paper, a porous octahedral (ZnO/CuO) composite is synthesized from zinc/copper-based metal-organic framework-199, and its applications in visible-light-driven photocatalytic degradation of dyes are demonstrated. The precursors of Zn-BTC, Cu-BTC, and Zn/Cu-BTC (BTC: benzene-1,3,5-tricarboxylate) were synthesized using a microwave-assisted method. Benzene-1,3,5-tricarboxylate acts as a sacrificial template and was removed from the precursors via thermal decomposition to form CuO, ZnO, and ZnO/CuO. ZnO/CuO with a large specific surface area of $32.5\,m^2{\cdot}g^{-1}$ is composed of porous octahedral particles of 5–10 $\mu$m in diameter. Methylene blue (MB) was utilized as the dye model for photocatalytic degradation reactions. The porous octahedral ZnO/CuO exhibits superior visible-light-driven photocatalytic degradation of MB compared with single CuO or ZnO. The kinetic model of photocatalytic degradation was proposed as $(1/K_L) \times \ln C + C = -k_r t + (1/K_L) \times \ln C_e + C_e$, where $K_L$ is the Langmuir equilibrium constant and $C_e$ is the MB concentration at equilibrium. The model significantly fits the kinetic data. In addition, the acquired catalyst manifests excellent photocatalytic degradation for several other dyes including phenol red, methyl orange, and Congo red.

## 1. Introduction

Metal oxide semiconductors are widely used for photocatalytic degradation of organic pollutants due to their high photosensitivity, nontoxic nature, and low cost. It is well known that titanium oxide ($TiO_2$) and zinc oxide (ZnO) can only be excited for photocatalysis. ZnO belongs to the *n*-type semiconductor and is considered one of the important semiconductor photocatalysts due to its high photosensitivity and stability [1, 2]. However, the constraint of ZnO among others is that it absorbs light only in the near UV region because of its large bandwidth of 3.2 eV. Unfortunately, sunlight constitutes only 4–5% of UV light [3, 4]. Therefore, the effective use of solar energy still remains a challenge in photocatalytic application. The photoresponse of narrow-band-gap semiconductors shifts much more to the visible wavelength range. However, these semiconductors are difficult to maintain their photoactivity for a long time due to the recombination of the photo-induced electron-hole pairs. To improve the visible-light-driven photocatalytic efficiency of ZnO, some metals or oxides are often introduced to its surface. Au-loaded ZnO can significantly enhance the activities of photogenerated electrons by suppressing the recombination of charge carriers [5]. Unlike pure ZnO, mesoporous $Fe_2O_3$/ZnO core-shell composites manifest an excellent photocatalytic degradation of Rhodamine B in both ultraviolet and visible light regions [6]. The nanostructure of cupric oxide (CuO) is the *p*-type semiconductor with a narrow band gap of 1.2–2.71 eV. Despite its high capacity of absorption in the visible light range, CuO is surprisingly not appealing in terms of catalytic behavior due to its fast recombination rate of the induced electron-hole pairs. Thus, in order to

achieve a high catalytic activity, a synergistic system may be expected by connecting CuO with ZnO, in which CuO acts as a cocatalyst and thus expands the visible-light response. Moreover, the possible formation of favorable *p-n* junctions at the nanostructure interface restrains the photo-induced carrier recombination. Various approaches have been accomplished to synthesize ZnO/CuO composites for photocatalytic application such as sol-gel and coprecipitation [7–9]. However, to achieve a high degree of homogeneous dispersion of each component still remains a major challenge with multimetal oxides.

Metal-organic frameworks (MOFs) are a class of crystalline materials that have coordination bonds between transition-metal cations and organic ligands. The metal-organic frameworks possess unique performance advantages, such as controllable pore size and pore surface, low density, and large surface area. These outstanding properties make MOFs widely used in many fields, for example, adsorption, photocatalysis, and biosensors [10–12]. HKUST-1 (Hong Kong University of Science and Technology) is one of the first MOFs made up of copper nodes with benzene-1,3,5-tricarboxylic (BTC) acid struts between them [13]. HKUST-1 (or MOF-199 or Cu-BTC) manifests remarkable potentials in photocatalysis [14, 15] and separation [16]. MOF-199 notably displays persistence in both water and air [13]. Zinc is a promising metal that constructs an isostructural analogue to Cu-BTC. Anbia et al. [17] reported the hydrothermal synthesis of Zn-BTC that can be a good material for hydrogen storage at room temperature. Zn-BTC is also synthesized through direct precipitation in solution under ultrasonic condition [18]. Xu et al. [19] reported the ionothermal synthesis of Zn-BTC using 1-ethyl-3-methylimidazolium bromide ionic liquid as a solvent. The use of ionic liquid in the synthesis of Zn-BTC has shown a vast range of possibilities of controlling the structures and obtaining new materials by tuning the properties of the ionic liquid. Zn-BTC possesses lower-than-expected surface areas (a few meters to a few dozen meters), or it completely collapses upon the removal of guest molecules [20]. Generally, synthetic conditions (temperature, atmosphere, and posttreatment) are critical to the formation of MOF diffractions as well as their physicochemical properties [17, 18, 21].

Multimetal component MOFs have widely been synthesized by simultaneously mixing several metal species with organic ligands [22, 23]. There exist several advantages of using multimetal-component MOFs as sacrificial templates compared with other conventional templates [24]. They are as follows:

(i) The metal species in MOFs are mixed at molecular levels

(ii) Homogeneous morphologies of MOFs are critical regarding the preparation of anisotropic multimetal oxides that are difficult to fabricate using classical methods

(iii) Undesired aggregation or structural collapse of the framework during thermolysis can be minimized due to their structural strength

Xu et al. successfully synthesized hierarchical porous $ZnO/ZnCo_2O_4$ using one-step thermal calcining the as-prepared Zn-Co-MOF precursor [25]. Huang et al. reported hierarchical $NiFe_2O_4/Fe_2O_3$ nanotubes prepared from MOFs for superior lithium-ion batteries [26]. Wu et al. developed a facile method for the synthesis of a hybrid $Zn_xCo_{(3-x)}O_4$ composite via the thermal oxidative decomposition of bimetallic (Zn/Co) zeolitic imidazolate frameworks (ZIFs) [27]. Recently, Lei et al. demonstrated the hollow CuO/ZnO materials derived from zeolite imidazole framework-8. This material is a very promising photocatalyst for tetracycline degradation [28]. However, so far, little work has been carried out to prepare ZnO/CuO from MOFs.

In the present paper, a porous octahedral (ZnO/CuO) composite is synthesized from zinc/copper-based metal-organic framework-199, and its applications in visible-light-driven photocatalytic degradation of dyes are demonstrated. The precursors of Zn-BTC, Cu-BTC, and Zn/Cu-BTC are synthesized with a microwave-assisted method. In addition, pure Zn-BTC and Cu-BTC are prepared for the sake of comparison. Benzene-1,3,5-tricarboxylic acts as a sacrificial template and is removed by calcination. The kinetic model of photocatalytic degradation is proposed by combining the heterogeneous catalysis for unimolecular reactions with adsorption isotherms.

## 2. Experimental

*2.1. Materials.* Benzene-1,3,5-tricarboxylic acid ($C_6H_3(COOH)_3$, ≥95%) (denoted as BTC), copper nitrate trihydrate ($Cu(NO_3)_2{\cdot}3H_2O$, 99.5%), zinc nitrate tetrahydrate ($Zn(NO_3)_2{\cdot}4H_2O$, 98.5%), methyl orange ($C_{14}H_{14}N_3NaO_3S$, 85%), phenol red ($C_{19}H_{14}O_5S$, 90%), and Congo red ($C_{32}H_{22}N_6Na_2O_6S_2$, 85%), potassium iodide (KI, 99%), benzoquinone ($C_6H_4O_2$, 98%), and isopropanol ($C_3H_7OH$) were purchased from Merck, Germany. Dimethylformamide ($(CH_3)_2NCHO$), ethanol ($C_2H_5OH$), methanol ($CH_3OH$, 99% purity), and methylene blue ($C_{16}H_{18}ClN_3S$, 82%—MB) were acquired from HiMedia, India. Methylene blue is used as the dye model. Potassium iodide and benzoquinone are used as scavengers in the current study.

*2.2. Apparatus.* Powder X-ray diffraction patterns (PXRD) were performed on a D8 Advance Bruker monochromator equipped with a Cu-K$\alpha$ radiation source ($\lambda = 1.5406$ Å). The morphologies of the obtained samples were analyzed using a scanning electron microscope (SEM) (Hitachi S-4800) and a high-resolution transmission electron microscope (HR-TEM) (JEM-2100). Thermo analysis (TG-DTA) was carried out using a TG-DTA instrument (DTG-60H Shimadzu) under atmospheric pressure at a heating rate of $10^{\circ}C{\cdot}min^{-1}$. Nitrogen adsorption/desorption isotherms were recorded on a Micromeritics ASAP 2020 instrument. The samples (200 mg) were degassed at 120°C for 24 h before measurements. The specific surface area was determined via the Brunauer-Emmett-Teller (BET) model with a relative pressure of 0.01–0.25 using adsorption data. Pore size distribution calculation was accomplished with the BJH (Barrett, Joyner, and Halenda) model using the adsorption branch of

the isotherms. The data of ultraviolet-visible diffuse reflectance spectroscopy (UV-Vis-DRS) were recorded on a Cary 5000 UV-Vis spectrometer (using $BaSO_4$ as the reference) at a collection speed of 600 nm·min$^{-1}$. X-ray photoelectron spectroscopy (XPS) was recorded with a Kratos Analytical spectrometer. All binding energies were referenced to the contaminant C 1s peak (at 284.6 eV) of adventitious carbon. The elemental compositions of Zn and Cu were analyzed with atomic absorption spectroscopy (AAS) using ZEEnit 7000. The elemental analysis of C and H was performed using Elemental Analyzer EA3000. Photoluminescence spectra of the obtained materials were measured at room temperature with a photoluminescence spectrophotometer (Horiba FL3). The concentration of dyes was measured using a UV-Vis spectrophotometer (V-630 Jasco) at $\lambda_{max}$ 644 nm for methylene blue, 464 nm for methyl orange, 431 nm for phenol red, 500 nm for Congo red, and 270 nm for phenol. The degree of MB mineralization was calculated based on TOC (total organic carbon). The concentration of TOC was determined using a TOC analyzer (TOC-$V_{CPH}$).

*2.3. Preparation of Zn/Cu-BTC, Cu-BTC, Zn-BTC, ZnO/CuO, CuO, and ZnO.* Benzene-1,3,5-tricarboxylic acid (0.4410 g, 0.0021 mol), $Cu(NO_3)_2{\cdot}3H_2O$ (0.2289 g, 0.00095 mol), and $Zn(NO_3)_2{\cdot}4H_2O$ (0.5757 g, 0.0022 mol) were first dissolved in a mixture (21 mL) of ethanol, distilled water, and dimethylformamide (1 : 1 : 1 in *v*/*v*) and stirred magnetically for 5 min. The resultant mixture was then loaded into a 250 mL Erlenmeyer flask and placed in a hand-made microwave device (Sharp R-203VN-M with a power of 250 W) [29] and irradiated for 30 min. The solid was collected by centrifugation, washed with DMF three times, dried at 180°C for 8 h, and designated as Zn/Cu-BTC [29]. Zn-BTC and Cu-BTC were synthesized with the same procedure. Oxides (ZnO/CuO, ZnO, and CuO) were prepared by annealing Zn/Cu-BTC, Zn-BTC, and Cu-BTC at 500°C for 5 h at a heating rate of 5°C·min$^{-1}$ under atmospheric pressure in an electric furnace (Vulcan 3-550 PD). The oxides were stored in a desiccator and used as a catalyst without any further treatment.

*2.4. Photocatalytic Activity*

*2.4.1. Photocatalytic Performance.* A beaker containing 500 mL of an aqueous suspension of MB (5–30 ppm) and 400 mg of catalyst was placed under a lamp bracket. The light source is a 160 W metal halide lamp (Philips) equipped with a wavelength cut-off filter ($\lambda \leq 420$ nm) (or Philips, Actinic BL 18 W, $\lambda = 365$ nm). Prior to illumination, the suspension was stirred magnetically in the dark for 60–180 min to ensure adsorption equilibrium. Three millilitres of the suspension was withdrawn at a certain time interval and centrifuged to remove the solid catalyst. The concentration of MB in the obtained clear liquid was analyzed using a UV-Vis spectrophotometer at $\lambda = 664$ nm. Further, the concentration of MB during illumination was determined using the aforesaid steps. In the scavenging test, potassium iodide, benzoquinone, and isopropanol were used as scavengers. A suspension of 100 mL MB (10 ppm) and 80 mg catalyst was first stirred in the dark, and 1 mL of the scavenger solution ($2.4 \times 10^{-2}$ M) was then added to the mixture under illumination.

*2.4.2. Kinetic Analysis.* The photocatalytic dye degradation kinetic is often investigated according to the *pseudo*-first-order kinetic model or the Langmuir-Hinshelwood model [30, 31] for heterogeneous catalysis as follows:

$$\ln \frac{C}{C_0} = -k \cdot t, \tag{1}$$

where $C_0$ and $C$ are the initial concentration at time $t$ (mg·L$^{-1}$) and $k$ is the rate constant (min$^{-1}$).

However, the experimental design often involves two consecutive steps of dark adsorption and photocatalytic degradation. The problem to discuss here is the concentration $C_0$ in equation (1): whether it is the initial concentration or the equilibrium concentration just before illumination ($C_e$). Both of them seem unreasonable because $C_e$, in this case, is not an independent variable, but it depends on the balance of the dye in the solution and the adsorbent. $C_0$ is the initial concentration. However, as soon as the photocatalytic reaction occurs, the initial concentration is not $C_0$ but $C_e$. Most studies have ignored this issue. In order to overcome this obstacle, a new kinetic model is proposed by combining the heterogeneous catalysis for unimolecular reactions with the adsorption isotherms.

A heterogeneous catalyst first adsorbs the dye molecule from the aqueous solution onto its surface and then catalyzes the reaction under irradiation (two steps).

Step 1: adsorption

$$\text{Dye} + \text{surface} \longleftrightarrow \text{dye(adsorbed)(fast)} \tag{2}$$

Step 2: photocatalytic reaction

$$\text{Dye(adsorbed)} \longrightarrow \text{products(slow)} \tag{3}$$

It can be assumed that the first step occurs until equilibrium, whereas the second is rate limiting.

For the first step, the equilibrium adsorption capacity $q_e$ (mg·g$^{-1}$) can be calculated according to

$$q_e = V \cdot \frac{C_0 - C_e}{m}, \tag{4}$$

where $C_0$ and $C_e$ are the initial and equilibrium dye concentrations (mg·L$^{-1}$); $V$ and $m$ are the solution volume (L) and mass of catalyst (g), respectively.

Further, $C_e$ and $q_e$ are related following the Langmuir isotherm.

$$q_e = q_m \cdot \frac{K_L \cdot C_e}{1 + K_L \cdot C_e}, \tag{5}$$

where $q_m$ (mg·g$^{-1}$) and $K_L$ (L·mg$^{-1}$) are the maximum monolayer adsorption capacity and the Langmuir equilibrium constant, respectively.

The photocatalytic degradation rate can be expressed by

$$r = k_r \cdot \theta, \tag{6}$$

where $k_r$ is the apparent rate constant (mg·L$^{-1}$·min$^{-1}$) and $\theta$ is the coverage fraction (dimensionless), which can be represented by the Langmuir isotherm. Therefore, equation (6) can be rewritten as

$$r = k_r \cdot \frac{K_L \cdot C}{1 + K_L \cdot C} = -\frac{dC}{dt}. \tag{7}$$

Now, integrating equation (7) with the boundary conditions of $C = C_e$ at $t = 0$ min (subtracted the time required for saturated adsorption) and $C = C$ at $t = t$.

$$\frac{1}{K_L} \cdot \ln C + C = -k_r \cdot t + \frac{1}{K_L} \cdot \ln C_e + C_e. \tag{8}$$

The values of $k_r$ can be obtained from the slope of the linear plot $((1/K_L) \cdot \ln C + C)$ vs. $t$.

## 3. Results and Discussion

*3.1. Synthesis of the Porous Octahedral ZnO/CuO Composite from Zn/Cu-BTC.* The compositional phase of the as-prepared materials is investigated using XRD (Figure 1). The reflection peaks of Cu-BTC appear as (200), (220), (311), (222), (400), (331), (420), (422), (511), (440), (600), (444), (511), (553), and (751) [32, 33], which indicates that the obtained Cu-BTC is MOF-199 with a space group of $Fm\bar{3}m$ [13]. Zn-BTC can exist in different forms depending on the synthesis conditions. The XRD pattern of the prepared Zn-BTC is consistent with that of Zn-BTC synthesized with the microwave-assisted method [21] but is different from that synthesized from $Zn(CH_3COO)$ with the solvothermal method [17] and with the ultrasound-assisted method [18]. The XRD patterns of Zn/Cu-BTC are consistent with those of Cu-BTC with a characteristic peak of Zn-BTC at 10.5°, indicating that Zn/Cu-BTC is constituted from Cu-BTC and Zn-BTC.

The thermal behaviors of BTC compounds are studied via TG-DTA (Figure 2). For Zn-BTC and Cu-BTC, an exothermic peak appears at around 472 and 327°C, respectively, accompanied by large weight losses (approximately 42 and 39%), which is attributed to the combustion of BTC in the compounds (see Table S1). The complete decomposition temperature is around 470°C for Cu-BTC (400°C reported by reference [34], 670°C reported by reference [35]) and 500°C for Zn-BTC. In the case of Zn/Cu-BTC, an endothermic peak at 100°C with a weight loss of approximately 27% is assigned to the evaporation of the physically adsorbed water. Two exothermic peaks at 334 and 387°C with a weight loss of around 47% are due to the decomposition of Cu-BTC and Zn-BTC in Zn/Cu-BTC. The complete decomposition of Zn/Cu-BTC also takes place at around 500°C, and

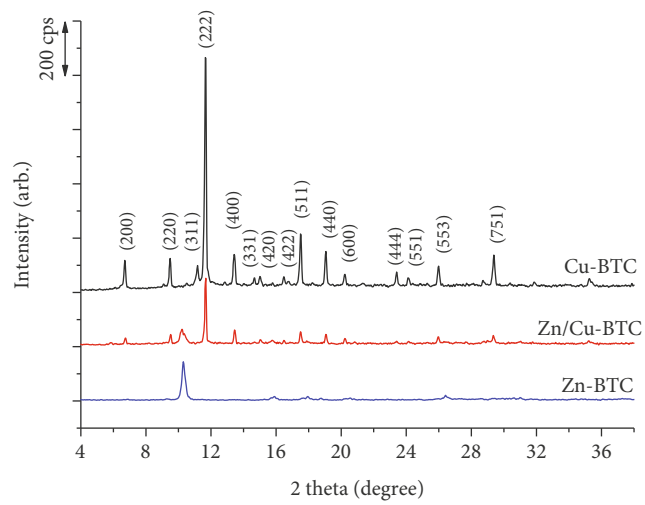


Figure 1: XRD patterns of Cu-BTC, Zn-BTC, and Zn/Cu-BTC.

therefore, this temperature is selected to calcinate the precursors to obtain the oxides.

During the calcination for 5 hours, hexagonal wurtzite ZnO, monoclinic CuO (JCPDS card No. 48–1548 and 36–1451, respectively), and bimetallic ZnO/CuO are formed (Figure 3). No unknown peaks are observed in the XRD diagrams, indicating that pure single oxides and a bimetallic oxide (ZnO/CuO) are obtained. In addition, the presence of peak broadening reveals that a grain refinement occurs in ZnO/CuO possibly due to the formation of heterojunction structures. The average particle size of ZnO and CuO in the octahedral ZnO/CuO nanocomposite is ~44 nm and ~23 nm (calculated using Scherrer's equation from the line broadening of (101) and (111) diffraction peak for ZnO and CuO, respectively).

Figure 4 displays the morphologies of the as-prepared materials before and after calcination. Cu-BTC yields smooth octahedral crystals of ~10 $\mu$m size (Figure 4(a1)); however, during calcination, the structural framework of Cu-BTC collapses to form irregular particles (Figure 4(a2)). To prevent this collapse, the calcination temperature was set to ~400°C (Figure S1). Zn-BTC comprises nanorods of diameter ~200 nm (Figure 4(b1)), and after calcination, they yield in ZnO nanofibers (consisted of nanoparticles of 30~50 nm size) (Figure 4(b2)). As for Zn/Cu-BTC, octahedral particles with flocculent substances (Zn-BTC) on the crystal surface are formed (Figure 4(c1)). Bimetallic ZnO/CuO octahedrons of diameter 5–10 $\mu$m remain unaltered after calcination (Figure 4(c2)). The TEM images show that ZnO/CuO octahedrons comprise nanoparticles of ~50 nm size (Figure 4(d1)). On the HR-TEM images of ZnO/CuO, it can be seen that the interplanar spacing of lattice fringes is 0.232 nm (corresponding to the (111) plane of monoclinic CuO (JCPDS card No. 48–1548)) and 0.281 nm (corresponding to the (100) plane of hexagonal ZnO (JCPDS card No. 36–1451)). Hence, the intragranular location of both oxide phases could enhance the efficiency of semiconductor coupling effects.

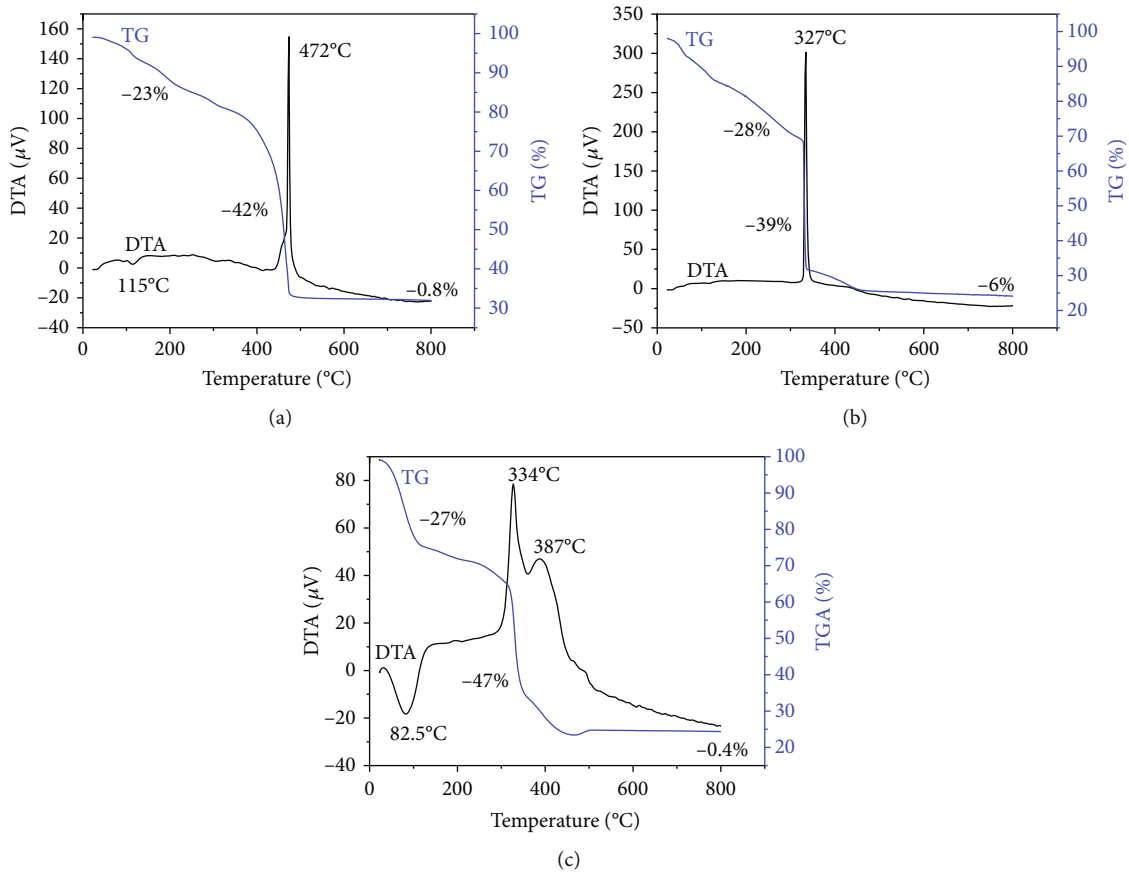


Figure 2: TG-DTA diagrams of (a) Zn-BTC, (b) Cu-BTC, and (c) Zn/Cu-BTC.

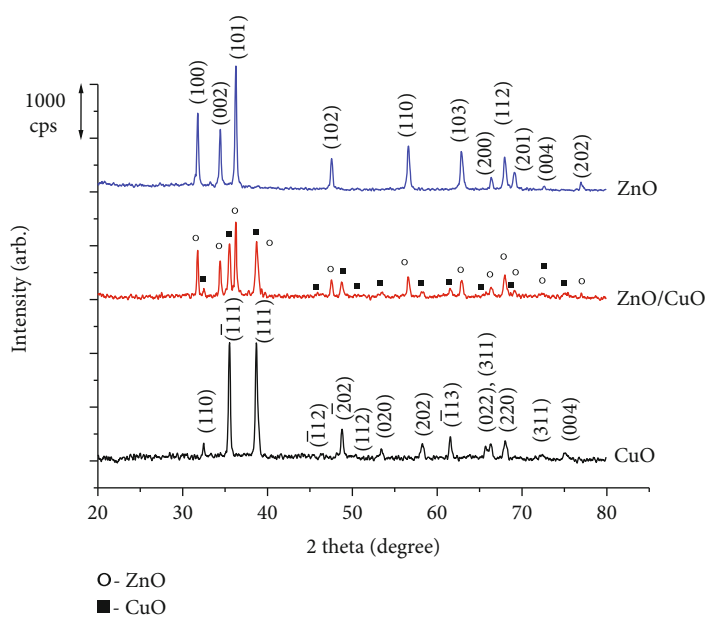


Figure 3: XRD patterns of ZnO, CuO, and ZnO/CuO.

The elemental analysis of C, H, Zn, and Cu in the as-prepared materials is presented in Table 1. No carbon is present in ZnO/CuO, indicating the complete removal of the organic templates. The molar ratio of Zn/Cu in Zn/Cu-BTC and ZnO/CuO analyzed with AAS and EDX (Figure S2) is practically identical (0.42/1 and 0.39/1 for

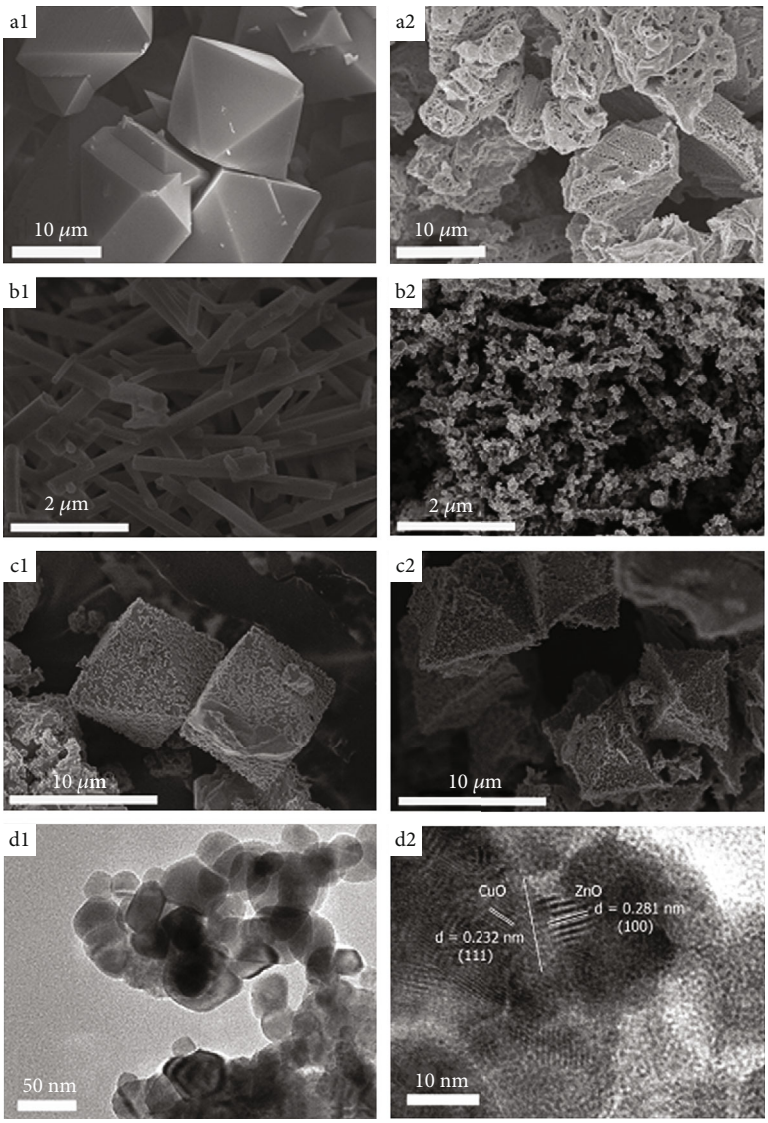


Figure 4: SEM observations of (a1) Cu-BTC, (b1) Zn-BTC, (c1) Zn/Cu-BTC, (a2) CuO, (b2) ZnO, and (c2) ZnO/CuO; (d1) TEM observation of ZnO/CuO; (d2) HR-TEM of ZnO and CuO region.

Table 1: Elemental analysis of C, H, Zn, and Cu in Zn/Cu-BTC and ZnO/CuO.

| Notation | Elemental composition (% mass) | | | | Zn/Cu (mol/mol) | |
|---|---|---|---|---|---|---|
| | C* | H* | Zn** | Cu ** | (**) | (***) |
| Zn/Cu-BTC | 36.18 | 1.93 | 7.49 | 17.19 | 0.42/1 | 0.39/1 |
| ZnO/CuO | 0.00 | 0.00 | 20.18 | 62.56 | 0.31/1 | 0.30/1 |

*Elemental analysis; **AAS analysis; ***EDX analysis.

Zn/Cu-BTC and 0.31/1 and 0.30/1 for ZnO/CuO), implying a high dispersion of bimetallic oxides. However, this molar ratio is significantly lower than the initial one (Zn/Cu = 7/3 = 2.33/1), signifying that a large number of $Zn^{2+}$ ions remain in the solution instead of transforming into ZnO. It might happen due to the lower affinity of Zn (electronegativity, 1.65) to carboxyl groups in BTC compared with that of Cu to BTC (electronegativity, 1.9).

The textural properties of the as-synthesized materials were investigated using nitrogen adsorption/desorption isotherms (Figure 5). According to IUPAC, the obtained BTC compounds can be assigned to I-type (microporous materials) [36, 37]. BTC compounds except Zn-BTC exhibit a large surface area as those published in the literature [13]. The BET surface areas of Cu-BTC, Zn-BTC, and Zn/Cu-BTC are 1635 $m^2 \cdot g^{-1}$, 3 $m^2 \cdot g^{-1}$, and 844.4 $m^2 \cdot g^{-1}$, respectively (see Table S2). Feldblyum et al. [20] asserted that the low surface area of Zn-BTC is because of its densified surface crystal, presumably due to pore collapse. The blocking of large pores at the surface effectively inhibits adsorbates such as $N_2$ gas from entering the bulk structure [20]. After calcination, the isotherm of ZnO remains in type I, while the other oxides exhibit the type-IV isotherm with an H3

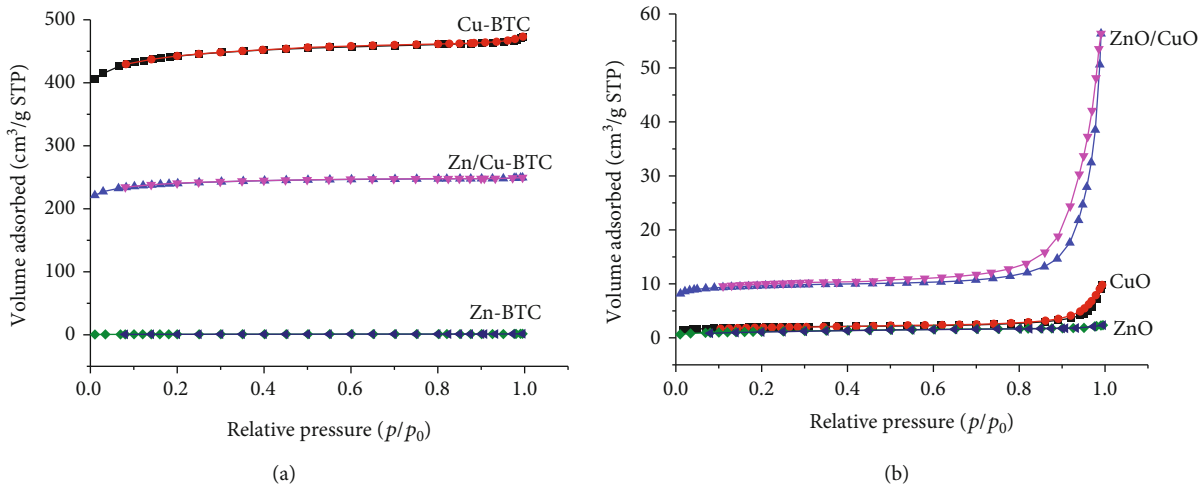


Figure 5: Nitrogen adsorption/desorption isotherms of Cu-BTC, Zn-BTC, Zn/Cu-BTC, CuO, ZnO, and ZnO/CuO.

hysteresis loop at a relative pressure ranging from 0.5 to 0.9, manifesting the presence of mesopores and micropores [36, 38]. The specific surface area of calcined materials except ZnO reduces significantly to 6.7 $m^2 \cdot g^{-1}$ for CuO and 32.5 $m^2 \cdot g^{-1}$ for ZnO/CuO. It is worth noting that the specific surface area of the octahedral ZnO/CuO nanocomposite in this study is significantly higher than that of ZnO and CuO and approximately two to four times as high as that of several ZnO/CuO composites synthesized with other methods [7, 39, 40]. This result confirms the advantages of synthesizing multimetal oxide from MOF precursors.

The XPS spectra of the ZnO/CuO nanocomposite are presented in Figure 6. The survey spectrum shows that the presence of Zn, Cu, and O without any foreign species except for carbon whose 1s peak (284 eV) is employed to calibrate the acquired spectra (Figure 6(a)). The XPS spectrum of Cu has a doublet of $Cu2p_{3/2}$ (at 933 eV) and $Cu2p_{1/2}$ (at 952 eV) along with other satellite peaks at higher binding energies [39] (Figure 6(b)). Both peaks are very typical for the XPS spectrum of $Cu^{2+}$ [28]. Zn(II) manifests a doublet of $Zn2p_{3/2}$ at 1022 eV and $Zn2p_{1/2}$ at 1045 eV (Figure 6(c)) [41]. Therefore, it can be inferred that ZnO/CuO is a compound containing Zn (II), Cu (II), and O.

The band gap energies ($E_g$) of ZnO, CuO, and ZnO/CuO are calculated using UV-Vis-DRS measured at room temperature (Figure 7(a)). ZnO exhibits an absorption band with wavelengths of 350–390 nm (band gaps of 3.5–3.2 eV) in the ultraviolet region. CuO manifests a broad peak in the visible light region. The characteristic absorption bands of ZnO and CuO are observed in the spectrum of ZnO/CuO. The absorption band of CuO shifts toward shorter wavelengths and integrates with the absorption band of ZnO, signifying that the band edges of *p*-type CuO and *n*-type ZnO are well-matched [8]. Tauc's plot [42] is illustrated in Figure 7(b). The $E_g$ values of ZnO and CuO are 3.19 eV and 1.94 eV, respectively (previously reported as 3.2–3.3 eV for ZnO [43, 44] and 1.4–1.85 eV for CuO [44–46]) (see Table S3). ZnO/CuO has an $E_g$ value of 2.63 eV, manifesting a remarkable shift toward the longer wavelength region.

Figure 8 shows the photoluminescence spectra (PL) of the obtained materials with an excitation wavelength of 300 nm. The maximum PL intensity is at 387.4 nm for CuO and 510.2 nm for ZnO. However, the PL intensity of ZnO/CuO composite is significantly weaker than those of the CuO and ZnO. It is well known that low PL intensity means low recombination of electron and holes, then the opposite would be high PL intensity would increase recombination rate and reduce photocatalytic activity. These results demonstrate that the combinations ZnO and CuO have reduced the recombination of photonic electrons and photogenic holes, which may increase the photocatalytic activity of the material.

### 3.2. Visible-Light-Driven Photocatalytic Degradation of Dyes

*3.2.1. Decolorization of MB with Different Catalysts.* Figure 9(a) displays the process of MB decolorization over Zn-BTC, Cu-BTC, and Zn/Cu-BTC. It is apparent that the adsorption equilibrium is reached after 60 min, and the BTC compounds exhibit high adsorption capacities. Zn/Cu-BTC displays the highest decolorization efficiency ($F$) at ~69%, followed by Cu-BTC (~66%) and Zn-BTC (~22%) ($F = 100 \times (C_0 - C_t)/C_0$, where $C_0$ and $C_t$ are the initial concentration and at time $t$). However, the decolorization efficiency of Cu-BTC decreases to 41–50% after 60 min of UV/Vis irradiation. This indicates that desorption occurs during irradiation. Zn-BTC exhibits weak photocatalytic activity upon UV or Vis irradiation and yields a decolorization efficiency of ~50% after 420 min of UV illumination and 38% after 420 min of Vis irradiation. This may be due to its very low surface area which decreases the number of active sites for MB to adsorb and decompose.

In contrast, all calcinated materials manifest poor adsorption with a very low decolorization efficiency of ~5%. This is

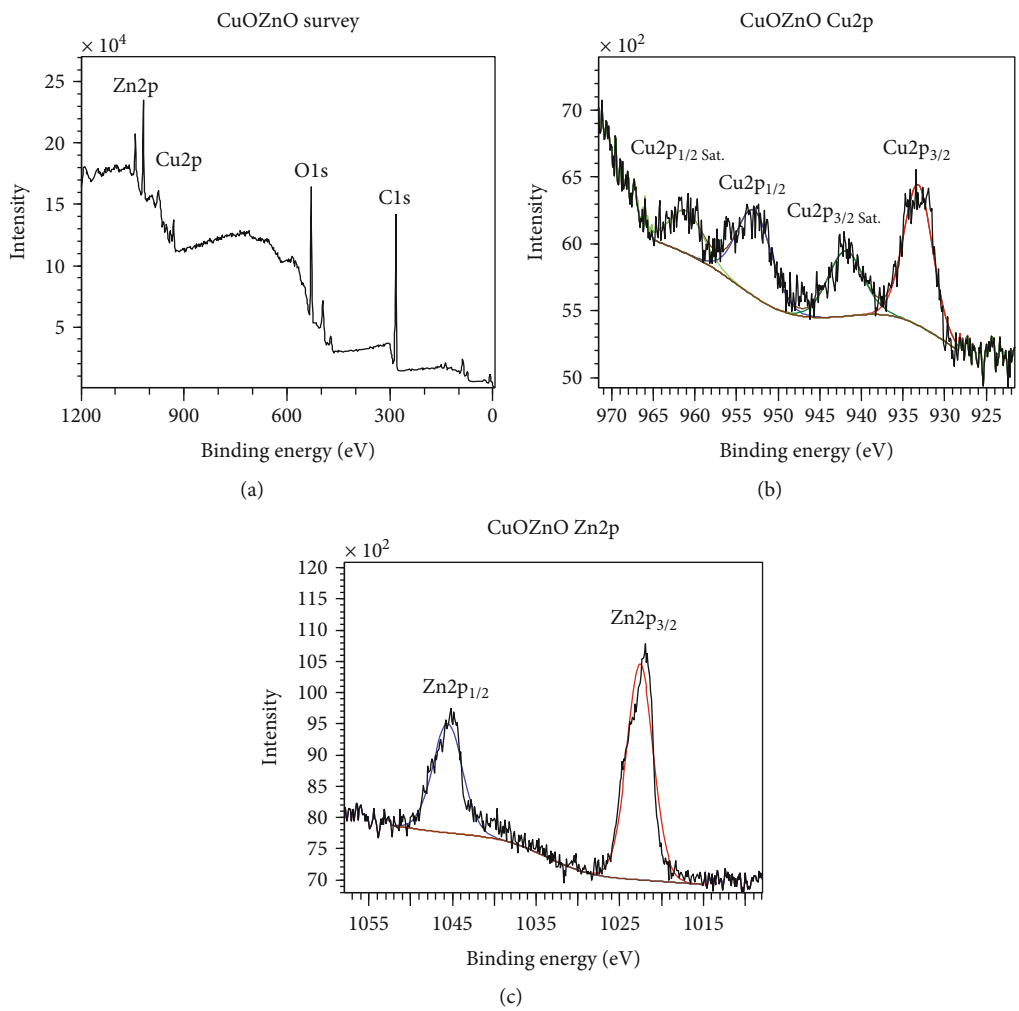


Figure 6: XPS spectra of ZnO/CuO (a) survey spectrum, (b) Cu2p where Sat denoted as satellite peaks, and (c) Zn2p1/2 spectrum.

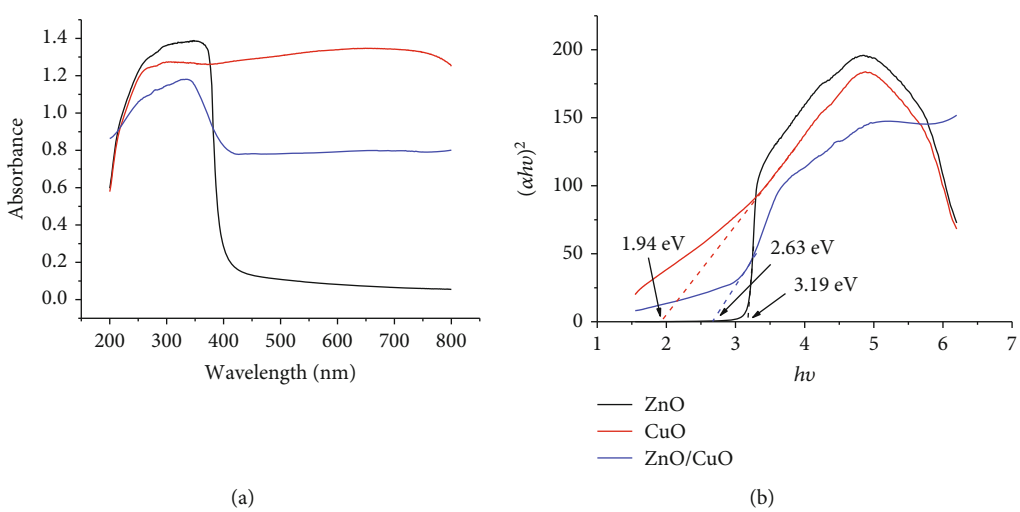


Figure 7: (a) UV-Vis diffuse reflectance spectra and (b) Tauc's plots of ZnO, CuO, and ZnO/CuO.

the result of the collapse of the porous structure after calcination, leading to the disappearance of the adsorption sites. As can be seen from Figure 9(b), CuO could not catalyze any MB degradation, while ZnO and ZnO/CuO exhibit photocatalytic activities in both visible and ultraviolet regions. It is worth noting that ZnO/CuO demonstrates an excellent

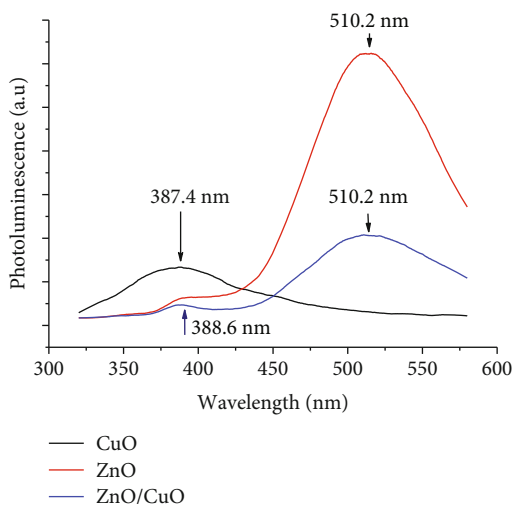


Figure 8: Photoluminescence spectra of CuO, ZnO, and ZnO/CuO.

photocatalytic activity, and the complete decolorization of MB occurs after 120 min under visible illumination. Meanwhile, ZnO (UV) and ZnO (Vis) decolorize MB up to 95 and 90%, respectively, after 240 min of illumination. The ZnO/CuO composite also catalyzes MB degradation faster than pure CuO or ZnO under visible light illumination. In fact, after 120 minutes, its decolorization efficiency is 1.57 and 7.7 times as high as that of ZnO and CuO, respectively. The porous ZnO/CuO composite with a large surface area would provide the heterojunction structure and an effective environment for a larger number of surface active sites. This increases MB–ZnO/CuO interaction and thus promoting photodegradation. In other words, the combination of ZnO and CuO causes the synergistic effect in the catalytic degradation of methylene blue.

*3.2.2. Effect of pH and Leaching Experiment.* Effect of pH on decolorization of MB over ZnO/CuO catalyst is shown in Figure 10(a). The decolorization performance seems to be unchangeable in pH range from 2 to 7 and increases significantly when pH increases. The point of zero charge ($pH_{pzc}$) for ZnO/CuO, determined using the pH drift method, is around 7.9 (Figure 10(b)) [47]. At lower pH (lower than $pH_{pzc}$), the surface of ZnO/CuO is positively charged. When pH increases from 2 to 7, the surface becomes less positive and the decolorization efficiency increases slightly. At higher pH (higher than $pH_{pzc}$), the surface of ZnO/CuO is negatively charged; hence, MB and the catalyst attract each other through electrostatic interaction; thus, the decolorization efficiency increases significantly.

During the leaching experiment, the catalyst was filtered after 30 min and the decolorization of MB under illumination almost stops (Figure 10(c)). In addition, the decolorization of MB without the catalyst is not observed after 70 min of illumination, indicating that MB is stable in the visible light region. Therefore, it can be inferred that ZnO/CuO acts as a heterogeneous catalyst in the photocatalytic degradation of methylene blue.

*3.2.3. Visible-Light-Driven Photocatalytic Degradation of MB with ZnO/CuO Composite.* The absorption bands at 292 nm and at 664 nm on the UV-Vis absorption spectra of MB can be attributed to the benzene ring and the conjunction color group –N=N–, respectively (Figure 11(a)). The intensity of these bands decreases with the increasing illumination time, and they almost disappear after 90 min of the reaction. The decolorization of MB occurs due to the disappearance of the color conjunction group during illumination. The TOC test also proves the mineralization of MB during photocatalytic degradation (Figure 11(b)). The TOC of MB reduces significantly from 6.35 $mg{\cdot}L^{-1}$ for initial solution to 0.72 $mg{\cdot}L^{-1}$ after 140 min of illumination, indicating complete mineralization of MB over ZnO/CuO composite.

In order to clarify the radical mechanism of the degradation reaction, three radical scavengers (KI for electron holes, isopropanol for $^{\cdot}OH$, and benzoquinone for $O^{2\cdot-}$) were used in the present experiment. It is evident that the addition of isopropanol causes a moderate reduction in photocatalytic activity, while KI practically impedes the photocatalytic degradation of MB (Figure 12). Benzoquinone hinders degradation by around 50%. This infers that electron holes and superoxides play an important role in MB degradation.

A mechanism of photocatalysis on a semiconductor is employed to explain the photocatalytic activities in the visible light region. Since the band gap positions for the conduction band of CuO and ZnO are −0.43 eV and −0.15 eV *vs.* NHE, respectively [9, 48], and the band gaps of CuO and ZnO are 1.94 and 3.19 eV, then the band gap positions for valence bands are 1.51 eV for CuO and 3.04 eV for ZnO (see Table S3). Due to the strong light adsorption capacity of CuO in the visible light region, electrons are excited from VB to CB to form photogenerated $h^+/e^-$ pairs. The position of CB in CuO is more negative than that in ZnO; hence, the transfer of the excited electrons to $E_{CB}$ (ZnO) prevents the fast recombination of photoexcited $e^-/h^+$ pairs (equations (9) and (10)). On the other hand, the state of MB (1.17 eV) could be excited to MB* (−0.69 eV) by visible light [49, 50] (equation (11)). The work function of the photoexcited MB* (−0.69 eV) is more negative than that of CuO and ZnO [49, 50]. MB acts as the photosensitizer to provide additional photogenerated electrons into CBs of CuO and ZnO through the formed downstream channel (equations (12) and (13)). The VB potential for CuO (1.51 eV) is more positive than that of MB (1.17 eV); therefore, $h^+$ could easily oxidize MB to form degradation products (equation (14)). On the other hand, the CB edge position of CuO (−0.43 eV) is more negative than that of $E^0$ $(O_2/O_2^{\cdot-})$ (−0.33 eV) [51]; thus, electrons on the conduction band of CuO reacts with $O_2$ to produce superoxide radical $O_2^{\cdot}$, which could substantially oxidize MB to form degradation products (equations (15) and (16)). In principle, $h^+$ (1.51 eV) could not oxidize $H_2O$ ($E(H_2O/^{\cdot}OH) = 2.6$ eV), but the experimental result still indicates the role of $^{\cdot}OH$ in the oxygenation of dye as shown in Figure 12. This is still a challenging problem possibly due to the deviation between theoretical and practical estimation. The transfer path of

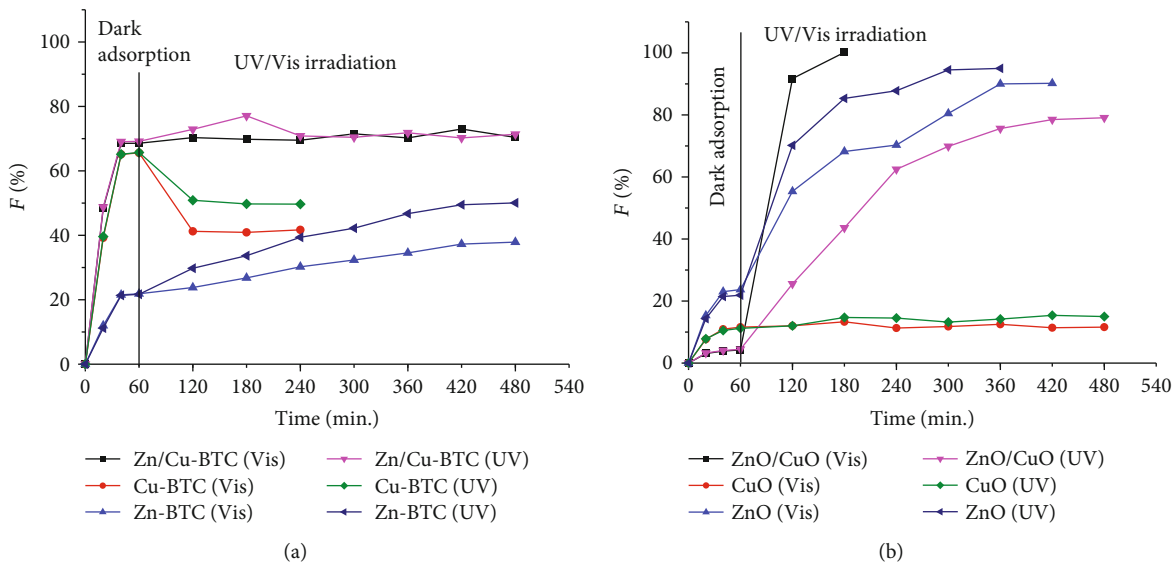


Figure 9: Decolorization of MB over (a) as-prepared Zn-BTC, Cu-BTC, Zn/Cu-BTC, and (b) CuO, ZnO, and ZnO/CuO under UV and visible irradiation (conditions: $V = 500$ mL; $m_{catalyst} = 400$ mg; concentration of MB = 10 ppm).

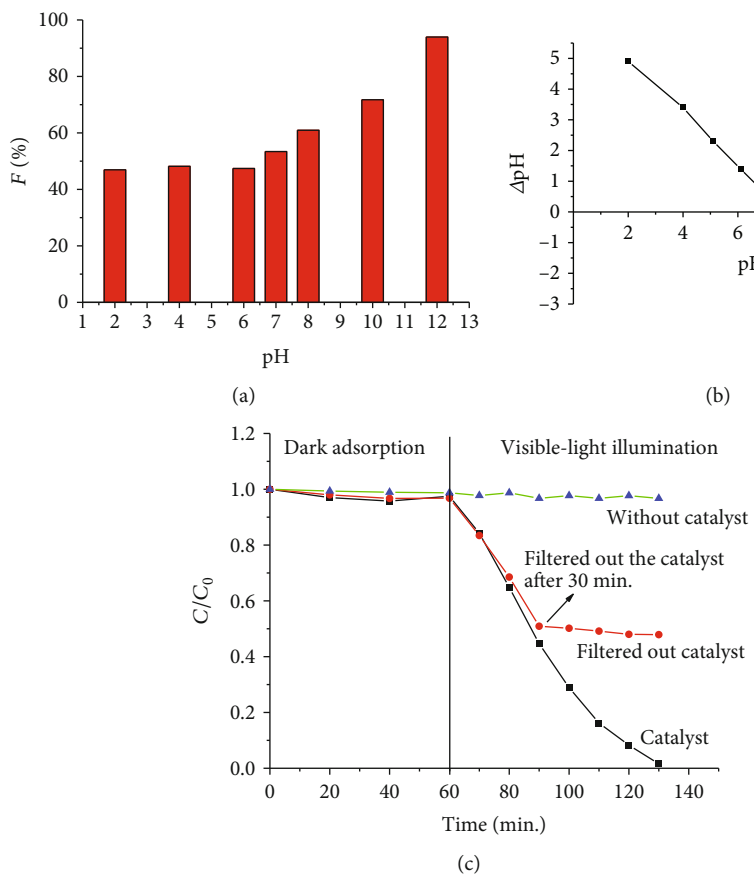


Figure 10: (a) Effect of pH on decolorization of MB over porous ZnO/CuO octahedron catalyst; (b) the point of zero charge obtained from the pH drift method ($V = 100$ mL, $C_0 = 10\ \mathrm{mg \cdot L^{-1}}$; $m_{catalyst} = 80$ mg; adsorption time = 60 min; illumination time = 70 min); (c) leaching experiment ($V = 500$ mL; $C_0 = 10\ \mathrm{mg \cdot L^{-1}}$; $m_{catalyst} = 400$ mg, adsorption time = 60 min).

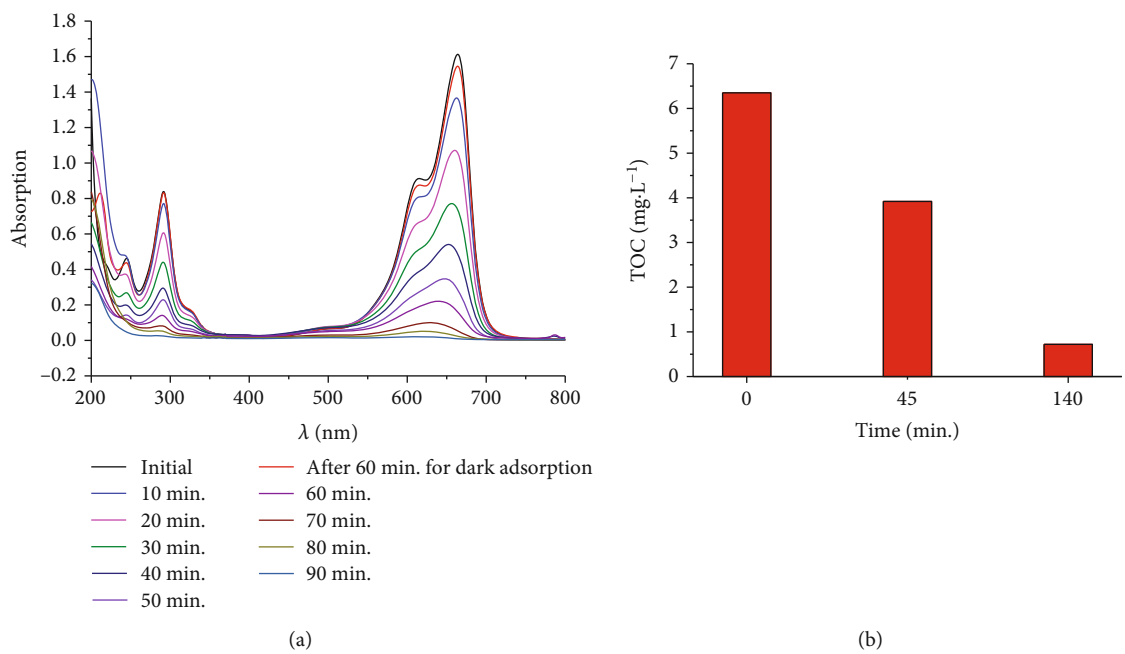


Figure 11: (a) UV-Vis absorption spectra at different times and (b) TOC of MB solution in the photocatalytic degradation ($V = 500$ mL; $C_0 = 10$ ppm; $m_{catalyst} = 400$ mg; adsorption time = 60 min).

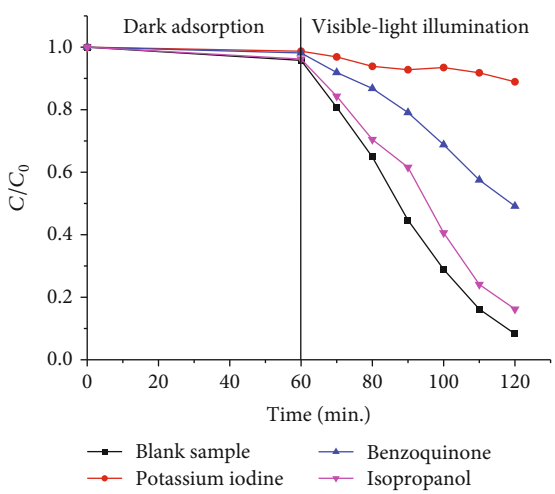


Figure 12: Effect of radical scavengers (potassium iodide, isopropanol, and benzoquinone) on MB decolorization over porous ZnO/CuO octahedrons catalyst ($V = 100$ mL; $C_0 = 10$ ppm; $m_{catalyst} = 80$ mg; adsorption time = 60 min; concentration of scavenger solution: $2.4 \times 10^{-4}$ M).

photogenerated charge carriers under visible light illumination is illustrated in Figure 13.

$$\mathrm{ZnO/CuO} + h\nu \longrightarrow \mathrm{ZnO/CuO}\left(\mathrm{h}^+ + \mathrm{e}^-\right) \quad (9)$$

$$\mathrm{ZnO/CuO}\left(\mathrm{e}^-/\mathrm{CB}\right) \longrightarrow \left(\mathrm{e}^-/\mathrm{CB}\right)\mathrm{ZnO/CuO} \quad (10)$$

$$\mathrm{MB} + h\nu \longrightarrow \mathrm{MB}^* \quad (11)$$

$$\mathrm{MB}^* \longrightarrow \mathrm{e}^- + \mathrm{MB}^{*+} \quad (12)$$

$$\mathrm{MB}^{*+} \longrightarrow \mathrm{MB} + \mathrm{h}^+ \quad (13)$$

$$\mathrm{CuO}\left(\mathrm{h}^+\right) + \mathrm{MB} \longrightarrow \text{degradation products} \quad (14)$$

$$\mathrm{CuO}\left(\mathrm{e}^-/\mathrm{CB}\right) + \mathrm{O_2} \longrightarrow \mathrm{O_2}^{\bullet-} + \mathrm{ZnO} \quad (15)$$

$$\mathrm{O_2}^{\bullet-} + \mathrm{MB} \longrightarrow \text{degradation products} \quad (16)$$

*3.2.4. Kinetics of MB Photocatalytic Degradation.* The kinetics of adsorption and photocatalytic degradation is presented in Figure 14(a). It is evident that the adsorption reaches equilibrium after 60 min in the dark (MB concentrations of 5~30 ppm). The values of the maximum monolayer adsorption capacity ($q_m$) and the Langmuir equilibrium constant (obtained from the nonlinear plot of $q_e$ vs. $C_e$ (equation (5))) are 1.63 mg·g$^{-1}$ and 0.047 L·mg$^{-1}$, respectively (Figure S3 and Table S4). Equation (8) becomes

$$\frac{1}{0.047} \cdot \ln C + C = -k_r \cdot t + \frac{1}{0.047} \cdot \ln C_e + C_e. \quad (17)$$

The values of $k_r$ can be calculated from the slope of equation (17) $(((1/0.047) \times \ln C + C)$ vs. $t$, Figure 14(b) and Table 2). The classical kinetic model (*pseudo*-first-order-kinetic model) in the linear form as equation (1) is employed to analyze the kinetic data for comparing the goodness of fit (Table 2). The paired sample $t$ test with $\alpha = 0.05$ shows that the proposed model provides statistically higher determination coefficients than the *pseudo*-first-order kinetic model ($t(4) = 5.899$, $p$ value = 0.002 (<0.05)), indicating that the proposed model fits the data more accurately than the classical kinetic model.

It is difficult to compare the catalytic activity of ZnO/CuO composite in the present with that of other catalysts

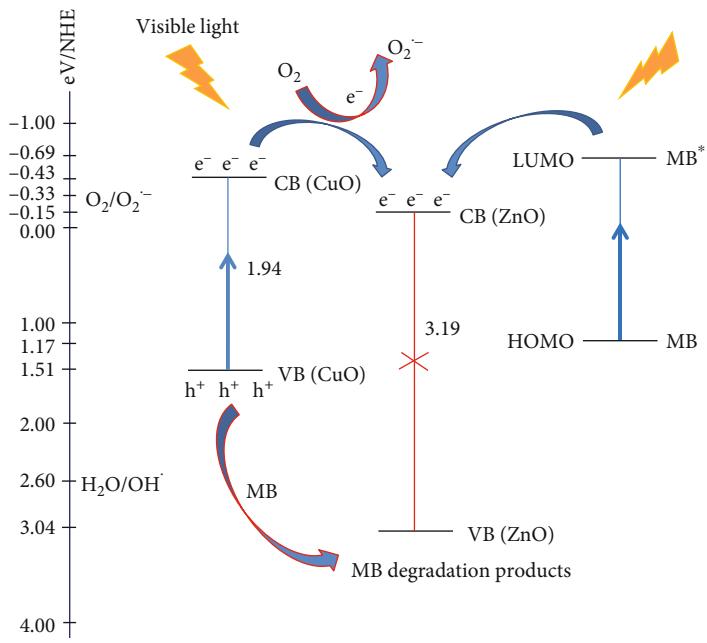


Figure 13: Energy of valence band edge and conduction band edge for ZnO/CuO coupling semiconductor (HOMO: highest occupied molecular orbital and LUMO: lowest unoccupied molecular orbital).

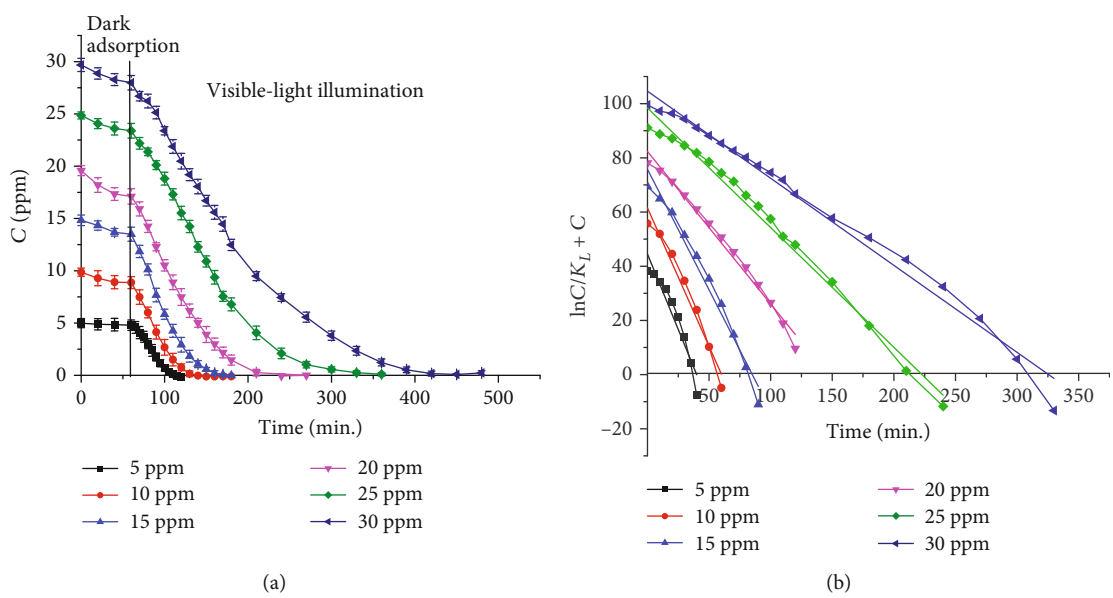


Figure 14: (a) Kinetics of adsorption and photocatalytic degradation of methylene blue over octahedral ZnO/CuO catalyst; (b) linear plots of the proposed kinetic model (conditions: $V = 500$ mL, $C_0 = 5 - 30$ mg $\cdot$ L$^{-1}$, $m_{catalyst} = 400$ mg, temperature = 35°C).

previously reported due to different light sources (UV or Vis), the initial concentration of reactants, the amount of catalyst, the reaction volume, etc. The *pseudo*-first-rate constant appears to be relevant because several authors report the catalytic activity in terms of this value (Table 3). The value of the *pseudo*-first-rate constant for the degradation on the present catalyst in the visible region is lower than that for graphene-like carbon/$TiO_2$ and ZnO/graphene oxide in the UV region and compatible with commercial P25, but higher than that for other catalysts reported such as Ta-ZnO, g-$C_3N_4$/CdS, and Ce-$TiO_2$.

*3.2.5. Recyclability.* Recyclability is an important factor in heterogeneous catalysis. After the cycling experiment, the ZnO/CuO catalyst was first separated by centrifugation, then washed with water and ethanol for three times to remove the dye, and finally dried at 120°C for 15 h. The photocatalytic degradation efficiency of ZnO/CuO decreases from 100% to 97.2% after three cycles (Figure 15(a)). The XRD patterns of the recycled ZnO/CuO samples stay unaltered; therefore, it can be inferred that ZnO/CuO remains stable during photocatalytic degradation reactions (Figure 15(b)).

Table 2: Determination coefficients of the proposed model in the linear form and apparent rate coefficients.

| Initial MB concentration $C_0$ (mg·L$^{-1}$) | $R^2$ (proposed model) | Apparent rate coefficient, $k_r$ (mg·L$^{-1}$·min$^{-1}$) | $R^2$ (*pseudo*-first-order kinetic model) | *Pseudo*-rate constant $k$ (min$^{-1}$) |
|---|---|---|---|---|
| 5 | 0.919 | 1.1138 | 0.8303 | 0.0721 |
| 10 | 0.968 | 1.0219 | 0.8832 | 0.0532 |
| 15 | 0.978 | 0.8909 | 0.9146 | 0.0447 |
| 20 | 0.988 | 0.5629 | 0.8816 | 0.0367 |
| 25 | 0.988 | 0.4417 | 0.9630 | 0.0179 |
| 30 | 0.986 | 0.3213 | 0.9330 | 0.0132 |

Table 3: Comparison of the *pseudo*-first-order rate constant of the present catalyst with that of other catalysts.

| Catalyst | $S_{BET}$ (m$^2$·g$^{-1}$) | Light source (nm, power) | $C_0$ (mg·L$^{-1}$)/volume (mL)/ $m_{catalyst}$ (mg) | Pseudo-first-order rate constant, $k$ (min$^{-1}$) | References |
|---|---|---|---|---|---|
| ZnO | 8.21 | UV, 20 W | 10/100/50 | 0.022 | [52] |
| ZnO/graphene oxide | 31.58 | UV,20 W | 10/100/50 | 0.098 | [52] |
| Pristine $TiO_2$ (P25) | — | 254, 11 W | 10/100/50 | 0.009 | [53] |
| Graphene-like carbon/$TiO_2$ | — | 254, 11 W | 10/100/50 | 0.248 | [53] |
| Pristine $TiO_2$ (P25) | 51 | ≤370, 18 W | 9.6/100/50 | 0.043 | [54] |
| Sm-$TiO_2$ | 46 | 370, 18 W | 9.60/100/50 | 0.020 | [54] |
| Ce-$TiO_2$ | 46 | 370, 18 W | 9.60/100/50 | 0.024 | [54] |
| $TiO_2$ | 50 | 340, 125 W | 23/2750/375 | 0.025 | [55] |
| CdS | 111.2 | >420, 500 W | 25/200/80 | 0.0079 | [56] |
| g-$C_3N_4$ | 9.8 | >420, 500 W | 25/200/80 | 0.0039 | [56] |
| g-$C_3N_4$-CdS | 166.5 | >420, 500 W | 25/200/80 | 0.0121 | [56] |
| Ag/ZnO | — | >570 (high pressure sodium lamp) | 5/–/150 | 0.006 | [57] |
| Ta-ZnO | 36 | >420, 300 | 10/50/50 | 0.0401 | [58] |
| $CeO_2$-$TiO_2$ | 66 | >420, 160 | 10/100/80 | 0.0341 | [59] |
| ZnO/CuO | 33 | >420, 160 | 10/500/400 | 0.0532 | This work |

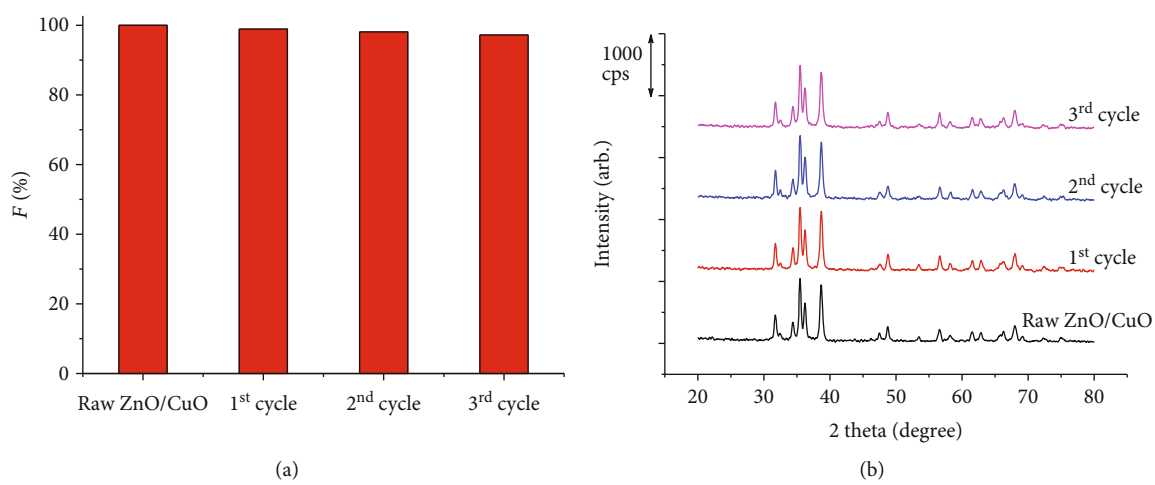


Figure 15: (a) Photocatalytic degradation efficiency of used catalysts; (b) XRD patterns of ZnO/CuO after the third cycle ($V$ = 1000 mL, $C_0$ = 10 ppm, $m_{catalyst}$ = 800 mg; adsorption time = 60 min; light illumination time = 80 min).

In addition, the obtained catalyst manifests excellent photocatalytic degradation of several other dyes, including phenol, phenol red, methyl orange, and Congo red (Figure 16). Porous octahedral ZnO/CuO composite exhibits superior visible-light-driven photocatalytic degradation of MB compared with single CuO or ZnO.

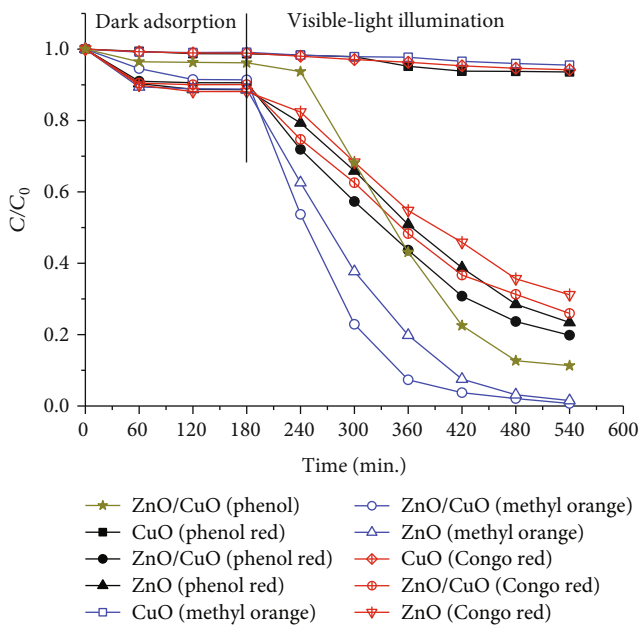


Figure 16: Visible-light driven photocatalytic degradation of several dyes over ZnO, CuO, and porous octahedral ZnO/CuO composite (condition: concentration of dyes = 10 ppm; $V$ = 500 mL; $m_{catalyst}$ = 400 mg; illumination time = 540 min).

## 4. Conclusions

In this study, a porous octahedral ZnO/CuO composite was synthesized from Zn/Cu-based MOF-199. The fabricated ZnO/CuO composite possesses a hierarchical 3D structure consisted of porous octahedral particles of 5–10 $\mu$m in size. Compared with pure ZnO and CuO, the as-prepared ZnO/CuO composite exhibits superior photocatalytic degradation of phenol and different dyes (methyl blue, methyl orange, phenol red, and Congo red) in the visible light region. The formation of a stable $p$–$n$ junction that efficiently separates the photogenerated electron-hole pairs within each semiconductor material is responsible for the degradation. The synthesized photocatalyst remains stable after four cycles of application. The kinetic model of photocatalytic degradation with a unimolecular reaction over heterogeneous catalyst combined with the Langmuir adsorption isotherm is proposed. This model is statistically consistent with the experimental data. The porous ZnO/CuO octahedron composite is an active and stable visible-light-driven catalyst and may serve as a potential catalyst for practical use in the treatment of dye pollutants in aquatic effluents.

## Data Availability

The data used to support the findings of this study are available from the corresponding author upon request.

## Conflicts of Interest

The authors declare that they have no conflicts of interest.

## Acknowledgments

This research was sponsored by Hue University under Decision No. 1208/QĐ-DHH.

## Supplementary Materials

Table S1 presents the weight loss and temperature range derived from TG–DTA measurement of Cu-BTC, Zn-BTC, and Zn/Cu-BTC. The specific surface areas calculated by using the BET model, porous diameters, and volumes for the resulting materials were obtained from the analysis of nitrogen adsorption isotherm data (Table S2). Band gap energy and band edge position of CuO, ZnO, and ZnO/CuO calculated by using Tauc's equation are listed in Table S3. The parameters of the Langmuir and Freudlich isotherm models in linear forms are listed in Table S4 and illustrated in Figure S3. CuO prepared by the pyrolysis of Cu-BTC at 400°C for 5 h retained the octahedral particles as intimal Cu-BTC (Figure S1). The EDX measurement revealed that zinc and copper coexisted in ZnO/CuO sample. *(Supplementary Materials)*

## References

[1] A. Janotti and C. G. Van de Walle, "Fundamentals of zinc oxide as a semiconductor," *Reports on Progress in Physics*, vol. 72, no. 12, article 126501, 2009.

[2] D. C. Reynolds, D. C. Look, and B. Jogai, "Optically pumped ultraviolet lasing from ZnO," *Solid State Communications*, vol. 99, no. 12, pp. 873–875, 1996.

[3] Z.-L. Liu, J.-C. Deng, J.-J. Deng, and F.-F. Li, "Fabrication and photocatalysis of CuO/ZnO nano-composites via a new method," *Materials Science and Engineering: B*, vol. 150, no. 2, pp. 99–104, 2008.

[4] C. Xu, L. Cao, G. Su et al., "Preparation of ZnO/$Cu_2O$ compound photocatalyst and application in treating organic dyes," *Journal of Hazardous Materials*, vol. 176, no. 1–3, pp. 807–813, 2010.

[5] P. Li, Z. Wei, T. Wu, Q. Peng, and Y. Li, "Au–ZnO hybrid nanopyramids and their photocatalytic properties," *Journal of the American Chemical Society*, vol. 133, no. 15, pp. 5660–5663, 2011.

[6] W. Wu, S. Zhang, X. Xiao et al., "Controllable synthesis, magnetic properties, and enhanced photocatalytic activity of spindlelike mesoporous $\alpha$-$Fe_2O_3$/ZnO core–shell heterostructures," *ACS Applied Materials & Interfaces*, vol. 4, no. 7, pp. 3602–3609, 2012.

[7] R. Saravanan, S. Karthikeyan, V. Gupta, G. Sekaran, V. Narayanan, and A. Stephen, "Enhanced photocatalytic activity of ZnO/CuO nanocomposite for the degradation of textile dye on visible light illumination," *Materials Science and Engineering: C*, vol. 33, no. 1, pp. 91–98, 2013.

[8] B. Li and Y. Wang, "Facile synthesis and photocatalytic activity of ZnO–CuO nanocomposite," *Superlattices and Microstructures*, vol. 47, no. 5, pp. 615–623, 2010.

[9] A. Kargar, Y. Jing, S. J. Kim, C. T. Riley, X. Pan, and D. Wang, "ZnO/CuO heterojunction branched nanowires for photoelectrochemical hydrogen generation," *ACS Nano*, vol. 7, no. 12, pp. 11112–11120, 2013.

[10] Y. Zhang, S. Yuan, G. Day, X. Wang, X. Yang, and H.-C. Zhou, "Luminescent sensors based on metal-organic frameworks," *Coordination Chemistry Reviews*, vol. 354, pp. 28–45, 2018.

[11] H.-C. J. Zhou and S. Kitagawa, Eds., "Metal–organic frameworks (MOFs)," *Chemical Society Reviews*, vol. 43, no. 16, pp. 5415–5418, 2014.

[12] K. K. Gangu, S. Maddila, S. B. Mukkamala, and S. B. Jonnalagadda, "A review on contemporary metal–organic framework materials," *Inorganica Chimica Acta*, vol. 446, pp. 61–74, 2016.

[13] S. S.-Y. Chui, S. M.-F. Lo, J. P. H. Charmant, A. G. Orpen, and I. D. Williams, "A chemically functionalizable nanoporous material $[Cu_3(TMA)_2(H_2O)_3]n$," *Science*, vol. 283, no. 5405, pp. 1148–1150, 1999.

[14] S. L. Ho, I. C. Yoon, C. S. Cho, and H.-J. Choi, "A recyclable metal-organic framework MOF-199 catalyst in coupling and cyclization of $\beta$-bromo-$\alpha$,$\beta$-unsaturated carboxylic acids with terminal alkynes leading to alkylidenefuranones," *Journal of Organometallic Chemistry*, vol. 791, pp. 13–17, 2015.

[15] Y. Jiang, X. Zhang, X. Dai et al., "Microwave-assisted synthesis of ultrafine Au nanoparticles immobilized on MOF-199 in high loading as efficient catalysts for a three-component coupling reaction," *Nano Research*, vol. 10, no. 3, pp. 876–889, 2017.

[16] E. Ghorbani-Kalhor, "A metal-organic framework nanocomposite made from functionalized magnetite nanoparticles and HKUST-1 (MOF-199) for preconcentration of Cd(II), Pb(II), and Ni(II)," *Microchimica Acta*, vol. 183, no. 9, pp. 2639–2647, 2016.

[17] M. Anbia, M. Faryadras, and A. Ghaffarinejad, "Synthesis and characterization of $Zn_3(BTC)_2$ nanoporous sorbent and its application for hydrogen storage at ambient temperature," *Journal of Applied Chemical Research*, vol. 9, no. 3, pp. 33–41, 2015.

[18] A. A. Tehrani, V. Safarifard, A. Morsali, G. Bruno, and H. A. Rudbari, "Ultrasound-assisted synthesis of metal–organic framework nanorods of Zn-HKUST-1 and their templating effects for facile fabrication of zinc oxide nanorods via solid-state transformation," *Inorganic Chemistry Communications*, vol. 59, pp. 41–45, 2015.

[19] L. Xu, E.-Y. Choi, and Y.-U. Kwon, "Ionothermal synthesis of a 3D Zn–BTC metal-organic framework with distorted tetranuclear $[Zn_4(\mu_4\text{-O})]$ subunits," *Inorganic Chemistry Communications*, vol. 11, no. 10, pp. 1190–1193, 2008.

[20] J. I. Feldblyum, M. Liu, D. W. Gidley, and A. J. Matzger, "Reconciling the discrepancies between crystallographic porosity and guest access as exemplified by Zn-HKUST-1," *Journal of the American Chemical Society*, vol. 133, no. 45, pp. 18257–18263, 2011.

[21] C. T. Pereira da Silva, B. N. Safadi, M. P. Moisés et al., "Synthesis of Zn-BTC metal organic framework assisted by a home microwave oven and their unusual morphologies," *Materials Letters*, vol. 182, pp. 231–234, 2016.

[22] H. Guo, T. Li, W. Chen et al., "General design of hollow porous $CoFe_2O_4$ nanocubes from metal–organic frameworks with extraordinary lithium storage," *Nanoscale*, vol. 6, pp. 15168–15174, 2014.

[23] S. Chen, M. Xue, Y. Li et al., "Porous $ZnCo_2O_4$ nanoparticles derived from a new mixed-metal organic framework for supercapacitors," *Inorganic Chemistry Frontiers*, vol. 2, pp. 177–183, 2015.

[24] H. D. Mai, K. Rafiq, and H. Yoo, "Nano metal-organic framework-derived inorganic hybrid nanomaterials: synthetic strategies and applications," *Chemistry–A European Journal*, vol. 23, pp. 5631–5651, 2017.

[25] X. Xu, K. Cao, Y. Wang, and L. Jiao, "3D hierarchical porous $ZnO/ZnCo_2O_4$ nanosheets as high-rate anode material for lithium-ion batteries," *Journal of Materials Chemistry A*, vol. 4, pp. 6042–6047, 2016.

[26] G. Huang, F. Zhang, L. Zhang, X. Du, J. Wang, and L. Wang, "Hierarchical $NiFe_2O_4/Fe_2O_3$ nanotubes derived from metal organic frameworks for superior lithium ion battery anodes," *Journal of Materials Chemistry A*, vol. 2, pp. 8048–8053, 2014.

[27] R. Wu, X. Qian, K. Zhou, J. Wei, J. Lou, and P. M. Ajayan, "Porous spinel $Zn_xCo_{3-x}O_4$ hollow polyhedra templated for high-rate lithium-ion batteries," *ACS Nano*, vol. 8, pp. 6297–6303, 2014.

[28] X. Lei, Y. Cao, Q. Chen, X. Ao, Y. Fang, and B. Liu, "ZIF-8 derived hollow CuO/ZnO material for study of enhanced photocatalytic performance," *Colloids and Surfaces A: Physicochemical and Engineering Aspects*, vol. 568, pp. 1–10, 2019.

[29] T. T. Minh, N. H. Phong, H. Van Duc, and D. Q. Khieu, "Microwave synthesis and voltammetric simultaneous determination of paracetamol and caffeine using an MOF-199-based electrode," *Journal of Materials Science*, vol. 53, no. 4, pp. 2453–2471, 2018.

[30] H. Wang, X. Yuan, Y. Wu et al., "Synthesis and applications of novel graphitic carbon nitride/metal-organic frameworks mesoporous photocatalyst for dyes removal," *Applied Catalysis B: Environmental*, vol. 174-175, pp. 445–454, 2015.

[31] W.-T. Xu, L. Ma, F. Ke et al., "Metal–organic frameworks MIL-88A hexagonal microrods as a new photocatalyst for efficient decolorization of methylene blue dye," *Dalton Transactions*, vol. 43, pp. 3792–3798, 2014.

[32] V. Stavila, J. Volponi, A. M. Katzenmeyer, M. C. Dixon, and M. D. Allendorf, "Kinetics and mechanism of metal–organic framework thin film growth: systematic investigation of HKUST-1 deposition on QCM electrodes," *Chemical Science*, vol. 3, pp. 1531–1540, 2012.

[33] L. H. Wee, M. R. Lohe, N. Janssens, S. Kaskel, and J. A. Martens, "Fine tuning of the metal–organic framework $Cu_3(BTC)_2$ HKUST-1 crystal size in the 100 nm to 5 micron range," *Journal of Materials Chemistry*, vol. 22, pp. 13742–13746, 2012.

[34] N. M. Mahmoodi and J. Abdi, "Nanoporous metal-organic framework (MOF-199): synthesis, characterization and photocatalytic degradation of basic blue 41," *Microchemical Journal*, vol. 144, pp. 436–442, 2019.

[35] T. V. N. Thi, C. L. Luu, T. C. Hoang et al., "Synthesis of MOF-199 and application to $CO_2$ adsorption," *Advances in Natural Sciences: Nanoscience and Nanotechnology*, vol. 4, no. 3, article 035016, 2013.

[36] X. Zhang, H. Li, X. Lv et al., "Facile synthesis of highly efficient amorphous Mn-MIL-100 catalysts: formation mechanism and structure changes during application in CO oxidation," *Chemistry - A European Journal*, vol. 24, no. 35, pp. 8822–8832, 2018.

[37] L. Cui, D. Zhao, Y. Yang, Y. Wang, and X. Zhang, "Synthesis of highly efficient $\alpha$-$Fe_2O_3$ catalysts for CO oxidation derived from MIL-100(Fe)," *Journal of Solid State Chemistry*, vol. 247, pp. 168–172, 2017.

[38] Y. Yang, H. Dong, Y. Wang, C. He, Y. Wang, and X. Zhang, "Synthesis of octahedral like Cu-BTC derivatives derived from

MOF calcined under different atmosphere for application in CO oxidation," *Journal of Solid State Chemistry*, vol. 258, pp. 582–587, 2018.

[39] P. Sathishkumar, R. Sweena, J. J. Wu, and S. Anandan, "Synthesis of CuO-ZnO nanophotocatalyst for visible light assisted degradation of a textile dye in aqueous solution," *Chemical Engineering Journal*, vol. 171, no. 1, pp. 136–140, 2011.

[40] S. Pal, S. Maiti, U. N. Maiti, and K. K. Chattopadhyay, "Low temperature solution processed ZnO/CuO heterojunction photocatalyst for visible light induced photo-degradation of organic pollutants," *CrystEngComm*, vol. 17, no. 6, pp. 1464–1476, 2015.

[41] L. Xu, B. Wei, W. Liu, H. Zhang, C. Su, and J. Che, "Flower-like ZnO-$Ag_2O$ composites: precipitation synthesis and photocatalytic activity," *Nanoscale Research Letters*, vol. 8, no. 1, p. 536, 2013.

[42] J. Tauc, "Optical properties and electronic structure of amorphous Ge and Si," *Materials Research Bulletin*, vol. 3, no. 1, pp. 37–46, 1968.

[43] K.-F. Lin, H.-M. Cheng, H.-C. Hsu, L.-J. Lin, and W.-F. Hsieh, "Band gap variation of size-controlled ZnO quantum dots synthesized by sol–gel method," *Chemical Physics Letters*, vol. 409, no. 4–6, pp. 208–211, 2005.

[44] Y. Xu and M. A. A. Schoonen, "The absolute energy positions of conduction and valence bands of selected semiconducting minerals," *American Mineralogist*, vol. 85, no. 3-4, pp. 543–556, 2000.

[45] Y. S. Chaudhary, A. Agrawal, R. Shrivastav, V. R. Satsangi, and S. Dass, "A study on the photoelectrochemical properties of copper oxide thin films," *International Journal of Hydrogen Energy*, vol. 29, no. 2, pp. 131–134, 2004.

[46] K. Santra, C. Sarkar, M. Mukherjee, and B. Ghosh, "Copper oxide thin films grown by plasma evaporation method," *Thin Solid Films*, vol. 213, no. 2, pp. 226–229, 1992.

[47] M. V. Lopez-Ramon, F. Stoeckli, C. Moreno-Castilla, and F. Carrasco-Marin, "On the characterization of acidic and basic surface sites on carbons by various techniques," *Carbon*, vol. 37, no. 8, pp. 1215–1221, 1999.

[48] B. Dhale, S. Mujawar, S. Bhattar, and P. Patil, "Chemical properties of n-ZnO/p-CuO heterojunctions for photovoltaic applications," *Der Chemica Sinica*, vol. 5, pp. 59–64, 2014.

[49] H. Seema, K. C. Kemp, V. Chandra, and K. S. Kim, "Graphene–$SnO_2$ composites for highly efficient photocatalytic degradation of methylene blue under sunlight," *Nanotechnology*, vol. 23, no. 35, article 355705, 2012.

[50] T. Shen, Z.-G. Zhao, Q. Yu, and H.-J. Xu, "Photosensitized reduction of benzil by heteroatom-containing anthracene dyes," *Journal of Photochemistry and Photobiology A: Chemistry*, vol. 47, no. 2, pp. 203–212, 1989.

[51] M. J. Islam, D. A. Reddy, J. Choi, and T. K. Kim, "Surface oxygen vacancy assisted electron transfer and shuttling for enhanced photocatalytic activity of a Z-scheme $CeO_2$–AgI nanocomposite," *RSC Advances*, vol. 6, no. 23, pp. 19341–19350, 2016.

[52] H. Fan, X. Zhao, J. Yang et al., "ZnO–graphene composite for photocatalytic degradation of methylene blue dye," *Catalysis Communications*, vol. 29, pp. 29–34, 2012.

[53] Y. Wang, R. Shi, J. Lin, and Y. Zhu, "Significant photocatalytic enhancement in methylene blue degradation of $TiO_2$ photocatalysts via graphene-like carbon in situ hybridization," *Applied Catalysis B: Environmental*, vol. 100, no. 1-2, pp. 179–183, 2010.

[54] P. Du, A. Bueno-Lopez, M. Verbaas et al., "The effect of surface OH-population on the photocatalytic activity of rare earth-doped P25-$TiO_2$ in methylene blue degradation," *Journal of Catalysis*, vol. 260, no. 1, pp. 75–80, 2008.

[55] A. Houas, H. Lachheb, M. Ksibi, E. Elaloui, C. Guillard, and J.-M. Herrmann, "Photocatalytic degradation pathway of methylene blue in water," *Applied Catalysis B: Environmental*, vol. 31, no. 2, pp. 145–157, 2001.

[56] F. Jiang, T. Yan, H. Chen, A. Sun, C. Xu, and X. Wang, "Ag-$C_3N_4$–CdS composite catalyst with high visible-light-driven catalytic activity and photostability for methylene blue degradation," *Applied Surface Science*, vol. 295, pp. 164–172, 2014.

[57] T.-J. Whang, M.-T. Hsieh, and H.-H. Chen, "Visible-light photocatalytic degradation of methylene blue with laser-induced Ag/ZnO nanoparticles," *Applied Surface Science*, vol. 258, no. 7, pp. 2796–2801, 2012.

[58] J.-Z. Kong, A.-D. Li, X.-Y. Li et al., "Photo-degradation of methylene blue using Ta-doped ZnO nanoparticle," *Journal of Solid State Chemistry*, vol. 183, no. 6, pp. 1359–1364, 2010.

[59] D. A. Quang, T. T. T. Toan, T. Q. Tung, T. T. Hoa, T. X. Mau, and D. Q. Khieu, "Synthesis of $CeO_2$/$TiO_2$ nanotubes and heterogeneous photocatalytic degradation of methylene blue," *Journal of Environmental Chemical Engineering*, vol. 6, no. 5, pp. 5999–6011, 2018.